

THESIS FOR THE DEGREE OF DOCTOR OF PHILOSOPHY

**First principles study of tungsten-based alloys:  
From defect thermodynamics to phase diagrams**

LEILI GHARAEI

Department of Physics  
Chalmers University of Technology  
Göteborg, Sweden 2017

First principles study of tungsten-based alloys:  
From defect thermodynamics to phase diagrams

LEILI GHARAEI

ISBN 978-91-7597-571-9

© Leili Gharaee, 2017

Doktorsavhandlingar vid Chalmers tekniska högskola

Ny serie nr 4252

ISSN 0346-718X

Department of Physics

Chalmers University of Technology

SE-412 96 Göteborg, Sweden

Telephone +46 31 772 8417

Cover: Schematic illustration of a binary alloy phase diagram. The heat map represents the temperature change, and the configurations on the x-axis demonstrate different alloy compositions.

Typeset in  $\text{\LaTeX}$  with Linux Libertine and Sans Serif. Figures created using Gnuplot, OVITO [1], Inkscape, and Blender.

Chalmers reproservice

Göteborg, Sweden 2017

First principles study of tungsten-based alloys:  
From defect thermodynamics to phase diagrams  
LEILI GHARAEI  
Department of Physics  
Chalmers University of Technology

## Abstract

Nuclear fusion is a very attractive option for energy production as it is clean, safe and efficient. The major obstacle in construction of fusion power plants is the development of materials that can tolerate the extreme operational condition especially high-energy neutron flux. Tungsten is the prime candidate as armor material in fusion reactors due to its high strength and excellent high temperature properties. Tungsten alloys are interesting in this context because of the transmutation of tungsten to other elements upon neutron irradiation. In this thesis, properties of tungsten alloys were studied by means of first-principles calculations based on density functional theory (DFT). I investigated the thermodynamic and kinetic properties of intrinsic and extrinsic defects in tungsten. Ti, V and Re were shown to trap self-interstitials. Whereas mixed-interstitial migration was found to proceed via a non-dissociative mechanism with a lower barrier than that of vacancies.

A closer look at trapping effects in W-Re, W-V, and W-Ti alloys showed that mixed-interstitials in all systems are strongly attracted to each other with large binding energies. They form interstitial pairs aligned along parallel first-neighbor  $\langle 111 \rangle$  strings. This behavior is caused by the very large and anisotropic strain field of these interstitial defects. Low barriers for defect translation and rotation enable defect agglomeration and alignment even at moderate temperatures. Re-rich clusters that are observed in irradiated tungsten, at concentrations below the solubility limit, may eventually transform into intermetallic phases, which can affect materials hardness and embrittlement. To explain the formation of these precipitates, I carried out DFT calculations to characterize the landscape for diffusion. My results were subsequently used by collaborators to parametrize a kinetic Monte Carlo model. Simulations based on this model showed that both vacancy and interstitial mediated transports control cluster nucleation. Re-rich precipitates were seen to grow by attracting more mixed interstitials bringing solute atoms, which in turn attracted vacancies leading to recombination and solute agglomeration.

The heat of mixing for the previously mentioned alloying elements was investigated further. For W-Ti, the equilibrium phase diagram below 1700 K is not known due to experimental difficulties. The present study revealed a negative heat of formation on the W-rich side, which is consistent with the experimentally observed asymmetric solubility. A revised solubility limit at low temperatures of the W-Ti phase diagram was derived on the basis of these calculations.

Finally I assessed the performance of constraint-based functionals and considered the recently-developed consistent-exchange van der Waals density functional version vdW-DF-cx, the semi-local PBE and PBEsol functionals as well as the AM05 meta-functional. Structural and thermophysical properties of 3d, 4d, and 5d non-magnetic transition metals were computed at finite temperatures. It was shown that overall vdW-DF-cx provides an accurate description of thermophysical properties that is typically superior to the other functionals considered. It can thus be used to study systems that have both sparse and dense electron distributions .

**Keywords:** tungsten alloys, point defects, irradiation, structural materials, first-principles calculations.



## LIST OF PUBLICATIONS

This thesis consists of an introductory text and the following papers:

- I A first-principles investigation of interstitial defects in dilute tungsten alloys**  
Leili Gharaee and Paul Erhart  
Journal of Nuclear Materials **467**, 448-456 (2015).
- II The role of interstitial binding in radiation induced segregation in W-Re alloys**  
Leili Gharaee, Jaime Marian and Paul Erhart  
Journal of Applied Physics **120**, 025901 (2016).
- III Mechanism of Re precipitation in irradiated W-Re alloys from kinetic Monte Carlo simulations**  
Chen-Hsi Huang, Leili Gharaee, Yue Zhao, Paul Erhart and Jaime Marian  
arXiv preprint arXiv:1702.03019 (2017).
- IV Finite-temperature properties of non-magnetic transition metals: Comparison of the performance of constraint-based semi and nonlocal functionals**  
Leili Gharaee, Paul Erhart and Per Hyldgaard  
Physical Review B **95**, 085147 (2017)
- V Structurally driven asymmetric miscibility in the phase diagram of W-Ti**  
Leili Gharaee, Mattias Ångqvist, Magnus Rahm and Paul Erhart  
(In manuscript)

The author's contribution to the papers:

- I The author carried out the calculations, analysis, and wrote most of the paper.
- II The author carried out the calculations, analysis, and wrote most of the paper.
- III The author carried out the DFT and NEB calculations and assisted in writing the paper.
- IV The author did most of the calculations and assisted in writing the paper.
- V The author carried out the DFT calculations, extracted the free energies, constructed the phase diagram and wrote the first draft of the paper.



# Contents

<b>1</b>	<b>Introduction</b>	<b>1</b>
<b>2</b>	<b>Background</b>	<b>5</b>
2.1	Radiation and high energy particles . . . . .	5
2.2	Applications of high energy irradiation . . . . .	6
2.2.1	Nuclear fission reactor . . . . .	6
2.2.2	Nuclear fusion reactor . . . . .	8
2.3	Radiation-induced point defects . . . . .	12
2.3.1	Defects in crystalline materials . . . . .	12
2.4	Tungsten as a first wall material . . . . .	13
2.4.1	Behavior under irradiation . . . . .	13
<b>3</b>	<b>Computational details and methodology</b>	<b>15</b>
3.1	The quantum-mechanical many-body problem . . . . .	15
3.2	The Born-Oppenheimer approximation . . . . .	16
3.3	Density functional theory . . . . .	16
3.3.1	The Hohenberg-Kohn theorems . . . . .	16
3.3.2	The Kohn-Sham equations . . . . .	17
3.3.3	Exchange-correlation functionals . . . . .	18
3.3.4	Plane wave basis sets and pseudopotentials . . . . .	20
3.4	Convergence considerations for point defects calculations . . . . .	20
3.4.1	Size dependence . . . . .	20
3.4.2	Brillouin zone sampling . . . . .	22
3.4.3	Semicore states . . . . .	22
3.5	Point defects thermodynamics . . . . .	23
3.5.1	Defect formation energies . . . . .	23
3.5.2	Formation volume tensors . . . . .	24
3.5.3	Defect kinetics . . . . .	24
3.6	Atomic scale modeling of alloys . . . . .	26
3.6.1	Alloy cluster expansions . . . . .	26
3.6.2	CE construction . . . . .	27
3.6.3	Monte-Carlo simulations . . . . .	28

<b>4</b>	<b>Results and conclusion</b>	<b>31</b>
4.1	Point defects and radiation-induced precipitation . . . . .	31
4.1.1	Paper I . . . . .	31
4.1.2	Paper II . . . . .	33
4.1.3	Paper III . . . . .	34
4.2	Description of thermophysical properties in density functional theory . . . . .	35
4.2.1	Paper IV . . . . .	35
4.3	W-Ti phase diagram . . . . .	36
4.3.1	Paper V . . . . .	37
4.4	Conclusion and outlook . . . . .	39
	<b>Acknowledgments</b>	<b>41</b>
	<b>Bibliography</b>	<b>43</b>
	<b>Papers</b>	<b>51</b>

# Introduction

The world energy demand grows rapidly as the global population expands, countries grow economically, and people desire higher standards of living. In this regard, nuclear fusion is expected to play a key role because it is a clean and sustainable source of energy. Fusion offers important advantages such as no carbon emissions and therefore no air pollution, unlimited fuel supply and intrinsically safe technology, which would make a massive contribution to mitigating concerns about energy safety and climate change.

Currently, three main projects, JET (Joint European Torus), ITER (International Thermonuclear Experimental Reactor), and DEMO (DEMONstration Power Plant), are hoping to pave the way for commercially viable power generation using nuclear fusion.

JET, located in Oxfordshire, UK, set the world record in 1997, for achieving (16 MW) fusion power in deuterium-tritium operation [2], the fuel proposed for the first generation of fusion power plants. The follow-up programme, ITER, will attempt to go one step further and generate more power, 500–700 MW [3], than is used to start the process. This project attempts to demonstrate the feasibility of magnetic-confinement nuclear fusion and is currently under construction in Cadarache, France.

ITER, however, does not represent the final step; It is the bridge toward DEMO, the first plant that will demonstrate large-scale production of electrical power and tritium fuel self-sufficiency. Planning for DEMO design and operation is still ongoing as it depends also on the results of the early years of operation in ITER. Conceptual designs of DEMO sketch a machine that is larger than ITER with the ability to produce fusion power output in range of 30 to 50 times larger than the input power. The size of the machine is determined by the radius of the plasma cross-section, which is confined in a doughnut-shaped vessel. Its radius for DEMO ranges from 6 to 10 metres. In comparison, the radius in ITER measures 6.2 meters and that of the largest tokamak in operation, JET, measures about half of that [2, 3, 4, 5].

One of the main concerns during reactor operation is the severe radiation conditions expected in fusion reactors, which requires the development of new materials able to withstand the harsh environment including thermal loads and radiation. The high-energy and high-intensity neu-

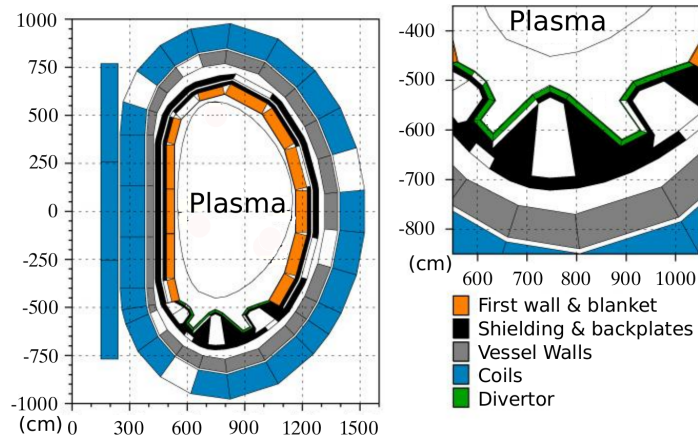


Figure 1.1: A toroidal section through a simplified DEMO model. (Source of image: Ref. [6])

tron fluxes produced by the fusion plasma have a significant lifetime-limiting impact on fusion reactor components via altering mechanical and thermophysical properties.

The fusion reaction takes place in the reactor chamber inside a vacuum vessel. The vacuum vessel is the container, which houses the fusion reaction and acts as a first safety containment barrier. At the very bottom of the vacuum vessel, the divertor is located as the next plasma-facing component, see Fig. 1.1, and its function is to extract heat and helium ash –both products of the fusion reaction– and other impurities from the plasma.

The average neutron fluence on the first wall material in ITER is  $0.57\text{--}0.8\text{ MWa/m}^2$  and the neutron flux at the first wall will reach up to  $\sim 10^{23}\text{ n/m}^2\text{s}$ . The average neutron fluence for DEMO is expected to be up to  $15\text{ MWa/m}^2$  with neutron fluxes being at least a hundred times larger. The plasma current varies from  $4.8\text{ MA}$  in JET to  $15\text{--}17\text{ MA}$  in ITER and  $30\text{ MA}$  in DEMO. As a result, higher heat flux and higher neutron loads in DEMO, will lead to higher displacements per atom (dpa) of up to  $\sim 30\text{ dpa}$ , compared to ITER with  $< 3\text{ dpa}$  in a full operational life [3, 4, 5, 7, 8, 9, 10, 11].

More energetic fusion neutrons in higher doses cause far more damage and transmutation products. Transmutation in turn, results in a change in material composition and will thus influence thermal, chemical, and mechanical properties of the wall materials, which eventually has a great influence on the resistance to radiation.

While for JET, initially carbon tiles were used to cover the interior wall of the vacuum vessel, they were recently replaced with beryllium and tungsten tiles. In ITER, beryllium has been chosen to cover the first wall, while interior surfaces of the vacuum vessel will be made of high-strength copper and stainless steel.

Since the size of the vacuum vessel dictates the volume of the fusion plasma, DEMO will produce a greater amount of power and higher radiation load compared to ITER and therefore stronger materials are required. In this regard tungsten is considered for structural applications in fusion reactors due to its superior high temperature properties. Plasma-facing components

---

of the divertor, which withstand the highest surface heat loads in ITER, are being made of tungsten [3, 4, 5, 7].

Tungsten has a high melting point, low coefficient of thermal expansion, high thermal conductivity, and excellent resistance to physical sputtering. This combination of properties makes tungsten an attractive choice as a coating material on the high heat flux components.

Yet, tungsten generally exhibits ductile behavior at high temperatures and brittle behavior at low temperatures. The ductile operating window for tungsten is about 700-1200 °C, and tungsten exhibits brittle behavior at temperatures lower than about 300 °C. Its ductile to brittle transition temperature (DBTT) lies between 150 °C and 400 °C [9]. The DBTT for tungsten is known to be relatively high, however its exact range is very much dependent on the details of the manufacturing process and the history of the material. The operational temperature for plasma facing components at the ITER divertor ranges from ~200 °C at water cooled operation to 3000 °C at full operation, which also include the temperature range that tungsten shows brittle behavior. To solve this problem, alloying, for example by Re, has been suggested as a means to lower temperature range in which, the fracture mode of pure tungsten changes from ductile to brittle [4, 9, 11, 12, 13, 14, 15].

Alloy formation will also occur naturally due to nuclear transmutation caused by high energy neutron exposure. In this fashion, pure tungsten will gradually evolve into an W-Re-Os-Ta alloy [6, 16, 17]. As an example, the variation in concentrations of He, Re and Ta, produced in pure tungsten under neutron irradiation as a function of position in the divertor and first wall of a DEMO design is presented in Fig. 1.2.

Alloying either intentionally or implicitly affects many properties of importance such as mechanical performance, thermal conductivity, swelling resistance and oxidation behavior under irradiation. While these properties are reasonably well understood for pure tungsten, the situation is quite different in the case of alloys, especially under irradiation conditions.

Irradiation leads to the localized production of lattice defects such as vacancies and interstitials. Whereas vacancies are relatively immobile, interstitials in pure tungsten, which are commonly referred to as self-interstitial atoms, can readily migrate allowing for efficient defect recombination, which is an important factor with respect to radiation tolerance. In an alloy an attractive interaction between solute atoms and interstitials can lead to trapping of intrinsic defects, increasing the defect density after bombardment and thus accelerating damage build-up. Thus, while alloying might improve mechanical properties it can potentially simultaneously cause a degradation of the irradiation tolerance.

Void induced swelling is another challenge for tungsten as a structural material. Swelling causes dimensional changes and variations in materials properties resulting in serious problems for the reactor design. The swelling of tungsten is shown to be strongly reduced when alloyed with rhenium [18].

In addition, specific developments are aimed at suppressing the production of volatile tungsten oxide in case of a loss-of-coolant accident with air ingress so as to reduce the risk of releasing radioactive material. One proposed solution is to add small amounts of silicon and chromium to tungsten, which leads to a glassy protection layer on the tungsten surface and can reduce the tungsten oxidation rate by up to four orders of magnitude [13].

In the present thesis, I employ computational calculations to gain insight into the response

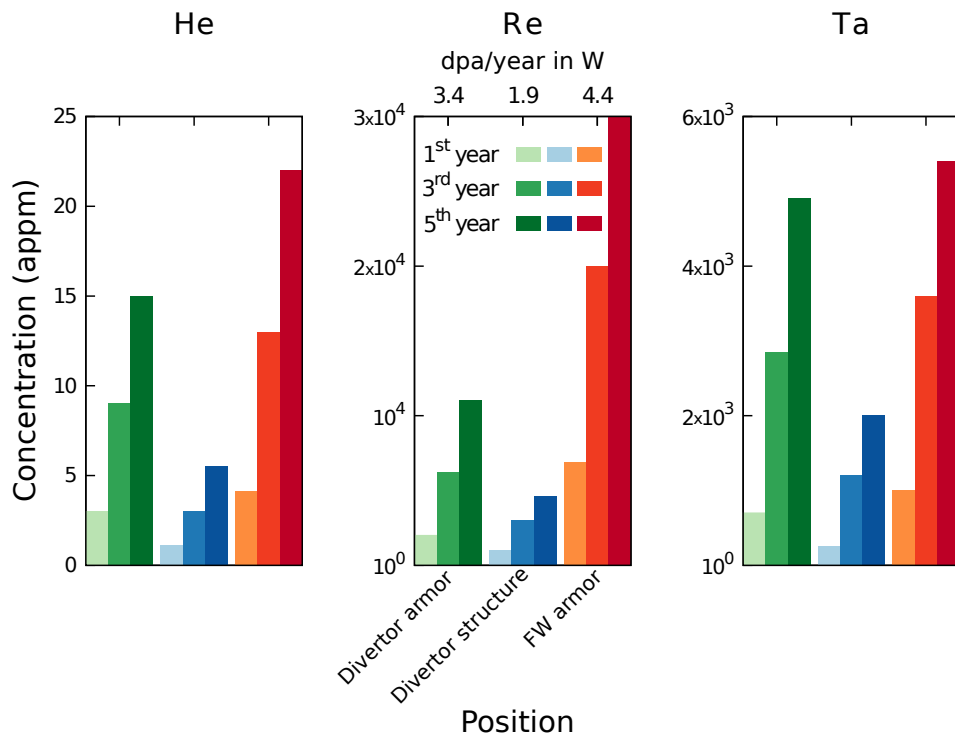


Figure 1.2: Variation in concentrations of He, Re and Ta, produced in pure tungsten under neutron irradiation as a function of position (and depth) in the divertor and first wall of the DEMO design. The equivalent dpa/year in pure tungsten are also given for each position. Units of concentrations are given in atomic parts per million (appm). (Source of data for the figure: Ref. [6])

of the material to neutron irradiation, enabling the assessment of the structural integrity of components in a fusion power plant. I provide an assessment of tungsten-based alloys for applications in fusion environments by studying different types of point defects, their interactions and diffusion as well as phase diagrams.

## Background

### 2.1 Radiation and high energy particles

Irradiation is the process of exposing an object to radiation. One of the immediate effects of irradiation of a material is the displacement of some atoms from their equilibrium lattice sites. Energies vary for different radiation sources and high energy particles have a stronger impact on the material compared to the low energy ones.

Charged particles like electrons and ions, depending on their mass, interact with materials and lead to scattering. For example a 1 MeV electron in copper (Cu) can penetrate 350  $\mu\text{m}$  on average, while a proton of the same energy penetrates 380 nm in Cu on average. Due to its larger mass, a proton produces more damage, loses more energy while scattering, and stops in lower depth compared to electrons. A gold (Au) ion of the same energy penetrates only 96 nm in Cu as it is heavier [19, 20].

Neutrons are not stable elementary particles and have a half-life of about 11 minutes. Free neutrons do, however, exist in situations like natural radioactive decay, which produces neutrons with energies of a few MeV. Reactions taking place in reactors produce neutrons with energies of about 2 and 14 MeV for nuclear fission and fusion respectively. Whereas neutrons do not interact significantly with electrons in the material, they interact with the atomic nuclei via the nuclear forces. Based on their energies, neutrons can interact via several different processes. While low energy neutrons interact with atoms via elastic scattering, for neutrons with energies above 1 MeV, inelastic neutron scattering becomes important. During this process, the kinetic energy is not preserved and is partially transferred into the excitation of the nucleus.

Nuclear reactions become significant for neutrons with energies above 8 MeV. During this process a nucleus absorbs the high energy neutron and generates transmutation products. This reaction is very important as it changes the composition of the material and may thereby eventually alter the properties of the material and in particular its response to irradiation [19].

## 2.2 Applications of high energy irradiation

High energy irradiation is an important research area with applications in various fields of technology, including diagnostic techniques and energy generation in nuclear power stations. High energy radiation is widely used in radiography for imaging the interior of objects, and in radiotherapy for medical reasons. The radiation energy varies from kilo to mega electron volts and even higher based on the type of the treatment [21, 22]. Exposure to irradiation in very large doses or for long times can be harmful and destructive for healthy tissue and therefore the dose and duration need to be selected carefully.

Another application of high energy irradiation is energy generation in nuclear power stations, where the energy of fission or fusion reactions is converted into heat and subsequently electricity. Like medical irradiation and all its other applications, irradiation in nuclear reactors has a twofold effect. On one hand, irradiation energy is converted into useful energy and on the other hand, it damages the surrounding material and degrades its properties. The issue of finding materials that can withstand high irradiation is the subject of extensive research especially for fusion reactors. In the following two subsections, a more detailed description of fission and fusion reactors is presented.

### 2.2.1 Nuclear fission reactor

#### 2.2.1.1 Background

Nuclear fission is a process in which the nucleus of an atom splits. The splitting of a nucleus occurs due to radioactive decay or by bombardment by other subatomic particles. In either case, the resulting components have less combined mass compared to the original nucleus and the missing mass is converted into kinetic energy.

Radioactive fission happens primarily with the heavier elements. In this process, a nucleus of an unstable atom loses energy by emitting for instance alpha particles, beta particles, gamma rays and neutrons. Isotopes of uranium (U) by releasing hundreds of MeV energy decay to fission products such as krypton (Kr), barium (Ba), technetium (Tc), ruthenium (Ru), or palladium (Pd).

In the second mechanism, when a large fissile nucleus such as uranium-235 ( $^{235}\text{U}$ ) or plutonium-239 ( $^{239}\text{Pu}$ ) absorbs a neutron, it may undergo nuclear fission. The heavy nucleus splits into two or more lighter nuclei –the fission products– releasing kinetic energy, gamma radiation, and free neutrons. A portion of these neutrons may later be absorbed by other fissile atoms and trigger further fission events, which will release more neutrons. This is known as a nuclear chain reaction. This procedure releases a significant amount of energy compared to the energy of the neutron that started the procedure. Bombarding uranium with neutrons of a few eV, splits the nucleus, releasing a few hundred MeV and neutrons of  $\sim 2\text{-}3$  MeV [23, 24]. Controlled reactions of this sort are used to release energy within nuclear power plants. Uncontrolled reactions can fuel nuclear weapons.

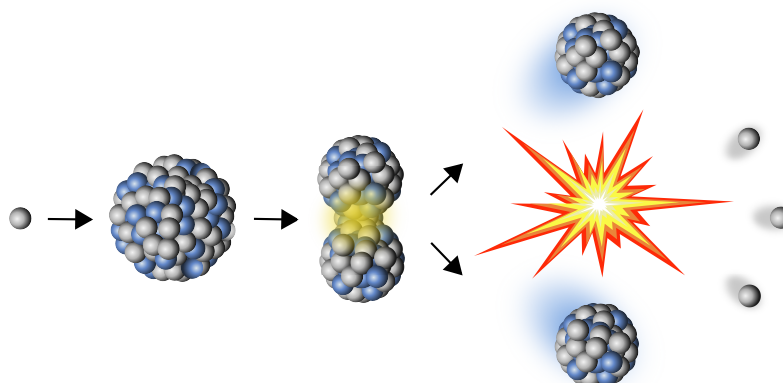


Figure 2.1: Schematic illustration of a fission process in which the nucleus of an atom breaks into smaller nuclei due to bombardment by a neutron, which results in the production of energy.

### 2.2.1.2 Fission reaction in nuclear reactors and electricity generation

Similar to the plants that burn coal, oil and natural gas, nuclear plants produce electricity by boiling water into steam. This steam drives turbines that produce electricity. Nuclear fuel for this process, includes two types of uranium,  $^{238}\text{U}$  and  $^{235}\text{U}$ , as well as plutonium. Fuel comes in the shape of solid ceramic pellets that are packaged into long tubes.  $^{238}\text{U}$  constitutes an important share of the fuel,  $^{235}\text{U}$  is, however, more unstable and splits quickly. This process releases neutrons, which start the chain fission reaction. Neutrons hit other uranium atoms resulting in the release of more neutrons along with heat. When a chain reaction occurs, fission becomes self-sustaining.

In order to control the nuclear reaction, special rods are inserted among the fuel tubes in order to slow down or accelerate the reaction. They are composed of chemical elements such as boron, silver, indium and cadmium that are capable of absorbing many neutrons without undergoing fission themselves [25, 26]. Fuel tubes in the reactor are surrounded by water. The heat produced during the fission reaction turns this water into steam. The steam drives turbines that power generators to create electricity.

Nuclear power provides many big advantages. It is a clean energy and does not contribute to climate change. Almost no greenhouse gases such as carbon dioxide are emitted into the atmosphere. In addition, nuclear fission has large power-generating capacity and produces roughly a million times more energy per unit weight than fossil fuel alternatives.

There are, however, negative sides to this way of energy production. Uranium sources are just as finite as other fuel sources and are expensive to mine, purify and transport. They also always possess a contamination risk. In addition, during nuclear reactor operation, a high-level radioactive waste is generated from the fuel. Lower-level radioactive waste is also generated in radiated parts and equipments, and disposal of radioactive waste is a complicated problem.

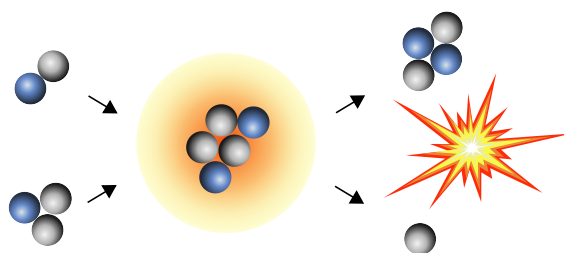


Figure 2.2: Schematic illustration of a fusion process in which deuterium and tritium fuse together, form a helium nucleus and a neutron, and release a large amount of energy.

## 2.2.2 Nuclear fusion reactor

With its high energy yield, low nuclear waste production, lack of air pollution and virtually limitless fuel available, fusion, the same source that powers stars, could provide an alternative to conventional energy sources.

### 2.2.2.1 Background

Fusion is a nuclear reaction that occurs when two or more light nuclei collide at very high speed, combine, and form a heavier atomic nucleus. A great amount of energy is released during this process in which matter is not conserved. As the total mass of the new atom is less than that of the two, from which it was formed, thus some of the matter of the fusing nuclei is converted into energy.

Fusion is the process at the core of the Sun and other stars, where hydrogen nuclei collide, fuse into heavier helium atoms and release enormous amounts of energy [27, 28]. Creating a controlled fusion reaction on Earth, however, has proven to be very difficult so far, as the two protons or hydrogen nuclei repel each other. Very specific conditions including enormous temperature and pressure are required to make it happen. The tremendous heat of the Sun, which is around ten million degrees, and its high pressure are achieved by the large mass of the Sun and the force of gravity compressing this mass in the core. This heat accelerates the atoms to the point where their momentum overcomes the Coulomb repulsion [28].

Scientists are nowadays looking for ways to control the energy produced during nuclear fusion. To this end, very high temperatures of about 100 million degrees are required, under which a hydrogen plasma is formed. Plasma is an extremely high-energy state of matter with electrons separated from the nuclei. The system is overall charge neutral yet composed of charged particles and as a result it is responsive to electromagnetic forces [28].

There are different atomic combinations, which can lead to a fusion reaction, among which, the deuterium-tritium (D-T) reaction has been identified as the most efficient combination for generating power on Earth. ITER and the future demonstration power plant DEMO, will use this combination of elements to fuel the fusion reactor [4]. In this reaction, deuterium and tritium nuclei combine to form a nucleus of Helium-4, release a neutron, and an energy of 17.6

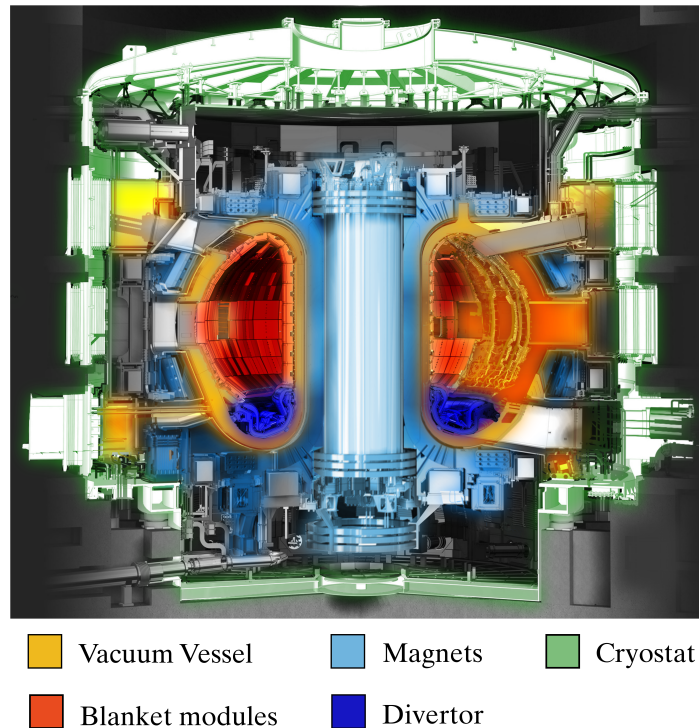


Figure 2.3: ITER tokamak reactor and its main parts including vacuum vessel, blanket modules, magnets, divertor, and the cryostat. (Source of image: Ref. [4]. The image is further customized for better illustration.)

MeV per reaction, see Fig. 2.2. Considering that billions of reactions occur in each second, one can realize the potential efficacy of the fusion reaction for generating power [28].

Deuterium is a non-radioactive isotope of hydrogen, containing a single proton and a neutron. It is widely available as it can be distilled from all forms of water. Tritium is the other isotope of hydrogen and contains one proton and two neutrons. It is a fast-decaying radioactive element, which is more challenging to locate in large quantities on Earth. Rather than attempting to find it naturally, the most reliable method is to bombard lithium with neutrons to create this element. During the fusion reaction in ITER, tritium is produced, when neutrons escaping the plasma interact with lithium contained in the blanket wall of the tokamak [4].

### 2.2.2.2 The working principle of a fusion reactor

In large scale commercial designs of fusion reactors, heat generated from the fusion reaction is used to operate steam turbines that drive electrical generators as in existing fossil fuel and nuclear fission power stations.

Fusion reactors are these days, however, in experimental stages and various operational concepts have been developed so far for power generation. The two main approaches to initiate

## Chapter 2. Background

---

nuclear fusion reactions on Earth are inertial confinement fusion and magnetic confinement fusion.

Inertial confinement is a fusion energy approach that uses high-energy laser beams to initiate the reaction by heating up and compressing a fuel target. Fuel is often provided in the form of a pellet and consists of a deuterium-tritium mixture. High energy flux laser beams are directed onto the fuel pellet, which leads to the outer layer evaporating/exploding outward. The reaction force compresses the rest of the pellet inwards. The density of the core of the pellet and subsequently its temperature rise enormously enabling it to reach the ignition point for fusion.

In the magnetic confinement approach, which is relatively more developed and well funded, neutral particle beams from accelerators are used to heat a stream of hydrogen gas and turn it into a plasma by transferring kinetic energy. This plasma is squeezed by super-conducting magnets, forcing the plasma nuclei closer to each other and thereby allowing a fusion reaction to occur. The most efficient shape for compressing the plasma is a doughnut shape or toroid in which, hot plasma is circulated in a magnetically confined ring. A reactor of this shape is called a tokamak. When completed, ITER will be the world's largest tokamak [3, 4].

The main parts of the ITER tokamak reactor, as shown in Fig 2.3, are vacuum vessel, blanket modules, magnetic field coils, cooling equipment and divertor.

The vacuum vessel is a torus-shaped double-wall structure made of steel, which houses the fusion reaction. It provides a high-quality vacuum for the plasma and serves as the first safety barrier for heat and radiation produced by the fusion reactions. Between the two walls of vacuum vessel, cooling water is circulating in order to remove the heat, which is generated during operation.

Blanket modules are located at the inner surface of the vacuum vessel and shield vacuum vessel and magnets from fusion reaction products, see Fig. 2.3. As the part which directly faces the hot plasma, neutrons reach the blanket first, slow down and lose their kinetic energy. The energy is subsequently transformed into heat and collected by the cooling water system. Eventually the heat is used to produce electricity. There are 440 blanket modules in ITER each of them measures 1×1.5 square meters and weighs up to 4.6 tonnes, see Fig. 2.3. As blanket modules face the radiation directly, the design and the choice of material for them is critical and dependent on the position in the inner surface. Beryllium for covering the first wall, and copper and stainless steel for the rest of the blanket, are the materials that have been chosen to construct blanket modules.

In ITER, magnets are placed around the vacuum vessel as well as the center in the shape of a solenoid. The function of the magnet system is to confine, shape, and control the plasma inside the vacuum vessel. It will weigh 10,000 tonnes and when completed will be the largest and most powerful magnet in the world. All ITER coils are superconducting and compared to conventional magnets carry higher current and generate a stronger magnetic field. To achieve superconductivity, magnets are cooled down using liquid helium, to temperatures of around 4 Kelvin (-269 °C). Niobium-tin ( $\text{Nb}_3\text{Sn}$ ) and niobium-titanium (Nb-Ti) have been used so far to build the magnets.

The ITER cryostat is manufactured from stainless steel. It surrounds vacuum vessel and magnets and provides high vacuum and ultra-cool environment for the inner parts. With a weight of 3800 tonnes, the ITER cryostat is the largest vacuum chamber in the world with the



Figure 2.4: ITER divertor, which is placed at the bottom of the vacuum vessel, withstands the highest heat flux from the ITER plasma. (Source of image: Ref. [4])

ability to provide a vacuum that is 1 million times less dense than air.

Finally the divertor, situated at the bottom of the vacuum vessel, extracts waste gas and impurities from the plasma, which are generated during the fusion reaction, see Figs. 2.3 and 2.4. It comprises two main parts, a supporting structure made primarily from stainless steel, and the plasma-facing armor component, which will be made of tungsten. Tungsten has the highest melting point of all metals and it makes it a suitable choice for the plasma-facing components of the ITER divertor as it will be exposed to the highest heat load in the machine [3, 4].

In ITER, first a stream of deuterium and tritium fuel is heated to form a high-temperature plasma. In order to bring the plasma to about 150 million degrees Celsius, several heating methods will work concurrently. One source of heat is the changing magnetic field, which also controls the plasma. Magnetic fields induce a high-intensity electrical current that when it travels through the plasma, energizes electrons and ions and causes them to collide. Such collisions create resistance, which results in heat, but as the temperature of the plasma rises, this resistance—and therefore the heating effect—decreases. In order to reach higher temperatures, additional heating methods like neutral beam injection must be applied from outside the tokamak. A neutral beam injector, as an external source of heating, injects high-energy particles from the accelerator into the plasma. These neutral particles collide with plasma particles and transfer their energy to them. This helps the plasma to reach the temperature necessary for fusion.

When the fusion reaction occurs, the high energy neutrons generated during the fusion reaction will be absorbed by lithium blankets and produce more tritium fuel. This process in turn, increases the temperature of the blanket, for which cooling mechanisms are employed to decrease the temperature of the blanket by using the heat for turning water into steam and eventually producing electricity [3, 4, 29].

It has, however, been one of the big challenges to come up with a non-destructive way of performing fusion. Interior walls of the reactor are exposed to high energy neutron irradiation and high heat fluxes. High-energy fusion neutrons, when they escape the plasma, can strongly interact with the atoms of the wall material and cause structural changes via processes like atomic displacements and elemental transmutations, which may eventually lead to material degradation. It is, as a result, an essential step in fusion research to find suitable wall materials with high radiation tolerance at high temperatures.

## 2.3 Radiation-induced point defects

During the operation of a nuclear reactor, the immediate surrounding of the plasma is exposed to extreme neutron irradiation. When a neutron enters the wall material a collision happens and some atoms are displaced from normal lattice sites. The atomic displacement process starts with the creation of a primary knock on atom (PKA), which is any target atom struck by neutron as irradiation particle.

Neutron-atom interactions can be elastic or inelastic. Elastic interactions are important in the context of damage or defect generation as they can produce Frenkel pairs (vacancies and self-interstitials) and rearrange atoms on their lattice sites. During elastic collisions, the initial kinetic energy of PKA dissipates via two processes. The first part is lost to electronic excitations, which do not contribute to damage creation but mainly act as a viscous medium. The second dissipation channel is by elastic collisions with surrounding atoms, subsequently resulting in a cascade of collision events. Inelastic excitations, on the other hand, have a small direct effect on damage production and a significant part of the neutron energy is transferred to excite the nucleus that it strikes.

In addition to creation of the PKA, which causes displacement damage, neutron-atom interaction can lead to the transmutation. Nuclear reactions can create foreign elements or impurities, which can undergo further collisions themselves. Under high energy irradiation, the concentration of such defects increases dramatically, which affects the physical properties of the material. As this eventually changes the performance of material under irradiation, one needs to develop a detailed understanding of the structure and behavior of such defects.

### 2.3.1 Defects in crystalline materials

In a perfect crystal in equilibrium, all atoms are at their specific atomic sites. Real crystals and particularly materials exposed to irradiation, however, contain imperfections such as point, line, surface (planar) or volume (bulk) defects, which locally disturb the regular arrangement of the atoms.

Defects can be classified according to their dimensionality. Zero dimensional defects are called point defects and are the main focus of this work. There are two types of point defects in materials. Native defects are intrinsic to the material, such as vacancies (missing atoms) and self-interstitials (additional atoms incorporated on sites other than substitutional sites), see Fig. 2.5. In addition to intrinsic point defects, crystals may also contain extrinsic point defects, which are impurity atoms on substitutional or interstitial sites.

In addition to point defects, there are one dimensional defects, called line defects. An example of these defects are dislocations, which govern plastic deformation in many materials. Planar defects such as stacking faults and grain boundaries, are two dimensional defects. Volume or bulk defects are three dimensional crystal defects. Precipitates, voids and bubbles belong to this category of defects [30].

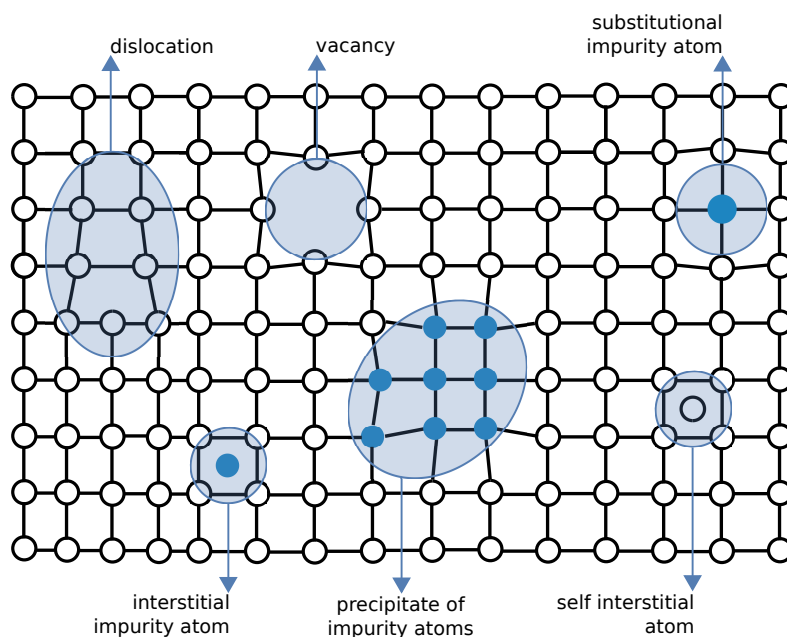


Figure 2.5: Schematic illustration of a number of crystallographic defects.

## 2.4 Tungsten as a first wall material

Plasma-wall interaction issues are among the most serious obstacles to the realization of fusion energy production. This interaction is a key factor, which determines the safety and lifetime of the wall components and subsequently the overall cost-effectiveness of the facility.

The structural materials have to meet a vast numbers of criteria to be safe, suitable and efficient for a fusion environment. For example they have to show low erosion, which favors heavy elements such as Mo or W. It is also required for these materials to have high melting point and high thermal conductivity, for which the candidate materials are C and W. With regard to low radiation loss and low nuclear activation lighter elements such as Be and C are good candidates. Low propensity to absorb tritium is also very important; W and –to a lesser extent– steel and beryllium meet this criterion.

Tungsten and tungsten alloys are therefore considered for structural applications in fusion reactors, especially for armor materials at the divertor and first wall [11, 31, 32, 33]. In ITER, tungsten is suggested for plasma-facing armor components of the divertor as the region with highest heat load, see Fig. 2.3 and 2.4 and to this end, the behavior of these materials under irradiation has to be investigated carefully.

### 2.4.1 Behavior under irradiation

During fusion reactor operation, as a result of high energy neutron exposure, displacement damage occurs and several defects are formed and interact. Nuclear transmutation happens as

well, and results in compositional changes and additional defect interactions. Tungsten is also exposed to hydrogen and helium particles arriving at its surface from the plasma.

Vacancies and interstitials are among the point defects generated under irradiation. Whereas vacancies are relatively immobile, interstitials in pure tungsten can readily migrate, allowing for efficient defect recombination, which is an important factor with respect to radiation tolerance [34, 35, 36]. In an alloy, an attractive interaction between solute atoms and interstitials can lead to trapping of defects, increasing the defect density compared to the pure material. Thus alloying can potentially cause a degradation of the irradiation tolerance.

Tungsten transmutes to rhenium, osmium and tantalum in a fusion neutron environment. At the first wall armor of a nuclear fusion device, it has been estimated that after five years of operation, pure tungsten transmutes into an alloy containing Re and Ta with concentration of 3% Re and 0.6% Ta [6], see Fig. 1.2. Another study predicted that W transmutes to an end-of-service alloy composition of approximately 91 at% W, 6 at% Re and 3 at% Os at the first wall armor [37]. The amount of He produced in the divertor armor was found to be negligible compared to other transmuted elements. After a five-year full-power irradiation the He concentration was found to be about 20 appm (0.0020%) or less depending on position [6, 37]. The amount of transmuted elements in armor tungsten varies with the magnitude of the neutron flux and the position in the first wall.

In addition to neutrons, tungsten is also exposed to hydrogen particles. Under continuous high-flux radiation at moderate temperatures (<800 K) blistering occurs for tungsten surfaces. The hydrogen concentration can locally increase and exceed the solubility limit of the tungsten, which may be the cause of blistering [38, 39].

Blistering also occurs by helium bombardment. Formation of holes and bubbles by helium at higher temperatures (>1600 K) is a drawback of tungsten under irradiation conditions. The formation of these defects has been attributed to the accumulation of helium in defects and vacancy sites. The size of such nanostructures is found to be dependent on the surface and exposure temperature, and the incident ion energy [39, 40, 41, 42].

Finally tungsten exhibits brittle behavior at low temperatures and ductile behavior at high temperatures. The brittle-to-ductile transition temperature (BDTT) of pure tungsten is high, which poses a challenge with respect to its applications in fusion environment [11, 14, 43]. It has been found that the ductility of tungsten can be improved by alloying with rhenium, which is also a transmutational element in tungsten [16, 44, 45]. On the other hand, Re and Os are shown to precipitate under irradiation with the solute concentration below their solubility limit. Such radiation-induced precipitation (RIP) of Re is observed in W in the form of intermetallic  $\sigma$  and  $\chi$  phases. Os is also seen to precipitate in W under irradiation and the crystal structure of the precipitate is close to the  $\sigma$  phase. Such incoherent precipitates can hinder dislocation motion and eventually lead to radiation hardening and embrittlement. In this sense, irradiation of W would be harmful [37].

# Computational details and methodology

## 3.1 The quantum-mechanical many-body problem

In principle, most properties of a system can be derived from the quantum mechanical wave function of the system. This wave function can be obtained by solving the time independent Schrödinger equation

$$H\Psi(\mathbf{r}_1, \mathbf{r}_2, \dots, \mathbf{R}_1, \mathbf{R}_2, \dots) = E\Psi(\mathbf{r}_1, \mathbf{r}_2, \dots, \mathbf{R}_1, \mathbf{R}_2, \dots). \quad (3.1)$$

Here  $\Psi(\mathbf{r}_1, \mathbf{r}_2, \dots, \mathbf{R}_1, \mathbf{R}_2, \dots)$  is the quantum mechanical wave function of the system and  $\mathbf{r}_i$  and  $\mathbf{R}_I$  denote the positions of the  $i$ th electron and the  $I$ th nucleus.  $E$  corresponds to the ground state energy of the system.

The complete Hamiltonian operator of the system is

$$H = -\frac{1}{2} \sum_i \nabla_i^2 - \frac{1}{M_I} \sum_I \nabla_I^2 + \frac{1}{2} \sum_{i \neq j} \frac{1}{|\mathbf{r}_i - \mathbf{r}_j|} - \sum_{i,I} \frac{Z_I}{|\mathbf{r}_i - \mathbf{R}_I|} + \frac{1}{2} \sum_{I \neq J} \frac{Z_I Z_J}{|\mathbf{R}_I - \mathbf{R}_J|}, \quad (3.2)$$

where atomic units have been used ( $\hbar = m_e = e = 4\pi\epsilon_0 = 1$ ) and  $Z_I$  and  $M_I$  denote charge and mass of the nuclei, respectively. Equation (3.2) can be written as

$$H = T_e(\mathbf{r}) + T_N(\mathbf{R}) + V_{ee}(\mathbf{r}) + V_{eN}(\mathbf{r}, \mathbf{R}) + V_{NN}(\mathbf{R}), \quad (3.3)$$

where  $T_e$  and  $T_N$  are the kinetic energy operators for the electrons and nuclei respectively and  $V_{ee}$ ,  $V_{eN}$ , and  $V_{NN}$  represent the potentials due to Coulomb interactions between electrons and nuclei.

Obtaining a direct numerical solution for the Schrödinger equation is a difficult task because any finite-size piece of material contains a number of electrons and nuclei on the order of Avogadro's constant ( $N_A \sim 10^{23}$ ). Since the exact solution is only possible for very small systems, simplifications and approximations to this equation are required.

## 3.2 The Born-Oppenheimer approximation

A key point when applying quantum mechanics to atoms is that atomic nuclei are much heavier than individual electrons, which means that electrons respond much more rapidly to changes in their surrounding than the nuclei. The Born-Oppenheimer approximation takes advantage of this observation and makes the assumption that the ions are stationary and their motion can be treated classically, while solving the electronic Schrödinger equation. As a result, the physical problem is split into two parts, the electronic structure problem and the ionic problem. The wave function of the system then becomes the product of electronic and ionic wave functions, and the electronic Hamiltonian reduces to

$$H_e = T_e(\mathbf{r}) + V_{ee}(\mathbf{r}) + V_{ext}(\mathbf{r}, \mathbf{R}), \quad (3.4)$$

where  $T_e$  and  $V_{ee}$  have been introduced above, and  $V_{ext}$  is the external potential from the nuclei including the electrostatic interactions between nuclei. In this approximation, wave function and ground state energy depend parametrically on the positions of the nuclei

$$H\Psi(\{\mathbf{r}\}; \{\mathbf{R}\}) = E(\{\mathbf{R}\})\Psi(\{\mathbf{r}\}; \{\mathbf{R}\}). \quad (3.5)$$

Here, the function  $E(\{\mathbf{R}\})$  represents the so-called Born-Oppenheimer potential energy surface, and the nuclei are considered as classical point particles, which move on the Born-Oppenheimer potential energy surface.

Despite the fact that at this point the Hamiltonian of the system became simpler, see Eq. (3.4), still a complex term remains in the formula. The second term, which represents the electron-electron interactions requires all the electrons in the system to be treated simultaneously. For the hydrogen atom it is possible to obtain an exact numerical solution to the Schrödinger equation using this Hamiltonian, but for larger systems a different approach is required.

## 3.3 Density functional theory

Density functional theory (DFT) was developed as a means to solve the Schrödinger equation for a large number of atoms. In quantum mechanics, the wave function for a system of  $N$  interacting electrons is a function of the positions of all electrons in the system, equivalent to  $3N$  variables. In density functional theory, the problem of determining this quantum mechanical wave function is replaced by the problem of finding the electron density of the ground state. The electron density is only a function of three spatial coordinates, which simplifies the problem considerably.

### 3.3.1 The Hohenberg-Kohn theorems

The entire field of density functional theory rests on two fundamental theorems proved by Kohn and Hohenberg and the derivation of a set of equations by Kohn and Sham in the mid-1960s [46, 47].

The first theorem proved by Hohenberg and Kohn states that the ground state wave function is a unique functional of the ground state electron density [46]. This implies that when the ground state density is known, the ground state wave function, energy and all other ground state properties of the system can be determined.

The second theorem states the relation between energy and the ground state density. For a system with electron density  $n(\mathbf{r})$ , the energy can be expressed as a functional of the density

$$E[n(\mathbf{r})] = F[n(\mathbf{r})] + \int n(\mathbf{r}) V_{\text{ext}}[n(\mathbf{r})] dr, \quad (3.6)$$

in which,  $F[n(\mathbf{r})]$  contains the kinetic energy and contributions from electron-electron interactions. The minimum of the energy functional is given by the ground state density  $n_0(\mathbf{r})$  and corresponds to the ground state energy  $E_0$  of the system

$$E_0 = E[n_0(\mathbf{r})] = \min_{n(\mathbf{r})} E[n(\mathbf{r})]. \quad (3.7)$$

Thus, by minimizing the energy functional, the ground state electron density can be found. However, this is still a complex problem as the functional, which contains all effects of electron-electron interactions, is unknown.

### 3.3.2 The Kohn-Sham equations

In 1965 Kohn and Sham [47] presented a scheme that replaces the problem of *interacting electrons in an external potential* with the problem of *noninteracting electrons in an effective potential*. They suggested that the unknown functional  $F[n(\mathbf{r})]$  can be divided into three terms

$$F[n(\mathbf{r})] = T_s[n(\mathbf{r})] + E_H[n(\mathbf{r})] + E_{xc}[n(\mathbf{r})], \quad (3.8)$$

where  $T_s$  is the kinetic energy of the non-interacting electrons and  $E_H[n]$  is the Hartree energy given by

$$E_H[n(\mathbf{r})] = \int \frac{1}{2} \frac{n(\mathbf{r})n(\mathbf{r}')}{|\mathbf{r} - \mathbf{r}'|} d\mathbf{r}d\mathbf{r}'. \quad (3.9)$$

The third term,  $E_{xc}[n]$ , is the energy due to exchange and correlation effects. It contains many-body contributions to the kinetic energy, exchange effects related to the Pauli principle and correlation effects due to electrostatic repulsion.

By this definition, as the kinetic energy of the system of non-interacting electrons is separated, the original system can be replaced by an equivalent system of non-interacting electrons moving in an effective potential

$$V_{\text{eff}}(\mathbf{r}) = V_H(\mathbf{r}) + V_{xc}(\mathbf{r}) + V_{\text{ext}}(\mathbf{r}), \quad (3.10)$$

where the Hartree contribution is

$$V_H(\mathbf{r}) = \int \frac{n(\mathbf{r}')}{|\mathbf{r} - \mathbf{r}'|} d\mathbf{r}', \quad (3.11)$$

and the exchange-correlation potential is

$$V_{xc}(\mathbf{r}) = \frac{\delta E_{xc}[n(\mathbf{r})]}{\delta n(\mathbf{r})}. \quad (3.12)$$

The system of non-interacting electrons, which are coupled through the electron density, now can be described by the Kohn-Sham equations

$$\left[ -\frac{1}{2}\nabla^2 + V_{eff}(\mathbf{r}) \right] \psi_i(\mathbf{r}) = E_i \psi_i(\mathbf{r}), \quad (3.13)$$

where  $\psi_i$  is the single particle wave function with corresponding Kohn-Sham eigenenergy  $E_i$ . The total electron density is  $n(\mathbf{r}) = \sum_i f_i |\psi_i(\mathbf{r})|^2$ , where  $f_i$  is the occupation number of the one-electron state  $i$ . Since the single particle wave function is dependent on the effective potential  $V_{eff}$ , and  $V_{eff}$  is dependent on the electron density, these equations should be solved iteratively to obtain a self-consistent solution.

The ground state energy corresponding to the ground state electron density can be expressed as

$$E_0 = \sum_i f_i E_i - E_H[n_0(\mathbf{r})] + E_{xc}[n_0(\mathbf{r})] - \int n_0(\mathbf{r}) V_{xc}(\mathbf{r}) d\mathbf{r}. \quad (3.14)$$

At this point, by introducing the Kohn-Sham approach, the problem has been simplified significantly. However finding the exact solution is still a difficult task due to the presence of  $E_{xc}[n(\mathbf{r})]$ , which includes all the complex many-body effects of the system.

### 3.3.3 Exchange-correlation functionals

So far, no approximation has been made and Kohn-Sham theory is, in principle, exact. In the Kohn-Sham equation the exchange-correlation functional contains all many-body effects. The exact form of the exchange-correlation functional is, however, not known and so far many approximations have been presented with different levels of complexity. These approximations generally follow two main approaches. Functionals are either fitted to an experimental data set or constructed to satisfy physical constraints. These two approaches are also combined in the design of some functionals. In this thesis four constraint-based functionals are considered including PBE, PBESol, AM05 and vdW-DF-cx. These functionals are briefly introduced in the rest of this section.

In the local density approximation (LDA), the exchange-correlation energy depends only on the local electronic density

$$E_{xc}^{LDA}[n] = \int_{\mathbf{r}} n(\mathbf{r}) \epsilon_{xc}^{LDA}[n(\mathbf{r})], \quad (3.15)$$

where the exact form of  $\epsilon_{xc}^{LDA}$  can be determined from the exact exchange-correlation energy of the homogeneous electron gas (HEG) meaning  $\epsilon_{xc}^{LDA}[n(\mathbf{r})] = \epsilon_{xc}^{HEG}[n(\mathbf{r})]$ .

In spite of its simplicity, the LDA is surprisingly successful in describing a wide range of materials and properties. It provides, however, only modest accuracy when it comes to systems with rapidly varying electron densities.

To reach a better accuracy in describing systems with inhomogeneous electron density, the generalized gradient approximation (GGA) was introduced. It is a collective name for approximations that use information contained in the density  $n(\mathbf{r})$  as well as its gradient  $|\nabla n(\mathbf{r})|$ . It is often specified in terms of an enhancement factor  $F_{xc}$  of the LDA exchange

$$E_{xc}^{\text{GGA}}[n] = \int_{\mathbf{r}} n(\mathbf{r}) \epsilon_x^{\text{LDA}}(n(\mathbf{r})) F_{xc}(n, |\nabla n|). \quad (3.16)$$

There are many GGA versions as there are many ways by which information from the gradient of the electron density can be included. The GGA version of Perdew, Bruke and Ernzerhof (PBE) [48], has been a particular successful general-purpose functional for systems with dense electron distributions including both individual molecules and hard materials [48, 49].

PBESol is another constraint-based functional, which is similar to PBE except for the gradient expansion is restored for exchange. By restoring the gradient expansion, the PBESol functional leads to a better description of solids and their surfaces [50].

The AM05 constraint-based functional, like PBESol, extracts the gradient-corrected correlation and performs very well at describing the structure of dense materials. It provides in principle, an exact account of exchange effects for surfaces, i.e., the boundary between regions of higher and lower electron densities, whereas for internal regions the surface-exchange description is merged with that of the LDA [51].

Several attempts have been made over the years to develop more accurate and general purpose exchange-correlation functionals. Especially the lack of van der Waals forces in the design of extensively used GGAs, necessitate the construction of new functionals with inclusion of such forces. Van der Waals forces arise from the non-local correlation between electrons. Due to their non-local nature, local or semi-local approximations cannot correctly capture these interactions. Therefore, several versions of van der Waals density functional (vdW-DF) have been developed over the years. In 2004, the van der Waals density functional for general geometries was presented, called vdW-DF or vdW-DF1 [52]. Here, the correlation in the vdW-DF method is obtained as a six-dimensional spatial integral, which non-locally depends on density

$$E_c^{\text{nl}}[n] = \frac{1}{2} \int_{\mathbf{r}, \mathbf{r}'} n(\mathbf{r}) \phi(\mathbf{r}, \mathbf{r}') n(\mathbf{r}'), \quad (3.17)$$

where the interaction kernel  $\phi(\mathbf{r}, \mathbf{r}')$  represents the non-local coupling of the electron densities at points  $\mathbf{r}$  and  $\mathbf{r}'$ . The full energy functional is

$$E^{\text{vdW-DF}}[n] = E_0[n] + E_c^{\text{nl}}[n], \quad (3.18)$$

where  $E_0$  contains the semi-local exchange and local correlation. In 2014, Berland and Hyldgaard [53] developed a consistent exchange (cx) part leading to the vdW-DF-cx functional that has been employed in the present work.

Calculations in papers I, II, and III included in the present thesis were obtained using the PBE functional. The performance of the PBE, PBESol, AM05 and vdW-DF-cx functionals was

compared in paper IV, and the vdW-DF-cx functional was used for the DFT calculations of paper V.

### 3.3.4 Plane wave basis sets and pseudopotentials

So far, by introducing the Kohn-Sham equations and the exchange-correlation functionals, we have simplified the original electronic structure problem. To find a solution to the Kohn-Sham equation, however, further considerations are required. To begin with, in practice one has to expand the wave function in a basis set. There are different basis sets available to employ. For crystalline systems it is natural to use plane wave basis sets, and to employ periodic boundary conditions due to the periodic nature of the crystal.

As a result of Bloch's theorem [54], a complete basis set is given by plane waves with wave vectors  $\mathbf{k}$  within the first Brillouin zone, according to

$$\Psi_{n,\mathbf{k}}(\mathbf{r}) = \sum_{\mathbf{G}} c_{n,\mathbf{k}+\mathbf{G}} e^{i(\mathbf{k}+\mathbf{G})\cdot\mathbf{r}}. \quad (3.19)$$

Here, the sum is over all reciprocal lattice vectors  $\mathbf{G}$ , and  $n$  is the index of the eigensolutions and corresponds to different bands. Since in theory there is an infinite set of  $\mathbf{G}$  vectors, the sum is truncated in practice by choosing a cut-off energy  $E_{cut}$ , which limits the number of  $\mathbf{G}$  vectors according to  $1/2|\mathbf{k} + \mathbf{G}|^2 < E_{cut}$ . For perfect crystalline systems, this approach is ideal since for representing properties of an infinite piece of material, primitive unit cells suffice.

While using a plane wave basis set simplifies the problem, the downside of this approach is that the sum converges very slowly for rapidly varying wave functions close to the nuclei. Core electrons, however, do not actively contribute to chemical bonding and as a result can be treated differently. It is therefore common to only include the valence electrons in DFT calculations. The potential of a nucleus is then replaced with an effective potential referred to as a pseudopotential, which includes the combined potential of nucleus and core electrons. The pseudopotential is constructed in a way that it produces a smooth function within the core region, which requires a lower cut off energy, while it reproduces the all-electron wave function outside the core region.

Employing pseudopotentials allows for density functional theory calculations to be performed with greater computational efficiency. Common schemes include norm-conserving pseudopotentials [55], ultrasoft pseudopotentials [56], and the projected augmented wave method (PAW) [57]. The latter has been employed for all DFT calculations in the present work.

## 3.4 Convergence considerations for point defects calculations

### 3.4.1 Size dependence

As seen in the previous section, the use of plane wave basis sets imposes periodic boundary conditions on the system. As long as the system has translational symmetry, this is not problematic.

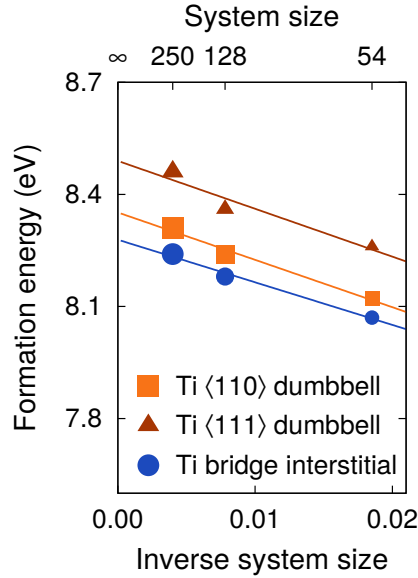


Figure 3.1: Finite size scaling of formation energies of Ti interstitial defects.

Introducing a defect into the system, however, breaks the symmetry and therefore modeling the system with periodic boundary conditions results in periodic repetition of the defects.

The most widely used methodology to describe defects in the dilute limit is the supercell approach, in which a larger cell, termed a supercell, containing the defect is constructed. If the supercell is *not* large enough, the defect will however interact with its neighboring defects because of the periodic boundary conditions, which introduces the so-called finite-size errors.

The simplest way to solve this problem is to study the convergence with respect to supercell size. When the property in question no longer changes with size, one therefore obtains the result for an isolated defect and the errors due to defect interactions are negligible. For point defects, there have been different studies in order to find a general expression for the error introduced by defect self interaction. The error has been shown to arise from two sources namely elastic and electrostatic interactions.

In the present thesis where the focus is on uncharged point defects, the dominant defect-defect interactions are elastic in nature. Elastic interactions arise from the fact that ions surrounding the defect will relax to lattice sites other than their pure equilibrium positions when the defect is introduced, resulting in lattice distortion. For a cubic supercell with size  $L$ , the elastic interaction scales with the inverse volume,  $L^{-3}$ .

In Fig. 3.1, finite size scaling of the formation energies<sup>1</sup> of Ti interstitial defects is presented, which clearly exhibit an inverse linear behavior with respect to volume. Relevant interstitial configurations are shown in Fig. 3.2. Smaller cells than the ones included here (e.g., a  $2 \times 2 \times 2$  16-atom cell) deviate from the inverse linear behavior because of the non-linear contributions associated with interacting defect cores.

<sup>1</sup>See Subsection 3.5.1 for the description of formation energies.

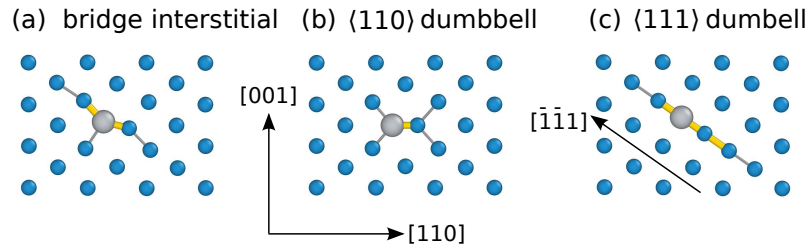


Figure 3.2: Representative configurations of (a) bridge, (b)  $\langle 110 \rangle$  dumbbell, and (c)  $\langle 111 \rangle$  dumbbell interstitial defects. The figure shows a slice parallel to a  $\{110\}$  plane of the structure. Small (blue) spheres indicate tungsten atoms whereas large (gray) spheres indicate alloying elements (like Ti) in the case of extrinsic and tungsten atoms in the case of intrinsic defects. Thicker (yellow) cylinders indicate bond lengths shorter than 2.3 Å whereas thinner (gray) cylinders indicate bond lengths shorter than 2.5 Å.

### 3.4.2 Brillouin zone sampling

The next source of error when calculating defects energetics using the supercell approach is related to the sampling of the Brillouin zone via a discrete  $k$ -point mesh. This aspect, which is more significant in metals, results from the fact that defects in materials act as perturbations, which can cause long-range oscillations in the electronic structure (Friedel oscillations). To capture these oscillations it is not uncommon that one requires a denser  $k$ -point mesh than for the corresponding defect free system.

I have studied the effect of Brillouin zone sampling for vacancies, substitutional and interstitial atoms and the results are presented in Fig. 3.3. For the tungsten vacancy one can clearly see that for a 250-atom cell ( $5 \times 5 \times 5$  conventional unit cells) at least a  $5 \times 5 \times 5$  Monkhorst-Pack mesh is required in order to converge the formation energy to better than 0.1 eV. In the case of interstitials, which are also strong perturbation centers, the formation energies exhibit a slightly smaller yet still pronounced variation than for the vacancy as illustrated in Fig. 3.3 (c). Finally for substitutional defects the effect is rather weak as shown for substitutional Ti in Fig. 3.3 (b).

### 3.4.3 Semicore states

In the present thesis, point defects in tungsten are studied extensively. For self-interstitial atom in tungsten, it has been argued that the inclusion of semicore states, specifically  $W-5p$  states, in the pseudopotential or PAW data set is important to correctly describe the formation energies [58, 59]. This is reasonable as interstitial configurations involve very short interatomic distances and can therefore be sensitive to the core radius of the pseudopotential/PAW data set.

To quantify the effect of including semicore states, in paper I, I carried out a systematic analysis for Ti, V, Zr, Nb, Hf, Ta, and Re defects in tungsten. Our results showed that the effect of semicore states varies for different defects and elements. For instance substitutional defects are influenced negligibly with the exception of V and possibly Zr. Interstitial defects energetics are generally affected more compared to substitutionals, however, the effect ranges from almost

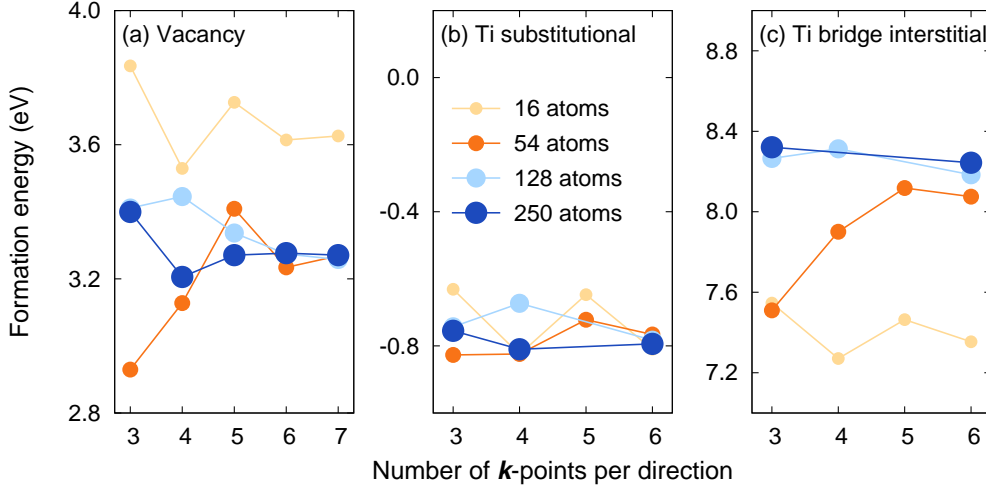


Figure 3.3: Convergence of the formation energies of (a) vacancy, (b) Ti substitutional, and (c) Ti bridge interstitial with  $k$ -point density for different system sizes.

zero (Zr, Nb) to 0.5 eV and above (Ti, V, Ta). The effect of including semicore states is typically larger for  $\langle 110 \rangle$  interstitials, which have the shortest interatomic separation, than for  $\langle 111 \rangle$  and bridge interstitial configurations.

This study furthermore showed that the effect of semicore states is only weakly dependent by Brillouin zone sampling and system size. As the computational effort increases significantly due to approximately twice as many electrons in the calculation, the results in the present thesis are obtained *not* including the semicore states, unless specified otherwise.

## 3.5 Point defects thermodynamics

### 3.5.1 Defect formation energies

Defect formation in materials is associated with a change in the Gibbs free energy. The Gibbs free energy of formation is a central property for describing the thermodynamics of a defect in the system and is expressed as

$$\Delta G_f = \Delta E_f + p\Delta V_f - T\Delta S_f. \quad (3.20)$$

The formation free energy is the difference in the free energy of the structure before and after the defect is created. In this process some of the atomic bonds are stretched or broken leading to a change in energy. The formation free energy of a defect is calculated as

$$G^f = G^{\text{defect}} - G^{\text{ideal}} - \sum \Delta n_i \mu_i, \quad (3.21)$$

where  $G^{\text{defect}}$  is the free energy of the defective system and  $G^{\text{ideal}}$  is the free energy of the perfect reference cell. The variation of the formation free energy with the chemical environment is

given by the last term in Eq. (3.21), which involves the chemical potentials of the constituents. The difference between the number of atoms of type  $i$  in the reference cell and the defective cell is denoted by  $\Delta n_i$ , where positive and negative values correspond to the addition and removal of an atom relative to the ideal cell, respectively. Here, we take the chemical potential  $\mu_i$  of each constituent to be identical to its cohesive energy per atom [60].

For a system in thermal equilibrium, the free energy of the system is minimum, and the dilute limit concentration of the defects is related to the formation free energy via

$$c = c_0 \exp\left(-\frac{\Delta G_f}{k_B T}\right), \quad (3.22)$$

where  $c$  is the equilibrium concentration of the defects,  $c_0$  is the concentration of available defect sites,  $k_B$  is the Boltzmann's constant, and  $T$  is the temperature.

### 3.5.2 Formation volume tensors

A defect can affect other point as well as line defects (dislocations) either via a direct “chemical” interaction or via long-range elastic interactions. The strain field can modify the saddle points during point defect migration [61]. Similarly, it can affect the barriers for dislocation kink nucleation and growth and thereby affect the plastic behavior [62].

Formation volumes quantify the induced strain in terms of linear elasticity theory and the formation volume tensors provide additional information concerning the orientation and anisotropy of the strain field.

Given the cell metrics of the ideal supercell  $L_0$  and the fully relaxed supercell containing the defect  $L$ , the formation volume tensor can be obtained from the relation [63, 64]

$$\begin{aligned} v^f &= \det(L_0) \ln(L_0^{-1}L) \\ &\simeq \det(L_0)(L - L_0)L_0^{-1}. \end{aligned} \quad (3.23)$$

The formation volume equals one third of the trace of the formation volume tensor. By diagonalizing the formation volume tensor one obtains the orientation and the strength of the strain field. The former is specified by the eigenvectors whereas the latter is related to the magnitude of the eigenvalues. In particular, in Paper I, we considered the anisotropy defined as the ratio of the largest to the smallest eigenvalue.

### 3.5.3 Defect kinetics

The migration processes of atoms in solids can be described as a sequence of jumps between neighbouring stable sites. In this description the migrating particle spends the majority of the time residing in a potential well, corresponding to a stable position. Collective vibrations of the system can be interpreted as attempts of the particle to break out of the well. If the temperature of the material is sufficiently high, the particle will occasionally succeed crossing a potential barrier and end up in the well corresponding to a neighboring site, see Fig. 3.4.

Fick's first law of diffusion provides a representation of diffusion processes

$$\mathbf{J}_i = -D_i \nabla c_i \quad (3.24)$$

in which,  $\mathbf{J}_i$  is the flux of atoms meaning the number of atoms of kind  $i$  passing the unit area perpendicular to the direction of  $\mathbf{J}$  per unit time.  $D$  is the diffusion coefficient, and  $\nabla c_i$  is the concentration gradient of atom type  $i$ .

Fick's second law of diffusion provides a more complete description of the process by presenting the evolution of concentration with time

$$\frac{\partial c_i}{\partial t} = \nabla(D_i \nabla c_i). \quad (3.25)$$

Here  $D_i$ , as the diffusion coefficient of atom type  $i$ , can be described by Arrhenius formula

$$D_i = D_{i0} \exp(-E_m/k_B T). \quad (3.26)$$

The pre-exponential factor  $D_{i0}$  is related to the lattice geometry and can be obtained by phonon calculations.  $E_m$  is the migration energy, which is required for the migrating species to move from the initial potential well to the next one, see Fig. 3.4, [65].

Diffusion can be altered by other processes in the system like interactions between defects and impurities. Such interactions can slow down the mobility of the defect if for instance it becomes trapped by the impurity atom. The binding energy between impurity and point defect is a key factor in understanding defect and solute atom migration.

In the present work, various binding energies are calculated for different types of point defects and impurities. For example the binding energy between impurity and self-interstitial is defined as the difference between the formation energy of mixed-interstitial and the sum of the formation energies of self-interstitial and substitutional defects

$$E_X^b = E^f([X - W])_W - E^f([W - W])_W - E^f(X)_W. \quad (3.27)$$

Note that by this definition, negative (positive) binding energies imply attractive (repulsive) interactions between the defects.

### 3.5.3.1 Nudged elastic band method

The Nudged elastic band (NEB) is a method to calculate the migration energy. It is an efficient method for finding the minimum energy path (MEP), and the saddle point of the potential energy surface between initial and final configurations of a transition such as chemical reactions and diffusion processes in solids [66].

The method works by minimizing the energy of a number of intermediate images along the MEP. The energy of each image is optimized in a way that all the neighboring images in this string of atoms maintain approximately equal spacing. To achieve this constrained optimization, only the perpendicular component of the true force and the parallel component of spring force are included. The saddle point corresponding to the highest energy along the path represents the activation energy barrier. This barrier enables estimating transition rates within the harmonic transition state theory [67].

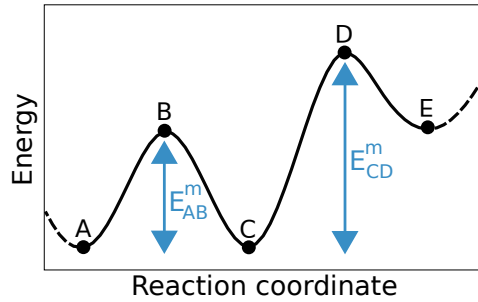


Figure 3.4: Example of potential energy along a migration path. In moving from point A to point E, the particle has to overcome two transition barriers with corresponding barrier heights of  $E_{AB}^m$  and  $E_{CD}^m$ .

It is important to make sure that the actual saddle point is found, therefore one of the images is made to climb up along the elastic band to converge on the saddle point. This modification is considered in the climbing image NEB (CI-NEB) method [68], which is employed in the calculations of this thesis.

## 3.6 Atomic scale modeling of alloys

The alloy cluster expansions (CE) approach is a powerful technique for computing thermodynamic properties in multicomponent systems. It is used extensively to determine the energy as a function of different arrangement of atoms over lattice sites. For this purpose a set of configurations is constructed and subsequently used for training the CE. The CE can be subsequently sampled using Monte Carlo (MC) simulations, which enables one to predict, e.g. alloy phase diagrams.

### 3.6.1 Alloy cluster expansions

An alloy cluster expansion (CE) can be regarded as a generalized Ising model. In atomic scale modeling of alloys, one is usually interested in configurations corresponding to a distribution of  $M$  different species over  $N$  sites. Each configuration can be described by a vector  $\sigma$  and a property  $Q$  of the system can be expressed as [69]

$$Q = \sum_{\alpha} m_{\alpha} J_{\alpha} \langle \Gamma_{\alpha}(\sigma) \rangle_{\alpha}, \quad (3.28)$$

where  $\alpha$  and  $m_{\alpha}$  denote a symmetrically unique cluster and its multiplicity, respectively. The coefficients  $J_{\alpha}$  are referred to as effective cluster interactions (ECIs), and  $\Gamma_{\alpha}$  are cluster functions, which represent the probability of finding cluster  $\alpha$  in configuration  $\sigma$ . The last term in the above expression represents the average over all symmetry equivalent cluster functions and the sum runs over all symmetrically distinct clusters (points, pairs, triplets, quadruplets, etc.) [69, 70, 71].

When all clusters  $\alpha$  are considered in the sum, Eq. (3.28) is exact [72]. In practice, however, the sum can be truncated due to the fact that interactions decay quickly with distance. ECIs are the unknown quantities of a CE and can be determined by fitting to the energy of a number of configurations obtained through first-principles calculations. The process of CE construction employed in paper V is described in details in the following subsection.

### 3.6.2 CE construction

In order to determine a certain property of a system, first a suitable set of structures should be selected for training and validation. The most simple way to perform this selection is to randomly choose the structures. This can be done by creating a supercell based on a primitive cell, and decorating it with A and B atoms. The energies of these configurations are then calculated using density functional theory.

However, this is not generally the optimum approach for generating structures, as random structures may fail to sample important parts of configuration space. In particular for larger cells, the probability of e.g., ordered configurations to occur decreases quickly with size.

Instead of randomly selecting the structures, a better approach is to perform a systematic structure enumeration. In this case, one can first start with creating all possible structures that have 2 atoms per unit cell, and then continue with creating all the different structures that contain 3, 4, 5 and more atoms in the unit cell. By increasing the size of the cell the number of structures, which are generated becomes larger. For our calculations, structures up to 12 atoms per unit cell were included, resulting in pools of 10850 structures for BCC and 5777 structures for HCP.

When the structures are selected, the next step is to *train* the CE to match as closely as possible a series of first-principles calculations. In order to perform such training, structures can be selected randomly from the set. An alternative, more refined approach compared to the random approach is to calculate all the cluster vectors for all the structures in the selection database and then pick them such that these cluster vectors are as orthogonal to each other as possible. One way of achieving that is to choose the cluster vectors to all lie on a hypersphere [73]. For the calculations in the present thesis a random selection has been performed.

In order to train a CE, a linear algebra problem of the following form should be solved

$$\bar{\Pi} \mathbf{J} = \mathbf{Q}, \quad (3.29)$$

where  $\bar{\Pi}$  is called the sampling matrix, which is obtained by stacking the vectors that represent the clusters present in each structure of the training set, i.e.  $\langle \Gamma_\alpha(\sigma) \rangle_\alpha$  in Eq. (3.28),  $\mathbf{J}$  represents ECIs, and  $\mathbf{Q}$  is the vector of target properties of interest, such as energy.

If the CEs are constructed conventionally, the number of elements in  $\mathbf{Q}$  is much larger than the number of ECIs. The set of equations is thus overdetermined. The optimal set of ECIs for fixed training set and cluster function basis is then obtained by minimizing the  $l_2$ -norm of  $\bar{\Pi} \mathbf{J} - \mathbf{Q}$

$$\mathbf{J}_{\text{opt}} = \arg \min_{\mathbf{J}} \{ \|\bar{\Pi} \mathbf{J} - \mathbf{Q}\|_2 \}. \quad (3.30)$$

A series of CEs corresponding to different basis set choices are then generated using common algorithms [69]. By comparing the performance of each CE by means of its Cross Validation Score (CVS) the best performing CE is selected.

An alternative approach is to solve an underdetermined problem, where the number of structures available for fitting in  $\mathcal{Q}$  is much smaller than the number of ECIs, and the solution obtained is consequently not unique. This alternative approach, which offers considerable advantages with regard to accuracy, transferability as well as efficiency, is based on the compressive sensing (CS) technique [74]. There are different algorithms to solve compressing sensing problems like LASSO (least absolute shrinkage and selection operator) and split-Bregman. The latter is the algorithm used in our calculations to find the ECIs.

When a fit has been performed it should be validated so that the ECIs are actually useful. To evaluate a CE a Cross Validation Score (CVS) can be used. The simplest form is the Leave-One-Out (LOO) CVS. Another way of evaluation the parameters used for the fitting algorithm is called sampling. By sampling, one samples many different choices on the training and validation set, and then takes an average over the root mean square errors of the validation sets.

After training and validation are done, it is time for the *analysis of the results*. For our calculations we analyzed average and standard deviation of the mixing energy vs concentration over the set of CEs that was obtained.

To obtain the final CE, the ECIs were averaged, after which clusters were removed for which the average ECI was smaller than half the standard deviation. In this fashion, statistically insignificant CEs were removed, leading to a smaller CE.

### 3.6.3 Monte-Carlo simulations

Once the CE is found to be satisfactory, the configuration space can be sampled using Monte Carlo (MC) simulations. In order to determine thermodynamic properties of alloys, a convenient way is to sample the semigrand canonical ensemble when performing a MC simulation. The semigrand canonical ensemble is defined as an intermediate between the canonical and grand canonical ensembles, in which the total number of particles and the difference in chemical potential of the species are fixed, i.e.  $N_{tot}$ ,  $\Delta\mu$ ,  $V$ , and  $T$  are constant. It is straightforward to calculate the free energy from  $\Delta\mu$  and  $c$  in this ensemble, however it has a major disadvantage when it comes to alloys with constituents that do not mix in all concentrations (immiscible systems). Since sampling of the free energy landscape inside the miscibility gap is not possible. For analyzing the W-Ti phase diagram in Paper V, we, however, require the free energy landscape for BCC and HCP phases as a *continuous* function of composition. This prevents us from using the semi-grand canonical (SGC) ensemble since it does not allow sampling multiphase regions, which are present for both BCC and HCP lattices.

To overcome this limitation the variance-constrained semigrand canonical (VCSGC) ensemble, has been proposed. This approach includes an additional term in the partition function that effectively imposes a constraint on the fluctuations of the concentration, which diverge in multi-phase regions. The VCSGC ensemble is sampled by randomly selecting a site in the system, swapping its chemical identity, and accepting this trial move with probability [75]

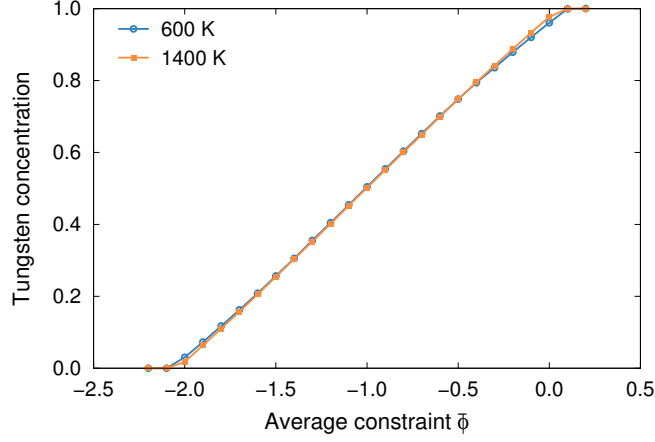


Figure 3.5: Tungsten concentration vs.  $\phi$  parameter for BCC phase at temperatures 600 K and 800 K. Figure is generated from the calculations of the present work.

$$\mathcal{P} = \min[\exp[-\beta\Delta E - \kappa\Delta N_B(\phi + \Delta N_B/N + 2N_B/N)]].$$

Here,  $\Delta E$  is the energy change associated with the move,  $\Delta N_B$  is the change in the number of particles of type  $B$ ,  $N$  is the total number of sites (atoms) in the simulation cell, and  $\phi$  and  $\kappa$  are the average and variance constraint parameters.

In several previous works, it has been shown that the variance constraint parameter  $\kappa$  can be chosen from a rather wide range, typically  $100 \lesssim \kappa \lesssim 1000$ . It must be chosen large enough to stabilize the system inside the miscibility gap and small enough not to affect the acceptance rate too negatively. The precise value for  $\kappa$  is, however, not very critical and values between 100 and  $\lesssim 500$  have been found to work regardless of the system. The average constraint parameter  $\phi$  can then be varied in steps of 0.02 from  $-2.2$  to  $0.2$  to sample the entire concentration range. Figure 3.5 shows tungsten concentration vs.  $\phi$  parameter for BCC phase at temperatures 600 K and 1400 K.

In the VCSGC ensemble the first derivative of the free energy is related to the (ensemble) average of the concentration  $\langle c_B \rangle = \langle N_B \rangle / N$ ,

$$\beta\partial\Delta F/\partial c = \kappa(\phi + 2\langle c_B \rangle), \quad (3.31)$$

which allows one to obtain the free energy of mixing.

From Eq. (3.31) one can obtain the first derivative of the mixing free energy with respect to concentration. Here,  $\partial\Delta F/\partial c \simeq \partial\Delta G/\partial c$ , since the volume-pressure term is small (In our calculations, ionic and cell relaxations are implicitly included in the ECIs.). For a binary alloy,  $\partial\Delta G/\partial c$  corresponds to the chemical potential difference between the two species, see Fig. 3.6 (a). Chemical potential difference can be further integrated using for example the trapezoidal rule, to yield the mixing free energy. In order to construct the free energy landscape, all different phases of the system (stable and metastable) should be considered.

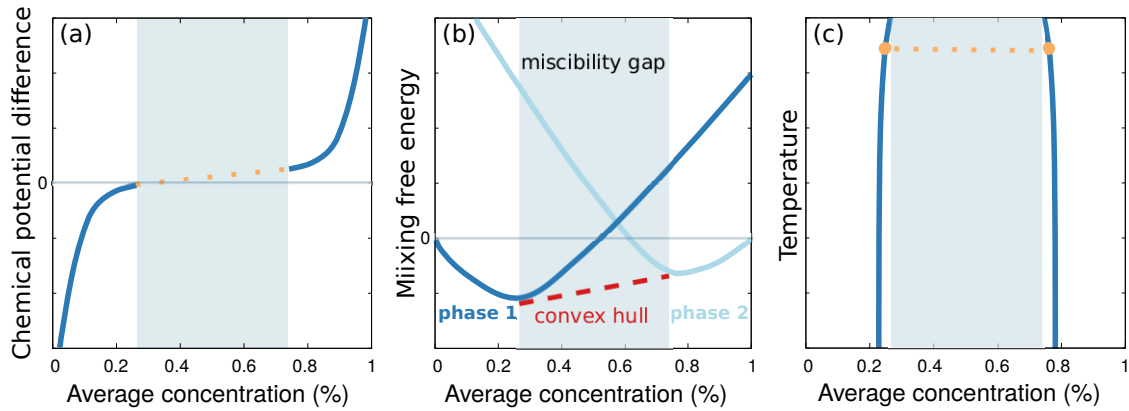


Figure 3.6: Schematic illustration of the steps for a phase diagram construction, for a binary system with a miscibility gap. General steps include (a) extracting the chemical potential difference vs. concentration, (b) constructing the convex hull of the mixing free energies, and (c) constructing the temperature-concentration phase diagram. A certain temperature corresponding to the convex hull shown in (b) is marked using orange dots in the phase diagram in (c).

After having determined the free energies of all phases (like BCC and HCP phases for the W-Ti system), one can construct the full temperature, composition, and structure dependent free energy landscape, from which the phase diagram can be extracted. To this end, the free energies for the different phases should be combined to construct a convex hull. Fig 3.6 (b) shows the mixing energy of two phases of a system at a certain temperature, for which the convex hull is constructed and shown with a dashed red line. The convex hull is then obtained for a temperature range and will be used to construct a temperature vs. concentration phase diagram, see Fig 3.6 (c). A certain temperature corresponding to the convex hull shown in Fig. 3.6 (b) is marked using orange dots in the phase diagram in Fig. 3.6 (c).

## Results and conclusion

### 4.1 Point defects and radiation-induced precipitation

Tungsten is a prime candidate for applications in fusion reactors as a first wall material, thus understanding its behavior under irradiation is crucial. It has been observed that needle-shaped Re-precipitates are formed in W and W-Re alloys under irradiation, at Re concentrations well below the solubility limit [76]. Formation of such precipitates can alter the mechanical properties of tungsten and can lead to alloy hardening and thermal conductivity losses [76, 77].

In papers I-III, we conducted a study in order to understand the mechanisms by which, nonequilibrium clusters of solute atoms are formed under irradiation. I started this study by calculating the basic properties of individual mixed-interstitials and further extended the study to di-interstitials and their interactions. For higher concentrations, defects mixing energies in tungsten were studied as well. We also determined the energy landscape for interstitial and vacancy diffusion. Using all these information, our collaborators constructed a kinetic Monte Carlo (kMC) model. This model provides a quantitative description of processes that are important for the actual irradiation process in terms of the formation of Re precipitates. Results from these three papers show that there are different regimes during formation and evaluation of these precipitates. Besides the vacancy drag mechanism, interstitials also contribute to cluster formation while the mutual coupling of these fluxes is responsible for the initial defect accumulation.

#### 4.1.1 Paper I

In paper I, by means of first-principles atomistic methods based on density functional theory (DFT), an extensive convergence study was performed first, to understand the effect of Brillouin zone sampling, size dependence, and semicore states on defect energetics. The results were

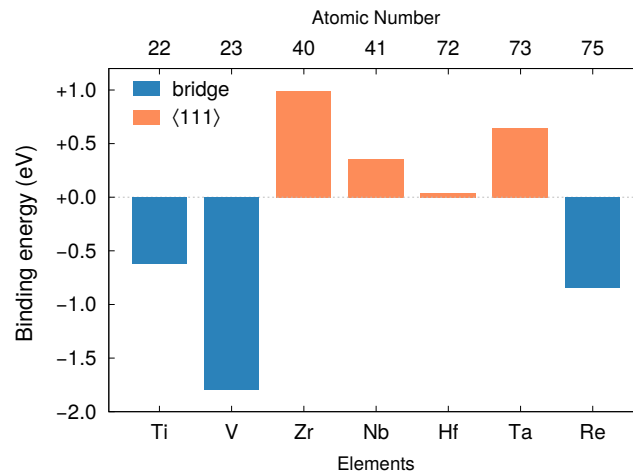


Figure 4.1: Binding energies between self-interstitial atoms and substitutional solute atoms relative to the respective most stable mixed-interstitial configuration. The figure is from paper I of the present thesis [78].

further used to calculate the properties of a number of solute atoms in tungsten in the dilute limit.

Interstitial defects possess positive large formation energies and are practically absent in equilibrium. They are, however, important under reactor relevant conditions. Mixed-interstitials are formed under irradiation after self-interstitial atoms (SIAs) diffuse through the lattice and become trapped by solute atoms. The binding energy was found to be very strong ( $\sim -0.6$  to  $-1.8$  eV) for Re, Ti, and V, indicating that thermal de-trapping was unlikely, see Fig. 4.1. Such interactions are important for materials under irradiation as they cause a reduction in interstitials mobility, which can accelerate damage build-up. Trapping is a precursor to segregation and may eventually lead to solute precipitation.

In addition to trapping, Re, Ti, and V mixed-interstitials were found to exhibit a pronounced anisotropy<sup>1</sup> in the defect formation volume tensor and possess not only strong but very anisotropic strain fields. The highly anisotropic nature of these interstitials further raise the question of possible defect-defect interactions especially at high concentrations. Such interactions may lead to the creation of separated phases in the material, which will eventually influence, for example the mechanical properties. In the next step, I therefore focused on understanding defect-defect interactions.

<sup>1</sup>Anisotropy is quantified by the ratio between the largest and smallest eigenvalues of the formation volume tensor.

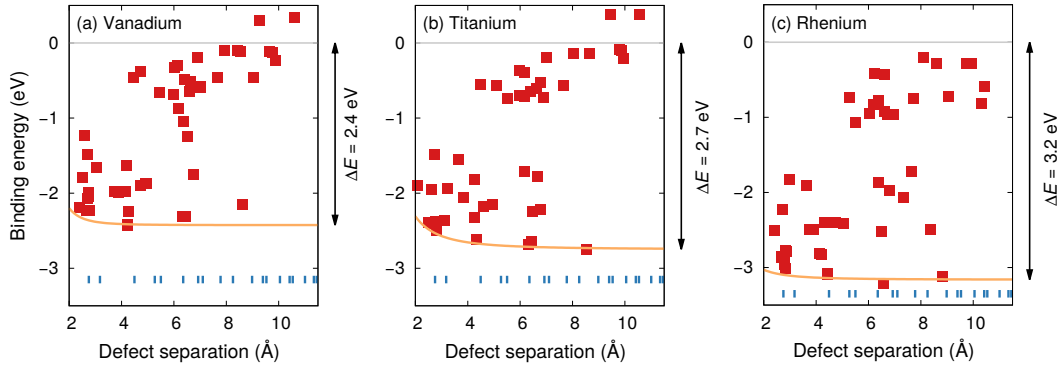


Figure 4.2: Binding energy between two (a) V–W, (b) Ti–W, and (c) Re–W mixed interstitials as a function of pair separation. The blue ticks indicate the positions of the neighbors shells in the perfect structure. The solid orange lines represent the repulsive interaction between two substitutional extrinsic atoms referred to the most strongly bound configuration. The figure is from paper II of the present thesis [79].

### 4.1.2 Paper II

In paper II, the behavior of di-interstitial was investigated considering Re, Ti, and V mixed-interstitials. We demonstrated that these mixed-interstitials are strongly attracted to each other with binding energies of several eV, see Fig 4.2.

We found that after mixed-interstitials were formed due to trapping, they were able to diffuse further via low-energy rotations and translations while dragging the solute atom along. Our results showed that a mobile mixed-interstitial atom could further meet another mixed-interstitial, bind strongly and become aligned. Throughout such a process, mixed-interstitials, via a 3D diffusion mechanism, can effectively transport solutes over long distances and, considering the large binding energy between di-interstitials, this could eventually result in clustering. These mixed di-interstitials are kinetically very stable due to their strong binding energies, which makes them preferential sites for more defect absorption. While additional interstitials approaching these small clusters may not be initially aligned, they are energetically favored to again rotate into alignment, increasing cluster size and forming a precipitate nucleus via interstitial accumulation.

To provide more evidence for the tendency of the system for interstitial agglomeration, I calculated the mixing energy of the defects. The mixing energy for interstitials is found to be positive and concentration dependent. It was shown to feature a maximum at about 15% and approach zero at approximately 30%. This suggests that if the concentration of mixed-interstitials reaches a concentration of  $\gtrsim 30\%$ , the structure becomes (locally) unstable and can transit into substitutional configurations.

The mechanism described above cannot on its own account for the radiation-induced precipitation observed in W–Re alloys since, e.g. in the real system vacancy migration will play a role. In paper III we extended our study by implementing the energetics and mechanisms presented

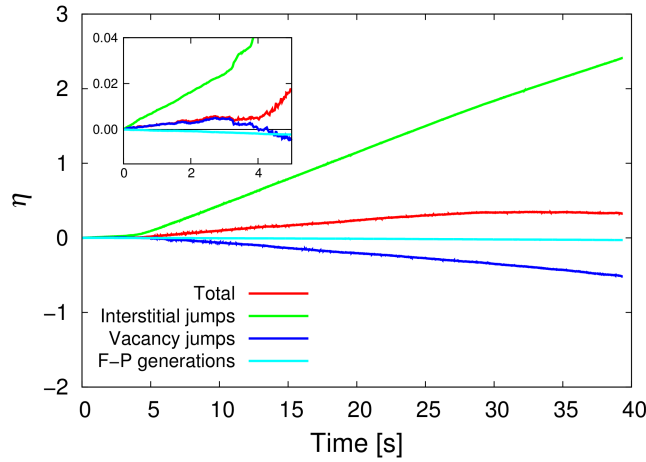


Figure 4.3: Evolution of the differential SRO during the nucleation and growth in the kMC simulations. The figure is from paper III of the present thesis [80].

here into a kMC model enabling us to suggest a more comprehensive mechanism for formation of Re precipitates in tungsten.

### 4.1.3 Paper III

In paper III, we investigated the mechanism that governs the formation of Re-rich clusters in tungsten. Such clusters are formed under high-temperature, high-dose neutron irradiation, at concentrations well below the solubility limit. They may eventually transform into brittle W–Re intermetallic phases, which can lead to high levels of hardening and thermal conductivity losses. Understanding the mechanism by which nonequilibrium clusters are formed under irradiation is crucial for predicting materials degradation and devise mitigation strategies. To this end, I carried out DFT calculations for the W–Re system and characterized the landscape for diffusion. My results were subsequently used by collaborators to parametrize a kMC model.

On the basis of our results, the sequence of events that leads to the formation of Re-rich precipitates in irradiated W–2Re (at%) alloys was found to be as follows. The process starts with inserting a Frenkel pair in the system, and after which interstitial and vacancy diffuse around. Interstitials perform a one dimensional (1D) diffusion in the system until they encounter an impurity atom, bind and form a mixed-interstitial. At this point interstitials are capable of transporting solute atoms in three dimensions (3D). Mixed-interstitial migration continues until mixed-interstitials encounter more impurities and become trapped. These solute–mixed-interstitials are now firmly bound and effectively immobile.

Vacancies also diffuse, eventually become trapped, and form small Re-vacancy complexes. These Re-vacancy complexes continue to grow. At high temperatures, however, vacancies can de-trap and continue migrating until they find immobilized interstitials and become trapped forming another small V-Re cluster. Throughout this process, both mixed-interstitial and vacancy hops contribute to an increasing SRO parameter, see Fig. 4.3.

Eventually one Re cluster grows larger than the rest, due to natural fluctuations. At this point the probability of vacancy–mixed-interstitial annihilation increases and the cluster growth continues by attraction of mixed-dumbbells. At this stage, vacancies reverse their role as solute-atom ‘hinges’ and begin to contribute to cluster dissolution. The differential SRO parameter decreases and becomes negative at this point, see Fig. 4.3.

While the precipitate continues to be the main pole of attraction for vacancy-interstitial recombinations, the system reaches a saturation point where most of the solute is consumed and the cluster stops further growth. In the absence of sinks or other precipitates, the existing cluster is the only focus of solute agglomeration, which allows it grow to its maximum possible size considering the Re content. During this saturation step the total differential SRO parameter flattens out, see Fig. 4.3. If there are competing solute sinks in the system, it is expected that the size of the precipitate would be comparably smaller or it is less solute-dense internally.

## 4.2 Description of thermophysical properties in density functional theory

### 4.2.1 Paper IV

I conducted my earlier calculations (Papers I-III) using the GGA functional PBE [48]. PBE is one of the most successful general-purpose functionals for systems with dense electron distributions like hard materials and metals. The accuracy of PBE, however, is limited as it, e.g., systematically overestimates lattice constants and usually underestimates the mechanical stiffness (elastic constants).

In paper IV, I therefore compared the performance of a number of commonly used constraint-based exchange-correlation functionals and studied structural and thermophysical properties of non-magnetic transition metal elements. Compared to other assessments, I specifically included vibrational effects, which are much expensive to evaluate but provide a more rigorous benchmark than energies alone.

Specifically I focused on constraint-based functionals and considered the new consistent-exchange van der Waals density functional version vdW-DF-cx, the semi-local PBE and PBEsol functionals as well as the AM05 meta-functional. Using the quasi-harmonic approximation, structural parameters, elastic response, and thermal expansion at finite temperatures were computed and compared to experimental data. I also computed cohesive energies explicitly including zero-point vibrations.

It was shown that overall vdW-DF-cx provides an accurate description of thermophysical properties and retains a level of transferability and accuracy that is at least comparable and usually better than the other functionals considered in this study. This demonstrates that vdW-DF-cx has general-purpose character and can be used to study systems that have both sparse and dense electron distributions.

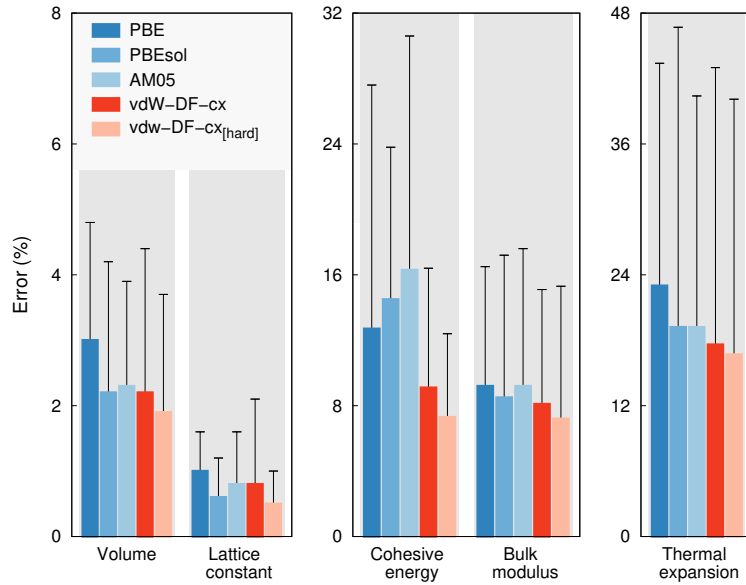


Figure 4.4: Performance of different constraint-based exchange-correlation functionals. Errors on the y-axis represent the mean average percentage errors (MAPEs), which were computed with regard to thermophysical properties measured at 300 K, with the exception of the cohesive energy, for which zero K values are compared. Standard deviations of the distribution of errors for each property and functionals are shown as black error bars. The figure is from paper IV of the present thesis [81].

### 4.3 W–Ti phase diagram

My prior calculations on different alloys suggested to take a closer look at W–Ti system. In paper I, the Ti substitutional formation energy was found to be negative indicating a tendency to form a solid solution with tungsten. In paper II, I showed furthermore that the mixing energy for the BCC solution is negative, which could result in an extended miscibility range. It was furthermore demonstrated that the W–Ti system exhibits a balance between HCP and BCC in terms of elemental reference structures and their energetics compared to W–V and W–Re systems. In addition, due to experimental difficulties, the existing low temperature phase diagrams of W–Ti system are based on a sparse set of data, which motivated a further investigation of this system.

In paper V, we established the low-temperature behavior of the W–Ti system especially on the W-rich side and showed that the asymmetric solubility results from the balance of stable and metastable lattice structures.

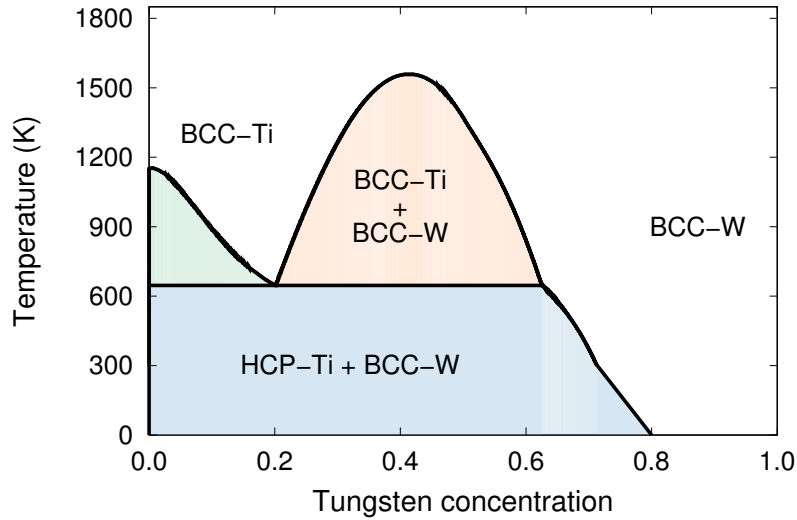


Figure 4.5: Phase diagram predicted based on the simulations in the present work in comparison with experimental data points and previous thermodynamic assessments. The figure is from paper V of the present thesis [82].

### 4.3.1 Paper V

Phase diagrams for the multi-component systems are very important since they represent crucial information for understanding and designing materials. They are, however, very time consuming to assess experimentally. In this work, we focused on the W–Ti binary alloys. For the W–Ti system, because of the high melting point of tungsten and the accompanying slow kinetics, the systematic exploration of the phase diagram, in particular on the W-rich side, has been very cumbersome. Since experimental data points for tungsten concentrations  $\gtrsim 30\%$  are only available down to 1473 K, the W–Ti system had been assessed using rather severe assumptions and need to be readdressed [83, 84, 85, 86, 87].

Using computational methods, the phase diagram of a binary alloy can be derived theoretically. In this regard, the type of interactions between the species in the system should be considered. If the interaction between the two constituents is repulsive (attractive) the system shows positive (negative) mixing energy. This interaction between the constituents is usually symmetric, in the sense that if A dissolves in B, so does B in A. One exception from this behavior is the Fe–Cr system, which has probably been studied the most extensively due to its technological importance. In the Fe–Cr system, Cr has been shown to be more soluble in Fe-rich side. The mixing energy goes through a sign inversion and the system features a broad miscibility gap. As a result of sign inversion in the mixing energy, the phase diagram is very asymmetric with a large solubility on the Fe-rich and a very small solubility on the Cr-rich side. This behavior, which at first sight might be unexpected given a very small size mismatch and identical lattice structures, can be rationalized in terms of the magnetic structure with Fe and Cr preferring ferro and antiferromagnetic ordering, respectively [88, 89, 90].

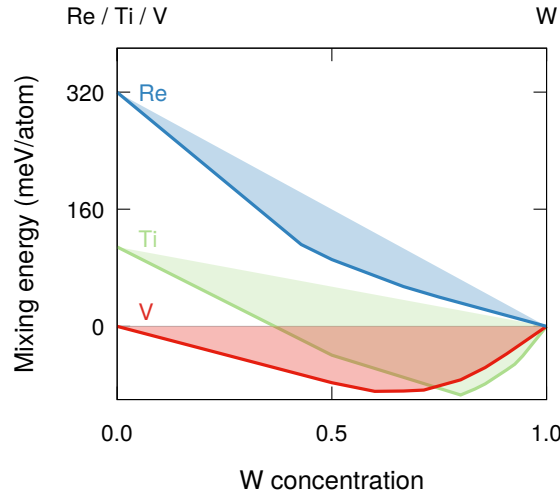


Figure 4.6: Schematic illustration of mixing energies for BCC structures of W–V, W–Ti, and W–Re based on data from paper II [79]. In the case of the latter two alloys, the energy offset in the Ti/Re-rich limit represents the HCP–BCC energy difference. The figure illustrates that the occurrence of a finite solubility at zero temperature in the case of W–Ti is the result of a combination of a negative mixing energy on the BCC lattice and not-too-large HCP–BCC energy difference.

In paper V, we showed that the phase diagram of W–Ti system was also strongly asymmetric for a different reason. In the non-magnetic W–Ti alloy, asymmetric phase diagram was found to emerge as a result of an asymmetry in lattice structures and their energetics.

The W–Ti binary alloy, at ambient conditions, comprises two different crystallographic phases, a BCC phase and a HCP one. The BCC phase is the most stable phase in the W-rich limit for low temperatures up to the melting point. The HCP phase prevails in the Ti-rich limit up to moderately high temperatures. In paper V, the mixing energies on both the BCC and HCP lattices were described using lattice models, specifically alloy cluster expansions (CEs). The CEs were sampled using Monte Carlo (MC) simulations in the variance constrained semi-grand canonical (VCSGC) ensemble, and thermodynamic data for the pure elements were taken from Ref. [91].

We demonstrated that the mixing energy on the BCC lattice is actually negative. This is in contrast to previous thermodynamic assessments based on experimental data, which have assumed a positive mixing energy over the entire composition range. This positive mixing energy was then found to be important for describing the low temperature solubility limit especially on the W-rich side. We showed that the solubility of Ti in W exceeds 20% down to zero temperature in stark contrast to previous thermodynamic assessments, while the inverse solubility is practically zero up to the HCP–BCC transition, see Fig. 4.5.

We concluded that such asymmetry in the phase diagram of the W–Ti system can be traced to the energy balance between BCC and HCP structures, which are stable and metastable, re-

spectively, on opposite ends of the phase diagram. It is important to note that while the low temperature regions of the phase diagrams of refractory metals are exceedingly difficult to sample in equilibrium, they are nonetheless relevant as they determine the driving forces under extreme non-equilibrium situations such as encountered during ion irradiation.

While our findings in the present paper pertain to our understanding of the W–Ti phase diagram, it has shown to have more general implications for alloy thermodynamics. Binary phase diagrams of metals that exhibit strongly asymmetric solubility limits are relatively rare. While as mentioned above in the case of the Fe–Cr system, they can arise from competing forms of magnetic order, we showed that this effect can also be observed in non-magnetic systems as a result of different lattice structures.

To illustrate this effect further, we considered two systems including W–V (BCC) and W–Re (BCC and HCP) in comparison with W–Ti (Fig. 4.6; data from paper II [79]). We showed that the W–Ti system emerges as an intermediate case compared to W–V and W–Re in terms of elemental reference structures and their energetics. V adopts a ground state BCC lattice and due to the difference in lattice constant at ambient conditions between W and V, the mixing energy was shown to be slightly asymmetric yet negative throughout the entire composition range.

As for Ti, the mixing energy of W–Re on the BCC lattice was shown to be negative but slightly positive for HCP (Fig. 5(c) from paper II). The HCP-BCC (free) energy difference for Re is, however, even larger than for Ti. As a result, the negative mixing energy of the BCC lattice is shifted upward such that the solubility of Re in BCC-W is very small and approaches zero with vanishing temperature.

The comparison with W–V and W–Re demonstrated that the occurrence of an asymmetric phase diagram in W–Ti is the result of a structural asymmetry on one hand and the rather small energy difference between BCC-Ti and HCP-Ti on the other hand. In turn, this implies that similar behavior can be expected in systems that combine different lattice structures, in particular if they are metastable.

## 4.4 Conclusion and outlook

In papers I-III, I performed extensive DFT calculations, which ultimately led to the parametrization of a new model for explaining the formation of W–Re precipitates (paper III). This model provides an improved understanding of the processes that are important for the actual irradiation process in terms of the formation of Re precipitates. Our results show that there are different regimes during formation and evaluation of W–Re precipitates. Besides the vacancy drag mechanism, interstitials also contribute to cluster formation while the mutual coupling of these fluxes is responsible for the initial defect accumulation. Understanding the mechanisms by which such nonequilibrium clusters form under irradiation is crucial to predict materials degradation and devise mitigation strategies.

In paper IV, I studied structural and thermophysical properties of non-magnetic transition metal elements employing a number of commonly used constraint-based exchange-correlation functionals as well as the vdW-DF-cx functional. I demonstrated that the vdW-DF-cx functional

provides an accurate description of the mentioned properties and its performance is at least comparable and usually better than that of the commonly used exchange-correlation functionals in the literature.

In paper V, I obtained the phase diagram of the W–Ti system and proposed a revision of the W-rich end of the phase diagram. Specifically it was shown that the solubility of Ti in BCC-W is much larger than predicted previously. Finally, by comparison with the W–V and W–Re systems, I demonstrated that structural asymmetry and energy balance of stable and metastable lattice structures are two important factors that can give rise to strongly asymmetric phase diagrams.

First and foremost, the results presented in this thesis provide an improved understanding of the W alloys. There are, however, still a number of areas that need to be addressed in the future. One interesting direction is a further investigation of the plastic deformation mechanisms in tungsten alloys. One of the concerns regarding the performance of tungsten as a structural material in fusion reactors, is the high brittle to ductile transition temperature of tungsten. The ductility of tungsten has been shown to be controlled by the mobility of screw dislocations and alloying of tungsten either intentionally or via transmutation alters this behavior [15, 30]. This area deserves to be investigated further.

Tungsten oxides are also relevant for understanding the performance tungsten in fusion reactors, as they are formed in the case of a breach of the reactor shell or reactor melt down. In such situations, tungsten readily forms oxides during air ingress into the vacuum vessel [92]. Among the tungsten oxides, tungsten trioxide is known to form a porous surface layer that cannot prevent continuous oxidation of the underlying metal. Understanding the mechanism of oxidation and which oxides of tungsten are formed should therefore be considered in the future work.

# Acknowledgments

I would first of all like to express my sincere gratitude to my supervisor, Paul Erhart. Thank you for giving me the opportunity to pursue this work and follow my dream of being a researcher. Your enthusiasm, immense knowledge, patience and continues support have always been a great help during my PhD studies. Thank you also for the instructive and fun experience of being your teaching assistant, I enjoyed it and learned a lot during that time. It was such a joy to start as the first PhD student in the group and see how the group grew and got stronger over the past five years. I also appreciate a lot the opportunity of having frequent meetings that did not change as the group grew, it was a great relief that I could always count on. I don't have more words to express my appreciation but to say *Ich danke dir sehr PAUL!*

I also would like to thank my examiner Göran Wahnström for discussions, professional advise and constructive comments. I learned a lot during the group meetings you arranged every week, and it was also so much fun joining our group activities. I will miss those a lot.

I acknowledge support from the Swedish Research Council and the European Research Council as well as computer time allocations by the Swedish National Infrastructure for Computing at NSC (Linköping), C3SE (Gothenburg), and PDC (Stockholm).

All my past and present colleagues should be thanked for making Origo Plan 7 a creative and positive environment. My special thanks goes to the ones at *joyful* Tuesday Fikas and Wednesday *Foxes* time! Thank you Mattias, Erik F, Magnus, Christopher, Anders, Erik J, Narjes, Joakim and Fredrik for all the fun talks sometime leading to challenging bets!, cheese and pepperoni half-pizzas, and suggestions on TV series. Well I might watch Game of Thrones one day! Still can't promise! I also would like to thank Daniel for the time we shared office, for long interesting discussions, dividing students assignments and hope they wouldn't pick the last one!

This is a great opportunity to acknowledge all the significant individuals without whom and their support and inspiration it was impossible for me to be here at this very moment. My friends here in Sweden and back in Iran. Azadeh, Samira, Siavash, Alireza, Jeroen and all my friends. You all mean a lot to me, and every one of you brought your own light and color into my life and shaped priceless memories for me.

This thesis is dedicated to my family. My deepest appreciation goes to my mom Farzaneh and my dad Mohammad, for truly unconditional love and support, for being my first teachers and leading me to the world of science and literature, and to my sister, my the other half, Shaili, for all the joys and happy moments we share. And finally David, thank you for your patience, love and support especially in the past few months and for sharing your fun and exciting world with me.



# Bibliography

- [1] A. Stukowski, *Visualization and analysis of atomistic simulation data with OVITO—the Open Visualization Tool*, Modelling and Simulation in Materials Science and Engineering **18**, 015012 (2010).
- [2] F. Sartori, G. De Tommasi, and F. Piccolo, *The joint European torus*, Control Systems, IEEE **26**, 64 (2006).
- [3] R. Aymar, P. Barabaschi, and Y. Shimomura, *The ITER design*, Plasma Physics and Controlled Fusion **44**, 519 (2002).
- [4] ITER, <https://www.iter.org>.
- [5] D. Maisonnier, I. Cook, S. Pierre, B. Lorenzo, D. P. Luigi, G. Luciano, N. Prachai, and P. Aldo, *DEMO and fusion power plant conceptual studies in Europe*, Fusion Engineering and Design **81**, 1123 (2006), proceedings of the Seventh International Symposium on Fusion Nuclear Technology ISFNT-7 Part B Proceedins of the Seventh International Symposium on Fusion Nuclear Technology.
- [6] M. Gilbert, S. Dudarev, S. Zheng, L. Packer, and J.-C. Sublet, *An integrated model for materials in a fusion power plant: transmutation, gas production, and helium embrittlement under neutron irradiation*, Nuclear Fusion **52**, 083019 (2012).
- [7] H. Bolt, V. Barabash, G. Federici, J. Linke, A. Loarte, J. Roth, and K. Sato, *Plasma facing and high heat flux materials—needs for ITER and beyond*, Journal of Nuclear Materials **307**, 43 (2002).
- [8] W. Wampler and R. Doerner, *The influence of displacement damage on deuterium retention in tungsten exposed to plasma*, Nuclear Fusion **49**, 115023 (2009).
- [9] V. Philipps, *Tungsten as material for plasma-facing components in fusion devices*, Journal of Nuclear Materials **415**, S2 (2011).
- [10] K. Tobita, S. Nishio, M. Enoeda, M. Sato, T. Isono, S. Sakurai, H. Nakamura, S. Sato, S. Suzuki, M. Ando, K. Ezato, T. Hayashi, T. Hayashi, T. Hirose, T. Inoue, Y. Kawamura, N. Koizumi, Y. Kudo, R. Kurihara, T. Kuroda, M. Matsukawa, K. Mouri, Y. Nakamura, M. Nishi, Y. Nomoto, J. Ohmori, N. Oyama, K. Sakamoto, T. Suzuki, M. Takechi, H. Tanigawa,

## Bibliography

---

- K. Tsuchiya, and D. Tsuru, *Design study of fusion DEMO plant at JAERI*, Fusion Engineering and Design **81**, 1151 (2006), proceedings of the Seventh International Symposium on Fusion Nuclear Technology ISFNT-7 Part B, Proceedings of the Seventh International Symposium on Fusion Nuclear Technology.
- [11] M. Rieth, S. Dudarev, S. Gonzalez de Vicente, J. Aktaa, T. Ahlgren, S. Antusch, D. Armstrong, M. Balden, N. Baluc, M.-F. Barthe, *et al.*, *Recent progress in research on tungsten materials for nuclear fusion applications in Europe*, Journal of Nuclear Materials **432**, 482 (2013).
- [12] *Yielding and fracture in tungsten and tungsten-rhenium alloys*, Journal of the Less Common Metals **17**, 133 (1969).
- [13] M. Kaufmann and R. Neu, *Tungsten as first wall material in fusion devices*, Fusion Engineering and Design **82**, 521 (2007), proceedings of the 24th Symposium on Fusion Technology SOFT-24.
- [14] T. Tietz and J. Wilson, *Behavior and Properties of Refractory Metals* (Stanford University Press, USA, 1965).
- [15] P. Gumbsch, J. Riedle, A. Hartmaier, and H. F. Fischmeister, *Controlling Factors for the Brittle-to-Ductile Transition in Tungsten Single Crystals*, Science **282**, 1293 (1998), Article-Type: research-article / Full publication date: Nov. 13, 1998 / Copyright (C) 1998 American Association for the Advancement of Science.
- [16] G. Cottrell, R. Pampin, and N. Taylor, *Transmutation and phase stability of tungsten armor in fusion power plants*, Fusion Science and Technology **50**, (2006).
- [17] T. Tanno, A. Hasegawa, M. Fujiwara, J.-C. He, S. Nogami, M. Satou, T. Shishido, and K. Abe, *Precipitation of Solid Transmutation Elements in Irradiated Tungsten Alloys*, Materials Transactions **49**, 2259 (2008).
- [18] A. Hasegawa, M. Fukuda, T. Tanno, and S. Nogami, *Neutron Irradiation Behavior of Tungsten*, MATERIALS TRANSACTIONS **54**, 466 (2013).
- [19] G. S. Was, *Fundamentals of radiation materials science* (Springer, USA, 2007).
- [20] *Radiation damage in materials*, [http://www.acclab.helsinki.fi/~knordlun/rad\\_dam\\_course](http://www.acclab.helsinki.fi/~knordlun/rad_dam_course).
- [21] N. Matsufuji, A. Fukumura, M. Komori, T. Kanai, and T. Kohno, *Influence of fragment reaction of relativistic heavy charged particles on heavy-ion radiotherapy*, Physics in Medicine and Biology **48**, 1605 (2003).
- [22] S. C. White and M. J. Pharoah, *Oral radiology: principles and interpretation* (Elsevier Health Sciences, USA, 2014).

- [23] M. I. Hoffert, K. Caldeira, G. Benford, D. R. Criswell, C. Green, H. Herzog, A. K. Jain, H. S. Kheshgi, K. S. Lackner, J. S. Lewis, *et al.*, *Advanced technology paths to global climate stability: energy for a greenhouse planet*, *Science* **298**, 981 (2002).
- [24] H. G. Graetzer, *Discovery of nuclear fission*, *American Journal of Physics* **32**, 9 (1964).
- [25] M. STEINBRÜCK, A. Meier, E. Nold, and U. Stegmaier, *Degradation and oxidation of B4C control rod segments at high temperatures*, *Wissenschaftliche Berichte FZKA* **6980**, (2004).
- [26] D. A. Petti, Z. Martinson, R. Hobbins, C. Allison, E. Carlson, D. Hagrman, T. Cheng, J. Hartwell, K. Vinjamuri, and L. Seifken, Technical report, Nuclear Regulatory Commission, Washington, DC (USA). Div. of Systems Research; EG and G Idaho, Inc., Idaho Falls, ID (USA) (unpublished).
- [27] K. Miyamoto, Technical report, National Inst. for Fusion Science, Toki, Gifu (Japan), Japan (unpublished).
- [28] J. A. Bittencourt, *Fundamentals of plasma physics* (Elsevier, USA, 2013).
- [29] Y. Wu, *Design analysis of the China dual-functional lithium lead (DFLL) test blanket module in ITER*, *Fusion Engineering and Design* **82**, 1893 (2007), proceedings of the 24th Symposium on Fusion Technology SOFT-24.
- [30] D. Hull and D. J. Bacon, *Introduction to Dislocations*, 4th ed. (Butterworth-Heinemann, UK, 2001).
- [31] S. J. Zinkle and N. M. Ghoniem, *Operating temperature windows for fusion reactor structural materials*, *Fusion Engineering and Design* **51**, 55 (2000).
- [32] S. P. Fitzgerald and D. Nguyen-Manh, *Peierls Potential for Crowdions in the bcc Transition Metals*, *Physical Review Letters* **101**, 115504 (2008).
- [33] C. Becquart and C. Domain, *An object Kinetic Monte Carlo Simulation of the dynamics of helium and point defects in tungsten*, *Journal of Nuclear Materials* **385**, 223 (2009).
- [34] R. S. Averback and T. Diaz de la Rubia, *Displacement Damage in Irradiated Metals and Semiconductors*, *Solid State Physics* **51**, 281 (1998).
- [35] W. H. Zhou, Y. G. Li, L. F. Huang, Z. Zeng, and X. Ju, *Dynamical behaviors of self-interstitial atoms in tungsten*, *Journal of Nuclear Materials* **437**, 438 (2013).
- [36] A. L. Bement, *Irradiation effects on structural alloys for nuclear reactor applications* (ASTM International, USA, 1971), Vol. 484.
- [37] T. Suzudo, M. Yamaguchi, and A. Hasegawa, *Stability and mobility of rhenium and osmium in tungsten: first principles study*, *Modelling Simul. Mater. Sci. Eng.* **22**, 075006 (2014).

## Bibliography

---

- [38] D. Kato, H. Iwakiri, Y. Watanabe, K. Morishita, and T. Muroga, *Super-saturated hydrogen effects on radiation damages in tungsten under the high-flux divertor plasma irradiation*, Nuclear Fusion **55**, 083019 (2015).
- [39] M. Baldwin and R. Doerner, *Helium induced nanoscopic morphology on tungsten under fusion relevant plasma conditions*, Nuclear Fusion **48**, 035001 (2008).
- [40] S. Kajita, W. Sakaguchi, N. Ohno, N. Yoshida, and T. Saeki, *Formation process of tungsten nanostructure by the exposure to helium plasma under fusion relevant plasma conditions*, Nuclear Fusion **49**, 095005 (2009).
- [41] H. Iwakiri, K. Yasunaga, K. Morishita, and N. Yoshida, *Microstructure evolution in tungsten during low-energy helium ion irradiation*, Journal of Nuclear Materials **283–287**, Part 2, 1134 (2000), 9th Int. Conf. on Fusion Reactor Materials.
- [42] S. Takamura, N. Ohno, D. Nishijima, and S. Kajita, *Formation of Nanostructured Tungsten with Arborescent Shape due to Helium Plasma Irradiation*, Plasma and Fusion Research **1**, 051 (2006).
- [43] M. Aguirre, A. Martín, J. Pastor, J. LLorca, M. Monge, and R. Pareja, *Mechanical properties of tungsten alloys with  $Y_2O_3$  and titanium additions*, Journal of Nuclear Materials **417**, 516 (2011).
- [44] A. Giannattasio and S. G. Roberts, *Strain-rate dependence of the brittle-to-ductile transition temperature in tungsten*, Philosophical Magazine **87**, 2589 (2007).
- [45] W. D. Klopp, *A review of chromium, molybdenum, and tungsten alloys*, Journal of the Less Common Metals **42**, 261 (1975).
- [46] P. Hohenberg and W. Kohn, *Inhomogeneous electron gas*, Physical Review **136**, .
- [47] W. Kohn and L. J. Sham, *Self-consistent equations including exchange and correlation effects*, Physical Review **140**, A1133 (1965).
- [48] J. P. Perdew, K. Burke, and M. Ernzerhof, *Generalized Gradient Approximation Made Simple*, Physical Review Letters **77**, 3865 (1996), erratum, *ibid.* **78**, 1396(E) (1997).
- [49] K. Burke, *Perspective on density functional theory*, The Journal of chemical physics **136**, 150901 (2012).
- [50] J. P. Perdew, A. Ruzsinszky, G. I. Csonka, O. A. Vydrov, G. E. Scuseria, L. A. Constantin, X. Zhou, and K. Burke, *Restoring the density-gradient expansion for exchange in solids and surfaces*, Physical Review Letters **100**, 136406 (2008).
- [51] R. Armiento and A. E. Mattsson, *Functional designed to include surface effects in self-consistent density functional theory*, Physical Review B **72**, 085108 (2005).

- 
- [52] M. Dion, H. Rydberg, E. Schröder, D. C. Langreth, and B. I. Lundqvist, *Van der Waals density functional for general geometries*, Physical review letters **92**, 246401 (2004).
- [53] K. Berland and P. Hyldgaard, *Exchange functional that tests the robustness of the plasmon description of the van der Waals density functional*, Physical Review B **89**, 035412 (2014).
- [54] C. Kittel and P. McEuen, *Introduction to solid state physics* (Wiley New York, ADDRESS, 1976), Vol. 8.
- [55] D. Hamann, M. Schlüter, and C. Chiang, *Norm-conserving pseudopotentials*, Physical Review Letters **43**, 1494 (1979).
- [56] D. Vanderbilt, *Soft self-consistent pseudopotentials in a generalized eigenvalue formalism*, Physical Review B **41**, 7892 (1990).
- [57] P. E. Blöchl, *Projector augmented-wave method*, Physical Review B **50**, 17953 (1994).
- [58] X.-S. Kong, X. Wu, Y.-W. You, C. S. Liu, Q. F. Fang, J.-L. Chen, G. N. Luo, and Z. Wang, *First-principles calculations of transition metal-solute interactions with point defects in tungsten*, Acta Materialia **66**, 172 (2014).
- [59] L. Ventelon, F. Willaime, C.-C. Fu, M. Heran, and I. Ginoux, *Ab initio investigation of radiation defects in tungsten: Structure of self-interstitials and specificity of di-vacancies compared to other bcc transition metals*, Journal of Nuclear Materials **425**, 16 (2012).
- [60] P. Erhart and K. Albe, *Thermodynamics of mono- and di-vacancies in barium titanate*, **102**, 084111 (2007).
- [61] C. S. Becquart and C. Domain, *Molecular dynamics simulations of damage and plasticity: The role of ab initio calculations in the development of interatomic potentials*, **89**, 3215 (2009).
- [62] M. Z. Hossain and J. Marian, *Stress-dependent solute energetics in W/Re alloys from first-principles calculations*, Acta Materialia **80**, 107 (2014).
- [63] S. A. Centoni, B. Sadigh, G. H. Gilmer, T. J. Lenosky, T. Diaz de la Rubia, and C. B. Musgrave, *First-principles calculation of intrinsic defect formation volumes in silicon*, Physical Review B **72**, 195206 (2005).
- [64] E. Jedvik, A. Lindman, M. P. Benediktsson, and G. Wahnström, *Size and shape of oxygen vacancies and protons in acceptor-doped barium zirconate*, Solid State Ionics **275**, 2 (2015).
- [65] A. R. Allnatt and A. B. Lidiard, *Atomic Transport in Solids* (Cambridge University Press, Cambridge, 2003).
- [66] H. Jónsson, G. Mills, and K. W. Jacobsen, in *Classical and Quantum Dynamics in Condensed Phase Simulations*, edited by B. J. Berne, G. Ciccotti, and D. F. Coker (World Scientific, Singapore, 1998), pp. 385–404.

## Bibliography

---

- [67] G. Henkelman and H. Jónsson, *Improved tangent estimate in the nudged elastic band method for finding minimum energy paths and saddle points*, **113**, 9978 (2000).
- [68] G. Henkelman, B. P. Uberuaga, and H. Jónsson, *A climbing image nudged elastic band method for finding saddle points and minimum energy paths*, *The Journal of Chemical Physics* **113**, 9901 (2000).
- [69] A. van de Walle, *Multicomponent multisublattice alloys, nonconfigurational entropy and other additions to the Alloy Theoretic Automated Toolkit*, *Calphad* **33**, 266 (2009).
- [70] A. van de Walle, *Methods for first-principles alloy thermodynamics*, *JOM* **65**, 1523 (2013).
- [71] L. J. Nelson, V. Ozoliņš, C. S. Reese, F. Zhou, and G. L. Hart, *Cluster expansion made easy with Bayesian compressive sensing*, *Physical Review B* **88**, 155105 (2013).
- [72] J. M. Sanchez, F. Ducastelle, and D. Gratias, *Generalized cluster description of multicomponent systems*, *Physica* **128**, 334 (1984).
- [73] L. J. Nelson, G. L. Hart, F. Zhou, V. Ozoliņš, *et al.*, *Compressive sensing as a paradigm for building physics models*, *Physical Review B* **87**, 035125 (2013).
- [74] E. Candes and M. Wakin, *An Introduction To Compressive Sampling*, *Signal Processing Magazine, IEEE* **25**, 21 (2008).
- [75] B. Sadigh and P. Erhart, *Calculations of excess free energies of precipitates via direct thermodynamic integration across phase boundaries*, *Phys. Rev. B* **86**, 134204 (2012).
- [76] *Property change mechanism in tungsten under neutron irradiation in various reactors*, *Journal of Nuclear Materials* **417**, 491 (2011), proceedings of ICFRM-14.
- [77] T. Tanno, A. Hasegawa, J.-C. He, M. Fujiwara, S. Nogami, M. Satou, T. Shishido, and K. Abe, *Effects of Transmutation Elements on Neutron Irradiation Hardening of Tungsten*, *MATERIALS TRANSACTIONS* **48**, 2399 (2007).
- [78] L. Gharaee and P. Erhart, *A first-principles investigation of interstitial defects in dilute tungsten alloys*, *Journal of Nuclear Materials* **467**, 448 (2015).
- [79] L. Gharaee, J. Marian, and P. Erhart, *The role of interstitial binding in radiation induced segregation in W-Re alloys*, *Journal of Applied Physics* **120**, 025901 (2016).
- [80] C. H. Huang, L. Gharaee, Y. Zhao, P. Erhart, and J. Marian, *Mechanism of Re precipitation in irradiated W-Re alloys from kinetic Monte Carlo simulations*, arXiv preprint arXiv:1702.03019, (2017).
- [81] L. Gharaee, P. Erhart, and P. Hyldgaard, *Finite-temperature properties of non-magnetic transition metals: Comparison of the performance of constraint-based semi and nonlocal functionals*, *Physical Review B* **95**, 085147 (2017).

- 
- [82] L. Gharaee, M. Ångqvist, M. Rahm, and P. Erhart, *Structurally driven asymmetric miscibility in the phase diagram of W-Ti*, In manuscript , (2017).
- [83] E. Rudy and S. Windisch, *Revision of titanium-tungsten system*, Trans. Metall. Soc. AIME **242**, 953 (1968).
- [84] J. L. Murray, *The Ti-W (Titanium-Tungsten) System*, Bull. Alloy Phase Diagrams **2**, 192 (1981).
- [85] L. Kaufman and H. Nesor, *Calculation of Superalloy Phase Diagrams: Part IV*, Metall. Trans. **6A**, 2123 (1975).
- [86] S. K. Lee and D. N. Lee, *CALCULATION OF PHASE DIAGRAMS USING PARTIAL PHASE DIAGRAM DATA*, Calphad **10**, 61 (1986).
- [87] S. Jönsson, *Reevaluation of the Ti-W system and prediction of the Ti-W-N phase diagram*, Zeitschr. Metallkunde **87**, 784 (1996).
- [88] P. Olsson, I. A. Abrikosov, and J. Wallenius, *Electronic origin of the anomalous stability of Fe-rich bcc Fe-Cr alloys*, Physical Review B **73**, 104416 (2006).
- [89] T. P. C. Klaver, R. Drautz, and M. W. Finnis, *Magnetism and thermodynamics of defect-free Fe-Cr alloys*, Phys. Rev. B **74**, 094435 (2006).
- [90] G. J. Ackland, *Magnetically Induced Immiscibility in the Ising Model of FeCr Stainless Steel*, Physical Review Letters **97**, 015502 (2006).
- [91] A. T. Dinsdale, *SGTE data for pure elements*, CALPHAD **15**, 317 (1991).
- [92] A. Litnovsky, T. Wegener, F. Klein, C. Linsmeier, M. Rasinski, A. Kreter, B. Unterberg, M. Vogel, S. Kraus, U. Breuer, C. Garcia-Rosales, A. Calvo, and N. Ordas, *Smart alloys for a future fusion power plant: First studies under stationary plasma load and in accidental conditions*, Nuclear Materials and Energy , (2016).



# Paper I

**A first-principles investigation of interstitial defects in dilute tungsten alloys**

Leili Gharaee and Paul Erhart

Journal of Nuclear Materials **467**, 448-456 (2015).





# A first-principles investigation of interstitial defects in dilute tungsten alloys



Leili Gharaee, Paul Erhart\*

Department of Applied Physics, Chalmers University of Technology, S-412 67 Gothenburg, Sweden

## ARTICLE INFO

### Article history:

Received 26 February 2015

Received in revised form

31 August 2015

Accepted 1 September 2015

Available online 6 September 2015

### Keywords:

Tungsten alloys

Defects

Interstitials

Ion irradiation

Trapping

Radiation-induced segregation

## ABSTRACT

The thermodynamic properties of intrinsic and extrinsic (Ti, V, Zr, Nb, Hf, Ta, Re) defects in tungsten have been investigated using density functional theory calculations. The formation energies of substitutional defects are discussed with respect to their thermodynamic solubility limits. Several different interstitial configurations have been identified as local minima on the potential energy surface. In addition to dumbbell configurations with orientations along  $\langle 111 \rangle$  and  $\langle 110 \rangle$ , a lower symmetry configuration is described, which is referred to as a bridge interstitial. This interstitial type is found to be the lowest energy configuration for mixed-interstitials containing Ti, V, and Re, and can be up to 0.2 eV lower in energy than the other configurations. According to the calculations Ti, V and Re also trap self-interstitial atoms, which can be produced in substantial numbers during ion irradiation, affecting the mobility of the latter.

© 2015 Elsevier B.V. All rights reserved.

## 1. Introduction

Tungsten alloys are considered for structural applications in fusion reactors, especially for armor materials at the divertor and first wall [1–4]. This interest is motivated by promising physical properties such as high melting point, low coefficient of thermal expansion, high thermal conductivity, and high sputtering resistance. Alloy formation occurs naturally during fusion reactor operation due to nuclear transmutation caused by high energy neutron exposure [5]. In this fashion pure tungsten will gradually evolve into an W–Re–Os–Ta alloy [6]. Alloying has also been suggested to lower the temperature range in which the fracture mode of pure tungsten changes from ductile to brittle [7,8]. The latter intersects with the operation temperature window of current and future fusion reactors [2,9], which causes concern with regard to mechanical integrity. Since alloying affects many properties of importance including mechanical performance, thermal conductivity, as well as swelling under irradiation, it is important to develop our understanding of tungsten alloys under the relevant conditions [10].

With regard to applications in fusion reactors one must in

particular consider the performance of the material under ion irradiation, which causes the localized production of lattice defects such as vacancies and interstitials [11,12]. Whereas vacancies are relatively immobile, interstitials in pure tungsten can migrate extremely fast [13] allowing for efficient defect recombination, which is a crucial factor with respect to radiation tolerance [14]. In alloys solute atoms and interstitials can potentially bind to each other, reducing the mobility of the latter and possibly accelerating damage buildup compared to the pure material.

An assessment of different alloys for applications in fusion environments should thus invoke information regarding the interaction of intrinsic point defects, solute atoms, and dislocations. As such information is difficult to obtain experimentally, computational modeling plays an important role in investigating the fundamental limits of materials performance. Since the problem at hand involves many length and time lengths, a multiscale modeling approach must be employed. In this context, first-principles calculations can provide critical microscopic parameters that cannot be accessed otherwise. While pure tungsten has been studied extensively, see e.g., Ref. [15], our understanding of alloy behavior is still in its infancy. Recent first-principles calculations considered the energetics of intrinsic defects and solute atoms for a range of transition elements and identified chemical trends across the periodic table [16]. The migration behavior has been investigated using a similar approach for the two dominant products of nuclear

\* Corresponding author.

E-mail address: [erhart@chalmers.se](mailto:erhart@chalmers.se) (P. Erhart).

transmutation (Re, Os) [6]. There is also information available regarding the interaction of substitutional Re with dislocations and its effect on lattice expansion [17].

The objective of the present paper is to deepen our understanding of the interaction of alloy elements with intrinsic defects (formation and binding energies) and to provide parameters that characterize the elastic long-range interactions between different defects (formation volume tensors) in particular with respect to dislocations [17]. The focus is on refractory elements that are close to W in the periodic table and possess a similar electronic structure. The paper provides a careful analysis of the computational parameters that affect the convergence of the respective data. For Ti, V, and Re, a low symmetry interstitial configuration is observed, referred to as a bridge interstitial, which is between 0.05 and 0.2 eV lower in energy than the commonly investigated dumbbell configurations [16]. For these three elements, we also find a strong binding to self-interstitial atoms (SIAs), on a scale which prohibits detrapping on realistic time scales. The analysis of the formation volume tensors reveals a very strong elastic anisotropy for the interstitial defects, which can be expected to enhance long-range defect–defect interaction and alignment.

## 2. Methodology

### 2.1. Computational details

Calculations were performed within density functional theory (DFT) using the projector augmented wave (PAW) method [18,19] as implemented in the Vienna *ab-initio* simulation package [20–23]. Exchange–correlation effects were treated within the generalized gradient approximation as parametrized by Perdew, Burke and Ernzerhof [24] and the occupation of electronic states was performed using the first order Methfessel–Paxton scheme with a smearing width of 0.2 eV. Defect configurations based on supercells with up to 250 atoms were considered corresponding to  $5 \times 5 \times 5$  repetitions of the conventional (2-atom) unit cell. For structural optimizations the atomic coordinates *as well as* the cell metric were relaxed until the atomic forces were converged to within 20 meV/Å and the residual stresses were less than 0.2 GPa. A plane wave energy cutoff energy of 300 eV was employed; increasing the cutoff energy up to 500 eV led to changes in formation and binding energies by less than 0.02 eV. We furthermore carefully considered the effects of Brillouin zone sampling, supercell size, and semi-core states on the formation and binding energies as detailed in Sect. 3.1 below.

### 2.2. Thermodynamic relations

Defect formation energies were calculated using a well established thermodynamic formalism [25] (also see Ref. [26])

$$E^f = E^{\text{defect}} - E^{\text{ideal}} - \sum_i \Delta n_i \mu_i, \quad (1)$$

where  $E^{\text{defect}}$  is the energy of the defective system and  $E^{\text{ideal}}$  is the total energy of the perfect reference cell. The variation of the formation energy with the chemical environment is given by the last term in Eq. (1), which involves the chemical potentials of the constituents. The difference between the number of atoms of type  $i$  in the reference cell and the defective cell is denoted by  $\Delta n_i$ , where positive and negative values correspond to the addition and removal of an atom relative to the ideal cell, respectively. Here, we take the chemical potential  $\mu_i$  of each constituent to be identical to its cohesive energy per atom [26].

The binding energy between solute atoms and point defects is a

key factor for understanding the thermodynamic properties of alloys [27,28]. It is given by the difference between formation energies of the mixed-interstitial,  $E^f([X-W]_{\text{W}})$ , and the sum of formation energy of the self-interstitial,  $E^f([W-W]_{\text{W}})$ , and substitutional configurations,  $E^f(X_{\text{W}})$ ,

$$E_X^b = E^f([X-W]_{\text{W}}) - E^f([W-W]_{\text{W}}) - E^f(X_{\text{W}}). \quad (2)$$

In this notation, the binding energy corresponds to the reaction enthalpy of the quasi-chemical reaction



Negative binding energies thus imply an attractive interaction between SIA and extrinsic substitutional defect.

The elastic distortion caused by a defect can be quantified by its formation volume tensor [29–31]. It determines the long-range elastic interaction between defects including but not limited to point and line defects. Given the cell metrics of the ideal supercell  $\mathbf{L}_0$  and the fully relaxed supercell containing the defect  $\mathbf{L}$ , the formation volume tensor can be obtained from the relation [29,31].

$$\mathbf{v}^f = \det(\mathbf{L}_0) \ln(\mathbf{L}_0^{-1} \mathbf{L}) \approx \det(\mathbf{L}_0) (\mathbf{L} - \mathbf{L}_0^{-1}) \mathbf{L}_0^{-1}. \quad (3)$$

The formation volume equals one third of the trace of the formation volume tensor. By diagonalizing the formation volume tensor one obtains the orientation and the strength of the strain field. The former is specified by the eigenvectors whereas the latter is related to the magnitude of the eigenvalues. In particular, we consider below the anisotropy defined here as the ratio of the largest to the smallest eigenvalue.

## 3. Results and discussion

### 3.1. Convergence considerations

#### 3.1.1. Brillouin zone sampling

The calculation of defect formation energies in metallic systems via density functional theory calculations and the supercell approach is subject to several sources of errors most importantly the sampling of the Brillouin zone via a discrete  $\mathbf{k}$ -point mesh, the interaction between periodic images of the same defect, and the treatment of semi-core states. The first aspect results from the fact that defects in metals act as perturbations, which can cause long-range oscillations in the electronic structure (Friedel oscillations). To capture these oscillations it is not uncommon that one requires a denser  $\mathbf{k}$ -point mesh than for the corresponding defect free system. This is illustrated in Fig. 1(a) for the W vacancy. It is apparent from these data that even for a 250-atom cell ( $5 \times 5 \times 5$  conventional unit cells) one requires at least a  $5 \times 5 \times 5$  Monkhorst–Pack mesh in order to converge the formation energy to better than 0.1 eV; this is equivalent to a  $25 \times 25 \times 25$  mesh with respect to the primitive unit cell. For comparison, a  $15 \times 15 \times 15$  Monkhorst–Pack is sufficient to converge the total energy of a primitive cell to better than 1 meV/atom. In the case of interstitials, which are also strong perturbation centers, the formation energies exhibit a slightly smaller yet still pronounced variation than for the vacancy as illustrated in Fig. 1(c). Finally, for substitutional defects the effect is rather weak as shown for substitutional Ti in Fig. 1(b). An extensive data set of calculated formation energies provided in the appendix demonstrates that the aforementioned effects are present for all alloying elements considered in the present study. All formation energies discussed in Sect. 3.2 were calculated using a  $6 \times 6 \times 6$  Monkhorst–Pack grid in

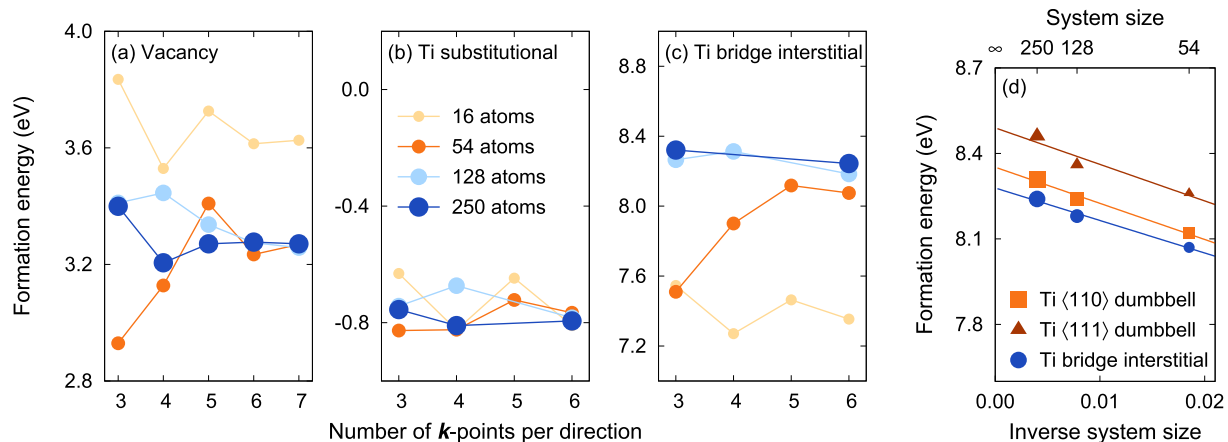


**Fig. 1.** Convergence of the formation energies of (a) vacancy, (b) Ti substitutional, (c) and Ti bridge interstitial with  $k$ -point density for different system sizes. (d) Finite size scaling of formation energies for Ti interstitial defects. The defect configurations are schematically shown in Fig. 3. The calculations shown here did not include semi-core states.

order to minimize Brillouin zone sampling errors.

### 3.1.2. Size dependence

The most widely methodology to describe defects in the *dilute* limit is the supercell approach, in which a defect is represented by a periodic array of identical configurations. The approach has significant computational advantages and avoids surface effects. Even with relatively large supercells there is, however, a contribution to the formation energy that results from the interaction of a periodic array of elastic dipoles.<sup>1</sup> In an elastically isotropic medium the elastic interaction scales with the inverse volume, i.e.

$$E_f(N) \approx E_f(N \rightarrow \infty) + a/V = E_f(N \rightarrow \infty) + b/N, \quad (4)$$

where  $a$  and  $b$  are constants of proportionality. This relation enables one to correct for this error by finite size scaling [33,34]. This is illustrated for Ti interstitial configurations in Fig. 1(d), which clearly exhibits an inverse linear behavior; the interstitial configurations are shown in Fig. 3. Note that smaller cells than the ones included here (e.g., a  $2 \times 2 \times 2$  16-atom cell) deviate from the inverse linear behavior because of non-linear contributions associated with interacting defect cores. The formation energies discussed in Sect. 3.2 were obtained using the same finite-size scaling approach as used in Fig. 1(d) based on the data compiled in the appendix. The error associated with fitting the data to Eq. (4) is 0.03 eV or less for all defect configurations.

### 3.1.3. Semi-core states

It has been argued that the inclusion of semi-core states, specifically  $W-5p$  states, in the pseudo-potential or PAW data set is important to correctly describe the formation energies of SIAs in tungsten [16,35]. This is reasonable as interstitial configurations involve very short interatomic distances and are therefore more sensitive to the core radius of the pseudo-potential/PAW data set. To quantify these effects for the present defects, we carried out a systematic analysis of the effect of including semi-core states. As the computational effort increases significantly due to approximately twice as many electrons in the calculation, the bulk of this study was restricted to 128-atom cells and a  $3 \times 3 \times 3$  Monkhorst-Pack  $k$ -point mesh, see table in the appendix. For a selected number of configurations including both interstitial and substitutional

defects, we also studied 250-atom cells as well as  $6 \times 6 \times 6$   $k$ -point grids. These data showed that the effect of semi-core states is only weakly dependent by Brillouin zone sampling and system size.

From the data in Table 2, one can deduce that semi-core states have a negligible influence on the formation energies of substitutional defects with the exception of V and possibly Zr. The situation is quite different in the case of the interstitial defects, for which the effect ranges from almost zero (Zr, Nb) to 0.5 eV and above (Ti, V, Ta). The energy shift varies between the different configurations and in some cases changes the energetic order (Ti, V). It is typically larger for  $\langle 110 \rangle$  interstitials, which have the shortest interatomic separation, than for  $\langle 111 \rangle$  and bridge interstitial configurations.

Given the computational expense associated not only with the treatment of semi-core states but system size and Brillouin zone sampling, we below present formation energies that are obtained as follows. We consider calculations that are based a  $6 \times 6 \times 6$  Monkhorst-Pack mesh and do not include semi-core states. These data are subjected to the finite-size scaling procedure described in Sect. 3.1.2, after which we add the shift in the formation energies due to semi-core states that was obtained using 128-atom cells and a  $3 \times 3 \times 3$  Monkhorst-Pack mesh. All respective formation energies are shown explicitly in Table 2. Based on the analysis in the present section, we conservatively estimate the error in the calculated formation energies to be about 0.1 eV for absolute numbers and 0.05 eV for energy differences.

## 3.2. Formation energies

### 3.2.1. Substitutional defects

The formation energies for substitutional solute atoms are compiled in Table 1 and are shown in Fig. 2. One observes that both the elements from group 4 (V, Nb, Ta) and group 5 (Ti, Zr, Hf) exhibit a non-monotonic variation as one passes the  $3d$  to the  $5d$  series. These observations are in accord with earlier calculations [16] although in the latter case the formation energy of Zr is slightly negative whereas it is slightly positive in the present case. As discussed in Sect. 3.1, various sources of errors have been very carefully considered in the present case and the full data set shown in Table 2 also shows the present data to be very consistent.

The formation energy of a substitutional defect is related to the slope of the mixing energy curve in the dilute limit. Negative formation energies therefore imply a tendency to form solid solutions over a wide temperature range with W and additionally indicate a tendency to form ordered phases at lower temperatures [39–41].

<sup>1</sup> In the case of semiconductors additional effects such as image charge interactions and potential alignment corrections need to be taken into account [32].

**Table 1**  
Formation energies and volumes of intrinsic and extrinsic point defects in tungsten.

Element	Formation energies				Formation volumes						
	Sub	$\langle 111 \rangle$ -int	$\langle 110 \rangle$ -int	bridge-int	$v_{Sub}^f$	$v_{\langle 111 \rangle}^f$	$A_{\langle 111 \rangle}$	$v_{\langle 110 \rangle}^f$	$A_{\langle 110 \rangle}$	$v_{bridge}^f$	$A_{bridge}$
W		10.16	10.59	10.17	–	1.63	9.05	1.66	6.16	1.64	12.10
DFT [36]		9.55	9.84								
DFT [37]		9.82	10.10								
Expt [38]		9.06±0.63									
Ti	−0.81	8.83	8.99	8.73	0.01	1.38	8.99	1.30	8.34	1.33	9.45
V	−0.60	8.00	8.10	7.77	−0.18	1.21	16.37	1.19	14.93	1.20	24.37
Zr	0.07	11.21	11.74	11.21	0.28	1.85	5.18	1.83	3.35	1.85	5.62
Nb	−0.32	10.22	10.74	10.19	0.12	1.73	7.42	1.74	4.44	1.73	7.49
Hf	−0.20	9.99	11.53	10.14	0.25	1.86	8.25	1.64	4.96	1.85	7.04
Ta	−0.47	10.34	11.01	10.33	0.06	1.70	7.58	1.67	5.48	1.69	8.03
Re	0.17	9.53	9.55	9.49	−0.02	1.56	15.25	1.63	8.72	1.60	18.68

For the group 5 elements one obtains consistently negative formation energies, which is consistent with the mixing energy curves calculated earlier for the W–V [41], W–Nb [39], and W–Ta [39,41] systems.

While in the case of the group 5 alloys all boundary phases possess a BCC lattice structure, the situation is more complicated in the case of the group 4 and group 7 (Re) elements, for which the low temperature boundary phases with the exception of W adopt a hexagonal-close packed (HCP) structure. In addition, in the case of the group 4 elements one furthermore observes a high-temperature BCC phase that is vibrationally stabilized, whereas it is mechanically unstable at low temperatures.

Experimentally, it is difficult to accurately assess the phase diagrams of W-based alloys down to low temperatures due to the slow kinetics of refractory systems even at relatively high temperatures. As a result, most of the information available to date is based on thermodynamic assessments, which are frequently based on assumptions concerning the nature of the interatomic interactions [42].

In the case of Ti the calculated phase diagram [42] suggests a very extended solubility region at high-temperatures but a vanishing solubility as the temperature approaches zero. Barring any experimental information for temperatures below approximately 1000 K [43], this assessment was based on the *assumption* that the mixing energy is positive over the entire concentration range [42]. The present finding suggests that this assumption needs to be revised and a better data basis is required to accurately determine

the solvus line for Ti in W. It should be noted that while this region of the phase diagram is difficult to access by thermodynamic equilibrium studies, it can nonetheless be relevant for the behavior of the material under irradiation conditions as it determines the thermodynamic driving forces.

The solubility limits of Zr [42], Hf [42] as well as Re [44] in W are not determined by the equilibrium between W and another elemental phase but rather several ordered structure including the  $\chi$  and  $\sigma$  phases [45]. This implies that the respective compound formation enthalpy should be used to determine the chemical boundary conditions that enter Eq. (1) in the form of the chemical potentials  $\mu_i$ . This level of analysis is beyond the scope of the present work.

### 3.2.2. Interstitial defects

A systematic exploration of interstitial configurations associated with solute atoms in BCC tungsten, revealed three distinct low energy configurations corresponding to different local minima on the potential energy surface; these configurations are shown in Fig. 3. In addition to the well known  $\langle 111 \rangle$  and  $\langle 110 \rangle$  dumbbell configurations [3,13,36] a third “bridge interstitial” configuration [see Fig. 3(a)] was identified. This configuration can be understood as a lower symmetry derivative of the  $\langle 111 \rangle$  dumbbell configuration, in which the solute atom has moved away from the  $\langle 111 \rangle$  direction along one of the three  $\langle 2\bar{1}1 \rangle$  directions. This results in a bond angle with the nearest neighbors of approximately  $150^\circ$  (compared to  $180^\circ$  in the case of the straight dumbbell interstitial).

A configuration similar to the bridge interstitial has been reported for SIAs [6,35] and for the Re mixed-interstitial [6], which in the latter reference was referred to as a  $\langle 11h \rangle$  interstitial. In both of those cases the energy difference relative to the respective  $\langle 111 \rangle$  interstitial configurations appeared to be rather small (less than 0.05 eV). In particular in the case of the SIA the energy difference between crowdion and bridge  $\langle 11h \rangle$  configurations is quite sensitive to supercell size and shape with the crowdion configuration being the most stable in the limit of large defect separations [35]. We have carried out a vibrational analysis of bridge and crowdion configurations that demonstrates the slow size convergence of the crowdion configuration (due its strongly delocalized nature [3]) and supports the earlier analysis and conclusion [35]. In absolute numbers our results are very close to previous calculations [36,37].

The formation energies of extrinsic interstitial configurations are compiled in Table 1 and shown in Fig. 4. The bridge interstitial is found to be the most stable configuration for Ti, V, and Re interstitials. In the case of Zr and Hf the  $\langle 111 \rangle$  dumbbell shows the lowest formation energy, while for Nb and Ta the bridge and  $\langle 111 \rangle$  dumbbell configurations are energetically practically degenerate (yet configurationally distinct). Our finding of a bridge interstitial for Re agrees the results presented in Ref. [6]. Note that bridge

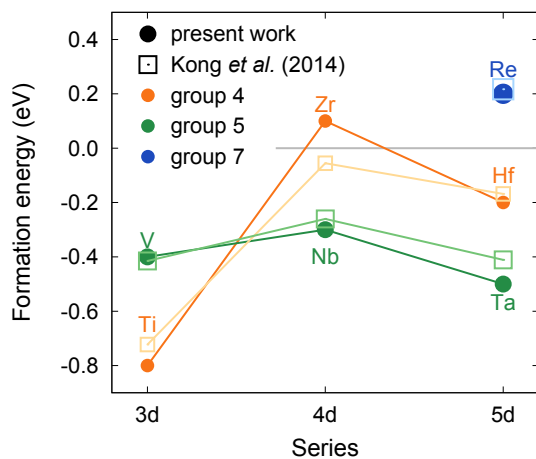


**Fig. 2.** Variation of the formation energies of substitutional defects across the periodic table according to the present calculations as well as prior calculations by Kong et al. [16].

**Table 2**  
Convergence of formation energies (in units of electronvolts) of intrinsic and extrinsic point defects in tungsten with respect to cell size,  $k$ -point sampling, and the treatment of semi-core states. Numbers in upright format correspond to calculations, in which the semi-core states (in particular the W-5p states) were *not* included. By contrast, italicized numbers show the results from calculations that did include semi-core states with numbers in brackets indicating the difference between the two types of calculations. Additional calculations with semi-core states were carried out for selected 250-atom supercell configurations. These calculations confirmed that the shift in the formation energies due to the neglect of semi-core states is only weakly dependent on system size. The last but one column reports the formation energies in the dilute limit from finite size scaling using data obtained in calculations without semi-core states (w/o sc) using  $6 \times 6 \times 6$   $k$ -point grids. The final column shows these data including a semi-core correction (w/sc) as described in Sect. 3.1.3.

Element	Defect	54-atom cells ( $3 \times 3 \times 3$ )				128-atom cells ( $4 \times 4 \times 4$ )			250-atom cells ( $5 \times 5 \times 5$ )			Extrapolated		
		$n_k$				$n_k$			$n_k$			$n_k$		
		3	4	5	6	3	4	6	3	4	6	6	6	
					w/o sc	w/sc	diff				w/o sc	w/sc		
self	$\langle 110 \rangle$ -int	9.21			9.83	10.15	<i>10.49</i>	(0.34)	10.20	10.07	10.24	10.16	10.25	<i>10.59</i>
	$\langle 111 \rangle$ -int	8.92	9.40	9.66	9.61	9.82	<i>10.09</i>	(0.27)	9.88	9.71	9.96	9.73	9.87	<i>10.16</i>
Ti	bridge-int	8.88			9.53	9.78	<i>10.10</i>	(0.32)	9.84	9.69	9.88	9.79	9.85	<i>10.17</i>
	sub	-0.83	-0.82	-0.72	-0.77	-0.74	<i>-0.76</i>	(-0.02)	-0.67	-0.78	-0.75	-0.81	-0.79	<i>-0.81</i>
V	$\langle 110 \rangle$ -int	7.66			8.12	8.30	<i>8.94</i>	(0.64)	8.33	8.24	8.36	8.31	8.35	<i>8.99</i>
	$\langle 111 \rangle$ -int	7.64			8.26	8.43	<i>8.77</i>	(0.34)	8.50	8.36	8.56	8.46	8.49	<i>8.83</i>
V	bridge-int	7.51			8.07	8.27	<i>8.72</i>	(0.45)	8.31	8.18	8.32	8.24	8.28	<i>8.73</i>
	sub	-0.44	-0.45	-0.41	-0.44	-0.42	<i>-0.59</i>	(-0.17)	-0.38	-0.44	-0.41	-0.46	-0.43	<i>-0.60</i>
Zr <sup>a</sup>	$\langle 110 \rangle$ -int	6.94			7.40	7.55	<i>8.04</i>	(0.49)	7.60	7.52	7.63	7.82	7.61	<i>8.10</i>
	$\langle 111 \rangle$ -int	6.87			7.49	7.65	<i>7.95</i>	(0.30)	7.71	7.59	7.78	7.67	7.70	<i>8.00</i>
Zr <sup>a</sup>	bridge-int	6.70			7.24	7.41	<i>7.76</i>	(0.35)	7.46	7.34	7.46	7.38	7.42	<i>7.77</i>
	sub	0.08	0.09	0.19	0.14	0.17	<i>0.11</i>	(-0.06)	0.23	0.13	0.18	0.09	0.13	<i>0.07</i>
Nb	$\langle 110 \rangle$ -int	10.71			11.33	11.66	<i>11.64</i>	(-0.02)	11.68	11.54	11.75	11.69	11.76	<i>11.74</i>
	$\langle 111 \rangle$ -int	10.14			10.86	11.10	<i>11.15</i>	(0.05)	11.18	10.98	11.27	11.13	11.16	<i>11.21</i>
Nb	sub	-0.30	-0.30	-0.27	-0.30	-0.29	<i>-0.32</i>	(-0.03)	-0.24	-0.30	-0.27	-0.31	-0.29	<i>-0.32</i>
	$\langle 110 \rangle$ -int	9.71			10.33	10.67	<i>10.64</i>	(-0.03)	10.70	10.57	10.76	10.68	10.77	<i>10.74</i>
Hf	$\langle 111 \rangle$ -int	9.22			9.91	10.13	<i>10.17</i>	(0.04)	10.21	10.02	10.28	10.15	10.18	<i>10.22</i>
	bridge-int	9.25			9.95	10.13	<i>10.16</i>	(0.03)	10.21	10.02	10.28	10.15	10.16	<i>10.19</i>
Hf	sub	-0.27	-0.25	-0.15	-0.19	-0.16	<i>-0.16</i>	(0.00)	-0.10	-0.20	-0.17	-0.23	-0.20	<i>-0.20</i>
	$\langle 110 \rangle$ -int	9.98			10.52	10.78	<i>11.47</i>	(0.69)	10.79	10.69	10.84	10.78	10.84	<i>11.53</i>
Ta	$\langle 111 \rangle$ -int	9.68			10.39	9.72	<i>10.01</i>	(0.29)	9.80	9.59	9.80	10.10	9.71	<i>9.99</i>
	bridge-int	8.91			9.56	9.76	<i>10.11</i>	(0.35)	9.85	9.65	9.88	9.77	9.79	<i>10.14</i>
Ta	sub	-0.48	-0.48	-0.45	-0.47	-0.45	<i>-0.46</i>	(-0.01)	-0.41	-0.47	-0.45	-0.47	-0.46	<i>-0.47</i>
	$\langle 110 \rangle$ -int	9.53			10.12	10.42	<i>10.90</i>	(0.48)	10.45	10.34	10.51	10.45	10.53	<i>11.01</i>
Re	$\langle 111 \rangle$ -int	9.06			9.74	9.97	<i>10.27</i>	(0.30)	10.04	9.86	10.11	10.01	10.04	<i>10.34</i>
	bridge-int	9.08			9.76	9.98	<i>10.27</i>	(0.29)	10.05	9.86	10.12	10.02	10.04	<i>10.33</i>
Re	sub	0.12	0.15	0.18	0.18	0.17	<i>0.17</i>	(0.00)	0.12	0.18	0.18	0.18	0.17	<i>0.17</i>
	$\langle 110 \rangle$ -int	8.29			8.91	9.23	<i>9.48</i>	(0.25)	9.28	9.14	9.29	9.21	9.30	<i>9.55</i>
Re	$\langle 111 \rangle$ -int	8.25			8.93	9.21	<i>9.44</i>	(0.23)	9.25	9.09	9.33	9.25	9.30	<i>9.53</i>
	bridge-int	8.24			8.86	9.14	<i>9.41</i>	(0.27)	9.18	9.06	9.23	9.15	9.22	<i>9.49</i>

<sup>a</sup> In the case of Zr, the bridge interstitial configuration always relaxed toward the  $\langle 111 \rangle$ -int configuration regardless of system size.

interstitial-type configurations were not considered in Ref. [16]. Furthermore, the binding of solute atoms was investigated relative to the  $\langle 111 \rangle$ -crowdion interstitial rather than with regard to the respective lowest energy configuration. For radiation induced segregation and precipitation processes, however, the latter quantity, which yields the thermodynamic binding energy, is the most relevant quantity.

In contrast to the present calculations for W–V, Muzyk et al. [41]

found the  $\langle 110 \rangle$  dumbbell interstitial to be the most stable configuration. The latter study, however, relied on calculations involving only 128-atom supercells and a  $3 \times 3 \times 3$   $k$ -point mesh. The analysis of computational errors provided in Sect. 3.1 suggests that these values are not fully converged.

For reference, Table 1 also contains data for SIAs, which have been extensively described before [6,35]. The geometries and energetics obtained here agree with these earlier calculations.

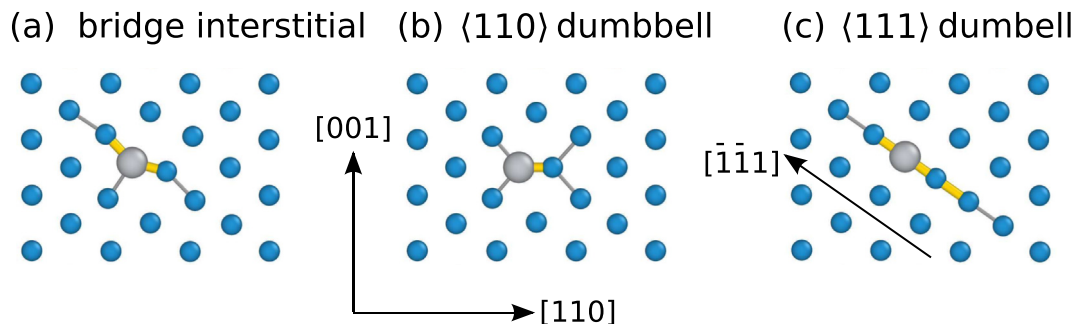


**Fig. 3.** Representative configurations of (a) bridge, (b)  $\langle 110 \rangle$  dumbbell, and (c)  $\langle 111 \rangle$  dumbbell interstitial defects. The  $\langle 111 \rangle$  crowdion configuration closely resembles the  $\langle 111 \rangle$  dumbbell configuration with a slightly larger spacing of the defect atoms along  $\langle 111 \rangle$  axis. The figure shows a slice parallel to a  $\{110\}$  plane of the structure. Small (blue) spheres indicate tungsten atoms whereas large (gray) spheres indicate alloying elements in the case of extrinsic and tungsten atoms in the case of intrinsic defects. Thicker (yellow) cylinders indicate bond lengths shorter than 2.5 Å whereas thinner (gray) cylinders indicate bond lengths shorter than 2.5 Å. (For interpretation of the references to color in this figure legend, the reader is referred to the web version of this article.)

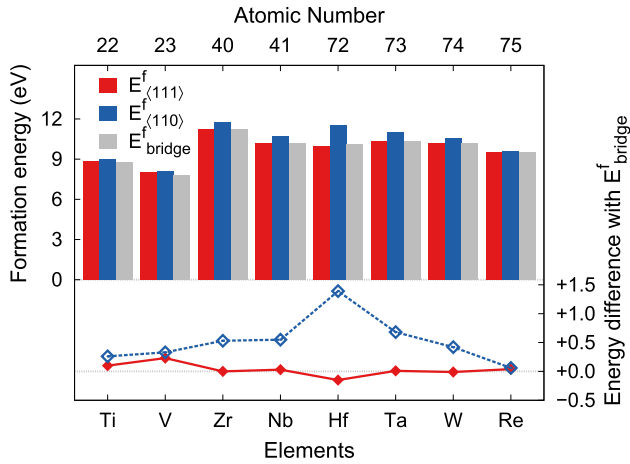


**Fig. 4.** Formation energy of bridge,  $\langle 111 \rangle$  and  $\langle 110 \rangle$  interstitials (left axis). Energy difference between  $\langle 111 \rangle$  and  $\langle 110 \rangle$  dumbbell interstitials with respect to bridge interstitial (right axis).

### 3.3. Binding energies

Interactions of impurities and alloying elements with point defects are of great importance for materials under irradiation as they can significantly affect the mobility of defects [4]. This can result in segregation, precipitation and/or the formation of secondary phases at grain boundaries. To assess the tendency of different elements to trap SIAs we have therefore calculated binding energies between impurities and interstitials. As shown in Fig. 5 negative values are obtained for Ti, V and Re interstitial configurations, while for the remaining elements the binding energies are positive.

A previous study [4] has also reported an attractive interaction between Re and SIAs of  $E^b = -0.8$  eV, the orientation of the mixed-interstitial was, however, not specified. The binding energies obtained in the present study are  $E_{bridge}^b = -0.62$  eV,  $E_{(111)int}^b = -0.52$  eV and  $E_{(110)int}^b = -0.36$  eV.

The negative binding energies for Ti, V and Re, which are also the three elements that favor bridge interstitial configurations, imply an attractive interactions with SIAs, whence these elements are expected to trap interstitials. The binding is very strong (-0.6–1.8 eV) in all three cases, indicating that thermal detrapping

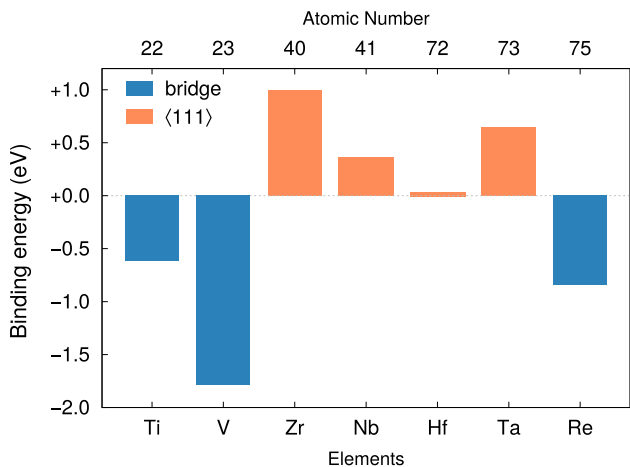


**Fig. 5.** Binding energies in units of electronvolts between self-interstitial atoms and substitutional solute atoms relative to the respective most stable mixed-interstitial configuration according to Eq. (2).

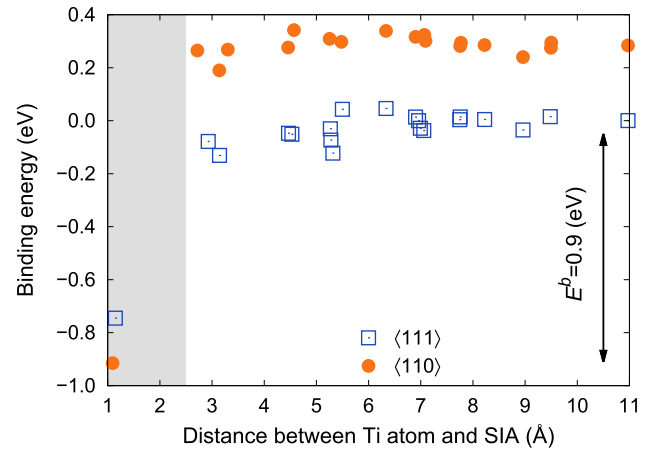


**Fig. 6.** Distance dependence of the binding energy between a self-interstitial atom (SIA) and a Ti atom. Open and closed circles represent configurations, in which the SIA is oriented along  $\langle 111 \rangle$  and  $\langle 110 \rangle$ , respectively. Calculations were carried out using 128-atom cells at constant volume.

is unlikely. Trapping is a precursor to segregation and associated with radiation-induced segregation and precipitation. Previous experimental studies have confirmed radiation-induced Re precipitation in tungsten [46,47], yet no equivalent experimental data has yet been reported for Ti and V.

SIAs travel with very high mobility along the crowdion direction with a migration barrier on the order of a few meV ( $\leq 0.046$  eV) [48]. The high diffusivity of SIAs is closely related to the effective delocalization of the defect center and the fact that their migration involves only small atomic displacements [3]. The strong tendency of impurities to bind with SIAs causes the interstitial to localize and reduces its mobility dramatically. In this context it is important to quantify the range of the SIA-solute interaction as it provides a measure for the effective capture radius associated with a substitutional solute atom. Fig. 6 shows the formation energy of solute-interstitial configurations as a function of the distance between interstitial center and solute atom for the case of Ti. The data indicate a short interaction range as binding is practically absent outside a radius of approximately 2.5 Å, which corresponds to the first nearest neighbor shell of the BCC lattice.

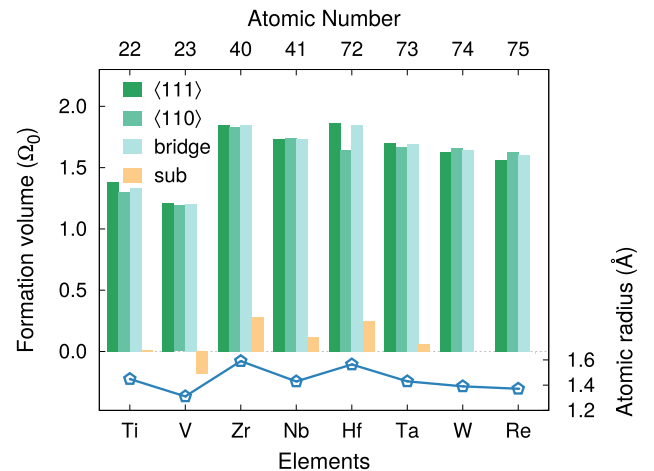


**Fig. 7.** Formation volumes of intrinsic and extrinsic defects in tungsten (left axis). For comparison the atomic radii are shown on the right axis.

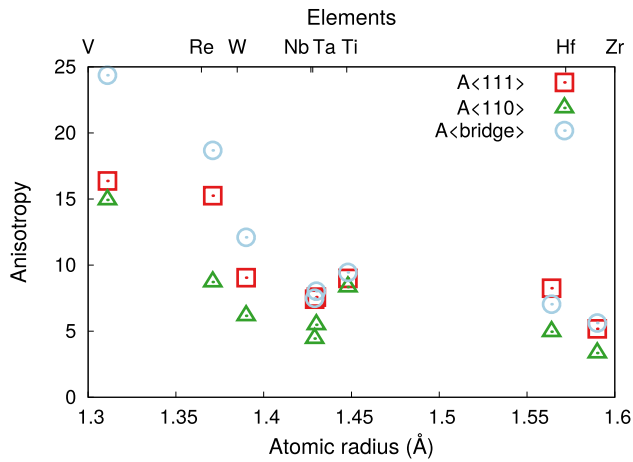


Fig. 8. Anisotropy of  $\langle 111 \rangle$  dumbbell,  $\langle 110 \rangle$  dumbbell and bridge interstitials with respect to atomic radius.

### 3.4. Formation volumes and formation volume tensors

A defect can affect other point as well as line defects (dislocations) either via a direct “chemical” interaction or via long-range elastic interactions. The strain field can modify the saddle points during point defect migration [49]. Similarly, it can affect the barriers for dislocation kink nucleation and growth and thereby affect the plastic behavior of the materials [17]. Formation volumes quantify the induced strain in terms of linear elasticity theory; the formation volume tensors provide additional information concerning the orientation and anisotropy of the strain field.

From constant pressure calculations we obtain the change in cell

shape due to defect formation  $L-L_0$ , from which one readily obtains the formation volume tensor  $\mathbf{v}^f$  using Eq. (3). All solute atoms are associated with a symmetric lattice relaxation when the formation volume tensor is simply  $\mathbf{v}^f = v^f \mathbf{I}$ , where  $v^f = (1/3)\text{Tr}\mathbf{v}^f$  is the formation volume. The values are compiled in Table 1 and Fig. 7, which shows that the formation volumes closely correlate with the atomic radii.

In the case of interstitial defects the formation volume tensor reflects the orientation of the dumbbell as illustrated in Fig. 9. The formation volumes are reported in Table 1 and Fig. 7. The strongly elongated shape of the ellipsoids in Fig. 9 indicates a large degree of anisotropy. The latter can be conveniently measured by the ratio  $A$  of the largest and smallest eigenvalues of the formation volume tensor, see Table 1. Large values of  $A$  are obtained with typical values in the range from 6 to 10. For Re and V the anisotropy is even larger with  $A$  values up to 24, see Fig. 8. It is remarkable that the three elements that favor the bridge interstitial configuration and trap SIAs, are also the three elements with the largest anisotropy ratio.

Finally, for the vacancy one obtains a formation volume that is very close to zero, which is an indication for the covalent bonding character that is characteristic for W.

## 4. Conclusions

Substitutional and interstitial defects in W associated with several alloying elements of interest were investigated by first-principles calculations based on density functional theory. A systematic investigation of computational parameters was carried out in order to establish the accuracy limits of the present calculations. The errors due to finite size, Brillouin zone sampling, and the treatment of semi-core effects were shown to be of similar

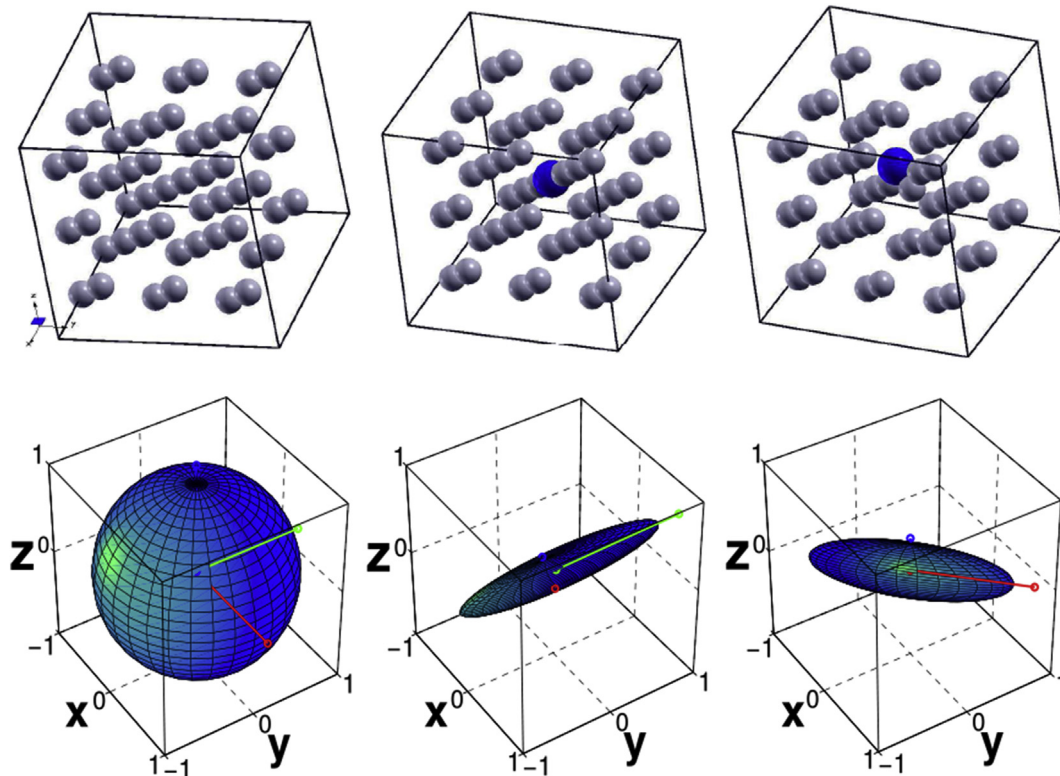


Fig. 9. Ellipsoids representing (formation) volume tensors corresponding to a (left) tungsten atom in the perfect lattice, (center) a Ti  $\langle 111 \rangle$  dumbbell interstitial, and (right) a Ti  $\langle 110 \rangle$  dumbbell interstitial.

magnitude and a procedure was described to account for each contribution.

Negative formation energies were obtained for substitutional Ti, V, Nb, Hf as well as Ta and positive values for Zr and Re. The negative values suggest a negative mixing energy for the BCC solutions, which should result in an extended miscibility range and possibly the formation of ordered phases at low temperatures, see Refs. [40,41]. This is partially at odds with phase diagrams based on thermodynamic calculations. As the latter are based on limited experimental data due to the refractory nature of the W-alloys, this suggests that further investigations should be carried out to establish the low temperature phase diagrams as they determine the thermodynamic driving forces that underpin the dynamic behavior of the material.

While interstitials are practically absent under equilibrium conditions due to their large formation energies, they are important under reactor relevant conditions when SIAs are produced by ion irradiation. In addition to high symmetry dumbbell configurations, here another interstitial configuration has been systematically investigated that was referred to as a bridge interstitial. For mixed-interstitials involving Ti, V, and Re the bridge interstitial configuration is found to be the most stable configuration.

The same three elements (Ti, V and Re) exhibit negative binding energies with respect to SIAs and are thus predicted to trap these defects. This causes a reduction of the interstitial mobility, which is likely to accelerate damage build up. It is also of interest in connection with radiation-induced segregation and precipitation, which has already been observed for Re.

Finally, the elastic strain field of both substitutional and interstitial defects was quantified in the form of formation volume tensors. Remarkably, again Ti, V, and Re interstitials are the defects that exhibit the strongest anisotropy as quantified by the ratio between the largest and smallest eigenvalues of the formation volume tensor. These parameters are suitable e.g., for the construction of kinetic Monte Carlo models of defect migration and dislocation mobility.

## Acknowledgments

This work was supported by the Swedish Research Council in the form of a Young Researcher grant, the European Research Council (Grant no. 322237) via a Marie Curie Career Integration Grant, and the *Area of Advance – Materials Science* at Chalmers. Computer time allocations by the Swedish National Infrastructure for Computing at NSC (Linköping) and C3SE (Gothenburg) are gratefully acknowledged.

## References

- [1] S.J. Zinkle, N.M. Ghoniem, Operating temperature windows for fusion reactor structural materials, *Fusion Eng. Des.* 51–52 (2000) 55–71, [http://dx.doi.org/10.1016/S0920-3796\(00\)00320-3](http://dx.doi.org/10.1016/S0920-3796(00)00320-3).
- [2] M. Rieth, S. Dudarev, S. Gonzalez de Vicente, J. Aktaa, T. Ahlgren, S. Antusch, D. Armstrong, M. Balden, N. Baluc, M.-F. Barthe, et al., Recent progress in research on tungsten materials for nuclear fusion applications in Europe, *J. Nucl. Mater.* 432 (1) (2013) 482–500.
- [3] S.P. Fitzgerald, D. Nguyen-Manh, Peierls potential for crowdions in the bcc transition metals, *Phys. Rev. Lett.* 101 (2008) 115504.
- [4] C. Becquart, C. Domain, An object kinetic monte carlo simulation of the dynamics of helium and point defects in tungsten, *J. Nucl. Mater.* 385 (2) (2009) 223–227.
- [5] T. Noda, M. Fujita, M. Okada, Transmutation and induced radioactivity of W in the armor and first wall of fusion reactors, *J. Nucl. Mater.* 258–263 (Part 1) (1998) 934–939, [http://dx.doi.org/10.1016/S0022-3115\(98\)00088-9](http://dx.doi.org/10.1016/S0022-3115(98)00088-9).
- [6] T. Suzudo, M. Yamaguchi, A. Hasegawa, Stability and mobility of rhenium and osmium in tungsten: first principles study, *Model. Simul. Mater. Sci. Eng.* 22 (7) (2014) 075006.
- [7] T. Tietz, J. Wilson, Behavior and Properties of Refractory Metals, Stanford University Press, 1965.
- [8] P. Gumbsch, J. Riedle, A. Hartmaier, H.F. Fischmeister, Controlling factors for the brittle-to-ductile transition in tungsten single crystals, *Science* 282 (5392) (1998) 1293–1295, <http://dx.doi.org/10.2307/2897296>.
- [9] M.V. Aguirre, A. Martín, J.Y. Pastor, J. Llorca, M.A. Monge, R. Pareja, Mechanical properties of tungsten alloys with  $\text{Y}_2\text{O}_3$  and titanium additions, *J. Nucl. Mater.* 417 (1–3) (2011) 516–519, <http://dx.doi.org/10.1016/j.jnucmat.2010.12.120>.
- [10] F. Hoffmann, D. Nguyen-Manh, M.R. Gilbert, C.E. Beck, J.K. Eliason, A.A. Maznev, W. Liu, D.E.J. Armstrong, K.A. Nelson, S.L. Dudarev, Lattice swelling and modulus change in a helium-implanted tungsten alloy: X-ray microdiffraction, surface acoustic wave measurements, and multiscale modelling, *Acta Mater.* 89 (2015) 352–363, <http://dx.doi.org/10.1016/j.actamat.2015.01.055>.
- [11] R.S. Averback, T. Diaz de la Rubia, Displacement damage in irradiated metals and semiconductors, *Solid State Phys.* 51 (1998) 281.
- [12] Y. Zhong, K. Nordlund, M. Ghaly, R.S. Averback, Defect production in tungsten: a comparison between field-ion microscopy and molecular-dynamics simulations, *Phys. Rev. B* 58 (5) (1998) 2361–2364, <http://dx.doi.org/10.1103/PhysRevB.58.2361>.
- [13] W.H. Zhou, Y.G. Li, L.F. Huang, Z. Zeng, X. Ju, Dynamical behaviors of self-interstitial atoms in tungsten, *J. Nucl. Mater.* 437 (1–3) (2013) 438–444, <http://dx.doi.org/10.1016/j.jnucmat.2013.02.075>.
- [14] A.L. Bement, Irradiation effects on structural alloys for nuclear reactor applications, *ASTM Int.* 484 (1971), <http://dx.doi.org/10.1520/STP484-EB>.
- [15] G.-H. Lu, H.-B. Zhou, C.S. Becquart, A review of modelling and simulation of hydrogen behaviour in tungsten at different scales, *Nucl. Fusion* 54 (8) (2014) 086001, <http://dx.doi.org/10.1088/0029-5515/54/8/086001>.
- [16] X.-S. Kong, X. Wu, Y.-W. You, C.S. Liu, Q.F. Fang, J.-L. Chen, G.N. Luo, Z. Wang, First-principles calculations of transition metal–solite interactions with point defects in tungsten, *Acta Mater.* 66 (2014) 172–183, <http://dx.doi.org/10.1016/j.actamat.2013.11.044>.
- [17] M.Z. Hossain, J. Marian, Stress-dependent solute energetics in w–re alloys from first-principles calculations, *Acta Mater.* 80 (2014) 107–117, <http://dx.doi.org/10.1016/j.actamat.2014.07.028>.
- [18] P.E. Blöchl, Projector augmented-wave method, *Phys. Rev. B* 50 (24) (1994) 17953–17979, <http://dx.doi.org/10.1103/PhysRevB.54.11169>.
- [19] G. Kresse, D. Joubert, From ultrasoft pseudopotentials to the projector augmented-wave method, *Phys. Rev. B* 59 (3) (1999) 1758–1775, <http://dx.doi.org/10.1103/PhysRevB.59.1758>.
- [20] G. Kresse, J. Hafner, Ab initio molecular dynamics for liquid metals, *Phys. Rev. B* 47 (1) (1993) 558–561, <http://dx.doi.org/10.1103/PhysRevB.47.558>.
- [21] G. Kresse, J. Hafner, Ab initio molecular-dynamics simulation of the liquid-metal–amorphous-semiconductor transition in germanium, *Phys. Rev. B* 49 (20) (1994) 14251, <http://dx.doi.org/10.1103/PhysRevB.49.14251>.
- [22] G. Kresse, J. Furthmüller, Efficient iterative schemes for ab initio total-energy calculations using a plane-wave basis set, *Phys. Rev. B* 54 (1996) 11169, <http://dx.doi.org/10.1103/PhysRevB.54.11169>.
- [23] G. Kresse, J. Furthmüller, Efficiency of ab-initio total energy calculations for metals and semiconductors using a plane-wave basis set, *Comput. Mater. Sci.* 6 (1) (1996) 15–50, [http://dx.doi.org/10.1016/0927-0256\(96\)00008-0](http://dx.doi.org/10.1016/0927-0256(96)00008-0).
- [24] J.P. Perdew, K. Burke, M. Ernzerhof, Generalized gradient approximation made simple, *Phys. Rev. Lett.* 77 (18) (1996) 3865–3868, <http://dx.doi.org/10.1103/PhysRevLett.77.3865> erratum, *ibid.* 78, 1396(E) (1997).
- [25] S.B. Zhang, J.E. Northrup, Chemical potential dependence of defect formation energies in GaAs: Application to Ga self-diffusion, *Phys. Rev. Lett.* 67 (17) (1991) 2339–2342.
- [26] P. Erhart, K. Albe, Thermodynamics of mono- and di-vacancies in barium titanate, *J. Appl. Phys.* 102 (08) (2007) 084111, <http://dx.doi.org/10.1063/1.2801011>.
- [27] C. Wolverton, Solute–vacancy binding in aluminum, *Acta Mater.* 55 (17) (2007) 5867–5872, <http://dx.doi.org/10.1016/j.actamat.2007.06.039>.
- [28] P. Olsson, T.P.C. Klaver, C. Domain, Ab initio study of solute transition-metal interactions with point defects in bcc Fe, *Phys. Rev. B* 81 (5) (2010) 054102, <http://dx.doi.org/10.1103/PhysRevB.81.054102>.
- [29] S.A. Centoni, B. Sadigh, G.H. Gilmer, T.J. Lenosky, T. Diaz de la Rubia, C.B. Musgrave, First-principles calculation of intrinsic defect formation volumes in silicon, *Phys. Rev. B* 72 (2005) 195206.
- [30] K. Garikipati, M. Falk, M. Bouville, B. Puchalac, H. Narayanan, The continuum elastic and atomistic viewpoints on the formation volume and strain energy of a point defect, *J. Mech. Phys. Solids* 54 (9) (2006) 1929–1951.
- [31] E. Jedvik, A. Lindman, M. Benediktsson, G. Wahnström, Size and shape of oxygen vacancies and protons in acceptor-doped barium zirconate, *Solid State Ionics* 275 (2015) 2–8.
- [32] S. Lany, A. Zunger, Assessment of correction methods for the band-gap problem and for finite-size effects in supercell defect calculations: Case studies for ZnO and GaAs, *Phys. Rev. B* 78 (23) (2008) 235104, <http://dx.doi.org/10.1103/PhysRevB.78.235104>.
- [33] D. Grecu, P.H. Dederichs, The asymptotic behavior of the displacement field of point defects in ‘isotropic’ crystals, *Phys. Lett.* 36A (2) (1971) 135.
- [34] P.H. Dederichs, J. Pollmann, Elastic displacement field of point defects in anisotropic cubic crystals, *Z. Phys.* 255 (1972) 315.
- [35] L. Ventelon, F. Willaime, C.-C. Fu, M. Heran, I. Ginoux, Ab initio investigation of radiation defects in tungsten: Structure of self-interstitials and specificity of di-vacancies compared to other bcc transition metals, *J. Nucl. Mater.* 425 (1–3) (2012) 16–21, <http://dx.doi.org/10.1016/j.jnucmat.2011.08.024>.
- [36] D. Nguyen-Manh, A.P. Horsfield, S.L. Dudarev, Self-interstitial atom defects in

- bcc transition metals: Group-specific trends, Phys. Rev. B 73 (2) (2006) 020101, <http://dx.doi.org/10.1103/PhysRevB.73.020101>.
- [37] C.S. Becquart, C. Domain, Ab initio calculations about intrinsic point defects and he in w, Nucl. Instrum. Methods Phys. Res. Sect. B Beam Interact. Mater. Atoms 255 (1) (2007) 23–26, <http://dx.doi.org/10.1016/j.nimb.2006.11.006>
- computer Simulation of Radiation Effects in Solids Proceedings of the Eighth International Conference on Computer Simulation of Radiation Effects in Solids (COSIRES 2006) Computer Simulation of Radiation Effects in Solids.
- [38] H. Wollenberger, Point defects, in: Physical Metallurgy, 3rd ed., 1983.
- [39] V. Blum, A. Zunger, Prediction of ordered structures in the bcc binary systems of mo, nb, ta, and w from first-principles search of approximately 3,000,000 possible configurations, Phys. Rev. B 72 (2) (2005) 020104(R), <http://dx.doi.org/10.1103/PhysRevB.72.020104>.
- [40] P. Erhart, B. Sadigh, A. Caro, Are there stable long-range ordered  $\text{Fe}_{1-x}\text{Cr}_x$  compounds? Appl. Phys. Lett. 92 (14) (2008) 141904, <http://dx.doi.org/10.1063/1.2907337>.
- [41] M. Muzyk, D. Nguyen-Manh, K.J. Kurzydowski, N.L. Baluc, S.L. Dudarev, Phase stability, point defects, and elastic properties of w-v and w-ta alloys, Phys. Rev. B 84 (10) (2011) 104115, <http://dx.doi.org/10.1103/PhysRevB.84.104115>.
- [42] S.K. Lee, D.N. Lee, Calculation of phase diagrams using partial phase diagram data, Calphad 10 (1) (1986) 61.
- [43] E. Rudy, S. Windisch, Revision of titanium-tungsten system, Trans. Metall. Soc. AIME 242 (5) (1968) 953–&.
- [44] S.G. Fries, B. Sundman, Using Re-W  $\sigma$ -phase first-principles results in the Bragg-Williams approximation to calculate finite-temperature thermodynamic properties, Phys. Rev. B 66 (1) (2002) 012203, <http://dx.doi.org/10.1103/PhysRevB.66.012203>.
- [45] J.-C. Crivello, J.-M. Joubert, First principles calculations of the  $\sigma$  and  $\chi$  phases in the Mo-Re and W-Re systems, J. Phys. Condens. Matter 22 (3) (2010) 035402, <http://dx.doi.org/10.1088/0953-8984/22/3/035402>.
- [46] T. Tanno, A. Hasegawa, M. Fujiwara, J.-C. He, S. Nogami, M. Satou, T. Shishido, K. Abe, Precipitation of solid transmutation elements in irradiated tungsten alloys, Mater. Trans. 49 (10) (2008) 2259–2264.
- [47] R. Herschitz, D.N. Seidman, Radiation-induced precipitation in fast-neutron irradiated tungsten-rhenium alloys: An atom-probe field-ion microscope study, Nucl. Instrum. Methods Phys. Res. Sect. B Beam Interact. Mater. Atoms 7 (1985) 137–142.
- [48] T. Amino, K. Arakawa, H. Mori, Activation energy for long-range migration of self-interstitial atoms in tungsten obtained by direct measurement of radiation-induced point-defect clusters, Philos. Mag. Lett. 91 (2) (2010) 86–96, <http://dx.doi.org/10.1080/09500839.2010.533133>.
- [49] C.S. Becquart, C. Domain, Molecular dynamics simulations of damage and plasticity: The role of ab initio calculations in the development of interatomic potentials, Philos. Mag. 89 (2009) 3215–3234, <http://dx.doi.org/10.1080/14786430903250819P11917306934>.

# Paper II

**The role of interstitial binding in radiation induced segregation in W-Re alloys**

Leili Gharaee, Jaime Marian and Paul Erhart

Journal of Applied Physics **120**, 025901 (2016).



# The role of interstitial binding in radiation induced segregation in W-Re alloys

Leili Gharaee,<sup>1</sup> Jaime Marian,<sup>2</sup> and Paul Erhart<sup>1,a)</sup>

<sup>1</sup>Department of Physics, Chalmers University of Technology, S-412 96 Gothenburg, Sweden

<sup>2</sup>Department of Materials Science and Engineering, University of California, Los Angeles, California 90095, USA

(Received 18 April 2016; accepted 25 June 2016; published online 13 July 2016)

Due to their high strength and advantageous high-temperature properties, tungsten-based alloys are being considered as plasma-facing candidate materials in fusion devices. Under neutron irradiation, rhenium, which is produced by nuclear transmutation, has been found to precipitate in elongated precipitates forming thermodynamic intermetallic phases at concentrations well below the solubility limit. Recent measurements have shown that Re precipitation can lead to substantial hardening, which may have a detrimental effect on the fracture toughness of W alloys. This puzzle of subsolubility precipitation points to the role played by irradiation induced defects, specifically mixed solute-W interstitials. Here, using first-principles calculations based on density functional theory, we study the energetics of mixed interstitial defects in W-Re, W-V, and W-Ti alloys, as well as the heat of mixing for each substitutional solute. We find that mixed interstitials in all systems are strongly attracted to each other with binding energies of  $-2.4$  to  $-3.2$  eV and form interstitial pairs that are aligned along parallel first-neighbor  $\langle 111 \rangle$  strings. Low barriers for defect translation and rotation enable defect agglomeration and alignment even at moderate temperatures. We propose that these elongated agglomerates of mixed-interstitials may act as precursors for the formation of needle-shaped intermetallic precipitates. This interstitial-based mechanism is not limited to radiation induced segregation and precipitation in W-Re alloys but is also applicable to other body-centered cubic alloys. *Published by AIP Publishing.* [<http://dx.doi.org/10.1063/1.4956377>]

## I. MOTIVATION

Tungsten is being considered as a candidate material in magnetic fusion energy devices due to its high strength and excellent high temperature properties.<sup>1–4</sup> Upon fast neutron irradiation in the 600–1000 °C temperature range, W transmutes into Re by the way of beta decay reactions at a rate that depends on the neutron spectrum and the position in the reactor. For the DEMO (demonstration fusion power plant) reactor concept, calculations show that the transmutation rate is 2000 and 7000 atomic parts per 10<sup>6</sup> (appm) per displacements per atom (dpa) in the divertor and the equatorial plane of the first wall, respectively (where damage, in each case, accumulates at rates of 3.4 and 4.4 dpa/year).<sup>5,6</sup>

The irradiated microstructure initially evolves by accumulating a high density of prismatic dislocation loops and vacancy clusters, approximately up to 0.15 dpa.<sup>7,8</sup> Subsequently, a void lattice emerges and fully develops at fluences of around 1 dpa. After a critical dose that ranges between 5 dpa for fast ( $>1$  MeV) neutron irradiation<sup>8</sup> and 2.2 dpa in modified target rabbits in the HFIR,<sup>9</sup> W and W-Re alloys develop a high density of nanometric precipitates with acicular shape at Re concentrations well below the solubility limit.<sup>8</sup> The structure of these precipitates is consistent with  $\sigma$  (W<sub>7</sub>Re<sub>6</sub>) and  $\chi$  (WRe<sub>3</sub>) intermetallic phases, which under equilibrium conditions only occur at temperatures and Re concentrations substantially higher than those found in neutron irradiation studies. A principal signature of the formation of these intermetallic

structures in body-centered cubic (BCC) W is the sharp increases in hardness and embrittlement, as well as other detrimental effects.<sup>8,10</sup> Qualitatively similar observations were recently made on W-25Re alloys subjected to heavy ion irradiation,<sup>11</sup> clearly establishing a link between primary damage production and Re precipitation.

For a number of reasons, the formation of these non-thermodynamic phases is inconsistent with the standard picture of solute precipitation by a vacancy mechanism, even in the context of radiation enhanced diffusion (RED) and radiation induced precipitation (RIP). For example, the phase diagram points to the  $\sigma$  phase as the first one to emerge from the BCC solid solution, whereas electron diffraction studies show the co-occurrence of both phases, with even an initial preeminence of the  $\chi$  phase in some cases.<sup>12</sup> All this is suggestive of the role played by interstitial defects, such as mixed dumbbells and crowdions, in facilitating solute transport and potentially shifting phase boundary lines. Although detailed kinetic models linking solute transport and precipitation with irradiation defects exist (e.g., Ref. 13), self- and mixed-interstitial (solute) transport introduces a set of particularities that cannot be captured in effective models. Specifically, motion directionality and solute transport mechanisms are directly governed by crystal structure and the chemical nature of the defect-solute binding. These are processes that must be characterized at the atomistic scale using first principles calculations. There have been recent efforts to study interstitial defect energetics in W-based alloys, using density functional theory (DFT) calculations, in an attempt

<sup>a)</sup>erhart@chalmers.se

to establish the grounds for defect diffusion models.<sup>4,14,15</sup> These studies build on existing knowledge of self-interstitial atoms (SIA) in metals gained from electronic structure and semi-empirical calculations over the last 20 or so years.<sup>16,17</sup>

In any case, the formation of sub-soluble intermetallic phases in irradiated W and W-Re remains unexplained, and, to date, a detailed model of Re precipitation in irradiated W is still lacking. In this paper, we study the precipitation behavior of W-V, W-Ti, and W-Re alloys as a function of alloy composition with an emphasis on interstitials in order to understand and explain property changes of tungsten under irradiation conditions. The paper is organized as follows. In Sec. II, we describe the general approach as well as the computational methodology employed in this work. The results of interstitial binding in the dilute limit for V, Ti, and Re are given in Sec. III A. This is followed by a comprehensive investigation of the mixing energies of both substitutional and interstitial-based systems over the full composition range in Sec. III B before we then consider in Sec. III C the mobility of mixed interstitials. Finally, we formulate a mechanism that provides a rationale for the occurrence and shape of experimentally observed  $\sigma$  and  $\chi$ -phase precipitates in W-Re alloys.

## II. METHODOLOGY

### A. General approach

The present work is primarily centered around Re since as described above W-Re alloys are naturally formed due to nuclear transmutation under fusion conditions and are well known to exhibit RIP and RIS (radiation induced segregation).<sup>18</sup> Vanadium and titanium are included as well since it was determined in Ref. 15 that their mixed interstitial configurations exhibit a number of similarities with Re. Specifically, it was shown that all three elements adopt a bridge-like interstitial configuration [Fig. 1(a)] in the W matrix. The latter can be thought of as a dumbbell interstitial oriented along  $\langle 111 \rangle$  [Fig. 1(b)], in which the extrinsic atom is displaced along one of three  $\langle 211 \rangle$  directions perpendicular to the dumbbell orientation. This results in a bond angle with the nearest neighbors of approximately  $150^\circ$  as opposed to  $180^\circ$  in the case of the straight dumbbell interstitial [see Fig. 1(a)]. In addition, Re, Ti, and V trap SIAs, i.e., the

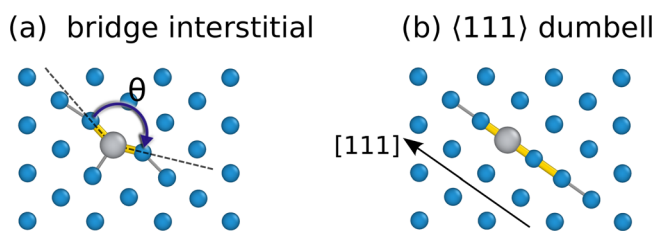


FIG. 1. Bridge (a) and  $\langle 111 \rangle$  dumbbell (b) interstitial defects in tungsten. The  $\langle 111 \rangle$  crowdion configuration closely resembles the  $\langle 111 \rangle$  dumbbell configuration with a slightly larger spacing of the defect atoms along the  $\langle 111 \rangle$  axis. The figure shows a slice parallel to  $\{110\}$ . Small (blue) spheres indicate tungsten atoms, whereas large (gray) spheres indicate extrinsic atoms (V, Ti, Re). Thicker (yellow) cylinders indicate bond lengths shorter than  $2.3 \text{ \AA}$ , whereas thinner (gray) cylinders indicate bond lengths shorter than  $2.5 \text{ \AA}$ . The bond angle  $\theta$  is indicated in (a).

reaction  $X_W + (W - W)_{\text{int}} \rightarrow (X - W)_{\text{int}}$  is exothermic, which strongly affects the migration behavior of SIAs. Finally, for all three elements, the defect formation volume tensor of the mixed interstitials is strongly anisotropic, which thus also applies to the strain field associated with these defects and provides a strong driving force for defect alignment. To investigate this behavior further, we considered several different types of configurations, the construction of which is described in the following.

### 1. Double-interstitial configurations

To quantify interstitial-interstitial interactions, defect configurations including two interstitials were created based on  $4 \times 4 \times 4$  conventional supercells (128 atoms). Configurations were constructed by systematically varying the distance as well as the relative orientation (rotation) of two bridge interstitials, yielding more than 100 initially distinct configurations.

### 2. Dilute substitution

The direct interaction of two Ti, V, or Re atoms in a body-centered cubic W matrix was studied using  $4 \times 4 \times 4$  conventional supercells. Their relative separation was varied to extract their (pair-wise) interaction as a function of distance.

### 3. Substitutional alloys

The energetics of concentrated alloys was determined in two ways. First,  $3 \times 3 \times 3$  conventional supercells (54-atoms) were employed, in which a number of extrinsic substitutional atoms was inserted corresponding to concentrations covering the entire concentration range in the case of V and the concentration range up to 50% in the case of Ti and Re. The latter restriction was imposed since the BCC lattice structure is mechanically unstable for these elements, whence Ti and Re-rich supercells do not maintain the BCC structure upon relaxation. Second, in the case of W-Ti, an alloy cluster expansion was constructed using the atomic alloy toolkit, from which a series of low energy structures was derived.

### 4. Interstitial based structures

As discussed in detail below, the defect supercell calculations indicated strong interstitial-interstitial interactions suggestive of defect clustering. To explore this effect, further additional structures were constructed in the following fashion.<sup>19</sup> First, ideal supercells were generated based on the primitive cell by applying an integer transformation matrix  $\mathbf{P}$  that relates the primitive cell metric  $\mathbf{h}_p$  to the supercell metric  $\mathbf{h}$  according to  $\mathbf{h} = \mathbf{P}\mathbf{h}_p$ . Subsequently, all distinct configurations were constructed that result from insertion of a bridge interstitial on one lattice site when taking into account the orientation of the interstitial. In this fashion, 166 “interstitial based” structures were obtained.

### B. Computational details

For all configurations described in Sec. II, density functional theory (DFT) calculations were carried out using the

projector augmented wave (PAW) method<sup>20,21</sup> as implemented in the Vienna *ab-initio* simulation package.<sup>22–25</sup> Since interstitial configurations involve short interatomic distances “hard” PAW setups that include semi-core electron states were employed with plane wave energy cutoffs of 343 eV, 290 eV, and 295 eV for V, Ti, and Re, respectively.

Exchange and correlation effects were described using the generalized gradient approximation,<sup>26</sup> while the occupation of electronic states was performed using the first order Methfessel-Paxton scheme with a smearing width of 0.2 eV. The Brillouin zone was sampled using Monkhorst-Pack grids of at least  $4 \times 4 \times 4$ . (A detailed discussion of the effect of different computational parameters on the results can be found in Ref. 15.) All structures were optimized allowing full relaxation of both ionic positions and cell shape with forces converged to below 15 meV/Å. Migration barriers were computed using  $4 \times 4 \times 4$  supercells and the climbing image-nudged elastic band method with up to five images.<sup>27</sup>

### III. RESULTS

#### A. Interstitial-interstitial binding

The SIA in tungsten has been shown to adopt a so-called crowdion configuration in which the atoms that form the defect are delocalized along  $\langle 111 \rangle$  directions of the lattice. Some extrinsic elements such as V, Ti, and Re bind to SIAs and cause the interstitial to localize.<sup>15</sup> These mixed-interstitial defects have very large defect formation volumes that range from 1.2 to 1.6 times the volume per atom of the ideal structure. The associated strain field is oriented along  $\langle 111 \rangle$  and highly anisotropic, which is evident from the ratio of the largest and smallest eigenvalues of the formation volume tensor.

When the concentration of solute atoms increases, the strain field produced by individual bridge mixed-interstitials remains unchanged. However, the reduction in the average distance between solute atoms implies that mixed-interstitials interactions become important, which due to the anisotropy of the strain field can be expected to exhibit a strong directionality. The system can thus reduce its strain energy by rearranging both defect location and orientation.

To test this possibility, we first consider the interaction of pairs of mixed-interstitials of V, Ti, and Re, which were constructed as described in Sec. II A. Specifically, we calculate the binding energy, which is defined as the difference between the formation energy of the di-interstitial configuration  $E^f(2[X - W]_W)$  and the sum of the formation energy of two individual mixed-interstitial defects,  $2E^f([X - W]_W)$

$$E_{2[X]}^b = E^f(2[X - W]_W) - 2E^f([X - W]_W). \quad (1)$$

Note that by this definition, two interstitials are attracted to each other if the binding energy is negative.

The calculations reveal strongly bound configurations for all three elements, with  $E_{2[X]}^b$  as high as  $-2.4$ ,  $-2.7$ , and  $-3.2$  eV for V, Ti, and Re, respectively [Fig. 2]. In addition, as mentioned above, the individual mixed interstitial defects have a large and very anisotropic strain field that could

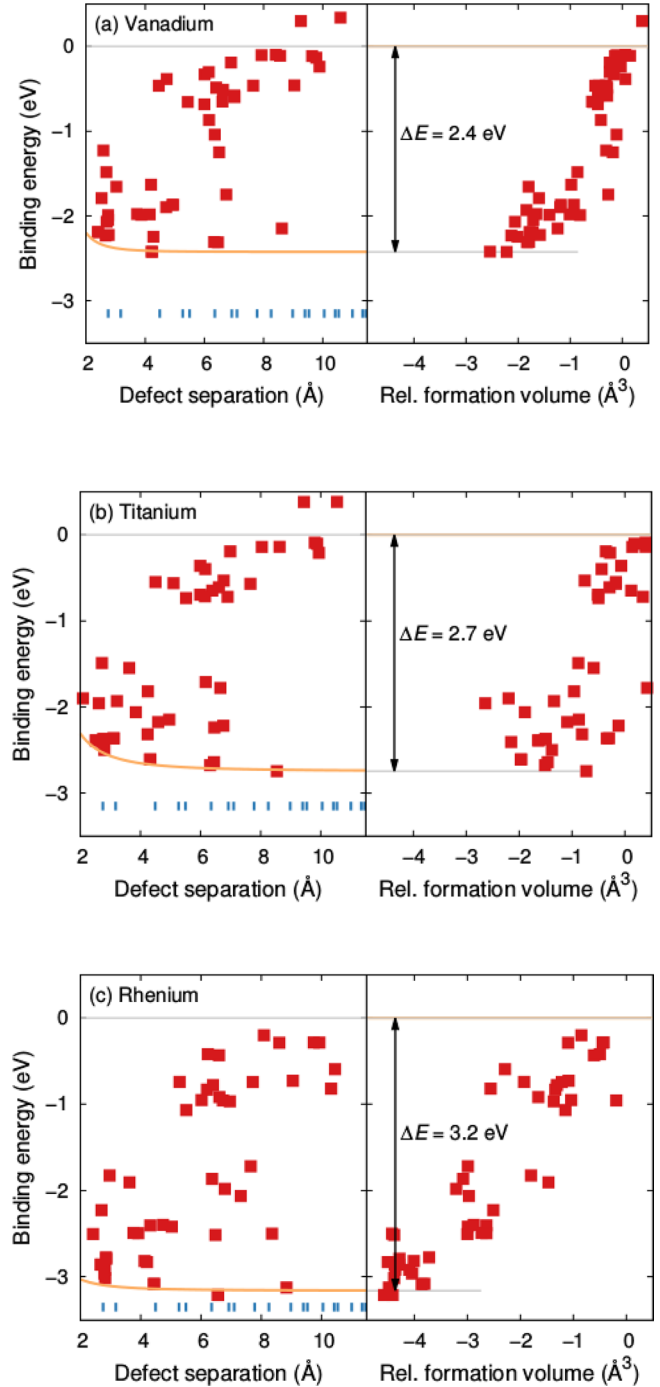


FIG. 2. Binding energy according to Eq. (1) between two (a) V–W, (b) Ti–W, and (c) Re–W mixed interstitials as a function of pair separation (left) as well as relative formation volume (right), where latter was computed according to Eq. (2). The blue ticks indicate the positions of the neighbors shells in the perfect structure. The solid orange lines represent the repulsive interaction between two substitutional extrinsic atoms (compare Fig. 4) referred to the most strongly bound configuration.

result in defect reorientation. This anisotropy should manifest itself in the formation volume of the di-interstitial configuration  $V^f(2[X - W]_W)$  relative to the individual defects  $V^f([X - W]_W)$ , which can be defined entirely analogously to the binding energy above as

$$\Delta V_{2[X]}^f = V^f(2[X - W]_W) - 2V^f([X - W]_W). \quad (2)$$

Here,  $V^f(2[X - W]_W)$  and  $V^f([X - W]_W)$  denote the formation volumes of the di-interstitial and (single) interstitial, respectively, which were computed as described in Refs. 15, 28, and 29.

In fact, we find a strong correlation between the binding energy  $E_{2[X]}^b$  and the change in the formation volume  $\Delta V_{2[X]}^f$  [Fig. 2]. While a strong binding is obtained for short defect separations, the lowest binding energies occur for somewhat longer distances. Yet, at the same approximate distance, one can obtain binding energies that cover the entire range between strong and no binding [compare, e.g., the data points near 6 Å in Fig. 2(a)]. This suggests that the relative orientation of defects is important.

A closer inspection of di-interstitial configurations reveals that in the structures that exhibit the strongest binding [structure (I) and (II) in Fig. 3(a)], the mixed-interstitials are aligned along parallel  $\langle 111 \rangle$  directions and the two strings hosting the extrinsic atoms are first nearest neighbors of each other [Figs. 3(b) and 3(c)]. If the mixed-interstitials are located either in the same string or in two strings that are second or farther nearest neighbors of each other [configuration (III) in Fig. 3(a)], the energy increases relative to the respective first-nearest neighbor configuration [Fig. 3(c)]. The behavior of defects that is located in the same string can be rationalized as being the result of strong repulsion due to overlapping strain fields. The situation for second and farther nearest neighbor configurations, on the other hand, is the result of a strong decrease in electronic coupling with distance. The short-range interaction between  $\langle 111 \rangle$  strings in BCC metals, in general, and W, in particular, is in fact also evident from the success of first-nearest neighbor string (Frenkel-Kontorova) models that have been used in the past to describe both interstitial and dislocation related features in these systems.<sup>3,30–32</sup> Finally, note that if the two mixed-interstitials are “far” apart and have no specific orientation relative to each other [configuration (IV) in Fig. 3(a)], their interaction vanishes and the binding energy decays to zero.

It is worth noting that in the case of first-nearest neighbor strings, the binding energy decreases with increasing distance. This effect can be attributed to the repulsive interaction between two extrinsic atoms of the same type, as it exhibits the same strength and distance dependence as the interaction between two corresponding *substitutional* atoms in a BCC W matrix [compare Figs. 2 and 4].

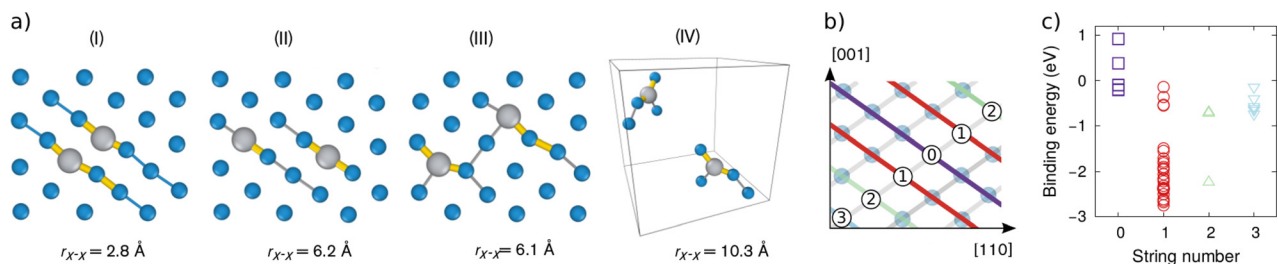


FIG. 3. (a) Defect configurations involving two  $(X - W)_W$  mixed-interstitials in which  $X$  corresponds to V, Ti, and Re atoms. The figure shows a slice parallel to a  $\{110\}$  plane of the structure. Small (blue) spheres indicate tungsten atoms, whereas large (gray) spheres indicate  $X$  atoms. Thicker (yellow) cylinders indicate bond lengths shorter than 2.3 Å, whereas thinner (gray) cylinders indicate bond lengths shorter than 2.5 Å. (b) An illustration of parallel  $\langle 111 \rangle$  strings in BCC tungsten. (c) Binding energy of a pair of titanium bridge mixed-interstitial with respect to string number.

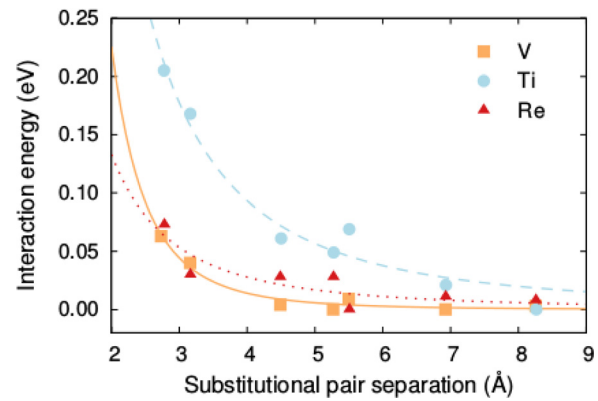


FIG. 4. Energy of a pair of V, Ti, and Re substitutional defects as a function of distance with respect to the infinite separation limit. Positive values indicate repulsion.

## B. Mixing energies and phase equilibria

The results described in Sec. III A provide clear evidence of the energetic preference for the alignment of mixed-interstitials. The magnitude of the binding energies, however, suggests an effect on the electronic structure that extends beyond strain effects. To shed more light on this aspect, we now consider substitutional alloy configurations along with a series of interstitial based structures that were constructed as described in Sec. II A. The mixing energy  $E_{mix}$  for a given alloy composition  $X_xW_{1-x}$  was computed using the fully relaxed configurations according to

$$E_{mix}(X_xW_{1-x}) = E(X_xW_{1-x}) - [xE(X) + (1-x)E(W)], \quad (3)$$

where  $x$  denotes the fraction of the alloying element  $X$ . Below, we first summarize the results for the substitutional alloys before addressing the interstitial-based structures, which exhibit a rather universal behavior.

### 1. Vanadium

Among the alloying elements included in this study, V is the only other element with a ground state BCC lattice, and it therefore gives rise to the simplest mixing energetics [see Fig. 5(a)]. The difference in lattice constant at ambient conditions between W and V is 5.9% (V: 2.989 Å, W: 3.177 Å according to PBE). The mixing energy is only slightly asymmetric and negative throughout the entire composition range. The low

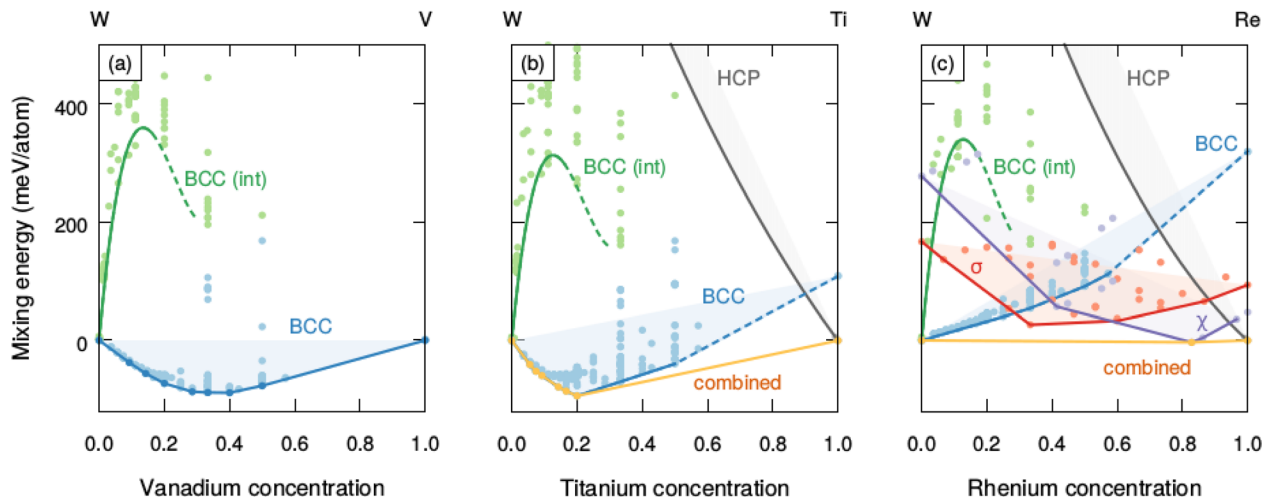


FIG. 5. Mixing energy of (a) V, (b) Ti, and (c) Re defects in tungsten-based structures obtained by substitution (squares) and interstitial insertion (circles). The solid (blue) line indicates the convex hull corresponding to the minimum mixing energy. The solid (yellow) line indicates the effective convex hull. Available data from W-V evaluated using cluster expansion are shown in plot (a) for comparison.<sup>33</sup>  $\sigma$  and  $\chi$  phases of a W-Re alloy<sup>34</sup> are presented as well in plot (c) as a function of defect concentration.

energy structures are closely spaced along the convex hull, and our calculations closely match the data from Muzyk *et al.*<sup>33</sup>

## 2. Titanium

While at ambient conditions Ti adopts a hexagonal close-packed (HCP) structure ( $\alpha$ -phase), it also exhibits a BCC polymorph ( $\beta$ -phase), which occurs at temperatures above 1200 K. Here, we focus on BCC-based structures on the W-rich side of the composition range.

As in the case of W-V, the mixing energy for BCC W-Ti is negative over the entire concentration range when referred to the elemental BCC phases [Fig. 5(b)]. Due to the energy difference between BCC Ti and HCP Ti, the mixing energy of BCC-based structure relative to the elemental ground states, i.e., BCC W and HCP Ti, however, turns positive at approximately 60%. The lowest mixing energy occurs at a composition of 20%. It belongs to space group  $R\bar{3}m$  and has the same structure of the  $W_4V$  structure described in Ref. 33.

W and Ti also mix on the HCP lattice as the energy of one substitutional W atom in HCP Ti is negative. The energy offset between HCP W and BCC W is, however, even larger than in the case of Ti, and thus, the mixing energy referred to the ground state structures is positive over the entire composition range. When combined, these data imply that one can expect a very asymmetric phase diagram with a large solubility for Ti in BCC-W but a very small solubility for W in HCP-Ti. In the high-temperature region of the phase diagram, which is experimentally accessible,<sup>35</sup> this is, indeed, the case. For lack of reliable low temperature data, previous thermodynamic models of the phase diagram, however, assumed a mixing energy that is positive over the entire composition range.<sup>36,37</sup> As a result, these models predict the solubility in both limits as the temperature approaches zero. A revision of the low temperature part of the phase diagram is therefore in order, which will be the subject of a separate study.<sup>38</sup>

## 3. Rhenium

As for Ti, the mixing energy of Re in W on BCC and HCP lattices is negative when referred to BCC and HCP elemental reference states, respectively (Fig. 5(c)). The HCP-BCC energy difference for Re is, however, even larger than for Ti, which causes the mixing energy for these two phases to be positive. This implies very small finite-temperature solubilities for both Re in BCC-W and W in HCP-Re in agreement with experiment.

In addition to the BCC and HCP phases, the W-Re system also features  $\sigma$  and  $\chi$  phases.<sup>34</sup> The  $\sigma$  phase [red line in Fig. 5(c); data from Ref. 34] experimentally occurs at high temperatures only, consistent with slightly positive mixing energies. The  $\chi$  phase, on the other hand [purple line in Fig. 5(c)], has a small negative mixing energy at about 83%, which is compatible with this phase being a ground state (zero K) phase.

## 4. Interstitial-based structures

Thus far, it has been shown that while the crystal structures of the elemental boundary phases differ between V, Ti, and Re, the substitutional alloys show common characteristics with both BCC and HCP based phases being miscible with respect to the elemental phase with the same crystal structure. One also observes strong similarities with respect to the interstitial-based structures. While some of them relax into substitutional structures, the majority remain close to the initial structure after relaxation. For all three elements (V, Ti, and Re), the mixing energies of these interstitial-based structures exhibit a similar dependence on concentration (green data points in Fig. 5). The mixing energies are positive and feature a maximum at about 15%. For concentrations of approximately 30% and above, the mixing energy approaches zero and the structures lose interstitial-characteristics, which is apparent from an analysis of the pair distribution functions. This suggests that if the concentration of mixed-interstitials reaches a concentration of  $\geq 30\%$ , the

structure becomes (locally) unstable with respect to a substitutional phase.

The concentration dependence of the mixing energy of interstitial-based structures thus suggests a miscibility-gap like behavior between dilute interstitial solutions and more concentrated structures, which contain 30% or more of the alloying element and can transition more readily into substitutional configurations. These results further support the notion that interstitial agglomeration is energetically favorable.

### C. Mixed-interstitial migration

Up to this point, we have shown that there is an energetic driving force for further interstitial agglomeration and that mixed-interstitials prefer an alignment along parallel nearest-neighbor  $\langle 111 \rangle$  strings. Next, we discuss migration energies of interstitial structures. For all elements considered here, the binding energy between a SIA and a substitutional defect is large (V:  $-1.8$  eV, Ti:  $-0.6$  eV, Re:  $-0.8$  eV).<sup>4,15,18</sup> Thus, if mixed-interstitial diffusion were to proceed via dissociation of the mixed-interstitial, defect migration would be very slow except at very high temperatures. It has, however, been shown for the case of Re that mixed-interstitial can migrate via a non-dissociative mechanism with a much lower barrier, which in the case of Re was computed to be 0.12 eV.<sup>18</sup>

This low barrier is obtained for a sequence of a short displacive transformation, which shifts the center of the mixed-interstitial by  $a_0\sqrt{3}/2$  along  $\langle 111 \rangle$ , a rotation of the mixed-interstitial orientation, and another short jump along  $\langle 111 \rangle$  [Fig. 6(a)]. As a result of these events, the interstitial center moves by one lattice constant along  $\langle 100 \rangle$ .

Note that during the rotation, the configuration effectively passes through a  $\langle 110 \rangle$  dumbbell configuration, which happens to be practically identical with the saddle point of that segment. The rotational barrier therefore closely corresponds to the energy difference between the bridge and the  $\langle 110 \rangle$  mixed-dumbbell, at least for V, Ti, and Re.

We have computed the landscape for this mechanism for all three extrinsic elements, see Fig. 6(b). For the initial translation barrier, we obtain values of 0.22, 0.07, and

0.11 eV for V, Ti, and Re, respectively. The latter value agrees well with earlier calculations.<sup>18</sup> The barriers for the rotation are 0.14, 0.02, and 0.07 eV for V, Ti, and Re, respectively. Since the rotational barrier is always smaller than the barrier for the translation segment, the effective barrier for the entire path is set by the latter. While Ti has the lowest barrier, the values for V and Re mixed-interstitials are similar in magnitude so that these defects should be mobile under reactor relevant conditions. Note that the order of the barriers correlates with the degree of anisotropy of the formation volume tensor of the bridge interstitials.<sup>15</sup>

### IV. DISCUSSION

One of the main motivations behind this work is to investigate the causes behind the sub-soluble precipitation of transmutation solutes (mainly Re) observed in W subjected to high-energy particle irradiation. We seek mechanisms that connect point defects to solute transport in binary systems below the solubility limit. While long term precipitation kinetics is governed by the onset of defect fluxes to sinks, which is well beyond the scope of electronic structure calculations, the underlying mechanisms responsible for solute-defect coupling can only be investigated at the atomic scale using high accuracy methods. Here, we have employed DFT calculations to study the fundamental energetics of interstitial-solute complexes in three different binary alloys, W-Re, W-Ti, and W-V. These three are the main implications of our findings:

- (1) For all binary systems considered, mixed interstitial configurations are energetically favored over SIA-solute complexes. This is consistent with previous work on the subject conducted on W alloys.<sup>15,18,39</sup>
- (2) These mixed interstitials all display a migration mechanism that involves low-energy ( $\leq 0.14$  eV) rotations in the bridge interstitial configuration, followed by short translations in the  $\langle 110 \rangle$  orientation. In contrast with the *interstitialcy* mechanism, which propagates the lattice perturbation leaving the solute behind, this “associative” mechanism can effectively transport solutes long distances in three dimensions, rendering it an efficient mass transport mechanism (in fact, due to the comparatively low migration energy barriers, interstitial-mediated transport could potentially surpass that due to vacancies<sup>18</sup>).
- (3) While the heat of solution of all substitutional solutes at 0 K is negative in the BCC W matrix, corresponding to compounds that form solid concentrated solutions, the formation energies of all mixed interstitials are positive. This of course results in a strong segregation driving force for mixed interstitials defects, which ultimately may result in solute precipitation by way of mixed-dumbbell clustering.

Another aspect worth considering related to the precipitation kinetics of sub-soluble transmutants in W is the acicular (elongated) shape of the resulting precipitates. Precipitates are seen to form in the intermetallic  $\sigma$  and  $\chi$  phases,<sup>7,8,11</sup> although there is experimental indication that they nucleate as solute-rich BCC clusters<sup>40</sup> that may ultimately undergo a structural transformation.<sup>41</sup> While the shape of these intermetallic precipitates is likely to be

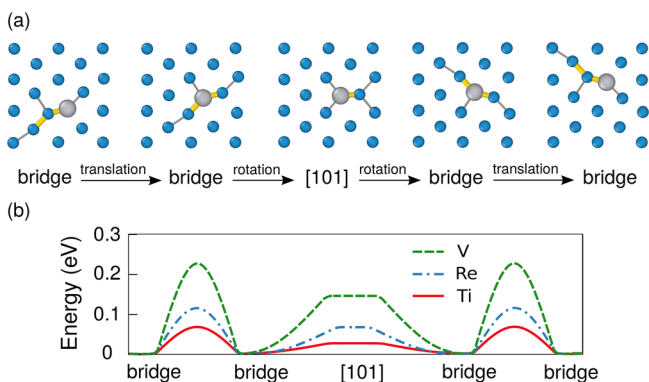


FIG. 6. Energetically favorable non-dissociative diffusion of a mixed-interstitial in dilute tungsten alloy. The configurations are presenting the  $[110]$  dumbbell mixed-interstitial translation along  $[100]$  direction including a  $90^\circ$  rotation. The plot in the lower row illustrates the corresponding migration barriers in eV. For a better comparison, the path, which connects bridge to  $[101]$  dumbbell mixed-interstitial via a rotation, is illustrated in the beginning of the migration barrier plot.

controlled by anisotropic interfacial energies and other thermodynamic features, here we put forward a mechanism based on the computed DFT energetics that may contribute to the incipient alignment of these clusters along crystallographic BCC  $\langle 111 \rangle$  directions. The mechanism is as follows:

- (i) Starting from a substitutional alloy of W and Re, irradiation leads to the production of SIAs, which diffuse along  $\langle 111 \rangle$  directions throughout the lattice until they become trapped by substitutional Re atoms due to a high binding energy.
- (ii) Mixed interstitials migrate associatively in 3D eventually resulting in clustering. The strong energetic driving force for clustering (see Sec. III A) and the low barriers for non-dissociative interstitial migration (see Sec. III C) facilitate defect co-alignment.
- (iii) These mixed di-interstitials are kinetically very stable due to the strong binding energies, which make them preferential sites for more defect absorption. While additional interstitials approaching these small clusters may not be initially aligned, they are energetically favored to again rotate into alignment, increasing cluster size and forming a precipitate nucleus.
- (iv) As interstitial accumulation proceeds, the local Re concentration increases and the system samples the mixing energy curve representing interstitial-based configurations [see Fig. 5(c)].

It is also worth mentioning that, as pointed out by Tanno and Hasegawa,<sup>7,8</sup> the formation of precipitates occurs at high accumulated doses ( $>5$  dpa), after sufficient transmutant buildup has occurred and the void-lattice stage subsides by recombination with large cascade-produced SIA clusters, resulting in an excess population of single SIAs and/or mixed interstitials. The above mechanism for interstitial-mediated solute transport and clustering is schematically depicted in Fig. 7. We recognize that this picture is somewhat speculative at this point, and we are currently implementing the energetics and the mechanisms presented here into long-term kinetic

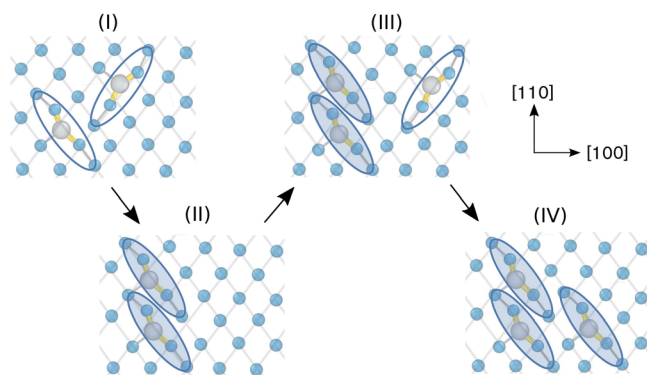


FIG. 7. Schematic illustration of the path to elongated solute-rich clusters. Shown is an atomic slice parallel to a  $\{110\}$  plane of the BCC lattice. (i) Initially mixed interstitials are trapped at substitutional extrinsic atoms with no particular orientation relationship. (ii) Via translations and rotations, the defects move into alignment with respect to each other, preferably in neighboring parallel  $\langle 111 \rangle$  strings. (iii) Other interstitials are attracted to the nucleus moving relatively freely as long as they have not achieved alignment with the other defects in the cluster. (iv) Full alignment yields the lowest energy configurations.

models capable of approaching doses of several dpa. In any case, the formation of these precipitates is one of the possible pitfalls associated with the development of W-based alloys for applications in fusion environments, as  $\sigma/\chi$  precipitates are known to cause very strong matrix hardening.<sup>42</sup>

## V. CONCLUSIONS

In conclusion, in the present study, we have demonstrated that mixed interstitials in BCC-W involving V, Ti, and Re are strongly attracted to each other with binding energies of several eV. This interaction leads to the alignment of interstitials along parallel first nearest neighbor  $\langle 111 \rangle$  strings.

All three systems exhibit mixing on the BCC lattice with respect to BCC boundary phases. In the case of Ti and Re, we also find negative formation energies for substitutional defects on the HCP lattice. The energetic offset between HCP-W and BCC-W on one side and BCC-Re and HCP-Re on the other side of the composition range, however, leads to very small solubilities in the boundary phases. In the case of Ti, the BCC/HCP energy difference is relatively smaller, which gives rise to an asymmetric solubility that is substantially larger on the W-rich side.

Furthermore, we have calculated the activation barriers for mixed interstitial motion, which are comparably low for all three elements. The migration mechanism involves defect migration and reorientation, resulting in effective solute transport in 3D.

The ease of rotation and strong binding of mixed interstitials could help explain the incipient formation of BCC solute-rich clusters oriented preferentially along  $\langle 111 \rangle$  directions. It is not clear whether this may help steer the formation of elongated  $\sigma$  and/or  $\chi$  phase precipitates, as this is a more complex process involving long term kinetics and structural transformations, but it is interesting to note that there is an intrinsic directionality associated with the formation of these clusters. The analogies among V, Ti, and Re with respect to defect and alloying properties suggest that similar mechanisms could also come into play in W-Ti and W-V alloys.

The impact of interstitial binding described here on cluster formation and subsequently mechanical properties deserves further study. This is motivated by the observation that interstitial clustering has been shown give rise to complex diffusion behavior in other BCC metals<sup>43,44</sup> and to impact swelling behavior.<sup>45</sup>

## ACKNOWLEDGMENTS

This work was supported the *Area of Advance–Materials Science* at Chalmers, the Swedish Research Council in the form of a Young Researcher grant, and the European Research Council via a Marie Curie Career Integration Grant. Computer time allocations by the Swedish National Infrastructure for Computing at NSC (Linköping) and C3SE (Gothenburg) are gratefully acknowledged. J.M. acknowledges support from US-DOE’s Early Career Research Program.

<sup>1</sup>S. J. Zinkle and N. M. Ghoniem, *Fusion Eng. Des.* **51–52**, 55 (2000).

<sup>2</sup>M. Rieth, S. L. Dudarev, S. M. Gonzalez de Vicente, J. Aktaa, T. Ahlgren, S. Antusch, D. E. J. Armstrong, M. Balden, N. Baluc, M. F. Barthe, W. W. Basuki, M. Battabyal, C. S. Becquart, D. Blagoeva, H. Boldyryeva, J. Brinkmann, M. Celino, L. Ciupinski, J. B. Correia, A. De Backer, C.

- Domain, E. Gaganidze, C. García-Rosales, J. Gibson, M. R. Gilbert, S. Giusepponi, B. Gludovatz, H. Greuner, K. Heinola, T. Höschen, A. Hoffmann, N. Holstein, F. Koch, W. Krauss, H. Li, S. Lindig, J. Linke, C. Linsmeier, P. López-Ruiz, H. Maier, J. Matejček, T. P. Mishra, M. Muhammed, A. Muñoz, M. Muzyk, K. Nordlund, D. Nguyen-Manh, J. Opschoor, N. Ordás, T. Palacios, G. Pintsuk, R. Pippa, J. Reiser, J. Riesch, S. G. Roberts, L. Romaner, M. Rosiński, M. Sanchez, W. Schulmeyer, H. Traxler, A. Ureña, J. G. van der Laan, L. Veleza, S. Wahlberg, M. Walter, T. Weber, T. Weitkamp, S. Wurster, M. A. Yar, J. H. You, and A. Zivelonghi, *J. Nucl. Mater.* **432**, 482 (2013).
- <sup>3</sup>S. P. Fitzgerald and D. Nguyen-Manh, *Phys. Rev. Lett.* **101**, 115504 (2008).
- <sup>4</sup>C. S. Becquart and C. Domain, *J. Nucl. Mater.* **385**, 223 (2009).
- <sup>5</sup>M. R. Gilbert and J.-C. Sublet, *Nucl. Fusion* **51**, 043005 (2011).
- <sup>6</sup>M. R. Gilbert, S. L. Dudarev, S. Zheng, L. W. Packer, and J.-C. Sublet, *Nucl. Fusion* **52**, 083019 (2012).
- <sup>7</sup>T. Tanno, A. Hasegawa, J. C. He, M. Fujiwara, M. Satou, S. Nogami, K. Abe, and T. Shishido, *J. Nucl. Mater.* **386–388**, 218 (2009).
- <sup>8</sup>A. Hasegawa, T. Tanno, S. Nogami, and M. Satou, *J. Nucl. Mater.* **417**, 491 (2011).
- <sup>9</sup>X. Hu, T. Koyanagi, Y. Katoh, M. Fukuda, B. D. Wirth, and L. L. Snead, “Defect evolution in neutron-irradiated single crystalline tungsten,” Semiannual Progress Report No. dOE/ER-0313/58, 30 June 2015.
- <sup>10</sup>T. Tanno, A. Hasegawa, J.-C. He, M. Fujiwara, S. Nogami, M. Satou, T. Shishido, and K. Abe, *Mater. Trans.* **48**, 2399 (2007).
- <sup>11</sup>A. Xu, C. Beck, D. E. J. Armstrong, K. Rajan, G. D. W. Smith, P. A. J. Bagot, and S. G. Roberts, *Acta Mater.* **87**, 121 (2015).
- <sup>12</sup>R. K. Williams, F. W. Wiffen, J. Bentley, and J. O. Stiegler, *Metall. Trans. A* **14**, 655 (1983).
- <sup>13</sup>A. Ardell, in *Materials Issues for Generation IV Systems*, NATO Science for Peace and Security Series B: Physics and Biophysics, edited by V. Ghetta, D. Gorse, D. Mazière, and V. Pontikis (Springer Netherlands, 2008), pp. 285–310.
- <sup>14</sup>T. Suzudo, M. Yamaguchi, and A. Hasegawa, *J. Nucl. Mater.* **467**, 418 (2015).
- <sup>15</sup>L. Gharaee and P. Erhart, *J. Nucl. Mater.* **467**, 448 (2015).
- <sup>16</sup>F. Willaime, C. C. Fu, M. C. Marinica, and J. Dalla Torre, *Nucl. Instrum. Methods Phys. Res. B* **228**, 92 (2005).
- <sup>17</sup>P. M. Derlet, D. Nguyen-Manh, and S. L. Dudarev, *Phys. Rev. B* **76**, 054107 (2007).
- <sup>18</sup>T. Suzudo, M. Yamaguchi, and A. Hasegawa, *Modell. Simul. Mater. Sci. Eng.* **22**, 075006 (2014).
- <sup>19</sup>P. Erhart, B. Sadigh, and A. Caro, *Appl. Phys. Lett.* **92**, 141904 (2008).
- <sup>20</sup>P. E. Blöchl, *Phys. Rev. B* **50**, 17953 (1994).
- <sup>21</sup>G. Kresse and D. Joubert, *Phys. Rev. B* **59**, 1758 (1999).
- <sup>22</sup>G. Kresse and J. Hafner, *Phys. Rev. B* **47**, 558 (1993).
- <sup>23</sup>G. Kresse and J. Hafner, *Phys. Rev. B* **49**, 14251 (1994).
- <sup>24</sup>G. Kresse and J. Furthmüller, *Phys. Rev. B* **54**, 11169 (1996).
- <sup>25</sup>G. Kresse and J. Furthmüller, *Comput. Mater. Sci.* **6**, 15 (1996).
- <sup>26</sup>J. P. Perdew, K. Burke, and M. Ernzerhof, *Phys. Rev. Lett.* **77**, 3865 (1996); erratum, *ibid.* **78**, 1396(E) (1997).
- <sup>27</sup>G. Henkelman, B. P. Uberuaga, and H. Jónsson, *J. Chem. Phys.* **113**, 9901 (2000).
- <sup>28</sup>S. A. Centoni, B. Sadigh, G. H. Gilmer, T. J. Lenosky, T. Diaz de la Rubia, and C. B. Musgrave, *Phys. Rev. B* **72**, 195206 (2005).
- <sup>29</sup>E. Jedvik, A. Lindman, M. T. Benediktsson, and G. Wahnström, *Solid State Ionics* **275**, 2 (2015).
- <sup>30</sup>S. Chiesa, M. R. Gilbert, S. L. Dudarev, P. M. Derlet, and H. V. Swygenhoven, *Philos. Mag.* **89**, 3235 (2009).
- <sup>31</sup>M. R. Gilbert and S. L. Dudarev, *Philos. Mag.* **90**, 1035 (2010).
- <sup>32</sup>H. Li, S. Wurster, C. Motz, L. Romaner, C. Ambrosch-Draxl, and R. Pippa, *Acta Mater.* **60**, 748 (2012).
- <sup>33</sup>M. Muzyk, D. Nguyen-Manh, K. J. Kurzydowski, N. L. Baluc, and S. L. Dudarev, *Phys. Rev. B* **84**, 104115 (2011).
- <sup>34</sup>J.-C. Crivello and J.-M. Joubert, *J. Phys. Condens. Matter* **22**, 035402 (2010).
- <sup>35</sup>E. Rudy and S. Windisch, *Trans. Metall. Soc. AIME* **242**, 953 (1968).
- <sup>36</sup>L. Kaufman and H. Nesor, *Metall. Trans. A* **6**, 2123 (1975).
- <sup>37</sup>S. K. Lee and D. N. Lee, *Calphad* **10**, 61 (1986).
- <sup>38</sup>L. Gharaee, M. Ångqvist, and P. Erhart, “Reassessment of the low-temperature part of the W–Ti phase diagram from first-principles calculations” (unpublished).
- <sup>39</sup>X.-S. Kong, X. Wu, Y.-W. You, C. Liu, Q. Fang, J.-L. Chen, G.-N. Luo, and Z. Wang, *Acta Mater.* **66**, 172 (2014).
- <sup>40</sup>P. D. Edmondson, A. Xu, L. R. Hanna, M. Dagan, S. G. Roberts, and L. L. Snead, *Microsc. Microanal.* **21**, 579 (2015).
- <sup>41</sup>P. Erhart, J. Marian, and B. Sadigh, *Phys. Rev. B* **88**, 024116 (2013).
- <sup>42</sup>L. L. Snead, L. M. Garrison, T. S. Byun, N. A. P. K. Kumar, and W. D. Lewis, “Evaluation of mechanical properties of tungsten after neutron irradiation,” in *Fusion Reactor Materials Program 55* (Oak Ridge National Laboratory, 2013).
- <sup>43</sup>C.-C. Fu, J. Dalla Torre, F. Willaime, J.-L. Bocquet, and A. Barbu, *Nat. Mater.* **4**, 68–74 (2005).
- <sup>44</sup>J. H. Evans, *J. Nucl. Mater.* **119**, 180–188 (1983).
- <sup>45</sup>Yu. N. Osetsky, D. J. Bacon, A. Serra, B. N. Singh, and S. I. Golubov, *Philos. Mag.* **83**, 61–91 (2003).

# Paper III

**Mechanism of Re precipitation in irradiated W-Re alloys from kinetic Monte Carlo simulations**

Chen-Hsi Huang, Leili Gharaee, Yue Zhao, Paul Erhart and Jaime Marian  
arXiv preprint arXiv:1702.03019 (2017).



# Mechanism of Re precipitation in irradiated W-Re alloys from kinetic Monte Carlo simulations

Chen-Hsi Huang,<sup>1</sup> Leili Gharaee,<sup>2</sup> Yue Zhao,<sup>1</sup> Paul Erhart,<sup>2</sup> and Jaime Marian<sup>1,3</sup>

<sup>1</sup>*Department of Materials Science and Engineering, University of California, Los Angeles, CA 90095, USA*

<sup>2</sup>*Department of Physics, Chalmers University of Technology, S-412 96 Gothenburg, Sweden*

<sup>3</sup>*Department of Mechanical and Aerospace Engineering, University of California, Los Angeles, CA 90095, USA*

High-temperature, high-dose, neutron irradiation of W results in the formation of Re-rich clusters at concentrations one order of magnitude lower than the thermodynamic solubility limit. These clusters may eventually transform into brittle W-Re intermetallic phases, which can lead to high levels of hardening and thermal conductivity losses. Standard theories of radiation enhanced diffusion and precipitation cannot explain the formation of these precipitates and so understanding the mechanism by which nonequilibrium clusters form under irradiation is crucial to predict materials degradation and devise mitigation strategies. Here we carry out a thermodynamic study of W-Re alloys and conduct kinetic Monte Carlo simulations of Re cluster formation in irradiated W-2Re alloys using a generalized Hamiltonian for crystals containing point defects parameterized entirely with electronic structure calculations. Our model incorporates recently-gained mechanistic information of mixed-interstitial solute transport, which is seen to control cluster nucleation and growth by forming quasi-spherical nuclei after an average incubation time of 20 s at 1800 K. These nuclei are seen to grow by attracting more mixed interstitials bringing solute atoms, which in turn attracts vacancies leading to recombination and solute agglomeration. The clusters grow to a maximum size of approximately 4-nm radius, and are not fully dense with Re, containing 50% or less near the center. Our simulations are in reasonable agreement with recent atom probe examinations of ion irradiated W-2Re systems at 773 K.

Keywords: W-Re alloys; Solute precipitation; Neutron irradiation; kinetic Monte Carlo

## I. INTRODUCTION

Tungsten is the prime candidate material in magnetic fusion energy devices due to its high strength and excellent high temperature properties [1–4]. Upon fast neutron irradiation in the 600-1000°C temperature range, W transmutes into Re by the way of beta decay reactions at a rate that depends on the neutron spectrum and the position in the reactor. For the DEMO (demonstration fusion power plant) reactor concept, calculations show that the transmutation rate is 2000 and 7000 atomic parts per million (appm) per displacements per atom (dpa) in the divertor and the equatorial plane of the first wall, respectively (where damage, in each case, accumulates at rates of 3.4 and 4.4 dpa/year) [5, 6]. The irradiated microstructure initially evolves by accumulating a high density of prismatic dislocation loops and vacancy clusters, approximately up to 0.15 dpa [7–10]. Subsequently, a void lattice emerges and fully develops at fluences of around 1 dpa. After a critical dose that ranges between 5 dpa for fast (>1 MeV) neutron irradiation [9] and 2.2 dpa in modified target rabbits in the HFIR [10, 11], W and W-Re alloys develop a high density of nanometric precipitates with acicular shape at Re concentrations well below the solubility limit [9, 10]. The structure of these precipitates is consistent with  $\sigma$  (W<sub>7</sub>Re<sub>6</sub>) and  $\chi$  (WRe<sub>3</sub>) intermetallic phases, which under equilibrium conditions only occur at temperatures and Re concentrations substantially higher than those found in neutron irradiation studies [12]. A principal signature of the formation of these intermetallic structures in body-centered cubic (bcc) W is the sharp increase in hardness and embrittlement [8–10]. Qualitatively similar observations have been recently made in W-2Re and W-1Re-10s alloys subjected to heavy ion irradiation [13, 14], clearly establishing a link between primary damage production and Re precipitation.

Precipitation of nonequilibrium phases in irradiated materials is commonplace. The standard theory of irradiation damage includes radiation enhanced diffusion (RED) and radiation induced precipitation (RIP) as mechanisms that can drive the system out of equilibrium due to the onset of point defect cluster fluxes towards defect sinks [15–17]. Within this picture, Re precipitation in W or W-Re alloys under irradiation would then, in principle, be unsurprising were it not for the fact that Re clustering is seen to occur at concentrations still below the solubility limit even after RED has taken place. In spite of this, recent work using energy models based on the cluster expansion formalism for the W-Re system, and fitted to density functional theory (DFT) calculations, have revealed a direct relationship between excess vacancy concentrations and the formation of Re solute-rich clusters [18]. These calculations are substantiated by recent neutron irradiation experiments of pure W at 900°C up to 1.6 dpa in the HFR in Petten [19]. Post-irradiation examination of the irradiated specimens reveals the formation of a fine distribution of voids with average 5 nm size surrounded by Re-rich clouds. However, the relative concentration of Re around the voids is still on the order of 12-18% (from a nominal overall concentration of 1.4% from transmutation), well below the precipitation limit of Re in W at 900°C. However, in the ion beam irradiation experiments of W-2Re alloys by Xu *et al.* at 300 and 500°C, Re-rich clusters with bcc structure are seen to form with concentrations between 12 and 30% Re with no indication of vacancies forming part of the clusters [13, 14]. Another piece of evidence against a strong association between vacancies and Re atoms comes from irradiation tests of W-Re alloys performed at EBR-II in the 1970s and 80s [20–24]. In these studies, the presence of Re was seen to suppress swelling, which would seem to suggest a decoupling between vacancy clusters and Re atoms. Clearly, equilibrium thermodynamics involving va-

cancies alone may not suffice to explain the precipitation tendencies in irradiated W-Re alloys.

All this is suggestive of alternative solute transport mechanisms that may be unique to W-Re systems. Indeed, several recent studies using electronic structure calculations have independently reported a peculiar association between self-interstitial atoms (SIA) and Re solutes that results in very high solute transport efficacy [25–27]. This mechanism consists of a series of mixed dumbbell rotations and translations such that the mixed nature of the dumbbell is preserved and solutes can be transported over long distances without the need for vacancy exchanges. Furthermore, this mechanism effectively transforms one-dimensional SIA diffusion into a 3D mixed-dumbbell transport process at activation energies considerably lower than that of vacancy diffusion. The objective of this paper is to study the kinetics of Re precipitation in irradiated W accounting for both vacancy and mixed-interstitial solute transport. To this effect, we develop a lattice kinetic Monte Carlo (kMC) model of alloy evolution parameterized solely using first principles calculations. We start in Section II by describing the essential elements of our kinetic model as well as the parameterization effort based on DFT calculations. In Section III we provide our main results, including semi-grand canonical Monte Carlo calculations of ternary W-Re-vacancy and W-Re-SIA systems, and kMC simulations and analysis of the Re-precipitate nucleation and growth. We finish with a discussion of the results and the conclusions in Section IV.

## II. THEORY AND METHODS

### A. Energy model

The energy model employed throughout this work is a cluster expansion Hamiltonian based on pair interactions truncated to the 2<sup>nd</sup>-nearest neighbor (2nn) shell:

$$\mathcal{H} = \sum_i \sum_{\alpha,\beta} n_{\alpha-\beta}^{(i)} \varepsilon_{\alpha-\beta}^{(i)} \quad (1)$$

where  $(i)$  specifies the type of nearest-neighbor interaction (first or second),  $\alpha$  and  $\beta$  refer to a pair of lattice sites, separated by a distance specified by the index  $i$ ,  $n_{\alpha-\beta}$  denotes the number of occurrences (bonds) of each  $\alpha$ - $\beta$  pair, and  $\varepsilon_{\alpha-\beta}$  is bond energy. In a previous work, we have shown how this Hamiltonian can be reduced to a generalized Ising Hamiltonian involving solvent and solute atoms (A and B), vacancies (V), and pure and mixed interstitials (AA, BB, and AB) [28]. The Hamiltonian is then expressed as a sum of polynomial terms of various degrees involving spin variables  $\sigma_\alpha$  and  $\sigma_\beta$  in the manner of the Ising model:

$$\mathcal{H} = \sum_{n,m} \sum_{\alpha,\beta} \sigma_\alpha^n \sigma_\beta^m \quad (2)$$

One of the advantages of using this notation is that the values assigned to the spin variables conserve the number of atoms  $N$  of the system. We refer the reader to ref. [28] for more details

about this notation. In this paper we focus on the parameterization exercise for irradiated W-Re alloys<sup>1</sup>.

### B. Semi-Grand Canonical Monte Carlo for AB systems

The thermodynamic phase diagram of the W-Re system can be studied using semi-grand canonical Monte Carlo (SGMC) calculations as a function of temperature and solute concentration [29–34]. We seek to minimize the thermodynamic potential of the semi-grand canonical ensemble, characterized by a constant temperature  $T$ , a constant number of particles  $N$ , and a constant chemical potential  $\mu$ . In each SGMC step, an A atom is randomly flipped into a B atom and the new state is accepted with probability:

$$p_{ij} = \exp\left(-\frac{\Delta\mathcal{H}_{ij} - N_B\Delta\mu}{k_B T}\right) \quad (3)$$

where  $\Delta\mathcal{H}_{ij}$  is the energy difference between the initial and final states,  $i$  and  $j$ ,  $N_B = NX$  is the number of solute atoms ( $X$ : solute concentration),  $\Delta\mu$  is the change in chemical potential per atom after the transition, and  $k_B$  is Boltzmann's constant. In this work, each transition is defined by changing the chemical nature of one atom chosen at random. In terms of the change in spin variable (in the notation of the generalized Ising Hamiltonian, cf. eq. (2)), this always results in a change of  $\delta\sigma = -2$ , such that eq. (3) can be simplified to:

$$p_{ij} = \exp\left(-\frac{\Delta\mathcal{H}_{ij} + 2\Delta\mu}{k_B T}\right) \quad (4)$$

In the calculations, the chemical potential difference  $\Delta\mu$  and the temperature  $T$  are input variables, while the solute composition  $X$  and the equilibrium configurations are obtained when convergence is reached.

### C. Metropolis Monte Carlo calculations of ABV system configurations

During irradiation, the introduction of large amounts of defects has the potential to impact the thermodynamics of the system. It is therefore of interest to calculate phase diagrams with fixed defect concentrations using equilibrium (Metropolis) Monte Carlo. Defect concentrations are not thermodynamically equilibrated under irradiation—the number of vacancies or interstitials is not controlled by the chemical potential—, and so the AB system must be considered in conjunction with a fixed defect concentration. Take the case of vacancies for example, to properly obtain converged nonequilibrium configurations of ABV systems, we employ a *flip* and *swap* approach: (i) initially a system consisting of A atoms and a random distribution of vacancies is considered; (ii) a

<sup>1</sup> With A: W atoms; B: Re atoms; V: vacancies, AA: W-W dumbbell (or self-interstitial atom); BB: Re-Re dumbbell; AB: mixed W-Re dumbbell.

lattice point is selected at random; (iii) if that lattice point corresponds to an atom, a SGMC step is carried out, resulting in a change in the relative concentrations of A and B; if it, on the contrary, corresponds to a vacant site, then a canonical Monte Carlo step is carried out, leaving  $X$  unchanged, and the vacancy is swapped with a randomly-selected atom. This trial swap is then accepted according to the Boltzmann distribution:

$$p_{ij} = \exp\left(-\frac{\Delta\mathcal{H}_{ij}}{k_B T}\right) \quad (5)$$

In this fashion, equilibrated AB alloys containing a fixed vacancy concentration are obtained, from which one can determine the changes relative to the thermodynamic equilibrium configurations. Although interstitials are much higher in energy than vacancies (so that only very small concentrations need be explored), the procedure for the ABI system is identical to that of the ABV system.

#### D. Kinetic Monte Carlo simulations of ABVI systems

The kinetic evolution of W-Re alloys under irradiation is studied using standard lattice kMC. The system is evolved by events involving atomic jumps and time is advanced according to the residence-time algorithm [35]. Jump rates are calculated as:

$$r_{ij} = \nu \exp\left(-\frac{\Delta E_{ij}}{k_B T}\right) \quad (6)$$

where  $\nu$  is an attempt frequency and  $\Delta E_{ij}$  is the activation energy to jump from state  $i$  to state  $j$ .

##### 1. Vacancy migration model

Several models have been proposed to describe the activation energy based on different interpretations of the atomic migration process (see, e.g. [36] and [28] for recent reviews). In this work, the activation energy of vacancy jump is modeled by the saddle-point energy model (or cut-bond model) [37–40], according to which  $E_{ij}$  is given by the energy difference of the configuration when the jumping atom is at saddle point and the initial configuration:

$$\Delta E_{ij} = \sum_p \varepsilon_{\alpha-p}^{sp} - \sum_q \varepsilon_{\alpha-q}^{(i)} - \sum_{r \neq \alpha} \varepsilon_{V,r}^{(i)} + \sum \Delta E_{ij}^{\text{non-broken}} \quad (7)$$

where  $\alpha$  is the jumping atom,  $V$  is the vacancy, and  $\varepsilon^{sp}$  are the bond energies between the atom at the saddle point and the neighboring atoms. The first term on the r.h.s. of eq. (7) reflects the energy of the jumping atom at the saddle point. In this work, we consider interactions up to 2nn distances for this term<sup>2</sup>. The second and third terms on the r.h.s. of eq. (7)

are the energies of the jumping atom and the vacancy at the initial state  $i$ . Finally, the fourth term gives the energy difference between state  $i$  and  $j$  for the non-broken bonds due to local solute concentration changes. The dependence of bond coefficients on local solute concentration will be discussed in Section II E.

##### 2. Interstitial defect migration model

Here we consider self-interstitial atoms of the AA type, and mixed-interstitials AB. Due to their rarity, BB interstitials are omitted in our calculations. In bcc metals, AA SIAs are known to migrate athermally in one dimension along  $\langle 111 \rangle$  directions, with sporadic rotations to other  $\langle 111 \rangle$  orientations. These processes, however, are treated separately. In contrast to vacancy migration, activation energies of interstitial jumps are calculated using the direct final-initial system energy model [41–44]:

$$\Delta E_{ij} = \begin{cases} E_m + \Delta\mathcal{H}_{ij}, & \text{if } \Delta\mathcal{H}_{ij} > 0 \\ E_m, & \text{if } \Delta\mathcal{H}_{ij} < 0 \end{cases} \quad (8)$$

In addition, we include a bias due to the well-known phenomenon of *correlation*, by which a forward jump is slightly more likely to occur than a backward jump. This is reflected in a correlation factor  $f$  computed as the ratio of forward to backward jumps [45], which in our simulations is temperature dependent. Rotations between  $\langle 111 \rangle$  directions are simply characterized by an activation energy equal to a rotation energy  $E_r$ .

For their part, as pointed out in Section I, recent DFT studies have revealed a new migration mechanism for mixed dumbbells in W alloys. This mechanism involves a non-dissociative sequence of rotations and translations such that the solute atom is always part of the mixed dumbbell (in contrast with the *interstitialcy* or ‘knock-on’ mechanism commonly displayed by SIAs) [25–27, 46]. This effectively makes AB interstitials move in three dimensions with 2nn jumps along  $\langle 100 \rangle$  directions. Calculations for the W-Re system have shown that the migration energy in this case is very low, on the order of one tenth of an eV. As we shall see, this has extraordinary implications on the kinetic evolution of irradiated W-Re alloys.

##### 3. Spontaneous events: recombination and absorption

Any recombination event occurs spontaneously (no sampling involved) when the distance between an interstitial defect and a vacancy is within the 3<sup>rd</sup> nearest neighbor shell. Another reaction considered to be instantaneous is the transition of a SIA into an AB dumbbell when it encounters a solute atom: AA+B→AB+A. This is because the binding energy between a SIA and a Re solute atom has been calculated to be  $-0.8$  eV (negative binding energies represent attraction). The distance for this transformation is set to be equal to the 1nn separation.

<sup>2</sup> In the saddle-point configuration for vacancy migration, there are six 1nn bonds and six 2nn bonds, compared with eight and six for a lattice point configuration.

Defect absorption represents another type of spontaneous event. Absorption can occur at sinks, such as a plane located in a stationary position within the simulation box [47], or a free surface [28]. Sinks can potentially act also as defect emitters, as in the case of grain boundaries, dislocations, and free surfaces in real microstructures. Details about the implementation of these processes can be found in ref. [28].

#### 4. Frenkel pair generation

In this work, defects are generated as Frenkel pairs at a prescribed rate set by the damage rate. To insert a defect pair, two atomic sites are chosen at random, one is replaced by a vacancy and the other with an interstitial formed by an A atom and the lattice atom.

### E. Parameters

There are five distinct atomic species used in this work: W atoms (A), Re atoms (B), vacancies (V), SIAs (AA), and mixed-interstitials (AB). As mentioned above, our energy model consists of pairwise interactions up to the 2nn shell. After discounting interstitial-vacancy bonds, this amounts to 26 different types of bonds (13 for each nearest neighbor shell), all of which must be obtained using first-principles calculations. Moreover, as discussed by Martinez *et al.* and Senninger *et al.* [39, 40], several of these bond energies are sensitive to the local solute concentration and must be computed on the fly in each Monte Carlo step. Following Warczok *et al.* [48], we reduce the number of unknowns from 26 to 13 by partitioning bond energies according the following relation:

$$\varepsilon^{(2)} = \varepsilon^{(1)} \left( \frac{r_{2nn}}{r_{1nn}} \right)^{-6} \quad (9)$$

which is used unless both bond energies can be explicitly calculated. For the bcc lattice, this results in  $\varepsilon_{\alpha\beta}^{(1)}/\varepsilon_{\alpha\beta}^{(2)} = 0.421875$  for regular bond coefficients, and  $\varepsilon_{\alpha\beta}^{sp(1)}/\varepsilon_{\alpha\beta}^{sp(2)} = 0.194052$  for saddle-point bond coefficients.

The local solute concentration is always computed up to the 2nn shell. Next we describe the parameterization procedure for each set of bond energies.

#### 1. W-Re parameters

The W-Re bond coefficients are  $\varepsilon_{A-A}$ ,  $\varepsilon_{B-B}$ , and  $\varepsilon_{A-B}$ . They determine the thermodynamic equilibrium phase diagram of the alloy. The bond coefficients of  $\varepsilon_{A-A}$  and  $\varepsilon_{B-B}$  are obtained from the cohesive energy:

$$\begin{aligned} E_{coh}^A &= -\frac{z_1}{2} \varepsilon_{A-A}^{(1)} - \frac{z_2}{2} \varepsilon_{A-A}^{(2)} \\ E_{coh}^B &= -\frac{z_1}{2} \varepsilon_{B-B}^{(1)} - \frac{z_2}{2} \varepsilon_{B-B}^{(2)} \end{aligned} \quad (10)$$

where  $z_1$  and  $z_2$  are coordination numbers for the 1nn and 2nn shells, respectively. The cohesive energies calculated using DFT are given in Table I.<sup>3</sup>

TABLE I. Energetics of W-Re systems calculated with DFT.

Quantity	Value	Source
$E_{coh}^A$	8.3276	This work
$E_{coh}^B$	7.4070	This work
$\Delta H^{mix}$	-0.1571 - 0.2311X	Ref. [27]
$E_f^V$	3.1690	This work
$E_b^{(a)}$	-0.2096	This work
$E_b^{(b)}$	-0.1520	This work
$E_b^{(c)}$	-0.3079	This work
$E_b^{(d)}$	-0.2992	This work
$E_{b,1nn}^{V-V}$	-0.0146	This work <sup>(3)</sup>
$E_{b,2nn}^{V-V}$	0.3028	This work <sup>(3)</sup>
$E_f^{AA}$	10.16	Ref. [46]
$E_f^{AB}$	9.49	Ref. [46]
$E_{b,1nn}^{AA-B}$	-0.52	Ref. [46]
$E_{b,1nn}^{AB-B}$	-0.53	Ref. [49]
$E_{b,1nn}^{AA-AA}$	-2.12	Ref. [50]
$E_{b,1nn}^{AA-AB}$	-2.12	Assumed <sup>(4)</sup>
$E_{b,1nn}^{AB-AB}$	-3.2	Ref. [27]
$E_m^{V \rightarrow A} (A)$	1.623	This work
$E_m^{V \rightarrow B} (A)$	1.651	This work
$E_m^{V \rightarrow A(1)} (Fig. 2(c))$	1.7151	This work
$E_m^{V \rightarrow A(2)} (Fig. 2(c))$	1.6378	This work
$E_m^{V \rightarrow B(3)} (Fig. 2(c))$	1.577	This work
$E_m^{V \rightarrow A} (V)$	1.623	This work
$E_m^{V \rightarrow B} (V)$	1.651	This work

The coefficient for the A-B bond is obtained from the enthalpy of mixing of W-Re,  $\Delta H^{mix}$ , which can be written within the Bragg-Williams approximation [52–54] as:

$$\begin{aligned} \Delta H^{mix} &= \frac{z_1}{2} \left[ (1-X)\varepsilon_{A-A}^{(1)} + X\varepsilon_{B-B}^{(1)} + 2x(1-x)\Omega_s^{(1)} \right] \\ &+ \frac{z_2}{2} \left[ (1-X)\varepsilon_{A-A}^{(2)} + X\varepsilon_{B-B}^{(2)} + 2X(1-X)\Omega_s^{(2)} \right] \end{aligned} \quad (11)$$

where  $X$  is the global solute concentration, and  $\Omega_s$  is the *heat of solution*, defined as:

$$\Omega_s^{(1)} = \varepsilon_{A-B}^{(1)} - \frac{1}{2} \left( \varepsilon_{A-A}^{(1)} + \varepsilon_{B-B}^{(1)} \right) \quad (12)$$

$$\Omega_s^{(2)} = \varepsilon_{A-B}^{(2)} - \frac{1}{2} \left( \varepsilon_{A-A}^{(2)} + \varepsilon_{B-B}^{(2)} \right) \quad (13)$$

Combining eqs. (10) and (11),  $\Delta E^{mix}$  can be expressed as:

$$X(1-X)\Omega_s^* = \Delta H^{mix} + (1-X)E_{coh}^A + XE_{coh}^B \quad (14)$$

where  $\Omega_s^* = z_1\Omega_s^{(1)} + z_2\Omega_s^{(2)}$ . To ascertain the dependence on the solute concentration of the heat of solution, we fit the l.h.s.

<sup>3</sup> With xc-energy correction from Ref. [51]

of eq. (14) to the data points for the mixing enthalpies as a function of  $X$  calculated in our previous work [27]. The best fit, shown in Figure 1, is achieved when  $\Omega_s^*$  is expressed a linear function of the concentration:

$$\Omega_s^* = w_0 + w_1 X$$

with  $w_0 = -0.1571$  and  $w_1 = -0.2311$ . The negative values of  $w_0$  and  $w_1$  suggest a strong tendency towards ordering, which becomes larger as the solute concentration increases. Combining eqs. (9), (10), (12), and (14), one can obtain the values of  $\Omega_s^{(1)}$ ,  $\Omega_s^{(2)}$ ,  $\epsilon_{A-B}^{(1)}$ , and  $\epsilon_{A-B}^{(2)}$ . A non-constant  $\Omega_s^*$  effectively implies that  $\epsilon_{A-B}$  is also a function of the concentration. Moreover, to reflect local composition variations in the W-Re alloys, we make the assumption that the dependence of  $\epsilon_{A-B}^{(1)}$  and  $\epsilon_{A-B}^{(2)}$  on  $X$  can be transferred to the local environment of each atom, such that both bond energy coefficients are functions of the local composition, which we term  $x$ , and must be computed on the fly for each solute atom in the system.

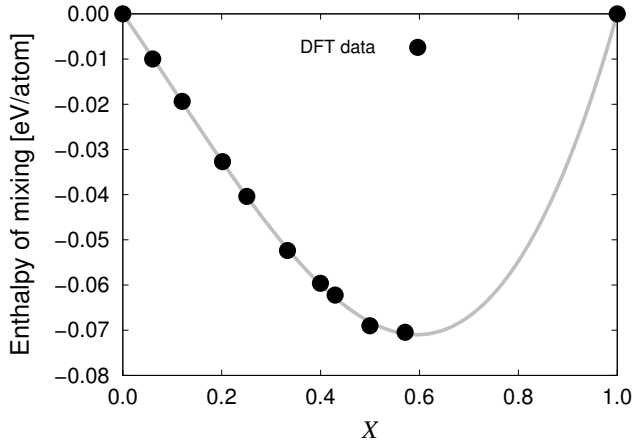


FIG. 1. Enthalpy of mixing as a function of solute concentration from ref. [27] and 3<sup>rd</sup>-degree polynomial fit.

## 2. Vacancy parameters

The vacancy bond coefficients are  $\epsilon_{A-V}$ ,  $\epsilon_{B-V}$ , and  $\epsilon_{V-V}$ .  $\epsilon_{A-V}$  can be readily obtained from the value of the vacancy formation energy:

$$E_f^V = E_{coh}^A - z_1 \epsilon_{A-V}^{(1)} - z_2 \epsilon_{A-V}^{(2)} \quad (15)$$

where  $E_f^V$  is the vacancy formation energy in pure W (given in Table I).  $\epsilon_{B-V}$  can be obtained from the binding energies of V-Re configurations. The binding energy of a configuration involving  $m$  solute atoms and  $n$  vacancies is defined as:

$$E_b^{B_m V_n} = E_f^{B_m V_n} - m E_f^B - n E_f^V \quad (16)$$

where the  $E_f$  are the respective formation energies of each structure. In this work, binding energies for the four vacancy-solute configurations shown in Fig. (2) have been calculated

(cf. Table I). One can now rewrite eq. (16) as a function of the B-V bond coefficients  $\epsilon_{B-V}^{(1)}$  and  $\epsilon_{B-V}^{(2)}$  for each one of the configurations in the figure:

$$E_b^{(a)} = \epsilon_{B-V}^{(1)} + \epsilon_{A-A}^{(1)} - \epsilon_{A-B}^{(1)} - \epsilon_{A-V}^{(1)} \quad (17a)$$

$$E_b^{(b)} = \epsilon_{B-V}^{(2)} + \epsilon_{A-A}^{(2)} - \epsilon_{A-B}^{(2)} - \epsilon_{A-V}^{(2)} \quad (17b)$$

$$E_b^{(c)} = 2\epsilon_{B-V}^{(1)} + \epsilon_{B-B}^{(2)} + 2\epsilon_{A-A}^{(1)} + \epsilon_{A-A}^{(2)} - 2\epsilon_{A-V}^{(1)} - 2\epsilon_{A-B}^{(1)} - 2\epsilon_{A-B}^{(2)} + 14\Delta\epsilon_{A-B}^{(1)} + 10\Delta\epsilon_{A-B}^{(2)} \quad (17c)$$

$$E_b^{(d)} = 2\epsilon_{B-V}^{(2)} + 2\epsilon_{A-A}^{(2)} - 2\epsilon_{A-B}^{(2)} - 2\epsilon_{A-V}^{(2)} \quad (17d)$$

where  $\Delta\epsilon_{A-B}^{(m)}$  is the change in  $\epsilon_{A-B}^{(m)}$  due to the local solute concentration change resulting from the vacancy jump.

To define the dependence on  $x$  of  $\epsilon_{B-V}^{(1)}$ , we must consider two factors. First, our DFT calculations show that  $\epsilon_{A-V}^{(1)} > \epsilon_{B-V}^{(1)}$ . Second,  $x$  of  $\epsilon_{B-V}^{(1)}$  is seen to increase with local concentration. Both of these conditions are satisfied by assuming a dependence such as  $\epsilon_{B-V}^{(1)}(x) = \epsilon_{A-V}^{(1)} - ax^{-1}$ , where  $a$  is a fitting constant. As well,  $\epsilon_{B-V}^{(2)}$  is seen to independently increase with concentration, such that  $\epsilon_{B-V}^{(2)}(x) = bx + c$ , where  $b$  and  $c$  are fitting parameters

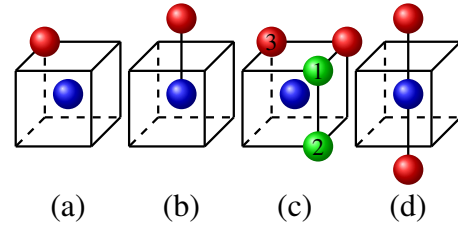


FIG. 2. Configurations of V-Re clusters used to extract bond energy coefficients  $\epsilon_{A-V}$  and  $\epsilon_{B-V}$ . Blue spheres represent vacancies, red spheres represents Re atoms. All other lattice sites are occupied by A atoms, which are omitted for clarity. Green spheres indicate the various equivalent sites for atoms to exchange positions with the vacancy

$\epsilon_{V-V}$  can be readily calculated by considering the binding energy of a di-vacancy:

$$E_{b,1nn}^{V-V} = \epsilon_{A-A}^{(1)} + \epsilon_{V-V}^{(1)} - 2\epsilon_{A-V}^{(1)} \quad (18)$$

$$E_{b,2nn}^{V-V} = \epsilon_{A-A}^{(2)} + \epsilon_{V-V}^{(2)} - 2\epsilon_{A-V}^{(2)} \quad (19)$$

It is interesting to note that, in accordance with several other studies [49, 55–58],  $E_{b,2nn}^{V-V}$  takes a positive value (cf. Table I), indicating repulsion between vacancies that are at 2nn distances of each other.

## 3. Interstitial defect parameters

The interstitial bond coefficients include  $\epsilon_{AA-A}$ ,  $\epsilon_{AB-A}$ ,  $\epsilon_{AA-B}$ ,  $\epsilon_{AB-B}$ ,  $\epsilon_{AA-AA}$ ,  $\epsilon_{AA-AB}$ , and  $\epsilon_{AB-AB}$ .  $\epsilon_{AA-A}$  and  $\epsilon_{AB-A}$

are calculated directly from the formation energies of SIAs and mixed dumbbells:

$$E_f^{AA} = -4\epsilon_{A-A}^{(1)} - 3\epsilon_{A-A}^{(2)} + 8\epsilon_{AA-A}^{(1)} + 6\epsilon_{AA-A}^{(2)} \quad (20)$$

$$E_f^{AB} = -4\epsilon_{A-A}^{(1)} - 3\epsilon_{A-A}^{(2)} + 8\epsilon_{AB-A}^{(1)} + 6\epsilon_{AB-A}^{(2)} \quad (21)$$

The other bond coefficients are obtained from various binding energies:

$$E_{b,1nn}^{AA-B} = \epsilon_{AA-B}^{(1)} + \epsilon_{A-A}^{(1)} - \epsilon_{AA-A}^{(1)} - \epsilon_{A-B}^{(1)} \quad (22)$$

$$E_{b,1nn}^{AB-B} = \epsilon_{AB-B}^{(1)} + \epsilon_{A-A}^{(1)} - \epsilon_{AB-A}^{(1)} - \epsilon_{A-B}^{(1)} \quad (23)$$

$$E_{b,1nn}^{AA-AA} = \epsilon_{AA-AA}^{(1)} + \epsilon_{A-A}^{(1)} - 2\epsilon_{AA-A}^{(1)} \quad (24)$$

$$E_{b,1nn}^{AA-AB} = \epsilon_{AA-AB}^{(1)} + \epsilon_{A-A}^{(1)} - \epsilon_{AA-A}^{(1)} - \epsilon_{AB-A}^{(1)} \quad (25)$$

$$E_{b,1nn}^{AB-AB} = \epsilon_{AB-AB}^{(1)} + \epsilon_{A-A}^{(1)} - 2\epsilon_{AB-A}^{(1)} \quad (26)$$

These formation and binding energies are all taken from the literature<sup>4</sup>.

All the bond energy coefficients, the equation used for their calculation, and the source of the numbers are compiled in Table II.

#### 4. Migration parameters

The attempt frequency ( $\nu$  in eq. (6)) used for vacancy jumps in this work is set to be equal to Debye frequency of W, or  $6.5 \times 10^{12}$  Hz [59], while for interstitials we use a value of  $1.5 \times 10^{12}$  Hz [45].

From eq. (7), there are six different saddle-point bond coefficients:  $\epsilon_{A-A}^{sp(m)}$ ,  $\epsilon_{A-B}^{sp(m)}$ ,  $\epsilon_{A-V}^{sp(m)}$ ,  $\epsilon_{B-A}^{sp(m)}$ ,  $\epsilon_{B-B}^{sp(m)}$ , and  $\epsilon_{B-V}^{sp(m)}$ , where  $m=1nn, 2nn$ . In this notation,  $\epsilon_{\alpha-\beta}^{sp(m)}$  represents the energy of the bond between the atom at the saddle point  $\alpha$  and its closest lattice neighbor  $\beta$ . This means  $\epsilon_{\alpha-\beta}^{sp(m)} \neq \epsilon_{\beta-\alpha}^{sp(m)}$ .

The saddle-point bond coefficients connected to a lattice atom A (W atom),  $\epsilon_{\alpha-A}^{sp(m)}$ , can be calculated as:

$$z_1^{sp} \epsilon_{\alpha-A}^{sp(1)} + z_2^{sp} \epsilon_{\alpha-A}^{sp(2)} = E_m + \sum_{n,q} \epsilon_{X-q}^{(n)} + \sum_{n,r \neq X} \epsilon_{V-r}^{(n)} \quad (27)$$

where  $z_1^{sp}$  and  $z_2^{sp}$  are the numbers of 1<sup>st</sup>- and 2<sup>nd</sup> nearest neighbor of an atom at the saddle point, which are both equal to 6 for the bcc lattice, and  $E_m$  is the migration energy. The term  $\Delta E_{ij}^{\text{non-broken}}$  in eq. (7) is zero here since no solute concentration change is involved in an A-atom jump.  $\epsilon_{\alpha-A}^{sp(2)}$  is obtained from  $\epsilon_{\alpha-A}^{sp(1)}$  using eq. (9). Vacancy bonds are calculated in a similar manner.

To calculate the saddle-point bond coefficients pertaining to B (Re) atoms,  $\epsilon_{\alpha-B}^{sp(m)}$ , one must consider local solute concentration changes. To this end, we resort to the configurations

shown in Fig. 2(c). The A-B saddle-point coefficients  $\epsilon_{A-B}^{sp(m)}$  are obtained from A-atom jumps, labeled ‘1’ and ‘2’ in Fig. 2(c), into the vacant site. The B-B saddle-point coefficient  $\epsilon_{B-B}^{sp(1)}$  is computed assuming a B-atom (labeled ‘3’ in the figure) jump into the vacancy. Equation (9) is then used to obtain the 2nn coefficients. All the necessary DFT calculations to calculate the saddle-point bond coefficients were performed as part of the present work, and are given in Table (III).

The migration energies of SIA and mixed-interstitials, the activation energy for SIA rotation, as well as the correlation factors at different temperatures are taken from the literature, and listed in Table (IV).

#### 5. DFT calculations

Density functional theory calculations were carried out using the projector augmented wave (PAW) method [60, 61] as implemented in the Vienna *ab-initio* simulation package [62–65]. Since interstitial configurations involve short interatomic distances “hard” PAW setups that include semi-core electron states were employed with a plane wave energy cutoff of 300 eV.

Exchange and correlation effects were described using the generalized gradient approximation [66] while the occupation of electronic states was performed using the first order Methfessel-Paxton scheme with a smearing width of 0.2 eV. The Brillouin zone was sampled using  $5 \times 5 \times 5$   $\vec{k}$ -point grids. (A detailed discussion of the effect of different computational parameters on the results can be found in Ref. [46]). All structures were optimized allowing full relaxation of both ionic positions and cell shape with forces converged to below 10 meV/Å. Migration barriers were computed using  $4 \times 4 \times 4$  supercells and the climbing image-nudged elastic band method with three images [67].

### III. RESULTS

#### A. Structural phase diagrams

Although our energy model includes thermodynamic information reflective of the phase stability of W-Re alloys, the model consists of a rigid lattice with bcc structure and is thus suitable only for a given, well-defined, concentration range. Our DFT calculations yield bond energies that are consistent with stable solid solutions from zero to approximately 40% at. Re [27]. This is confirmed by way of sgMC simulations performed as a function of composition and temperature in  $64 \times 64 \times 64$  computational cells. Figure 3 shows the set of stable compositions obtained as a function of the chemical potential for several temperatures. The figure shows a clear jump in the Re concentration at a temperature of approximately 100 K. This is typically indicative of a phase boundary, as two distinct phases characterized by widely different solute concentrations seem to coexist at the same temperature and chemical potential. This may be indicative of a miscibility

<sup>4</sup> The only exception being the binding energy between an AA and an AB interstitial, which is assumed to be equal to the binding energy between two AA.

TABLE II. Bond energy coefficients with the equation used for their calculation, and the literature source.  $x$  is the local solute concentration

$\epsilon_{A-A}^{(1)}$	-1.5815	cohesive energy, eq. (9)	This work
$\epsilon_{A-A}^{(2)}$	-0.6672	cohesive energy, eq. (9)	This work
$\epsilon_{B-B}^{(1)}$	-1.4067	cohesive energy, eq. (9)	This work
$\epsilon_{B-B}^{(2)}$	-0.5935	cohesive energy, eq. (9)	This work
$\epsilon_{A-B}^{(1)}$	$-1.5090 - 0.0219x$	mixing energy	Ref. [27]
$\epsilon_{A-B}^{(2)}$	$-0.6366 - 0.0092x$	eq. (9)	Ref. [27]
$\epsilon_{A-V}^{(1)}$	-0.4898	formation energy, eq. (9)	This work
$\epsilon_{A-V}^{(2)}$	-0.2067	formation energy, eq. (9)	This work
$\epsilon_{B-V}^{(1)}$	$-0.4898 - 0.009432/x$	formation energy fitted to $\epsilon_{B-V}^{(1)} = a + b/x$	This work
$\epsilon_{B-V}^{(2)}$	$-0.3311 + 0.036x$	formation energy fitted to $\epsilon_{B-V}^{(2)} = a + bx$	This work
$\epsilon_{V-V}^{(1)}$	0.5873	1nn binding energy	This work
$\epsilon_{V-V}^{(2)}$	0.5566	2nn binding energy	This work
$\epsilon_{AA-A}^{(1)}$	0.1740	formation energy, eq. (9)	Ref. [46]
$\epsilon_{AA-A}^{(2)}$	0.0734	formation energy, eq. (9)	Ref. [46]
$\epsilon_{AB-A}^{(1)}$	0.1104	formation energy, eq. (9)	Ref. [46]
$\epsilon_{AB-A}^{(2)}$	0.0466	formation energy, eq. (9)	Ref. [46]
$\epsilon_{AA-B}^{(1)}$	-0.2750	binding energy	Ref. [46]
$\epsilon_{AA-B}^{(2)}$	-0.1160	eq. (9)	Ref. [46]
$\epsilon_{AB-B}^{(1)}$	-0.3486	binding energy	Ref. [49]
$\epsilon_{AB-B}^{(2)}$	-0.1470	eq. (9)	Ref. [49]
$\epsilon_{AA-AA}^{(1)}$	-0.1905	binding energy	Ref. [50]
$\epsilon_{AA-AA}^{(2)}$	-0.0804	eq. (9)	Ref. [50]
$\epsilon_{AA-AB}^{(1)}$	-0.2505	binding energy	Assumed <sup>(4)</sup>
$\epsilon_{AA-AB}^{(2)}$	-0.1057	eq. (9)	Assumed <sup>(4)</sup>
$\epsilon_{AB-AB}^{(1)}$	-1.3977	binding energy	Ref. [27]
$\epsilon_{AB-AB}^{(2)}$	-0.5897	eq. (9)	Ref. [27]

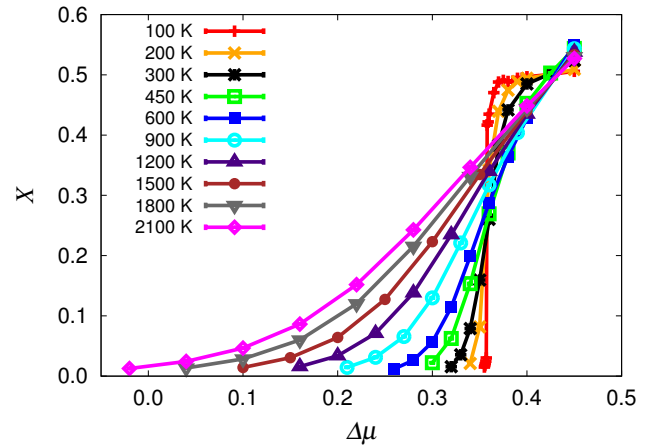
TABLE III. Saddle-point bond energy coefficients for vacancy jumps (in eV).

$\epsilon_{A-A}^{sp(1)}$	-2.5975	$\epsilon_{A-A}^{sp(2)}$	-0.5041
$\epsilon_{A-B}^{sp(1)}$	-2.6451	$\epsilon_{A-B}^{sp(2)}$	-0.5532
$\epsilon_{A-V}^{sp(1)}$	0.5465	$\epsilon_{A-V}^{sp(2)}$	0.1060
$\epsilon_{B-A}^{sp(1)}$	-2.5188	$\epsilon_{B-A}^{sp(2)}$	-0.4888
$\epsilon_{B-B}^{sp(1)}$	-2.5417	$\epsilon_{B-B}^{sp(2)}$	-0.4943
$\epsilon_{B-V}^{sp(1)}$	0.2902	$\epsilon_{B-V}^{sp(2)}$	0.0563

TABLE IV. Self-interstitial migration parameters. The jump distance for SIA migration is  $\delta = a_0\sqrt{3}/2$ .

$E_m^{AA}$	0.003	Ref. [25]
$E_r^{AA}$	0.43	Ref. [25]
$E_m^{AB}$	0.12	Ref. [27]
$f$	$2.93 - 0.00055T$	Ref. [45]

gap between Re concentrations of a few percent and approximately 50 at.%, *i.e.* beyond the thermodynamic validity of our rigid lattice model. To further characterize the configurations obtained, we calculate the short-range order (SRO) of

FIG. 3. Solute composition  $X$  as a function of chemical potential  $\Delta\mu$  at different temperatures.

the configurations obtained according to the Warren-Cowley

parameter [68]:

$$\eta = N_B^{-1} \sum_i^{N_B} \left( 1 - \frac{x_i(A)}{1-X} \right) \quad (28)$$

which gives the SRO parameter  $\eta$  of Re atoms w.r.t. matrix W atoms, with  $x_i(A)$  being the fraction of A atoms surrounding each solute atom  $i$ . The sum extends to all B atoms in the system.

According to this definition,  $\eta > 0$  implies phase separation,  $\eta = 0$  represents an ideal solid solution, and  $\eta < 0$  indicates ordering. However, the SRO parameter of a random solution has a range of  $-0.003$  to  $0.003$  regardless of solute composition due to the random occurrence of dimers, trimers, etc. Figure (4) shows the equilibrium SRO as a function of  $X$  for several temperatures. As the figure shows, the SRO parameter is near zero for dilute systems, and gradually becomes negative as the concentration increases. Based on the figure we conclude that equilibrium W-Re systems with up to  $\approx 40$  at.% solute content are consistent with random solid solutions with a weak tendency to ordering at higher concentrations. The corresponding  $T$ - $X$  phase diagram is provided in Figure 5.

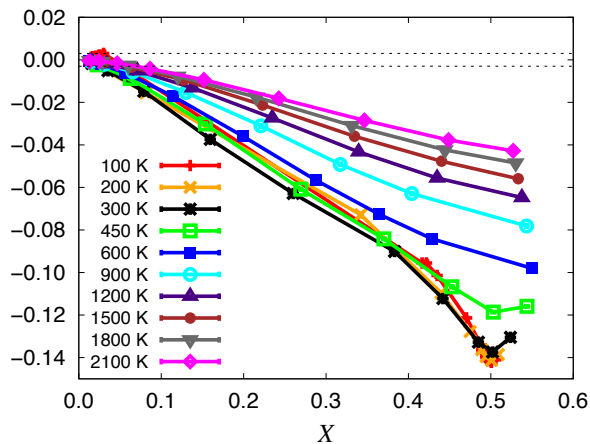


FIG. 4. Short range order parameter  $\eta$  as a function of global solute composition  $X$  at different temperatures. The dashed line indicate the SRO interval caused by normal concentration fluctuations during the generation of atomistic samples.

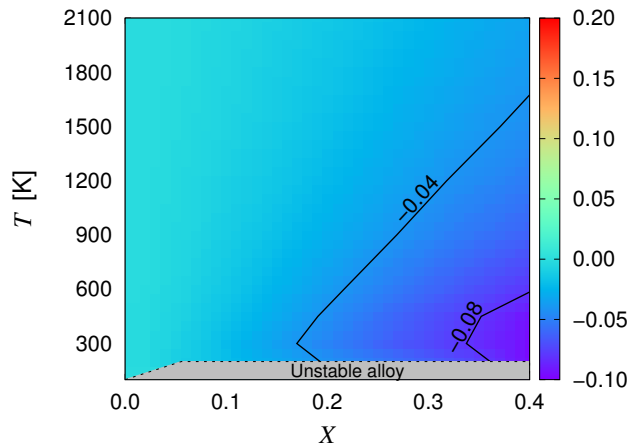


FIG. 5. Structural phase diagram showing regions of changing SRO. The dashed lines are the limits of applicability of the rigid bcc lattice model. The system displays slightly negative SRO throughout the entire temperature-concentration space, indicating a preference to be in a solid solution state.

### 1. Effect of vacancies on phase diagram

It is well known that non-equilibrium concentrations of defects can alter the thermodynamic behavior of an alloy. For the W-Re system, Wrobel *et al.* have studied the ternary W-Re-vacancy system and found that Re clustering occurs in the presence of non-thermodynamic vacancy concentrations [18]. Clusters appear as semi-ordered structures of alternating solute and vacancy planes—a necessity given the short-range repulsion between Re atoms on the one hand, and vacancies on the other (cf. Table I). Next, we carry out a similar study involving various vacancy concentrations, temperatures, and solute concentrations to obtain structural phase diagrams such as that shown in Fig. 5. Each configuration is optimized by combining sgMC steps with energy minimization steps following the process described in Sec. II C. Figure 6 shows the diagrams for vacancy concentrations of  $C_v = 0.01, 0.1, 0.2, 0.5$  at.% using  $64 \times 64 \times 64$  primitive cells.

As a representative example, Figure 7a shows the equilibrated configuration at 600 K, 1.8 at.% Re (which occurs for  $\Delta\mu = 0.26$ ), and  $C_v = 0.5$  at%. The figure shows several Re-vacancy clusters with an ordered structure, consistent with the study by Wrobel *et al.* [18]. Due to their ordered structure, these solute-vacancy clusters form only at Re concentrations that are commensurate with the vacancy concentration in the system, *i.e.* at values of  $X \lesssim 0.04$  in most cases.

### 2. Effect of interstitial defects on the phase diagram

Although vacancy concentrations such as those considered in this section are several orders of magnitude larger than the vacancy concentration in thermal equilibrium, one can expect such numbers under far-from-equilibrium conditions such as under high-dose or high-dose rate irradiation. The case is

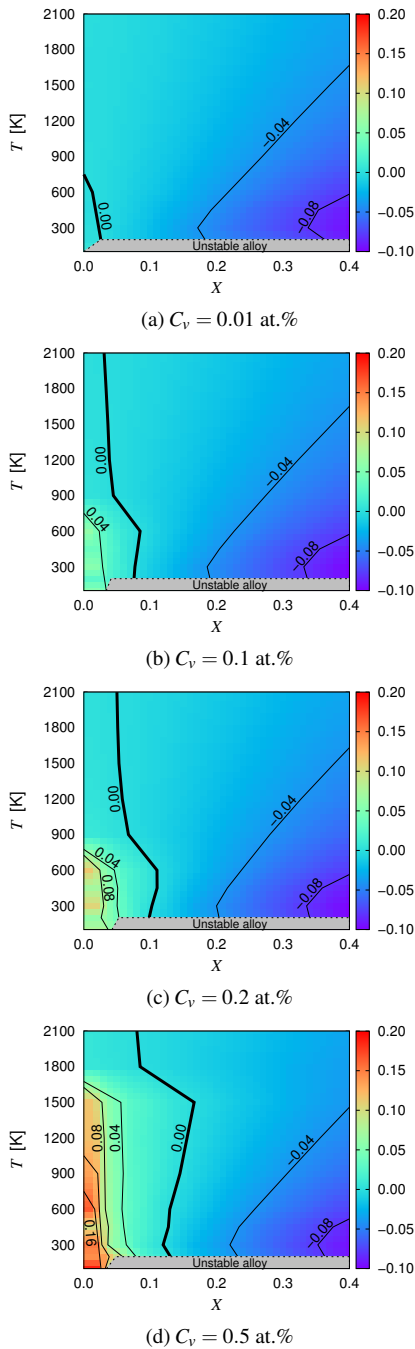
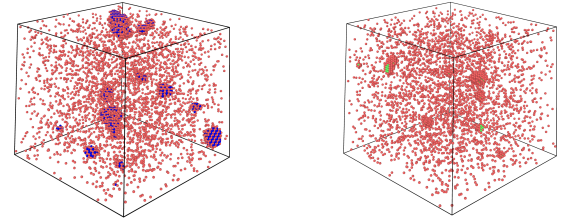


FIG. 6. Structural phase diagrams for four different vacancy concentrations. The diagrams clearly show the emergence of regions of solute segregation, characterized by positive SRO and a shifting of the transition phase boundary,  $\eta = 0$ , towards the right (higher concentrations).

much more difficult to make for SIAs due to their much higher formation energy (3.2 vs. 10.2 eV, to take two representative numbers [46]). However, given the inclination of single interstitials to convert into mixed dumbbells in the presence of solute, it is of interest to repeat the same exercise of looking at the clustering propensity of Re in such cases. The results are shown in Figure 8 for a defect concentration of



(a) W-1.8at%Re alloy, 0.5 at% vacancy concentration.

(b) W-1.4at%Re alloy, 0.1 at% mixed-interstitials.

FIG. 7. Equilibrated configurations for W-Re alloys containing different defect concentrations at 600 K. Red spheres represent Re atoms, colored blue or green ones represent the defect in each case.

0.1 at.%. The diagram reveals a stronger clustering tendency when interstitials are present compared to vacancies. Such an effect originates from both more attractive binding energies between mixed-interstitials and solute atoms, and between mixed-interstitials with themselves. A snapshot of the equilibrated atomistic configuration is shown in Fig. (7b), where the precipitates are seen to form platelet-like structures with a mixed dumbbell core surrounded by substitutional solute atoms.

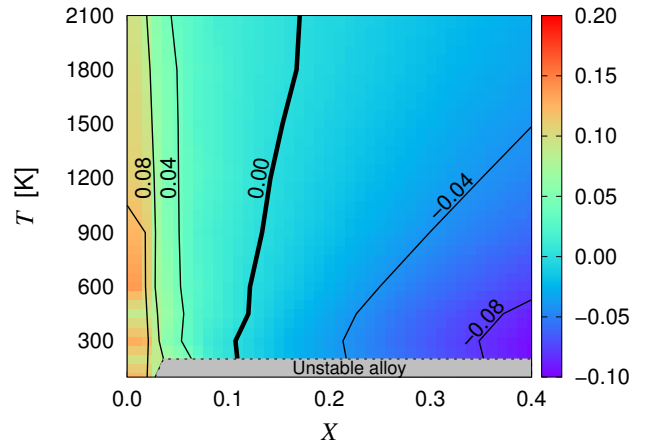


FIG. 8. Structural phase diagram for 0.1 at.% mixed-dumbbell concentration. The diagram shows the emergence of regions of solute segregation, characterized by  $\eta > 0$ , up to  $X = 0.1\%$ .

## B. Kinetic evolution of irradiated W-Re alloys

There are a number of factors that call for performing kMC simulations in W-Re systems.

1. First, equilibrium Monte Carlo calculations such as those performed in Section III A do not provide information about the precipitate nucleation and growth mechanisms, as well as the timescales involved.
2. Second, there is clear experimental evidence of Re-cluster formation in the absence of vacancies.

Hasegawa *et al.* [9, 69] and Hu *et al.* [10] have both reported the formation of W-Re intermetallic precipitates after high-dose, fast neutron irradiation. Moreover, recent irradiation experiments have revealed the formation of Re-rich clusters with bcc structure, *i.e.* prior to their conversion into  $\sigma$  and/or  $\chi$  precipitates. For example, Klimenkov *et al.* note that Re-rich particles not associated with cavities formed in neutron-irradiated single crystal W [19]. As well, using atom-probe tomography Xu *et al.* have performed detailed analyses of Re-rich atmospheres in bcc W without detecting significant numbers of vacancies [14].

3. New understanding regarding interstitial-mediated solute transport in W-Re alloys [26, 27], together with the results in Section III A 2, call for renewed simulation efforts incorporating these new mechanisms –in particular, the three-dimensional and associative nature of Re transport via mixed-dumbbell diffusion.

These considerations motivate the following detailed study of the Re precipitation kinetics under irradiation conditions. First, however, we proceed to calculate diffusion coefficients and transport coefficients for defect species and solute atoms.

### 1. Calculation of diffusion coefficients

Tracer diffusion coefficients (*i.e.*, in the absence of a concentration gradient) for vacancies, interstitials, and solute species in three dimensions are assumed to follow an Arrhenius temperature dependence:

$$D(T) = \nu f \delta^2 \exp\left(-\frac{E_a}{kT}\right) \quad (29)$$

where  $\nu$  is the so-called *attempt* frequency,  $f$  is the correlation factor,  $\delta$  is the jump distance,  $E_a$  is the activation energy, and  $D_0 = \nu f \delta^2$  is the so-called diffusion pre-factor. Defect diffusivities can be obtained directly from this equation, with  $E_a \equiv E_m$ . For solute diffusion the above expression must be multiplied times the probability of finding a vacancy in one of the 1nn positions, such that  $D_0 = z_1 \nu f \delta^2$  and  $E_a = E_m + E_f^V$ . However, to calculate the diffusivities of solutes and vacancies as a function of the global solute concentration, fluctuations in local chemistry prevent us from using equations for homogeneous systems such as eq. (29), and diffusivities must be obtained by recourse to *Einstein's* equation:

$$D = \frac{\langle \Delta r^2 \rangle}{6\Delta t} \quad (30)$$

where  $\langle \Delta r^2 \rangle$  is the *mean squared displacement* (msd) and  $\Delta t$  is the time interval. This formula assumes equilibrium defect concentrations, which are generally several orders of magnitude smaller than what a typical simulation cell can afford. For this reason, the time in eq. (30) is not directly the time clocked in the kMC simulations,  $\Delta t_{\text{kMC}}$ . Rather, it must be

rescaled by a coefficient that accounts for the difference in defect concentration [70, 71]:

$$\Delta t = \Delta t_{\text{kMC}} \frac{C^{\text{kMC}}}{C^{\text{eq}}} \quad (31)$$

where  $C^{\text{kMC}}$  and  $C^{\text{eq}}$  are the defect concentrations in the kMC simulations and in equilibrium, respectively. For simulations involving only one defect,  $C^{\text{kMC}}$  is simply equal to the inverse of the number of atoms in the computational cell,  $C^{\text{kMC}} = N^{-1}$ , while  $C^{\text{eq}} = \exp(-E_f/k_B T)$ , where  $E_f$  is the *instantaneous* defect formation energy, *i.e.* calculated accounting for the local chemical environment. This is the approach used for vacancy mediated diffusion, with  $E_f^V = \sum_i \epsilon_{V-\alpha_i}$ , where  $\alpha_i$  symbolizes the neighboring atoms forming a bond with the vacancy. During simulations of solute and vacancy diffusion,  $E_f^V$  is updated in every Monte Carlo time step and time rescaling is performed on the fly. The starting configuration for all calculations involving solute atoms is the equilibrated alloy as obtained in Section III A using sgMC simulations. The results for the vacancy and solute diffusivities,  $D_V$  and  $D_S$ , can be seen in Figure 9, while the parameters resulting from fitting the data points in the above figures to eq. (29) are collected in Table V. While  $D_V$  displays a moderate dependence with the solute concentration,  $D_V$  is quite insensitive to it.

TABLE V. Diffusion parameters for vacancy and solute diffusion as a function of solute concentration.

X [at. %]	$D_0$ [m <sup>2</sup> ·s <sup>-1</sup> ]	$E_m$ [eV]
Vacancy diffusion		
0.0 (eq. (29))	$4.84 \times 10^{-7}$	1.62
0.5	$6.86 \times 10^{-6}$	1.73
1.0	$6.92 \times 10^{-5}$	1.87
2.0	$1.26 \times 10^{-3}$	2.08
5.0	$2.57 \times 10^{-3}$	2.16
Solute diffusion		
0.0 (eq. (29))	$3.87 \times 10^{-6}$	$1.62 + 3.17 = 4.79$
0.5	$7.56 \times 10^{-7}$	4.67
1.0	$7.80 \times 10^{-7}$	4.67
2.0	$7.89 \times 10^{-7}$	4.66
5.0	$6.75 \times 10^{-7}$	4.59

As discussed in Sec. II E 4, self-interstitial migration occurs by way of fast sequences of  $\langle 111 \rangle$  transitions punctuated by sporadic rotations, whereas mixed dumbbell diffusion occurs via random  $\langle 100 \rangle$  hops in three dimensions. Interstitial diffusivities of both types can be calculated straightforwardly by using eq. (29) parameterized with the data in Table IV.

### 2. Calculation of transport coefficients

Within linear response theory, mass transport can be related to chemical potential gradients via Onsager's phenomenological coefficients. The value and sign of these transport coefficients can provide important physical information about the nature of solute and defect fluxes. On a discrete lattice, the transport coefficients  $L_{ij}$  coupling two diffusing species can

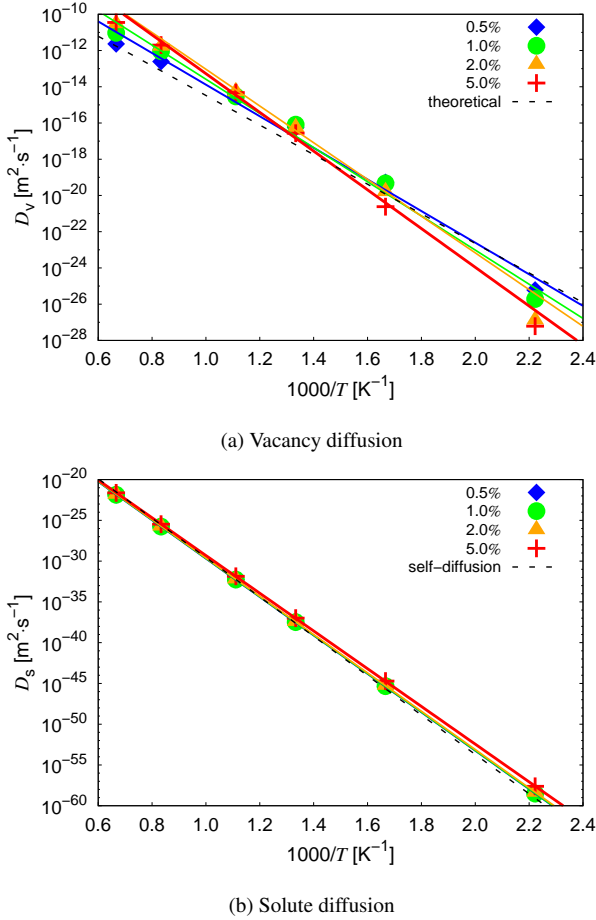


FIG. 9. Diffusivities of vacancies and solute atoms as a function of temperature and alloy concentration. The solid lines correspond to the Arrhenius fits shown in Table V, while the dashed line corresponds to eq. (29).

be calculated as [40, 72]:

$$L_{ij} = \frac{1}{6V} \frac{\langle \Delta r_i \Delta r_j \rangle}{\Delta t} \quad (32)$$

where  $V$  is the total volume of the system;  $\Delta r_i$  is the total displacement of species  $i$ , and  $\Delta t$  is the rescaled time. Here we focus on the relationship between solutes and vacancy and solute atoms,  $L_{B-B}$ , and  $L_{B-V}$ , as a function of temperature and solute content. Due to the associative transport mechanism of AB interstitials, the corresponding transport coefficient relating interstitials with solute atoms is always positive and we obviate its calculation. Figure 10a shows the results for  $L_{B-B}$ , which displays an Arrhenius temperature dependence and is always positive. The dependence with solute concentration is not significant up to 5%, with an average activation energy of 4.7 eV—very similar to the solute diffusion activation energy—and a prefactor of approximately  $3.9 \times 10^{20} \text{ m}^{-1} \cdot \text{s}^{-1}$ .  $L_{B-B}$  is by definition related to the solute diffusion coefficient presented above.

In Figure 10b we plot the ratio  $L_{B-V}/L_{B-B}$ . Two observations stand out directly from the figure. First, the value of

$L_{B-V}$  is always negative (the exception being at 450 K, when is almost zero). This indicates a reverse coupling between solutes and vacancies, *i.e.* vacancy fluxes would oppose solute fluxes. The implications of this calculation will become clearer when we study solute precipitation in the next section. Second,  $L_{B-V}$  is on average about an order of magnitude larger than  $L_{B-B}$ , which is to be expected for substitutional solutes moving by a vacancy mechanism.

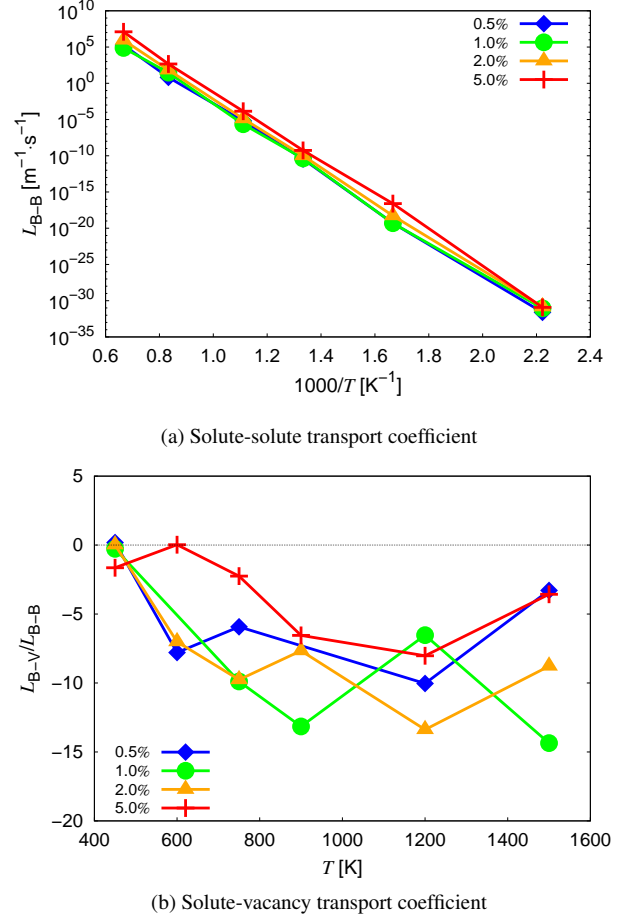


FIG. 10. Phenomenological transport coefficients for solute-solute and vacancy-solute interactions.

### 3. Kinetic Monte Carlo simulations

To narrow down the large parametric space associated with irradiation of W-Re alloys (Re concentration, temperature, dose, dose rate, etc.), we resort to the study performed in Secs. III A and III A 1. It was seen there that segregation occurs most favorably at low solute compositions. For this reason, and to enable comparison with the work by Xu *et al.* [13, 14], we choose a W-2.0% at. Re alloy for our study. By way of reference, this would correspond to the transmutation fraction attained after a dose of 12 dpa or 4 full-power years in DEMO's first wall according to Gilbert and Sublet [5]. When relatively high concentrations of defects are present—as one

might expect during irradiation—precipitation is also favored at high temperatures, so here we carry out our simulations between 1700 and 2000 K. We use box sizes of  $64^3$  and  $80^3$  with a damage insertion rate of  $10^{-3}$  dpa per second. As shown in Appendix A, the equivalence relation that exists between both box sizes enables us to compare them directly. The three different defect-sinks discussed in Sec. IID are all considered here.

We first investigate the kinetic evolution of a system with no sinks. Eight independent simulations were conducted. It is seen that after an average waiting time of  $\approx 21$  seconds (or  $\approx 0.02$  dpa) one precipitate starts to grow in all cases. This time can be regarded as the average *incubation* (nucleation) time for the conditions considered in the study. Figure 11 shows the mean size from all eight cases as a function of *growth* time, *i.e.* initializing the clock after the cluster nuclei are formed regardless of the observed incubation time. The dashed line in the figure is the associated spherical growth trend, which the precipitates are seen to follow for approximately 20 s. Subsequently, growth stops at a saturation radius of 4 nm, which is seen to be the stable precipitate size. A

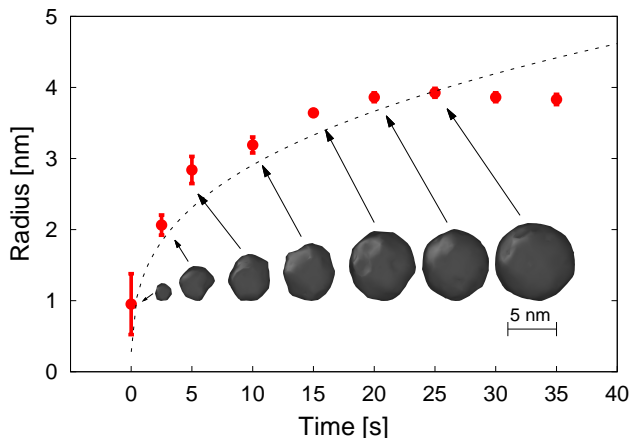


FIG. 11. Precipitate growth with time at 1800 K and  $10^{-3}$  dpa $\cdot$ s $^{-1}$  in a W-2.0% at. Re alloy. The dashed line represents perfect spherical growth (cf. A). A surface reconstruction rendition of one precipitate at various times is provided as inset.

surface reconstruction rendition of one of the precipitates is also provided in the figure as a function of time. This depiction as a compact convex shape is not intended to represent the true diffuse nature of the cluster, and is only shown as an indication of the cluster average size and shape.

The next question we address is the solute concentration inside the precipitate. Xu *et al.* [13, 14] have performed detailed atom probe analyses of radial concentration profiles at 573 and 773 K and find that the precipitates that form might be better characterized as ‘solute clouds’, reaching concentrations of around 30% in the center gradually declining as the radius increases. Our analysis is shown in Figure 12, with results averaged over the 8 cases tried here. The figure shows

that the concentration at the precipitate core (within the inner 1.5 nanometers) surpasses 50%—the thermodynamic limit for the formation of intermetallic phases—, which could provide the driving force for such a transformation. Because our energy model is not valid above the solid solution regime, we limit the interpretation of such phenomenon however. What is clear is that the precipitates are not fully-dense, even near their center. In fact, the relative solute concentration appears to diminish near the precipitate core once the saturation point has been reached.

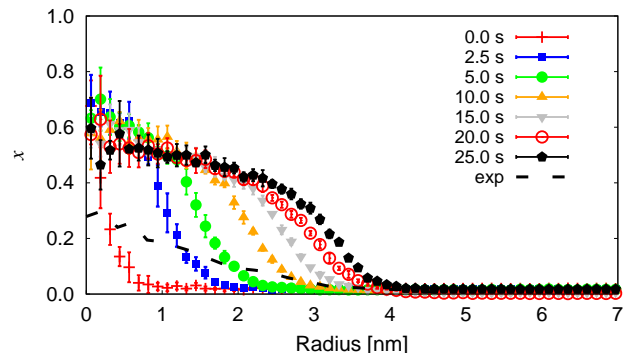


FIG. 12. Radial concentration profile as a function of time for the precipitates formed in the kMC simulations. The experimental results are taken from the work by Xu *et al.* [14].

Finally, we address the issue of whether it is vacancy or interstitial mediated transport that is primarily responsible for solute agglomeration and the formation of Re-rich clusters. To this end, we track the evolution with time of the incremental SRO change brought about by any given kMC event during the formation of one the precipitates discussed above. The results are given in Figure 13, where contributions from SIA and mixed interstitial jumps, vacancy jumps, and Frenkel pair insertion are plotted. These results conclusively demonstrate that mixed-interstitial transport is dominant among all other events to bring solute together. Vacancies, on the other hand, serve a dual purpose. They first act as a ‘hinge’ between solute atoms that would otherwise repel, much in the manner shown in Fig. 7a. This results in an initial positive contribution to the SRO, as shown in the inset to Fig. 13, by forming dimers, trimers, or other small solute clusters. However, once a critical nucleus forms and starts to grow, vacancies reverse this behavior and act to dissolve the precipitate (differential SRO turns negative in Fig. 13), mostly by making the precipitate/matrix interface more diffuse. As expected, Frenkel pair insertion has practically no effect on the overall precipitate evolution.

The precipitate grows by a sustained capture of mixed interstitials and subsequent attraction of vacancies. This gives rise to localized recombination at the precipitate, which makes the precipitates incorporate solute atoms over time. Figure 14 shows the spatial location of the recombination events during a period of 2.0 s before, during, and after precipitate growth. The figure clearly shows that, once formed, the precipitate becomes a preferential site for recombinations, which results

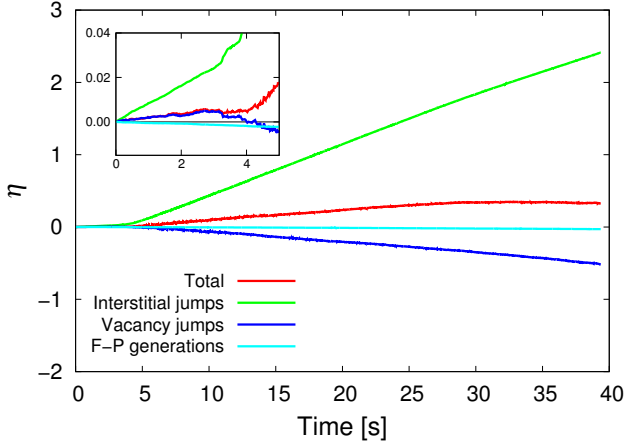


FIG. 13. Evolution of the differential SRO during the nucleation and growth in the kMC simulations.

in further growth and eventually in saturation. Because the primary source of solute is via interstitial transport, which also brings W atoms, the precipitates are never fully compact ( $x \sim 1$ ). Instead, maximum concentrations of around 50% are seen near the center when the precipitates reach their saturation size of 4-nm radius. As we will discuss in the next section, this is consistent with experimental measurements and observations of both coherent bcc clusters and incoherent  $\sigma$  and  $\chi$  phases.

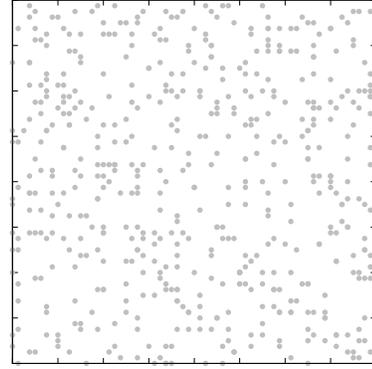
Simulations performed with defect sinks in the same temperature range simply result in solute segregation in the manner described in our previous work [28]. Radiation induced precipitation results from the onset of defect fluxes to the sinks, providing sufficient competition to delay the formation of bulk precipitates beyond the time scales coverable in our kMC simulations. More information is provided in the Supplementary Information.

## IV. DISCUSSION AND CONCLUSIONS

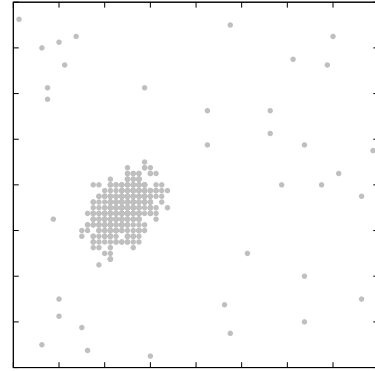
### A. Mechanism of nucleation and growth

On the basis of our results, the sequence of events that leads to the formation of Re-rich precipitates in irradiated W-2Re (at%) alloys is as follows:

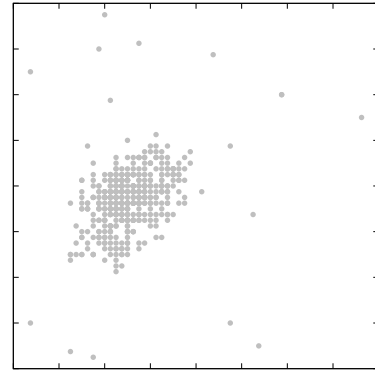
1. First, a Frenkel pair is inserted in the computational box following the procedure specified in Sec. II D. As interstitials enter the system, they perform a one-dimensional migration until they encounter a solute atom, after which they become mixed AB dumbbells capable of transporting solute in 3D. As these mixed dumbbells diffuse throughout the lattice, they encounter substitutional solute atoms and become trapped forming a B-AB complex with a binding energy of 0.15 eV (cf. Table I).
2. The vacancy in the Frenkel pair migrates throughout the



(a) During cluster nucleation.



(b) During precipitate growth



(c) After size saturation.

FIG. 14. Spatial distribution of recombination events for several stages of precipitate evolution.

lattice contributing to the formation of small Re complexes (dimers, trimers, tetramers, etc.). Vacancy motion does not necessarily imply solute drag, as indicated by the negative value of transport coefficients in Sec. III B 2. However, as the evidence from the Metropolis Monte Carlo simulations in Fig. 6 suggests, they can form small complexes of stable Re-V clusters.

3. The vacancy can become locally trapped in the small Re-V complexes mentioned above. However, at the high temperatures considered here, it is likely to de-trap and continue migrating until it finds the immobilized interstitial from (1), as this provides the largest thermodynamic driving force to reduce the energy of the crystal. When the vacancy and the interstitial meet, another small V-Re cluster is formed. Throughout this process, both mixed interstitial and vacancy hops are characterized by an increasing differential SRO parameter (cf. Fig. 13).
4. Eventually, one of these Re clusters grows larger than the rest due to natural fluctuations. When that happens the likelihood that the V-AB recombination will take place at that larger cluster grows. This signals the onset of the growth process, fueled by continued attraction of AB mixed dumbbells and the subsequent associated recombination. At this stage, vacancies reverse their role as solute-atom ‘hinges’ and begin to contribute to cluster dissolution (negative differential SRO parameter in Fig. 13). This results in the development of a more or less diffuse interface as the precipitate grows, which delays the next recombination event and slows down growth.
5. Although the precipitate continues to be the main pole of attraction for vacancy-interstitial recombinations (cf. Fig. 14), the system reaches a point where most of the solute is consumed into a diffuse precipitate that halts further growth. Vacancies then have more time to interact with the interface atoms before the next recombination event, which results in a smearing of the precipitate interface. In the absence of sinks, or other precipitates, the existing cluster is the sole focus of solute agglomeration, which allows it grow to its maximum size for the current alloy content of 2% Re. It is to be expected that with competing solute sinks, the precipitates might either be slightly smaller in size or less solute-dense internally.

This qualitative explanation is built on direct evidence and interpretation from our results, described in detail in Sec. III. However, to support some of the above points more explicitly, we provide additional details as Supplementary Information.

Interestingly, the essential features of our mechanism were originally proposed by Herschitz and Seidman [23, 24] on the basis of atom probe observations of neutron-irradiated W-25Re alloys. Remarkably, these authors had the intuition to propose the basic elements needed to lead to Re precipitate formation identified in our work with the more limited understanding available at the time.

### B. Brief discussion on the validity of our results

Our simulations are based on a highly-optimized implementation of the standard kMC algorithm. With the computational resources available to us, we can reasonably simulate

systems with less than 500,000 atoms into timescales of tens of seconds. This has proven sufficient to study Re clustering at high temperatures, where vacancy mobility is high and comparable to mixed-interstitial mobility. Recall from the previous section that the formation of clusters is predicated on the concerted action of both defect species, with mixed interstitials becoming trapped at small Re clusters followed by a recombination with a vacancy that makes the cluster grow over time. Clustering and precipitation of Re in irradiated W has been seen at temperatures sensibly lower than those explored here, such as 573 and 773 K for ion-irradiated W-Re [13, 14, 73], 773 and 1073 K for neutron irradiated W in HFIR [10], 1173 K in neutron irradiated W in the HFR reactor [19], and Williams et al. at 973~1173 K in EBR-II [22]. The work by Hasegawa *et al.* in JOYO [9, 74] does cover –by contrast– a similar temperature range as ours. The principle is that the mechanism proposed here can be conceivably extended to lower temperatures without changes with just a timescale adjustment due to the significantly slower mobility of vacancies at those temperatures. This would require simulated times that are far too long to cover with kMC.

An intrinsic limitation of our model is that it is based on a rigid bcc lattice and cannot thus capture the transition of precipitates to the intermetallic phase. As such, our model does not necessarily reflect the true microstructural state when the local concentration surpasses 40~50%, which is when phase coexistence is expected to occur according to the phase diagram [75]. However, our simulations are useful to determine the kinetic pathway towards the accumulation of Re concentrations in the vicinity of that amount. Neutron irradiation experiments such as those performed at JOYO and HFIR reveal the formation of acicular  $\sigma$  and  $\chi$  precipitates [9, 10, 22, 74], which presumably indicates reaching local values of Re concentration of or higher than 40~50% at the site of precipitate formation. However, in controlled ion irradiation experiments [13, 14, 73] there is clear evidence that the precursor to the formation of these intermetallic precipitates are non-compact Re-rich clusters with bcc structure. We cannot but speculate how the transition from these solute-rich clusters to well-defined line compounds  $\sigma$  and  $\chi$  takes place (perhaps via a martensitic transformation, as in Fe-Cu systems [76]), but it is clear that it is preceded by the nucleation and growth of coherent Re clusters. In our simulations, we find that the clusters have a maximum concentration of  $\approx 50\%$  in the center, in contrast with Xu *et al.*, who observe concentrations no larger than 30%. This disparity may simply be a consequence of the different temperatures considered relative to our simulations (773 vs 1800 K), as it is expected that the accumulation of solute by the mechanism proposed here will be accelerated by temperature.

As well, our Re clustering mechanism is predicated on the insertion of Frenkel pairs, when it is well known that fast neutron and heavy-ion irradiation generally result in the formation of clusters of vacancies and interstitials directly in displacement cascades. However, even here tungsten is somewhat of a special case. Recent work [77–79] suggests that most of the defects in high-energy (>150 keV) cascades in W appear in the form of isolated vacancies and interstitials.

This, together with the fact that most displacement cascades for non-fusion neutrons and heavy ions have energies well below the 150-keV baseline, gives us confidence that our mechanism would be operative even in such scenarios.

### C. Implications of our study

Beyond the obvious interest behind understanding the kinetics of Re-cluster formation in irradiated W-Re alloys, our model is useful to interpret other physical phenomena. For example, it is well known that swelling is suppressed in irradiated W-Re alloys compared to pure W [20]. By providing enhanced avenues for interstitial-vacancy recombination, small Re clusters capture mixed interstitials, allowing sufficient time for vacancies to subsequently find them and suppressing the onset of swelling. Intrinsic 3D mobility of mixed dumbbells is likely to favor recombination as well. Note that this explanation for swelling suppression is different to the one proposed for Fe-Cr alloys, where 1D migration of SIAs is restrained by Cr atoms [80].

Finally, the mechanisms proposed here refer to homogeneous nucleation, *i.e.* Re clustering occurs without any assistance from RED or RIP, and hence without the need for defect sinks. This is again a remarkable feature of these alloys, confirmed in several studies [14, 19, 24]. As noted by Herschitz and Seidman, “The coherent precipitates were not associated with either linear or planar defects or with any impurity atoms; *i.e.* a true homogeneous radiation-induced precipitation occurs in this alloy”, or by Klimenkov *et al.*, who point out that “The formation of Re-rich particles with a round shape was detected in the single crystal material. These particles were formed independently of cavities”. We leave out heterogeneous precipitation at voids, as the evidence in the literature is conflicting at this stage: discounted in some works [14, 24] and observed in others [19].

### ACKNOWLEDGEMENTS

C. H., Y. Z., and J. M.’s work has been supported by the US Department of Energy’s Office of Fusion Energy Sciences, grant DE-SC0012774:0001. Computer time allocations at UCLA’s IDRE Hoffman2 supercomputer are also acknowledged. L. G. and P. E. acknowledge support from the Swedish Research Council in the form of a Young Researcher grant, and the European Research Council via a Marie Curie Career Integration Grant. Computer time allocations by the Swedish National Infrastructure for Computing at NSC (Linköping) and C3SE (Gothenburg) are gratefully acknowledged.

### Appendix A: Size dependence of physical time in kMC simulations

As explained in Section IV, the mechanism of formation of Re clusters requires the concerted action of both interstitials and vacancies. In order to be able to capture their formation during reasonable computational times, the temperature regime considered must be one where the mobility of both species is comparable (1700 ~ 2000 K in our case). Then, the rate of arrival of solute atoms to a previously-nucleated Re cluster can be approximated by:

$$r_s = \frac{1}{t_{FP} + t_{diff}} \quad (\text{A1})$$

where  $t_{FP}$  and  $t_{diff}$  are the average time in between successive Frenkel-pair insertions and a characteristic diffusion time required by a vacancy and an interstitial to recombine with one another.  $r_s$  is measured in units of atoms per unit time. At the temperatures and dose rates considered here,  $t_{FP} \gg t_{diff}$ , such that  $r_s \approx t_{FP}^{-1}$ . Assuming then that for each Frenkel pair inserted a minimum of one solute atom is transported:

$$r_s = \frac{dN_B}{dt} = r_{dpa}N \quad (\text{A2})$$

where  $N_B$  is the total number of solute atoms in the precipitate.  $r_{dpa}$  in the above equation is the damage rate, expressed in units of [dpa·s<sup>-1</sup>]. The precipitate volume growth rate is directly equal to the atomic volume times  $r_s$ :

$$\dot{V}_{ppt} = \Omega_a r_s = \Omega_a \frac{dN_B}{dt} = \Omega_a r_{dpa}N \quad (\text{A3})$$

Assuming that the precipitate is close to spherical:

$$\dot{V}_{ppt} = 4\pi R_{ppt}^2 \dot{R}_{ppt} = \Omega_a r_{dpa}N$$

And, operating, we arrive at the equation for the evolution of the precipitate radius with time:

$$R_{ppt} = \left( \frac{\Omega_a r_{dpa} N t}{4\pi} \right)^{\frac{1}{3}} \quad (\text{A4})$$

which is the equation used for fitting in Fig. 11.

Then, from eq. (A2), for a given constant dpa rate, it is clear that the ratio  $r_s(V_1)N_1^{-1} = r_s(V_2)N_2^{-1} = \text{constant}$ , where  $V_1$  and  $V_2$  are two different box sizes. For as long as the approximation in eq. (A1) is valid, then:

$$t_{FP}^{(1)}N_1 = t_{FP}^{(2)}N_2 = \text{constant}$$

which allows us to compare simulations done on box sizes of 64<sup>3</sup> and 80<sup>3</sup> directly. We emphasize that at lower temperatures, and/or high dose rate, where  $t_{FP} \approx t_{diff}$ , this comparison is no longer valid.

### REFERENCES

- [1] S. J. Zinkle and N. M. Ghoniem, *Fusion Engineering and Design* **51–52**, 55 (2000).
- [2] M. Rieth, S. L. Dudarev, S. M. Gonzalez de Vicente, J. Aktaa, T. Ahlgren, S. Antusch, D. E. J. Armstrong, M. Balden, N. Baluc, M. F. Barthe, W. W. Basuki, M. Battabyal, C. S. Becquart, D. Blagoeva, H. Boldyryeva, J. Brinkmann, M. Celino, L. Ciupinski, J. B. Correia, A. De Backer, C. Domain, E. Gaganidze, C. García-Rosales, J. Gibson, M. R. Gilbert, S. Giusepponi, B. Gludovatz, H. Greuner, K. Heinola, T. Höschen, A. Hoffmann, N. Holstein, F. Koch, W. Krauss, H. Li, S. Lindig, J. Linke, C. Linsmeier, P. López-Ruiz, H. Maier, J. Matejcek, T. P. Mishra, M. Muhammed, A. Muñoz, M. Muzyk, K. Nordlund, D. Nguyen-Manh, J. Opschoor, N. Ordás, T. Palacios, G. Pintsuk, R. Pippan, J. Reiser, J. Riesch, S. G. Roberts, L. Romaner, M. Rosiński, M. Sanchez, W. Schulmeyer, H. Traxler, A. Ureña, J. G. van der Laan, L. Veleva, S. Wahlberg, M. Walter, T. Weber, T. Weitkamp, S. Wurster, M. A. Yar, J. H. You, and A. Zivelonghi, *J. Nucl. Mater.* **432**, 482 (2013).
- [3] S. P. Fitzgerald and D. Nguyen-Manh, *Phys. Rev. Lett.* **101**, 115504 (2008).
- [4] C. S. Becquart and C. Domain, *J. Nucl. Mater.* **385**, 223 (2009).
- [5] M. R. Gilbert and J.-C. Sublet, *Nuclear Fusion* **51**, 043005 (2011).
- [6] M. R. Gilbert, S. L. Dudarev, S. Zheng, L. W. Packer, and J.-C. Sublet, *Nuclear Fusion* **52**, 083019 (2012).
- [7] J. He, G. Tang, A. Hasegawa, and K. Abe, *Nuclear fusion* **46**, 877 (2006).
- [8] T. Tanno, A. Hasegawa, J. C. He, M. Fujiwara, M. Satou, S. Nogami, K. Abe, and T. Shishido, *J. Nucl. Mater.* **386–388**, 218 (2009).
- [9] A. Hasegawa, T. Tanno, S. Nogami, and M. Satou, *J. Nucl. Mater.* **417**, 491 (2011).
- [10] X. Hu, T. Koyanagi, M. Fukuda, N. K. Kumar, L. L. Snead, B. D. Wirth, and Y. Katoh, *Journal of Nuclear Materials* **480**, 235 (2016).
- [11] X. Hu, T. Koyanagi, Y. Katoh, M. Fukuda, B. D. Wirth, and L. L. Snead, “Defect evolution in neutron-irradiated single crystalline tungsten,” (2015), DOE/ER-0313/58-Semiannual Progress Report, June 30, 2015.
- [12] G. Cottrell, *Journal of nuclear materials* **334**, 166 (2004).
- [13] A. Xu, C. Beck, D. E. Armstrong, K. Rajan, G. D. Smith, P. A. Bagot, and S. G. Roberts, *Acta Materialia* **87**, 121 (2015).
- [14] A. Xu, D. E. Armstrong, C. Beck, M. P. Moody, G. D. Smith, P. A. Bagot, and S. G. Roberts, *Acta Materialia* **124**, 71 (2017).
- [15] G. S. Was, *Fundamentals of radiation materials science: metals and alloys* (Springer Science & Business Media, 2007).
- [16] G. J. Dienes and A. Damask, *Journal of Applied Physics* **29**, 1713 (1958).
- [17] R. Cauvin and G. Martin, *Journal of Nuclear Materials* **83**, 67 (1979).
- [18] J. S. Wrobel, D. Nguyen-Manh, K. J. Kurzydowski, and S. L. Dudarev, *ArXiv e-prints* (2016), arXiv:1604.03746 [cond-mat.mtrl-sci].
- [19] M. Klimenkov, U. Jntsch, M. Rieth, H. Schneider, D. Armstrong, J. Gibson, and S. Roberts, *Nuclear Materials and Energy*, (2016).
- [20] J. Matolich, H. Nahm, and J. Motteff, *Scripta Metallurgica* **8**, 837 (1974).
- [21] V. Sikka and J. Motteff, *Metallurgical and Materials Transactions B* **5**, 1514 (1974).
- [22] R. K. Williams, F. W. Wiffen, J. Bentley, and J. O. Stiegler, *Metall. Trans. A* **14**, 655 (1983).
- [23] R. Herschitz and D. Seidman, *Acta Metallurgica* **32**, 1155 (1984).
- [24] R. Herschitz and D. N. Seidman, *Nuclear Instruments and Methods in Physics Research Section B: Beam Interactions with Materials and Atoms* **7**, 137 (1985).
- [25] T. Suzudo, M. Yamaguchi, and A. Hasegawa, *Modelling and Simulation in Materials Science and Engineering* **22**, 075006 (2014).
- [26] T. Suzudo, M. Yamaguchi, and A. Hasegawa, *Journal of Nuclear Materials* **467, Part 1**, 418 (2015).
- [27] L. Gharaee, J. Marian, and P. Erhart, *Journal of Applied Physics* **120**, 025901 (2016), <http://dx.doi.org/10.1063/1.4956377>.
- [28] C.-H. Huang and J. Marian, *Journal of Physics: Condensed Matter* **28**, 425201 (2016).
- [29] K. Binder, J. L. Lebowitz, M. K. Phani, and M. H. Kalos, *Acta Metallurgica* **29**, 1655 (1981).
- [30] B. Dunweg and D. P. Landau, *Physical Review B* **48**, 14182 (1993).
- [31] C. Pareige, F. Soisson, G. Martin, and D. Blavette, *Acta Materialia* **47**, 1889 (1999).
- [32] F. Tavazza, D. P. Landau, and J. Adler, *Physical Review B* **70**, 184103 (2004).
- [33] L. Cannavacciuolo and D. P. Landau, *Physical Review B* **71**, 134104 (2005).
- [34] A. Biborski, L. Zosiak, R. Kozubski, R. Sot, and V. Pierron-Bohnes, *Intermetallics* **18**, 2343 (2010).
- [35] W. M. Young and E. W. Elcock, *Proceedings of the Physical Society* **89**, 735 (1966).
- [36] F. Soisson, C. S. Becquart, N. Castin, C. Domain, L. Malerba, and E. Vincent, *Journal of Nuclear Materials* **406**, 55 (2010).
- [37] F. Soisson, A. Barbu, and G. Martin, *Acta Materialia* **44**, 3789 (1996).
- [38] F. Soisson and C. Fu, *Physical Review B* **76**, 214102 (2007).
- [39] E. Martínez, O. Senninger, C. Fu, and F. Soisson, *Physical Review B* **86**, 224109 (2012).
- [40] O. Senninger, F. Soisson, E. Martínez, M. Nastar, C. Fu, and Y. Brechet, *Acta Materialia* **103**, 1 (2016).
- [41] F. G. Djurabekova, L. Malerba, C. Domain, and C. S. Becquart, *Nuclear Instruments and Methods in Physics Research Section B: Beam Interactions with Materials and Atoms* **255**, 47 (2007).
- [42] E. Vincent, C. S. Becquart, and C. Domain, *Journal of Nuclear Materials* **382**, 154 (2008).
- [43] E. Vincent, C. S. Becquart, C. Pareige, P. Pareige, and C. Domain, *Journal of Nuclear Materials* **373**, 387 (2008).
- [44] C. Reina, J. Marian, and M. Ortiz, *Physical Review B* **84** (2011), 10.1103/PhysRevB.84.104117.
- [45] W. Zhou, Y. Li, L. Huang, Z. Zeng, and X. Ju, *Journal of Nuclear Materials* **437**, 438 (2013).
- [46] L. Gharaee and P. Erhart, *Journal of Nuclear Materials* **467, Part 1**, 448 (2015).
- [47] F. Soisson, *Journal of Nuclear Materials* **349**, 235 (2006).
- [48] P. Warczok, J. Ženíšek, and E. Kozeschnik, *Computational Materials Science* **60**, 59 (2012).
- [49] W. Setyawan, G. Nandipati, and R. J. Kurtz, *Interaction of interstitial clusters with rhenium, osmium, and tantalum in tungsten*, Tech. Rep. DOE/ER-0313/60 (2016).
- [50] C. Becquart, C. Domain, U. Sarkar, A. DeBacker, and M. Hou, *Journal of Nuclear Materials* **403**, 75 (2010).

- [51] D. Kato, H. Iwakiri, and K. Morishita, *Journal of Nuclear Materials* **417**, 1115 (2011).
- [52] W. L. Bragg and E. J. Williams, *Proceedings of the Royal Society of London A: Mathematical, Physical and Engineering Sciences* **145**, 699 (1934), <http://rspa.royalsocietypublishing.org/content/145/855/699.full.pdf>.
- [53] W. L. Bragg and E. J. Williams, *Proceedings of the Royal Society of London A: Mathematical, Physical and Engineering Sciences* **151**, 540 (1935), <http://rspa.royalsocietypublishing.org/content/151/874/540.full.pdf>.
- [54] E. J. Williams, *Proceedings of the Royal Society of London. Series A, Mathematical and Physical Sciences* **152**, 231 (1935).
- [55] C. Becquart and C. Domain, *Nuclear Instruments and Methods in Physics Research Section B: Beam Interactions with Materials and Atoms* **255**, 23 (2007), computer Simulation of Radiation Effects in Solids Proceedings of the Eighth International Conference on Computer Simulation of Radiation Effects in Solids (COSIRES 2006) Computer Simulation of Radiation Effects in Solids.
- [56] L. Ventelon, F. Willaime, C.-C. Fu, M. Heran, and I. Ginoux, *Journal of Nuclear Materials* **425**, 16 (2012).
- [57] M. Muzyk, D. Nguyen-Manh, K. J. Kurzydłowski, N. L. Baluc, and S. L. Dudarev, *Phys. Rev. B* **84**, 104115 (2011).
- [58] Y. Oda, A. M. Ito, A. Takayama, and H. Nakamura, *Plasma and Fusion Research* **9**, 3401117 (2014).
- [59] M. R. Gilbert, S. L. Dudarev, P. M. Derlet, and D. G. Pettifor, *Journal of Physics: Condensed Matter* **20**, 345214 (2008).
- [60] P. E. Blöchl, *Phys. Rev. B* **50**, 17953 (1994).
- [61] G. Kresse and D. Joubert, *Phys. Rev. B* **59**, 1758 (1999).
- [62] G. Kresse and J. Hafner, *Phys. Rev. B* **47**, 558 (1993).
- [63] G. Kresse and J. Hafner, *Phys. Rev. B* **49**, 14251 (1994).
- [64] G. Kresse and J. Furthmüller, *Phys. Rev. B* **54**, 11169 (1996).
- [65] G. Kresse and J. Furthmüller, *Comput. Mater. Sci.* **6**, 15 (1996).
- [66] J. P. Perdew, K. Burke, and M. Ernzerhof, *Phys. Rev. Lett.* **77**, 3865 (1996), erratum, *ibid.* **78**, 1396(E) (1997).
- [67] G. Henkelman, B. P. Uberuaga, and H. Jónsson, *J. Chem. Phys.* **113**, 9901 (2000).
- [68] J. M. Cowley, *Phys. Rev.* **77**, 669 (1950).
- [69] T. Tanno, A. Hasegawa, J.-C. He, M. Fujiwara, S. Nogami, M. Satou, T. Shishido, and K. Abe, *Mater. Trans.* **48**, 2399 (2007).
- [70] Y. L. Bouar and F. Soisson, *Physical Review B* **65**, 094103 (2002).
- [71] M. Nastar and F. Soisson, *Physical Review B* **86**, 220102 (2012).
- [72] A. Allnatt and A. Lidiard, *Atomic Transport in Solids* (Cambridge University Press, 2003).
- [73] P. D. Edmondson, A. Xu, L. R. Hanna, M. Dagan, S. G. Roberts, and L. L. Snead, *Microscopy and Microanalysis* **21**, 579 (2015).
- [74] T. Tanno, A. Hasegawa, M. Fujiwara, J.-C. He, S. Nogami, M. Satou, T. Shishido, and K. Abe, *Mater. Trans.* **49**, 2259 (2008).
- [75] M. Ekman, K. Persson, and G. Grimvall, *Journal of Nuclear Materials* **278**, 273 (2000).
- [76] P. Erhart, J. Marian, and B. Sadigh, *Phys. Rev. B* **88**, 024116 (2013).
- [77] A. E. Sand, S. L. Dudarev, and K. Nordlund, *EPL (Europhysics Letters)* **103**, 46003 (2013).
- [78] X. Yi, A. E. Sand, D. R. Mason, M. A. Kirk, S. G. Roberts, K. Nordlund, and S. L. Dudarev, *EPL (Europhysics Letters)* **110**, 36001 (2015).
- [79] W. Setyawan, G. Nandipati, K. J. Roche, H. L. Heinisch, B. D. Wirth, and R. J. Kurtz, *Journal of Nuclear Materials* **462**, 329 (2015).
- [80] D. Terentyev, L. Malerba, and A. Barashev, *Philosophical magazine letters* **85**, 587 (2005).

# Paper IV

**Finite-temperature properties of non-magnetic transition metals: Comparison of the performance of constraint-based semi and nonlocal functionals**

Leili Gharaee, Paul Erhart and Per Hyldgaard

Physical Review B 95, 085147 (2017)



# Finite-temperature properties of nonmagnetic transition metals: Comparison of the performance of constraint-based semilocal and nonlocal functionals

Leili Gharaee and Paul Erhart\*

*Chalmers University of Technology, Department of Physics, Gothenburg, Sweden*

Per Hyldgaard†

*Chalmers University of Technology, Department of Microtechnology and Nanoscience, MC2, Gothenburg, Sweden*

(Received 2 December 2016; published 27 February 2017)

We assess the performance of nonempirical, truly nonlocal, and semilocal functionals with regard to structural and thermal properties of  $3d$ ,  $4d$ , and  $5d$  nonmagnetic transition metals. We focus on constraint-based functionals and consider the consistent-exchange van der Waals density-functional version vdW-DF-cx [Phys. Rev. B **89**, 035412 (2014)], the semilocal PBE functional [Phys. Rev. Lett. **77**, 3865 (1996)], and the PBEsol functional [Phys. Rev. Lett. **100**, 136406 (2008)], as well as the AM05 metafunctional [Phys. Rev. B **72**, 085108 (2005)]. Using the quasiharmonic approximation, the structural parameters, elastic response, and thermal expansion at finite temperatures are computed and compared to experimental data. We also compute cohesive energies explicitly including zero-point vibrations. It is shown that overall vdW-DF-cx provides an accurate description of thermal properties and retains a level of transferability and accuracy that is comparable to or better than some of the best constraint-based semilocal functionals. Especially, with regard to the cohesive energies, the consistent inclusion of spin-polarization effects in the atoms turns out to be crucial, and it is important to use the rigorous spin-vdW-DF-cx formulation [Phys. Rev. Lett. **115**, 136402 (2015)]. This demonstrates that vdW-DF-cx has general-purpose character and can be used to study systems that have both sparse and dense electron distributions.

DOI: [10.1103/PhysRevB.95.085147](https://doi.org/10.1103/PhysRevB.95.085147)

## I. INTRODUCTION

The adiabatic connection formula (ACF) enables a formal determination of all exchange-correlation (XC) effects in density-functional theory (DFT) [1–3]. The XC energy density functional (DF)  $E_{xc}$  can be seen as the electrostatic binding of electrons with its associated XC hole. Good  $E_{xc}$  approximations represent the core of DFT, and  $E_{xc}$  formulations reflect insight pertaining to the collective response of the interacting electron gas [2,3]. Important progress was achieved by enforcing hole conservation and other physical constraints in the formulation of the local density approximation (LDA) as well as semilocal functionals based on the generalized gradient approximation (GGA). Hole conservation underpins, for example, the PBE functional [4], that has proven to be highly successful as a general-purpose functional for problems in which physical behavior is governed by the response at large electron concentrations. Specifically, the PBE functional is accurate for both hard materials and individual molecules, and accordingly it has found widespread applications [5].

The past decade has witnessed the successful introduction of the van der Waals (vdW) density-functional (vdW-DF) method [6–10], launched as a systematic extension [11–13] of the LDA and the GGA. Unlike local and semilocal functionals such as the latter two, it describes also the much larger class of sparse systems [14], e.g., molecular solids, layered materials, and weak chemisorption cases, in which binding across

internal voids arises from a truly nonlocal, vdW-type binding. The Chalmers-Rutgers vdW-DF method is focused on the electron response and has both regular releases (vdW-DF1 [7], vdW-DF2 [15], and vdW-DF-cx [16]) and variants (including vdW-DF-C09 [17], optB88, optPBE [18], optB86b [19], and rev-vdW-DF2 [20]). It has recently been extended with a rigorous spin formulation that reflects the vdW-DF design logic [21]. There are also related but alternative formulations of the nonlocal-correlation term in the Vydrov–van Voorhis family (VV09 [22], vdW-DF-09 [23], and VV10 [24]) and approaches that emphasize multipole response and mutual coupling of exchange holes [25–27]. In addition, there are approaches that focus on the dipole and multipole response of orbitals, atoms, and clusters (typically obtained outside of the ground-state DFT framework), compute the mutual coupling energy, and add it to a traditional ground-state DFT description [28–39]. It is commonly required that the chosen approach must be accurate both when there are important regions of low-electron concentration, i.e., sparse matter such as in intermolecular binding [14], and when studying dense matter, i.e., harder materials such as transition metals.

The recent consistent-exchange version, vdW-DF-cx [9,13,16], uses the vdW-DF plasmon-pole response description also to determine the *semilocal* component of the vdW-DF method. vdW-DF-cx is determined by a dielectric-response description that automatically enforces current conservation in the screening response [7,13]. The vdW-DF-cx method effectively uses the same plasmon-pole response to define both gradient-corrected exchange and nonlocal correlations. This new vdW-DF version thereby minimizes a hidden crossover term  $\delta E_x^0$  that generally enters in the vdW-DF family of functionals [16].

\*erhart@chalmers.se

†hyldgaard@chalmers.se

vdW-DF-cx has already proven itself accurate and useful in a number of problems that involve both regions of sparse and dense electron distributions such as molecular dimers [16,40], layered materials [9,41–45], semiconductors [9,46], molecular crystals [47,48], adsorption processes [21,49], as well as weak chemisorption, molecular switching, and molecular self-assembly [21,49,50]. The ACF foundation and the emphasis on conservation laws in the vdW-DF-cx construction further suggests a general-purpose nature [9] and motivates a comprehensive investigation of its performance also for regular dense matter. This is particularly interesting since earlier members of the vdW-DF family have repeatedly been found to yield an inferior description of traditional bulk materials, in particular the late transition metals [49].

Here, we benchmark vdW-DF-cx for thermophysical properties of nonmagnetic transition metals, for which extensive experimental data are available for comparison [51–53]. Specifically, we consider lattice parameters, thermal expansion, and bulk moduli at finite temperature as well as the cohesive energies including zero-point contributions at the level of the quasiharmonic approximation (QHA). This data set explicitly tests not only the description of energy and structure but also forces, going beyond the set of properties commonly considered in comparative assessments of XC functionals. In addition to vdW-DF-cx, we consider the constraint-based semilocal functionals, PBE [4] and PBEsol [54], as well as AM05 [55].

We show that vdW-DF-cx meets and exceeds the performance of the PBE, PBEsol, and AM05 functionals for nonmagnetic transition metals. This suggests that vdW-DF-cx provides a good, balanced description of nonlocal exchange and nonlocal correlation also in these types of materials. vdW-DF-cx thus remains a candidate for serving as a general-purpose materials-theory tool, working for both hard and soft matter [9].

The remainder of this paper is organized as follows. The next section provides an overview of the constraint-based functionals considered in the present work, while methodological aspects are compiled in Sec. III A. Section IV describes the main results, and Sec. V provides a summary and conclusions. A detailed compilation of results including a per-element comparison with experimental data can be found in the supplementary material [56].

## II. CONSTRAINT-BASED NONLOCAL FUNCTIONALS

### A. General aspects

Comparisons among constraint-based nonlocal functionals are valuable in our drive to further improve truly nonlocal DFs. Several previous studies have shown that some vdW-DF approaches can work well for solids [9,18–20,39,57]. While this has helped build trust in the vdW-DF method, constraint-based functionals such as vdW-DF-cx, PBE, and PBEsol are all linked to the ACF and conservation [4,13,16,54] and can thus be expected to yield good transferability. Similarly, AM05 is linked to other constraints, interpolating between model systems [54,55]. Yet as briefly reviewed below, different physical aspects were emphasized in their construction, and one can thus expect to gain insight into strengths and

limitations of each approach exactly because these functionals are each representatives of a specific design logic. By focusing the present benchmark on constraint-based functionals, we are thus able to draw more general conclusions.

The four functionals considered in the present work share some common traits while also having some distinct differences in their design logic, making it interesting to contrast their performance. All matter has internal surfaces with a variation between higher and lower electron density regions, and insight from surface physics underpins all the designs. It led Langreth and Perdew to the early GGA [3] and it entered the specification of gradient-corrected correlation in PBEsol [54] and AM05 [55]. These concepts are also central to the development of the vdW-DF method [6,10], which takes the surface idea further than in the GGA. This is done by noting that a semilocal representation of the electron-gas response does not retain a full description of the electro-dynamical coupling among (GGA) XC holes [6,10–13]. The electro-dynamical coupling is relevant, for example, when there are multiple interacting density fragments (molecules or surfaces) separated by a region with low electron concentration [6,13].

The Fermi wave vector  $k_F(\mathbf{r}) = [3\pi^2 n(\mathbf{r})]^{1/3}$  sets a local energy scale via the LDA exchange energy per particle,  $\varepsilon_x^{\text{LDA}}(\mathbf{r}) = -(3/4\pi)k_F(\mathbf{r})$ . We take semilocal functionals to imply that the XC hole form or the energy per particle depend exclusively on the local (spin) density  $n(\mathbf{r})$  and the local scaled gradient  $s(\mathbf{r}) = |\nabla n|/[2n(\mathbf{r})k_F(\mathbf{r})]$ . Semilocal GGA functionals can be expressed via the local variation in the XC energy per particle,

$$\varepsilon_{xc}^{\text{GGA}}(\mathbf{r}) \equiv F_{xc}(n(\mathbf{r}), s(\mathbf{r}))\varepsilon_x^{\text{LDA}}(\mathbf{r}). \quad (1)$$

Here, the XC enhancement factor  $F_{xc}(n(\mathbf{r}), s(\mathbf{r}))$  reflects the physical nature of the associated semilocal XC hole [4,54].

In addition to functionals that (like PBE, PBEsol, AM05, and present vdW-DF versions) use a gradient-corrected exchange description, there are also ongoing developments of constraint-based meta-GGAs (MGGAs), including the new SCAN-MGGA and TM-MGGA [58–60]. These functionals also employ the variation in the local kinetic-energy density to refine the account of nonlocal XC effects. The inclusion of such higher-order XC effects is important for a description of weaker binding at intermediate distances, and it also improves the description of the bulk structure and cohesion over that of the constraint-based GGAs [59,60]; not considering dispersive interactions, the performance of such new MGGAs for bulk structure (as obtained in other codes) is better than what we are documenting here for vdW-DF-cx [59]. It is, however, beyond the present scope to also benchmark these new highly constraint-based MGGAs.

In a continued development of the vdW-DF method, we chose to focus on constraints. There are at least four important criteria that can help the design of robust and transferable density functionals:

(i) Conservation of the exchange-correlation (XC) hole [2,3,9,13,61–63].

(ii) Current conservation in the description of the electro-dynamical response that underpins the definition of the XC hole via the ACF [2,3,13,64].

(iii) Adherence to the global Lieb-Oxford bound (g-LOB) [65–67].

(iv) Most relevant for developing the vdW-DF method: avoidance of spurious exchange (non-vdW) binding arising at intermediate-to-far fragment separations [7,68,69].

Charge conservation, criterion (i), has long been understood as being essential for the design of robust, transferable density functionals. After all, the combination of the electron and its associated XC hole must be charge-neutral for the DFT treatment (as a noninteracting quasiparticle) to be sensible [3]. Compliance with criterion (ii) is essential in the definition of the vdW-DF method [7,10], and it was explicitly used in motivating the formulation of the vdW-DF-cx method [13]. Also, closely related insight on the  $F$ -sum rule was central in the definition of both the LDA [2,3,64] and the constraint-based GGAs (r)PW86 [69,70], PBE [4], and PBEsol [54]. Criterion (iv) is relevant for avoiding double counting in the present vdW-DF versions (which starts with gradient-corrected exchange [13]). Seeking a meta-vdW-DF (starting instead from the new MGGAs) is interesting since it may thus be possible to better discriminate between spurious and physical binding at intermediate distances [59,60]; at present, however, one is motivated to pick the exchange enhancement  $F_x(s) \sim s^{2/5}$  asymptotically [6,7,10,15,69]. The original and revised PW86 [69,70], PBE [4], PBEsol [54], as well as both the original vdW-DF and the new vdW-DF-cx should be seen as highly constrained: They incorporate the first two criteria [(i) and (ii)], while criteria (iii) and (iv) are expected to be fulfilled in actual calculations.

### B. The PBE functional

The PBE functional [4] is an important example of a constraint-based GGA [5,71]. The PBE was designed by first constructing a numerical GGA with an enhancement factor  $\tilde{F}_{xc}$  that reflects conditions on the shape of the semilocal XC hole description and, in a subsequent step, by extracting an analytical form for the PBE  $F_{xc}$  for practical use. One can expect a high degree of transferability because it is anchored in conservation laws [2,3]. In fact, the PBE functional has had a huge impact on materials theory and has turned out to be an extremely successful general-purpose functional for systems with dense electron distributions including both individual molecules and hard materials [5].

### C. The PBEsol functional

One of the best-performing constraint-based semilocal functionals for condensed matter is the PBEsol functional [54]. While, as in the case of PBE, the nature of screened many-body response and the XC hole were emphasized during its construction, its authors also relied on other formal results in its design. The GGA framework that underpins both PBE and PBEsol is very powerful, but it is not possible to satisfy all constraints at the same time.<sup>1</sup> The PBE functional is highly transferable and works very well for both molecular formation

<sup>1</sup>The relation between PBE and PBEsol reflects in part the physical insight used for picking the form of gradient-corrected exchange enhancements [54]. Both functionals use conserving (albeit different)

energies and the structure and energies of hard materials. As a result of the diagrammatic (gradient-expansion) emphasis, PBEsol yields an even better description of the structure of hard materials [54].

PBE and PBEsol are designed also to comply with a so-called local Lieb-Oxford bound (l-LOB). This condition is formulated as

$$F_x(s(r)) < 1.804. \quad (2)$$

By complying to Eq. (2), the g-LOB criterion (3) is automatically satisfied. It should also be noted that there exist densities (shell-like structure) for which breaking the l-LOB also means violating the g-LOB [65,67]. It is desirable to explicitly test compliance with the g-LOB criterion (3) for actual calculations when the GGA-exchange description can violate the l-LOB condition (2).

### D. The AM05 functional

The AM05 constraint-based functional [55] performs very well for describing the structure of dense materials. The AM05 provides, in principle, an exact account of exchange effects for surfaces, i.e., the boundary between regions of higher and lower electron densities, whereas for internal regions this surface-exchange description is merged with that of the LDA. It relies on reference input other than formal many-particle theory, and it is not usually counted as constraint-based [54,66], yet it is parameter-free and therefore included in this benchmarking. Like PBEsol, the AM05 functional extracts the gradient-corrected correlation from a study of the jellium surface energy. While it has different roots from those of PBE and PBEsol, it can be viewed as a semilocal functional since it is possible to express the energy per particle variation using Eq. (1). Like the regular GGAs, it lacks an account of truly nonlocal correlation effects. The exchange enhancement in AM05 is such that the l-LOB condition (2) can be broken, but it is not clear to what extent it will affect calculations for dense matter, e.g., transition metals and other bulk systems.

### E. The vdW-DF framework

The vdW-DF method [6–8,10,12,16] represents a systematic nonempirical extension of both LDA and the semilocal GGA description [9,13,21]. The very first version of this method was conceived two decades ago starting from a simple Ashcroft picture [11] of vdW binding in the itinerant electron gas [10,13]. It provides seamless integration with a GGA-type description while enforcing conservation laws on the underlying many-body response description [7,8,10,13]. The method predates the PBEsol and AM05 functionals, and its origin [12] actually coincides with the launching of the PBE functional [4]. The vdW-DF method captures

approximations for the semilocal XC hole. In the case of the PBE functional, one arrives at a small- $s$  expansion that is also suggested by exact-scaling results for atomiclike high-density regions [5,54,71]. By contrast, in the construction of PBEsol, one obtains a behavior consistent with diagrammatic results for pure exchange in the weakly perturbed electron gas.

vdW forces among dimers in the asymptotic and the binding limits [7,72–77] as well as attraction between two-dimensional layers [6,41–43,68]. Importantly, it also captures the more general problem when nonlocal correlation forces compete with other types of forces [9], for example, giving rise to binding across important regions of low electron densities [10,14]. The method was expected to be relevant in first-principles DFT for both pure vdW problems including regular physisorption [49,78–80], porous-materials gas absorption [81–90], and DNA base-pair interactions [91–95]. It was also quickly realized that truly nonlocal correlations affect materials descriptions much more broadly than what was perhaps originally anticipated [10,14,57,77,96–100]. The recent vdW-DF formulations are, for example, proving themselves valuable in the treatment of organic-inorganic interfaces and general weak-chemisorption problems [18,21,35,49,50,96,101–104].

The vdW-DF framework formally constitutes an ACF recast [7,10,13]

$$E_{xc} = \int_0^\infty \frac{du}{2\pi} \text{Tr}\{\ln[\nabla\varepsilon(iu) \cdot \nabla G]\} - E_{\text{self}}. \quad (3)$$

Here,  $E_{\text{self}}$  and  $G$  denote the Coulomb self-energy and Green function, respectively,  $u$  is a complex frequency, and  $\varepsilon$  denotes a suitable approximation for a scalar, nonlocal dielectric function. The trace is over all spatial coordinates. The vdW-DF framework has exact screening, and it defines  $\varepsilon$  via a plasmon-pole response description that reflects constraints such as the  $F$  sum rule [7,9,10,13]. The vdW-DF method begins with a plasmon-pole approximation for a screened response treated at the GGA level, i.e., by choosing  $\varepsilon(iu)$  so that it reflects the shape of an internal XC hole corresponding to a GGA-type semilocal functional  $E_{xc}^{\text{in}}$ . The vdW-DF method proceeds to define semilocal and nonlocal functional components,

$$E_{xc}^{\text{vdW-DF}} = E_{xc}^0 + E_c^{\text{nl}}, \quad (4)$$

where the semilocal component satisfies

$$E_{xc}^0 \approx E_{xc}^{\text{in}} \quad (5)$$

while the truly nonlocal XC energy term is defined as

$$E_c^{\text{nl}} = \int_0^\infty \frac{du}{2\pi} \text{Tr}\{\ln[\nabla\varepsilon(iu) \cdot \nabla G] - \ln[\varepsilon(iu)]\}. \quad (6)$$

The vdW-DF framework can be interpreted as a rigorous implementation of the Ashcroft picture of vdW forces since Eq. (6) formally counts the shifts in electronic zero-point energies that arise with an electrodynamic coupling between the internal GGA-type XC holes [13]. In the most widely used general-geometry versions, the evaluation of Eq. (6) involves a second-order expansion that allows an efficient universal kernel formulation [7,8,10]. The vdW-DF versions are entirely nonempirical and rest solely on the physics that underpins the LDA XC energy and the GGA-type gradient-corrected exchange in  $E_{xc}^0$  and  $E_{xc}^{\text{in}}$ .

Here we benchmark the finite-temperature performance of the recent consistent-exchange version vdW-DF-cx [16]. In this functional, the exchange component in  $E_{xc}^0$  is chosen to minimize

$$\delta E_x^0 \equiv E_{xc}^0 - E_{xc}^{\text{in}} \quad (7)$$

for small-to-medium values of the scaled density gradient  $s$ . In practice, this means that  $\Delta E_x^0 = 0$  is for all systems but atoms and small molecules [10,13,16] so that vdW-DF-cx effectively serves as an implementation of (an expanded form of) the full vdW-DF framework Eq. (3) [7,9,10,13]. Additional documentation for this new vdW-DF version can be found in Refs. [9,10,13].

In the design of vdW-DF2 and vdW-DF-cx, compliance with criteria (4) was prioritized over having compliance with the l-LOB condition (2), and hence an automatic, universal compliance with the g-LOB criteria (3). For the present focus on materials with dense electron distributions and metallic bonding, the l-LOB condition is not expected to be broken at any relevant spatial points. We also note that Refs. [16,105] show that the vdW binding among molecular fragments almost always arises from regions with small to moderate values of  $s > 2-3$ . There is no breaking of even the l-LOB condition from such regions (either) when using vdW-DF-cx.

### III. METHODOLOGY

#### A. Computational details

DFT calculations were carried out using the projector augmented wave (PAW) method [106] as implemented in the Vienna ab-initio simulation package (VASP) [107]. For vdW-DF-cx calculations, we used the patch released in Ref. [41]. In primitive cell calculations, the Brillouin zone was sampled using  $\Gamma$ -centered  $k$ -point grids with  $13 \times 13 \times 7$  divisions for hexagonal-close-packed (hcp) structures,  $14 \times 14 \times 14$  divisions for face-centered-cubic (fcc) structures, and  $15 \times 15 \times 15$  divisions for body-centered-cubic (bcc) structures. The plane-wave cutoff energy was chosen 30% larger than the commonly recommended value for each element in order to obtain very well converged forces and especially stresses. The values employed are tabulated in Table V of the supplementary material, which also provides details concerning the PAW setups. Generally, we employ PAW setups from the 2012 VASP database with the exception of W, for which we consider a semicore setup that includes the  $5p$  (but not the  $5s$  states) in the valence, the performance of which has been carefully assessed previously [108,109]. These PAW setups have been shown to yield very good agreement with respect to all-electron calculations [110,111].

#### B. Vibrational modeling

To evaluate finite-temperature properties, we employed the quasiharmonic approximation (QHA). First, the harmonic Helmholtz free energy  $F(T, V)$  was evaluated as a function of temperature at a fixed volume  $V$  according to [112,113]

$$F = \frac{1}{2} \sum_{q\nu} \hbar\omega_{q\nu} + k_B T \sum_{q\nu} \ln[1 - \exp(-\hbar\omega_{q\nu}/k_B T)]. \quad (8)$$

Here, the summations are the result of a discretization of the integral over the vibrational density of states and carried out over phonon modes with momentum  $\hbar\mathbf{q}$  and index  $\nu$ . The Gibbs free energy  $G(T, p)$  at constant pressure  $p$  is obtained by repeating the calculation of  $F(T, V)$  for a range of volumes and minimizing the sum of internal energy  $U(V)$ , Helmholtz

energy  $F(T, V)$ , and the pressure-volume term according to

$$G(T, p) = \min_V [U(V) + F(T, V) + pV]. \quad (9)$$

While the internal energy  $U(V)$  simply corresponds here to the Born-Oppenheimer energy as a function of volume, evaluation of the vibrational contribution Eq. (8) requires knowledge of the phonon dispersion on a dense  $\mathbf{q}$ -point mesh. Toward that end, force constants were calculated using the finite displacement method and  $4 \times 4 \times 4$  supercells. In the latter calculations, the Brillouin zone was sampled using  $\Gamma$ -centered  $3 \times 3 \times 3$   $\mathbf{k}$ -point grids. The minimization in Eq. (9) was carried out over volumes ranging from  $0.85V_0$  to  $1.15V_0$ , where  $V_0$  is the volume corresponding to the minimum of the Born-Oppenheimer energy landscape.

Knowledge of the Gibbs free energy as a function of volume and temperature allows one to readily extract, for example, the lattice parameter(s), the bulk modulus, and the thermal expansion coefficient(s) at finite temperatures. All of these thermophysical properties were extracted using the PHONOPY package [113]. Specifically, the bulk modulus was obtained by fitting the Gibbs free energy to the Vinet equation of state [114].

Furthermore, we calculated the cohesive energy  $E_{\text{coh}}$  at 0 K including the zero-point energy (ZPE) contribution,

$$E_{\text{coh}} = E_{\text{bulk}} + \frac{1}{2} \sum_{\mathbf{q}\nu} \hbar\omega_{\mathbf{q}\nu} - E_{\text{atom}}, \quad (10)$$

where  $E_{\text{bulk}}$  and  $E_{\text{atom}}$  denote the total energy of the bulk material and the atom, respectively. All terms in the latter equation were evaluated at the 0 K lattice constant corrected for zero-point effects.

### C. Atomic reference energies: Spin effects

In general, spin polarization must be included when calculating  $E_{\text{atom}}$ . While a consistent spin-polarized version of the vdW-DF method was recently introduced [21], it has so far only been implemented in the QUANTUM-ESPRESSO package [115]. The vdW-DF evaluation of nonlocal correlations amounts to tracking the total energy shift that arises with the electro-dynamical coupling of plasmons, which, in turn, represent a GGA-type response to external fields [13]. The vdW-DF approximations that are implemented in VASP [19] are not fully consistent since they ignore the fact that spin polarization will itself adjust these plasmons [21].

In the present study, we therefore proceeded as follows in order to obtain atomic reference energies and eventually cohesive energies for vdW-DF-cx. We calculated the non-spin-polarized atomic energy  $E_{\text{atom}}^{\text{ns}, \text{vasp}}$  using VASP and then added the atomic spin-polarization energy  $\Delta_{\text{spin}}^{\text{qe}}$  obtained using QUANTUM-ESPRESSO with the rigorous-spin vdW-DF-cx description [21]. That is, we obtained the atomic energies as

$$E_{\text{atom}} = E_{\text{atom}}^{\text{ns}, \text{vasp}} + \underbrace{E_{\text{atom}}^{\text{sp}, \text{qe}} - E_{\text{atom}}^{\text{ns}, \text{qe}}}_{\Delta_{\text{spin}}^{\text{qe}}}. \quad (11)$$

In effect, this procedure amounts to computing VASP and QHA-based cohesive-energy estimates  $E_{\text{coh}}^{\text{vasp}}$  and then adding a spin correction

$$\Delta_{\text{spin-corr}} = \Delta_{\text{spin}}^{\text{qe}} - \Delta_{\text{spin}}^{\text{vasp}}, \quad (12)$$

where  $\Delta_{\text{spin}}^{\text{vasp}} = E_{\text{atom}}^{\text{sp}, \text{vasp}} - E_{\text{atom}}^{\text{ns}, \text{qe}}$  represents the VASP approximation for the vdW-DF-cx atomic spin-polarization energy. A detailed compilation of the atomic reference energies can be found in Table VI of the supplementary material.

In the QUANTUM-ESPRESSO calculations of  $\Delta_{\text{spin}}$ , we relied on norm-conserving pseudopotentials (NCP) from the ABINIT package [116], using a plane-wave (density) cutoff of 80 Ry (400 Ry) so as to best mimic the fact the VASP calculations are based on hard PAW setups. This NCP choice was possible for all but the case of W, where the ABINIT NCP did not yield the correct spin-polarization state. For the W case alone, we therefore relied on a W ultrasoft pseudopotential in calculating  $\Delta_{\text{spin}}^{\text{correction}}$ .<sup>2</sup>

## IV. RESULTS

### A. General assessment

In this section, we provide an overview of the key results from our comparative analysis of constraint-based XC functionals. A complete compilation of the data obtained with each XC functional, including lattice constants, can be found in the supplementary material. To measure and compare the performance of different functionals, we consider the mean absolute percentage error (MAPE) defined as

$$M = \frac{1}{N} \sum_k \left| \frac{A_{\text{DFT}}^{(k)} - A_{\text{expt}}^{(k)}}{A_{\text{expt}}^{(k)}} \right|, \quad (13)$$

where  $A_{\text{DFT}}^{(k)}$  and  $A_{\text{ref}}^{(k)}$  denote predicted and experimental values of a property of structure  $k$ , and the average contains  $N$  samples.

Many properties exhibit characteristic variations across the transition-metal series, which follow the  $d$ -band filling (Fig. 1) and are reproduced by all XC functional considered here. While ZPE and thermal expansion effects are generally limited to a few percent of the volume, they are nonetheless crucial for an accurate assessment.

The performance comparison (Fig. 2 and Table I) confirms that PBEsol and, with the exception of the cohesive energy, also AM05 represent general improvements over PBE. The relatively large MAPEs (Table I) arise mostly from larger errors in just a few systems. In the case of PBE, the MAPE for the cohesive energy of bcc structures is particularly large. This issue is primarily caused by an inaccurate description of the electronic configuration of the isolated spin-polarized atoms, which impacts the atomic reference energy.

More interestingly, the comparison demonstrates that the truly nonlocal vdW-DF-cx performs at least at the level of PBEsol and AM05. In fact, considering all the properties, vdW-DF-cx provides the best overall agreement with the experimental reference data. This is especially remarkable since previous nonempirical versions of the DF method, namely vdW-DF1 [7] (in which exchange is approximated

<sup>2</sup>We also tested using the W NCP while constraining the spin polarization to the correct configuration, which yields a vdW-DF-cx value for the cohesive energy of W that is in even better agreement with experiment than when using the ultrasoft pseudopotential.

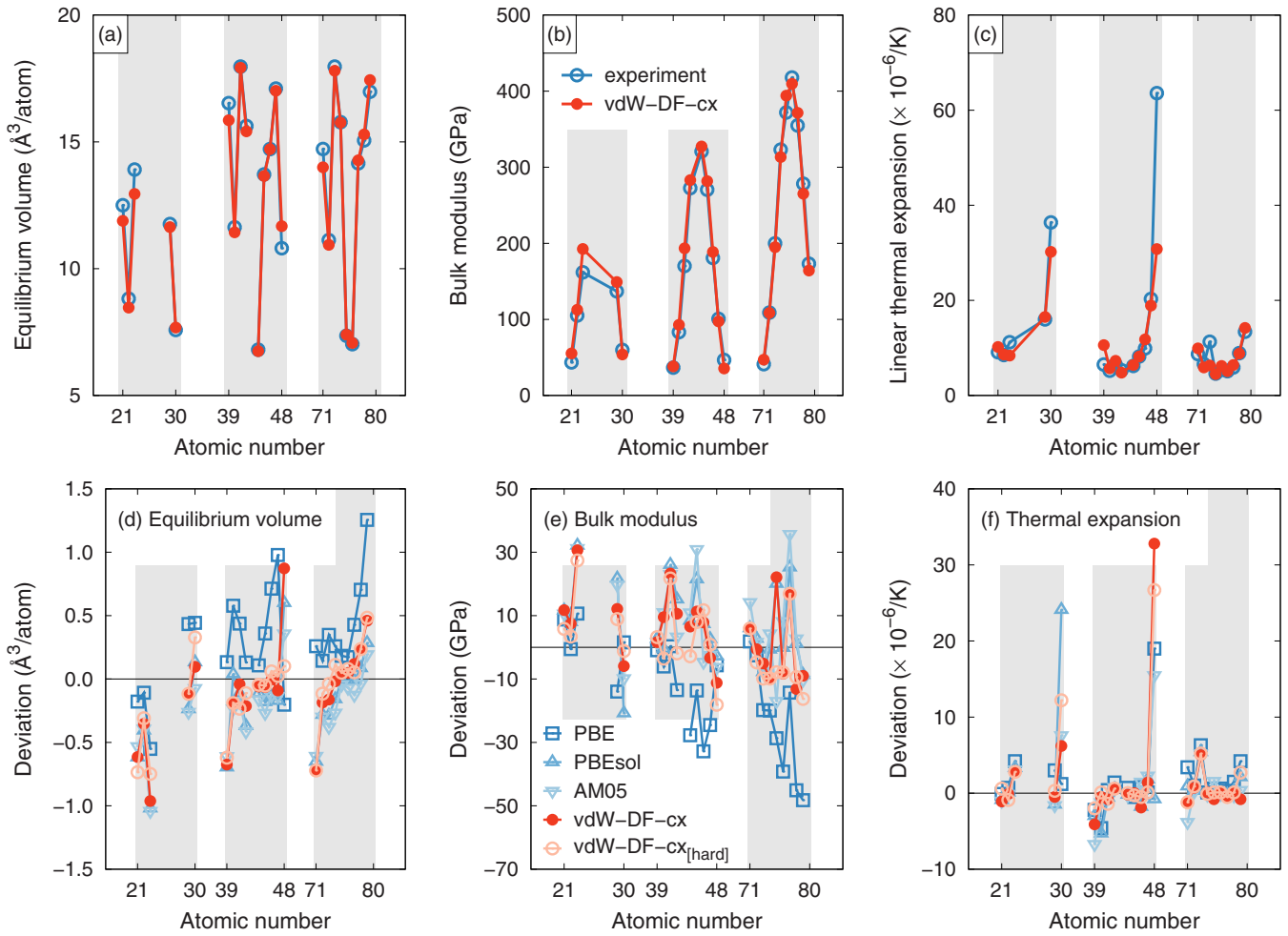


FIG. 1. Overview of thermophysical properties at 300 K obtained using the quasiharmonic approximation in conjunction with density-functional-theory calculations. (a) Equilibrium volume, (b) bulk modulus, and (c) coefficient of average linear thermal expansion from experiment (Refs. [52,53]) and calculations based on the vdW-DF-cx functional. Deviation between different XC functionals and experiment for (d) equilibrium volume, (e) bulk modulus, and (f) coefficient of linear thermal expansion. The shaded regions indicate the set of  $3d$ ,  $4d$ , and  $5d$  transition metals.

by the revPBE functional [117] and vdW-DF2 [15] (in which exchange is approximated by a revised version [69] of the PW86 functional [70]), perform rather poorly for the late transition metals. In particular, in the case of Ag and Au, the lattice constants are considerably overestimated in vdW-DF1 and vdW-DF2 [19], while vdW-DF-cx yields excellent results for these elements.

### B. Cohesive energies

Overall the constraint-based functionals considered here perform reasonably well with regard to the description of the cohesive energy (Fig. 3), although for most of the functionals there are problems with specific elements. Most notably, the vdW-DF-cx description clearly outperforms the other functionals in terms of the cohesive energies.

Moreover, the results demonstrate that the rigorous inclusion of spin effects in vdW-DF-cx [21] is important for an accurate description of the cohesive energy in nonmagnetic transition metals [Fig. 3(c)]. Since the atomic spin-polarization energies are very large in the middle of the transition-metal

bands [Fig. 3(d)], it is important to use the rigorous-spin vdW-DF-cx formulation [21]. The corrections are negative and systematically lead to larger values for  $\Delta_{\text{spin}}$  (see Table VI of the supplementary material). As a consequence, our rigorous-spin vdW-DF-cx calculations provide a systematic improvement for the description of nonmagnetic transition metals, lowering, for example, the MAPE from 9.1% to 7.3% when using hard PAW setups for vdW-DF-cx.

### C. Effect of PAW setups in the case of vdW-DF-cx

For computational efficiency, it is often desirable to employ PAW setups that contain only the highest occupied states in the valence. This not only limits the total number of states in the calculation, but it also often allows using relatively large core radii that require smaller plane-wave-basis cutoffs in order to obtain converged results. While so far we have only considered results obtained using such “standard” PAW setups, it is now instructive to examine the choice of the PAW setup more closely. Toward that end, we exclusively consider calculations

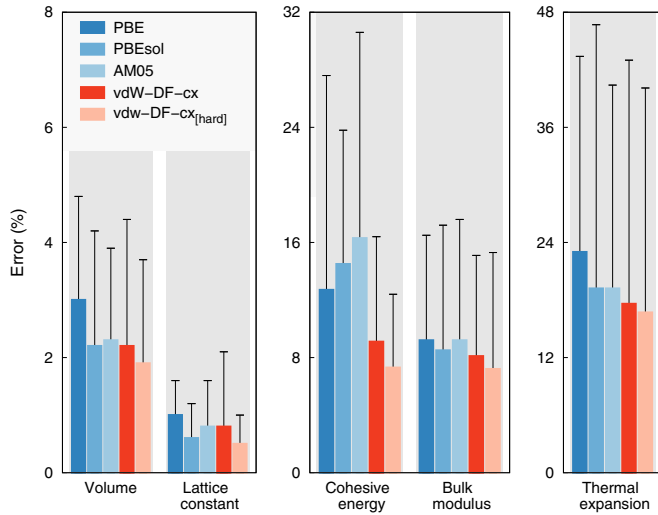


FIG. 2. Performance of different constraint-based XC functionals based on the data from Table I. The MAPEs were computed with regard to thermophysical properties measured at 300 K, with the exception of the cohesive energy, for which 0 K values are compared. Standard deviations of the distribution of errors for each property and functionals are shown as black error bars.

based on the vdW-DF-cx functional and “hard” PAW setups, as detailed in Table V of the supplementary material.

Using the hard PAW setups systematically improves the agreement with experiment, typically reducing the MAPE by a fraction of a percent (Table I and Fig. 2). Yet, the comparison clearly demonstrates that already the “standard” PAW setups yield very good result and are sufficient to achieve good results in many situations. It should be noted that the comparison here is restricted to the vdW-DF-cx method, but a similar improvement when moving from standard to hard setups is likely to be observable also for the other functionals.

Cadmium represents an exception, for which there is a pronounced difference between standard and hard setups. For example, the lattice constants at 300 K change from  $a = 3.168 \text{ \AA}$  and  $c = 5.373 \text{ \AA}$  to  $a = 3.023 \text{ \AA}$  and  $c = 5.512 \text{ \AA}$  when going from standard to hard PAW setups. The latter values are also in notably better agreement with the experimental numbers of  $a = 2.98 \text{ \AA}$  and  $c = 5.62 \text{ \AA}$  (Table II of the supplementary material). More generally, the late transition metals in hcp structure (Zn and Cd) are challenging for all XC functionals. This behavior is related to their special electronic structure, which manifests itself, e.g., in  $c/a$  ratios (experimentally  $c/a = 1.89$  and  $1.86$  for Cd and Zn, respectively) that are considerably larger than in the ideal hcp structure ( $c/a = 1.633$ ).

#### D. Structure trends, semilocal, and nonlocal functionals

The deviations between calculated and experimental data follow certain trends [Figs. 1(d)–1(f)]. While PBE tends to overestimate the equilibrium volume, the other functionals are overall in rather close agreement with the reference data.

Contrasting specifically the vdW-DF-cx and PBEsol performance (Fig. 4) shows that both functionals exhibit similar trends with respect to the variation of the accuracy with  $d$ -band filling. It is apparent that the data for the first and last

TABLE I. Performance of constraint-based XC functionals with respect to the description of thermophysical properties. The comparison includes the equilibrium volume  $V$ , bulk modulus  $B$ , as well as the linear coefficient of thermal expansion  $\alpha_l$  measured at room temperature, while in the case of the cohesive energy  $E_{\text{coh}}$  zero Kelvin data are compared, albeit including ZPE effects. Unless otherwise noted, the calculations were carried out using standard PAW setups. The comparison comprises 11 hcp, 7 fcc, and 5 bcc elements.

Functional		$V$	$B$	$\alpha_l$	$E_{\text{coh}}$
vdW-DF-cx	hcp	3.0%	9.9%	20.6%	10.9%
	fcc	1.0%	5.0%	5.9%	9.5%
	bcc	1.9%	8.4%	27.3%	4.5%
	total	2.2%	8.1%	17.6%	9.1%
vdW-DF-cx (hard PAW setups)	hcp	2.6%	8.5%	17.7%	7.8%
	fcc	1.0%	4.9%	5.5%	8.7%
	bcc	1.7%	7.7%	30.0%	4.2%
	total	1.9%	7.2%	16.7%	7.3%
PBE	hcp	2.3%	7.1%	23.6%	10.9%
	fcc	4.6%	15.1%	11.8%	8.1%
	bcc	2.2%	5.6%	37.4%	23.3%
	total	3.0%	9.2%	23.0%	12.7%
PBEsol	hcp	2.8%	9.9%	21.7%	14.7%
	fcc	1.1%	6.1%	8.4%	12.4%
	bcc	2.6%	9.0%	28.7%	16.8%
	total	2.2%	8.5%	19.2%	14.5%
AM05	hcp	2.7%	11.3%	22.3%	25.7%
	fcc	1.2%	6.8%	6.8%	9.7%
	bcc	3.0%	7.8%	29.8%	4.8%
	total	2.3%	9.2%	19.2%	16.3%

columns of the series are slightly under- and overestimated, respectively. The largest relative corrections of the volume arise for Zn and Cd, and those elements also have some of the largest vibrational corrections to the cohesive energies. In fact, most DFs provide an inaccurate description of these elements, which, as indicated above, exhibit a hcp structure with a very large axial ratio.

Larger deviations from the reference data are also observed for  $V$  (bcc) for all functionals. We ascribed this behavior to the low-temperature magnetism that has been reported in this element [118], while in the present calculations it is treated without spin polarization.

Similar trends as for the equilibrium volume can be observed for the bulk modulus [in reverse fashion, Fig. 1(e)] and the linear coefficient of thermal expansion [Fig. 1(f)], although the errors are more scattered. The latter effect is probably connected to a larger uncertainty in the experimental data, as will be discussed in the next section.

#### E. Bulk modulus and thermal expansion

So far we have used experimental values from compilations of standard values [52,53] as reference data for equilibrium volumes (lattice constants), bulk moduli, and thermal expansion coefficients. While the data for lattice constants are usually very accurate, it must be acknowledged that measurements of bulk moduli and thermal expansion coefficients can carry rather significant errors, which are usually not documented in

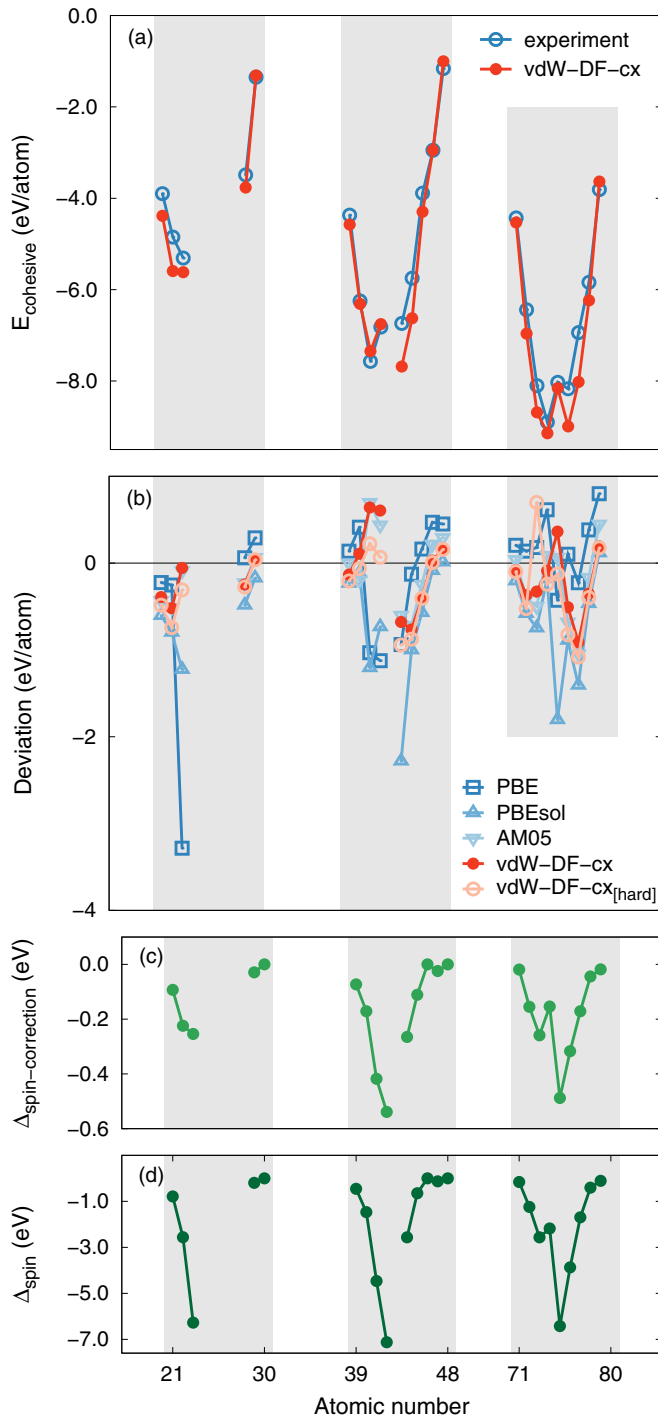


FIG. 3. (a) Cohesive energies at 0 K obtained using the quasi-harmonic approximation in conjunction with density-functional-theory calculations from experiment (Ref. [52]) and calculations based on the vdW-DF-cx functional including the spin correction according to Eq. (12). (b) Deviation between different XC functionals and experiment for cohesive energies. (c) Spin correction according to Eq. (12) that is added to the VASP data for our vdW-DF-cx benchmark to include a rigorous description of spin effects in the atomic reference energies. (d) Atomic spin polarization energies  $\Delta_{\text{spin}}$  defined in Eq. (11) as calculated in the spin vdW-DF-cx formulation (available via QUANTUM-ESPRESSO calculations).

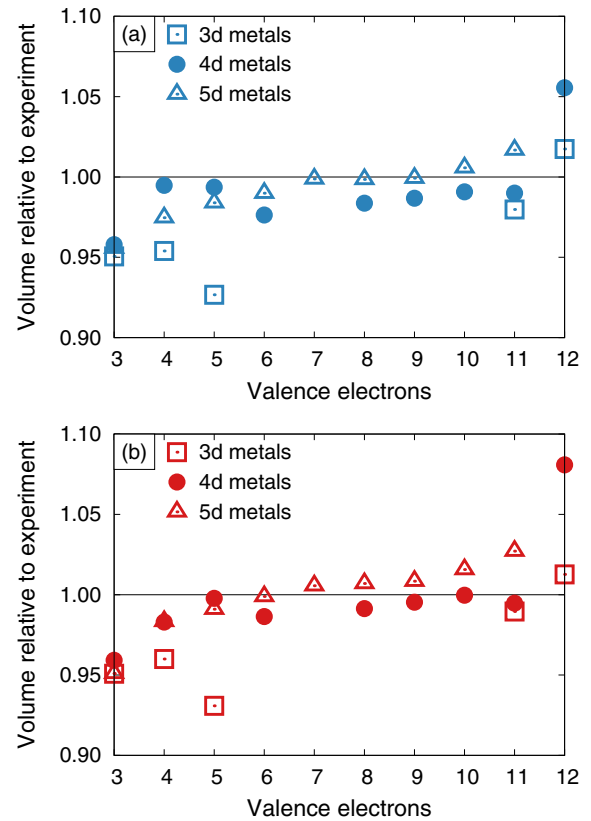


FIG. 4. Ratio of calculated to experimental equilibrium volumes for (a) PBEsol and (b) vdW-DF-cx (hard PAW setups). The transition from a volume underestimation converting to a volume overestimation is expected for GGAs and is found in both cases.

reference compendia. A closer inspection of experimental data available in the general scientific literature, however, reveals that at least in some cases these errors can be comparable to or even exceed the deviation between the best performing XC functionals and experiment.

For illustration purposes, we employ experimental data for the Young's moduli  $E$  and Poisson ratios  $\nu$  of polycrystalline samples of the fcc metals Ir, Pt, and Rh [119]. As the experimental data range from 300 to 1500 K, this also allows us to compare experiment and calculations over a wide temperature span. The experimental data can be converted to the bulk modulus using the relation  $B = E/3(1 - \nu)$ . This illustrates that there is considerable scatter in the experimental data with changing temperature, which does not appear to be associated with a specific trend (Fig. 5); this is particularly pronounced in the case of Pt. The calculations overestimate the experimental data, but overall the agreement is good with a similar temperature dependence.

## F. General discussion

High accuracy and transferability of vdW-DF-cx had been previously indicated by a range of successful applications to systems that combine regions of both sparse and dense electron distributions [9,16,21,42,47–50]. In the present paper, it has been demonstrated that, unlike the vdW-DF1 and

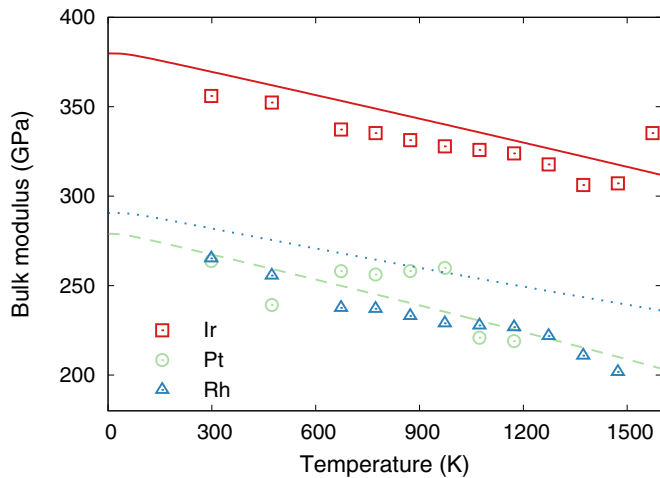


FIG. 5. Temperature dependence of the bulk modulus from experiment and calculation (vdW-DF-cx). The experimental data points were obtained by converting the data for Young's modulus  $E$  and the Poisson ratio  $\nu$  measured in Ref. [119] using the relation  $B = E/3(1 - \nu)$ .

vdW-DF2 versions, vdW-DF-cx also performs very well for hard materials.

The strong performance of PBEsol for traditional materials can be primarily traced to two of its features, namely a good form for gradient-corrected exchange and a good balance between this exchange part and the account of gradient-corrected correlation. The vdW-DF-cx strategy of seeking an ACF evaluation, see Eq. (3), implies picking a semilocal exchange component in  $E_{xc}^0$  that is given by a diagrammatic expansion and therefore is similar to that of PBEsol in the low-to-medium  $s$  regime. Yet, vdW-DF-cx still replaces the PBEsol description of gradient-corrected correlation entirely with a truly nonlocal XC term  $E_c^{nl}$ . The fact that DF-cx performs at a PBEsol level with respect to hard materials thus suggests that vdW-DF-cx achieves a good balance between exchange and correlation. This observation makes it plausible that one can obtain further functional improvements by relying on the ACF recast, Eq. (3), for descriptions of nonlocal correlation effects [7,10,13,16].

## V. SUMMARY

This study presents a comprehensive benchmark of constraint-based semilocal and nonlocal functionals with respect to finite-temperature thermophysical properties of nonmagnetic transition metals. The main outcome of this comparison is that, unlike its predecessors in the vdW-DF family, the recently developed nonlocal vdW-DF-cx version achieves good transferability and accuracy also for hard materials. This is crucial, for example, for investigations of weakly bound molecules at transition-metal surfaces. In the case of vdW-DF1 and vdW-DF2, the substantial overestimation of the lattice constants of the late transition metals, in particular Ag and Au, limited their application to these systems. The successful validation of vdW-DF-cx for these cases allows full ionic relaxation and thus tracking of the impact of, e.g., associated adsorption-induced surface modifications [9,19,50].

We note that Ambrosetti and Silvestrelli [39] recently presented a related benchmarking of several functionals, including vdW-DF-cx, for the coinage metals. Our findings are consistent with their results.

An excellent performance is expected for the other functionals considered here, but it is interesting to note that the truly nonlocal functional vdW-DF-cx has as good a performance and transferability, if not better. This is encouraging for further development that will build upon the vdW-DF framework.

Finally, we observe that quantitative comparisons, as shown in the tables included in the supplementary material, can also assist a crude benchmarking of future vdW-DF versions. This is because the tables implicitly provide a quantification of the net differences between the raw Kohn-Sham results and the associated room-temperature characterizations that are relevant for comparison with most experimental observations.

## ACKNOWLEDGMENTS

We thank Kristian Berland for discussions. This work has been supported by the Swedish Research council (VR) and the Knut and Alice Wallenberg Foundation as well as computer time allocations by the Swedish National Infrastructure for Computing at NSC (Linköping), HPC2N (Umeå), and C3SE (Gothenburg).

- 
- [1] J. Harris and R. O. Jones, *J. Phys. F* **4**, 1170 (1974).  
 [2] O. Gunnarsson and B. I. Lundqvist, *Phys. Rev. B* **13**, 4274 (1976).  
 [3] D. C. Langreth and J. P. Perdew, *Phys. Rev. B* **15**, 2884 (1977).  
 [4] J. P. Perdew, K. Burke, and M. Ernzerhof, *Phys. Rev. Lett.* **77**, 3865 (1996).  
 [5] K. Burke, *J. Chem. Phys.* **136**, 150901 (2012).  
 [6] H. Rydberg, M. Dion, N. Jacobson, E. Schröder, P. Hyldgaard, S. I. Simak, D. C. Langreth, and B. I. Lundqvist, *Phys. Rev. Lett.* **91**, 126402 (2003).  
 [7] M. Dion, H. Rydberg, E. Schröder, D. C. Langreth, and B. I. Lundqvist, *Phys. Rev. Lett.* **92**, 246401 (2004).  
 [8] T. Thonhauser, V. R. Cooper, S. Li, A. Puzder, P. Hyldgaard, and D. C. Langreth, *Phys. Rev. B* **76**, 125112 (2007).  
 [9] K. Berland, C. Arter, V. R. Cooper, K. Lee, B. I. Lundqvist, E. Schröder, T. Thonhauser, and P. Hyldgaard, *J. Chem. Phys.* **140**, 18A539 (2014).  
 [10] K. Berland, V. R. Cooper, K. Lee, E. Schröder, T. Thonhauser, P. Hyldgaard, and B. I. Lundqvist, *IOP Rep. Progr. Phys.* **78**, 066501 (2015).  
 [11] K. Rapcewicz and N. W. Ashcroft, *Phys. Rev. B* **44**, 4032(R) (1991).  
 [12] Y. Andersson, D. C. Langreth, and B. I. Lundqvist, *Phys. Rev. Lett.* **76**, 102 (1996).  
 [13] P. Hyldgaard, K. Berland, and E. Schröder, *Phys. Rev. B* **90**, 075148 (2014).  
 [14] D. C. Langreth, B. I. Lundqvist, S. D. Chakarova-Käck, V. R. Cooper, M. Dion, P. Hyldgaard, A. Kelkkanen, J. Kleis,

- L. Kong, S. Li, P. G. Moses, E. Murray, A. Puzder, H. Rydberg, E. Schröder, and T. Thonhauser, *J. Phys.: Condens. Matter* **21**, 084203 (2009).
- [15] K. Lee, É. D. Murray, L. Kong, B. I. Lundqvist, and D. C. Langreth, *Phys. Rev. B* **82**, 081101 (2010).
- [16] K. Berland and P. Hyldgaard, *Phys. Rev. B* **89**, 035412 (2014).
- [17] V. R. Cooper, *Phys. Rev. B* **81**, 161104(R) (2010).
- [18] J. Klimeš, D. R. Bowler, and A. Michaelides, *J. Phys.: Condens. Matter* **22**, 022201 (2010).
- [19] J. Klimeš, D. R. Bowler, and A. Michaelides, *Phys. Rev. B* **83**, 195131 (2011).
- [20] I. Hamada, *Phys. Rev. B* **89**, 121103(R) (2014).
- [21] T. Thonhauser, S. Zuluaga, C. A. Arter, K. Berland, E. Schröder, and P. Hyldgaard, *Phys. Rev. Lett.* **115**, 136402 (2015).
- [22] O. A. Vydrov and T. Van Voorhis, *Phys. Rev. Lett.* **103**, 063004 (2009).
- [23] O. A. Vydrov and T. Van Voorhis, *J. Chem. Phys.* **130**, 104105 (2009).
- [24] O. A. Vydrov and T. Van Voorhis, *J. Chem. Phys.* **133**, 244103 (2010).
- [25] A. D. Becke and E. R. Johnson, *J. Chem. Phys.* **127**, 154108 (2007).
- [26] A. D. Becke and E. R. Johnson, *J. Chem. Phys.* **123**, 154101 (2005).
- [27] A. D. Becke and E. R. Johnson, *J. Chem. Phys.* **122**, 154104 (2005).
- [28] S. Grimme, *J. Comput. Chem.* **27**, 1787 (2006).
- [29] A. Tkatchenko and M. Scheffler, *Phys. Rev. Lett.* **102**, 073005 (2009).
- [30] P. L. Silvestrelli, *Phys. Rev. Lett.* **100**, 053002 (2008).
- [31] P. L. Silvestrelli, *J. Phys. Chem. A* **113**, 5224 (2009).
- [32] S. Grimme, J. Antony, S. Ehrlich, and H. Krieg, *J. Chem. Phys.* **132**, 154104 (2010).
- [33] A. Ambrosetti and P. L. Silvestrelli, *Phys. Rev. B* **85**, 073101 (2012).
- [34] A. Tkatchenko, R. A. DiStasio, Jr., R. Car, and M. Scheffler, *Phys. Rev. Lett.* **108**, 236402 (2012).
- [35] V. G. Ruiz, W. Liu, E. Zojer, M. Scheffler, and A. Tkatchenko, *Phys. Rev. Lett.* **108**, 146103 (2012).
- [36] A. Ruzsinszky, J. P. Perdew, J. Tao, G. I. Csonka, and J. M. Pitarke, *Phys. Rev. Lett.* **109**, 233203 (2012).
- [37] J. Tao and J. P. Perdew, *J. Chem. Phys.* **141**, 141101 (2014).
- [38] J. Tao and A. M. Rappe, *Phys. Rev. Lett.* **112**, 106101 (2014).
- [39] A. Ambrosetti and P. L. Silvestrelli, *Phys. Rev. B* **94**, 045124 (2016).
- [40] P. Jurecka, J. Sponer, J. Cerny, and P. Hobza, *Phys. Chem. Chem. Phys.* **8**, 1985 (2006).
- [41] T. Björkman, *J. Chem. Phys.* **141**, 074708 (2014).
- [42] P. Erhart, P. Hyldgaard, and D. Lindroth, *ACS Chem. Mater.* **27**, 5511 (2015).
- [43] D. O. Lindroth and P. Erhart, *Phys. Rev. B* **94**, 115205 (2016).
- [44] M. Muruganathan, J. Sun, T. Imamura, and H. Mizuta, *Nano Lett.* **15**, 8176 (2015).
- [45] H. Sadeghi, S. Santarash, and C. J. Lambert, *Sci. Rep.* **5**, 9514 (2015).
- [46] M. Mehboudi, A. M. Dorio, W. Zhu, A. van der Zande, H. O. H. Churchill, A. A. Pacheco-Sanjuan, E. O. Harriss, P. Kumar, and S. Baraza-Lopez, *Nano Lett.* **16**, 1704 (2016).
- [47] T. Rangel, K. Berland, S. Sharifzadeh, F. Brown-Altwater, K. Lee, P. Hyldgaard, L. Kronik, and J. B. Neaton, *Phys. Rev. B* **93**, 115206 (2016).
- [48] F. Brown-Altwater, T. Rangel, and J. B. Neaton, *Phys. Rev. B* **93**, 195206 (2016).
- [49] J. Löfgren, H. Grönbeck, K. Moth-Poulsen, and P. Erhart, *J. Phys. Chem. C* **120**, 12059 (2016).
- [50] B. Borca, V. Schendel, R. Petuya, I. Pentegov, T. Michnowicz, U. Kraft, H. Klauk, A. Arnau, P. Wahl, U. Schlickum, and K. Kern, *ACS Nano* **9**, 12506 (2015).
- [51] N. Ashcroft and N. Mermin, *Solid State Physics*, Holt-Saunders International Editions: Science: Physics (Holt, Rinehart and Winston, Philadelphia, 1976).
- [52] C. Kittel, *Introduction to Solid State Physics* (Wiley, New York, 1996).
- [53] [https://en.wikipedia.org/wiki/Thermal\\_expansion\\_coefficients\\_of\\_the\\_elements\\_\(data\\_page\)](https://en.wikipedia.org/wiki/Thermal_expansion_coefficients_of_the_elements_(data_page)).
- [54] J. P. Perdew, A. Ruzsinszky, G. I. Csonka, O. A. Vydrov, G. E. Scuseria, L. A. Constantin, X. Zhou, and K. Burke, *Phys. Rev. Lett.* **100**, 136406 (2008).
- [55] R. Armiento and A. E. Mattsson, *Phys. Rev. B* **72**, 085108 (2005).
- [56] See Supplemental Material at <http://link.aps.org/supplemental/10.1103/PhysRevB.95.085147> for a detailed quantitative presentation of *ab initio*-based modeling and for a per element comparison with experimentally observed thermophysical properties. Tables I, II, and III provide a detailed comparison at 300 K for structural and thermophysical properties of *3d*, *4d*, and *5d* nonmagnetic transition-metal elements, respectively. Table IV represents a comparison of cohesive energies, while Table V provides a specification of the PAW setups and the plane-wave energy cutoffs used in the calculations of different elements. Finally, Table VI summarizes and compares the terms that enter the computation of the cohesive energy in the case of vdW-DF-cx.
- [57] E. Ziambaras, J. Kleis, E. Schröder, and P. Hyldgaard, *Phys. Rev. B* **76**, 155425 (2007).
- [58] J. Sun, B. Xiao, and A. Ruzsinszky, *J. Chem. Phys.* **137**, 051101 (2012).
- [59] J. Sun, A. Ruzsinszky, and J. P. Perdew, *Phys. Rev. Lett.* **115**, 036402 (2015).
- [60] J. Tao and Y. Mo, *Phys. Rev. Lett.* **117**, 073001 (2016).
- [61] D. C. Langreth and J. P. Perdew, *Phys. Rev. B* **21**, 5469 (1980).
- [62] D. C. Langreth and S. H. Vosko, *Phys. Rev. Lett.* **59**, 497 (1987).
- [63] J. P. Perdew and Y. Wang, *Phys. Rev. B* **46**, 12947 (1992).
- [64] L. Hedin and B. I. Lundqvist, *J. Phys. C* **4**, 2064 (1971).
- [65] E. H. Lieb and S. Oxford, *Int. J. Quantum Chem.* **19**, 427 (1981).
- [66] A. Ruzsinszky and J. P. Perdew, *Comput. Theor. Chem.* **963**, 2 (2011).
- [67] J. P. Perdew, A. Ruzsinszky, J. Sun, and K. Burke, *J. Chem. Phys.* **140**, 18A533 (2014).

- [68] D. C. Langreth, M. Dion, H. Rydberg, E. Schröder, P. Hyldgaard, and B. I. Lundqvist, *Int. J. Quantum Chem.* **101**, 599 (2005).
- [69] E. D. Murray, K. Lee, and D. C. Langreth, *J. Chem. Theor. Comput.* **5**, 2754 (2009).
- [70] J. P. Perdew and Y. Wang, *Phys. Rev. B* **33**, 8800 (1986).
- [71] A. D. Becke, *J. Chem. Phys.* **140**, 18A301 (2014).
- [72] A. Puzder, M. Dion, and D. C. Langreth, *J. Chem. Phys.* **124**, 164105 (2006).
- [73] S. Li, V. R. Cooper, T. Thonhauser, A. Puzder, and D. C. Langreth, *J. Phys. Chem. A* **112**, 9031 (2008).
- [74] K. Berland and P. Hyldgaard, *J. Chem. Phys.* **132**, 134705 (2010).
- [75] K. Berland, Ø. Borck, and P. Hyldgaard, *Comput. Phys. Commun.* **182**, 1800 (2011).
- [76] M. Callsen and I. Hamada, *Phys. Rev. B* **91**, 195103 (2015).
- [77] O. A. Vydrov, and T. Van Voorhis, in *Fundamentals of Time-Dependent Density Functional Theory*, edited by M. A. L. Marques, N. Maitra, F. Nogueira, E. K. U. Gross, and A. Rubio (Springer, Berlin, 2012).
- [78] K. Lee, A. K. Kelkkanen, K. Berland, S. Andersson, D. C. Langreth, E. Schröder, B. I. Lundqvist, and P. P. Hyldgaard, *Phys. Rev. B* **84**, 193408 (2011).
- [79] K. Lee, K. Berland, M. Yoon, S. Andersson, E. Schröder, P. Hyldgaard, and B. I. Lundqvist, *J. Phys.: Condens. Matter* **24**, 424213 (2012).
- [80] E. Londero, E. K. Karlson, M. Landahl, D. Ostrovskii, J. D. Rydberg, and E. Schröder, *J. Phys.: Condens. Matter* **24**, 424212 (2012).
- [81] Y. Yao, N. Nijem, J. Li, Y. J. Chabal, D. C. Langreth, and T. Thonhauser, *Phys. Rev. B* **85**, 064302 (2012).
- [82] K. Tan, N. Nijem, P. Canepa, Q. Gong, J. Li, T. Thonhauser, and Y. J. Chabal, *Chem. Mater.* **24**, 3153 (2012).
- [83] R. Poloni, B. Smit, and J. B. Neaton, *J. Phys. Chem. A* **116**, 4957 (2012).
- [84] H. Liu, V. R. Cooper, S. Dai, and D.-e. Jiang, *J. Phys. Chem. Lett.* **3**, 3343 (2012).
- [85] K. Lee, W. C. Isley, A. L. Dzubak, P. Verma, S. J. Stoneburner, L.-C. Lin, J. D. Howe, E. D. Bloch, D. A. Reed, M. R. Hudson, C. M. Brown, J. R. Long, J. B. Neaton, B. Smit, C. J. Cramer, D. G. Truhlar, and L. Gagliardi, *J. Am. Chem. Soc.* **136**, 698 (2014).
- [86] R. Poloni, K. Lee, R. F. Berger, B. Smit, and J. B. Neaton, *J. Phys. Chem. Lett.* **5**, 861 (2014).
- [87] K. Tan, S. Zuluaga, Q. Gao, N. Nijem, J. Li, T. Thonhauser, and Y. J. Chabal, *Chem. Mater.* **27**, 2203 (2015).
- [88] S. Zuluaga, E. M. A. Fuentes-Fernandez, K. Tan, F. Xu, J. Li, Y. J. Chabal, and T. Thonhauser, *J. Mater. Chem. A* **4**, 5176 (2016).
- [89] R. Poloni and J. Kim, *Int. J. Quantum Chem.* **116**, 569 (2016).
- [90] E. Kuisma, C. F. Hansson, T. B. Lindberg, C. A. Gillberg, S. Idh, and E. Schröder, *J. Chem. Phys.* **144**, 184704 (2016).
- [91] F. Ortmann, W. G. Schmidt, and F. Bechstedt, *Phys. Rev. Lett.* **95**, 186101 (2005).
- [92] V. R. Cooper, T. Thonhauser, A. Puzder, E. Schröder, B. I. Lundqvist, and D. C. Langreth, *J. Am. Chem. Soc.* **130**, 1304 (2007).
- [93] S. Li, V. R. Cooper, T. Thonhauser, B. I. Lundqvist, and D. C. Langreth, *J. Phys. Chem. B* **113**, 11166 (2009).
- [94] K. Berland, S. D. Chakarova-Käck, V. R. Cooper, D. C. Langreth, and E. Schröder, *J. Phys.: Condens. Matter* **23**, 135001 (2011).
- [95] D. Le, A. Kara, E. Schröder, P. Hyldgaard, and T. S. Rahman, *J. Phys.: Condens. Matter* **24**, 424210 (2012).
- [96] S. D. Chakarova-Käck, O. Borck, E. Schröder, and B. I. Lundqvist, *Phys. Rev. B* **74**, 155402 (2006).
- [97] J. Kleis, E. Schröder, and P. Hyldgaard, *Phys. Rev. B* **77**, 205422 (2008).
- [98] K. Johnston, J. Kleis, B. I. Lundqvist, and R. M. Nieminen, *Phys. Rev. B* **77**, 121404 (2008).
- [99] K. Berland, T. L. Einstein, and P. Hyldgaard, *Phys. Rev. B* **80**, 155431 (2009).
- [100] J. Klimeš and A. Michaelides, *J. Chem. Phys.* **137**, 120901 (2012).
- [101] S. D. Chakarova-Käck, E. Schröder, B. I. Lundqvist, and D. C. Langreth, *Phys. Rev. Lett.* **96**, 146107 (2006).
- [102] G. Li, I. Tamblyn, V. R. Cooper, H.-J. Gao, and J. B. Neaton, *Phys. Rev. B* **85**, 121409 (2012).
- [103] J. Maurer, V. G. Ruiz, and A. Tkatchenko, *J. Chem. Phys.* **143**, 102808 (2015).
- [104] A. Tkatchenko, L. Romaner, O. T. Hofmann, E. Zojer, C. Ambrosch-Draxl, and M. Scheffler, *MRS Bull.* **35**, 435 (2010).
- [105] K. Berland and P. Hyldgaard, *Phys. Rev. B* **87**, 205421 (2013).
- [106] P. E. Blöchl, *Phys. Rev. B* **50**, 17953 (1994); G. Kresse and D. Joubert, *ibid.* **59**, 1758 (1999).
- [107] G. Kresse and J. Hafner, *Phys. Rev. B* **47**, 558 (1993); G. Kresse and J. Furthmüller, *ibid.* **54**, 11169 (1996).
- [108] L. Gharaee and P. Erhart, *J. Nucl. Mater.* **467**, 448 (2015).
- [109] L. Gharaee, J. Marian, and P. Erhart, *J. Appl. Phys.* **120**, 025901 (2016).
- [110] K. Lejaeghere, G. Bihlmayer, T. Björkman, P. Blaha, S. Blügel, V. Blum, D. Caliste, I. E. Castelli, S. J. Clark, A. D. Corso, S. d. Gironcoli, T. Deutsch, J. K. Dewhurst, I. D. Marco, C. Draxl, M. Dułak, O. Eriksson, J. A. Flores-Livas, K. F. Garrity, L. Genovese, P. Giannozzi, M. Giantomassi, S. Goedecker, X. Gonze, O. Grånäs, E. K. U. Gross, A. Gulans, F. Gygi, D. R. Hamann, P. J. Hasnip, N. A. W. Holzwarth, D. Iuşan, D. B. Jochym, F. Jollet, D. Jones, G. Kresse, K. Koepnik, E. Küçükbenli, Y. O. Kvashnin, I. L. M. Locht, S. Lubeck, M. Marsman, N. Marzari, U. Nitzsche, L. Nordström, T. Ozaki, L. Paulatto, C. J. Pickard, W. Poelmans, M. I. J. Probert, K. Refson, M. Richter, G.-M. Rignanese, S. Saha, M. Scheffler, M. Schlipf, K. Schwarz, S. Sharma, F. Tavazza, P. Thunström, A. Tkatchenko, M. Torrent, D. Vanderbilt, M. J. v. Setten, V. V. Speybroeck, J. M. Wills, J. R. Yates, G.-X. Zhang, and S. Cottenier, *Science* **351**, aad3000 (2016).
- [111] <http://molmod.ugent.be/deltacodesdft>.
- [112] D. C. Wallace, *Thermodynamics of Crystals* (Dover, Mineola, NY, 1998).
- [113] A. Togo and I. Tanaka, *Scr. Mater.* **108**, 1 (2015).
- [114] P. Vinet, J. R. Smith, J. Ferrante, and J. H. Rose, *Phys. Rev. B* **35**, 1945 (1987).
- [115] P. Giannozzi, S. Baroni, N. Bonini, M. Calandra, R. Car, C. Cavazzoni, D. Ceresoli, G. L. Chiarotti, M. Cococcioni, I. Dabo, A. D. Corso, S. de Gironcoli, S. Fabris, G. Fratesi, R.

- Gebauer, U. Gerstmann, C. Gougoussis, A. Kokalj, M. Lazzeri, L. Martin-Samos, N. Marzari, F. Mauri, R. Mazzarello, S. Paolini, A. Pasquarello, L. Paulatto, C. Sbraccia, S. Scandolo, G. Sclauzero, A. P. Seitsonen, A. Smogunov, P. Umari, and R. M. Wentzcovitch, *J. Phys.: Condens. Matter* **21**, 395502 (2009).
- [116] X. Gonze, G. M. Rignanese, M. Verstraete, J. M. Beuken, Y. Pouillon, R. Caracas, F. Jollet, M. Torrent, G. Zerah, M. Mikami, P. Ghosez, M. Veithen, J. Y. Raty, V. Olevanov, F. Bruneval, L. Reining, R. Godby, G. Onida, D. R. Hamann, and D. C. Allan, *Z. Kristall.* **220**, 558 (2005).
- [117] Y. Zhang and W. Yang, *Phys. Rev. Lett.* **80**, 890 (1998).
- [118] Y. M. Smirnov and V. A. Finkel, *Sov. Phys. JETP* **22**, 750 (1966).
- [119] J. Merker, D. Lupton, M. Töpfer, and H. Knake, *Platinum Met. Rev.* **45**, 74 (2001).

# Paper V

**Structurally driven asymmetric miscibility in the phase diagram of W-Ti**

Leili Gharaee, Mattias Ångqvist, Magnus Rahm and Paul Erhart

(In manuscript)



# Structurally driven asymmetric miscibility in the phase diagram of W-Ti

Laili Gharaee, Mattias Ångqvist, Magnus Rahm, and Paul Erhart\*  
*Chalmers University of Technology, Department of Physics, Gothenburg, Sweden*

Phase diagrams for multi-component systems represent crucial information for understanding and designing materials but are very time consuming to assess experimentally. Computational modeling plays an increasingly important role in this regard but has been largely focused on systems with matching lattice structures and/or stable boundary phases. Here, using a combination of density functional theory calculations, alloy cluster expansions, free energy integration, and Monte Carlo simulations, we obtain the phase diagram of W-Ti, a system that features metastable boundary phases on both sides of the phase diagram. We find that the mixing energy on the body-centered cubic (BCC) lattice is asymmetric and negative with a minimum of about  $-120$  meV/atom, whereas for the hexagonal closed packed (HCP) lattice the mixing energy is positive. By combining these data with a model for the vibrational free energy, we derive a propose a revision of the W-rich end of the phase diagram with a much larger solubility of Ti in BCC-W than predicted previously. Finally, by comparison with the W-V and W-Re system we demonstrate how strongly asymmetric phase diagrams can arise from a subtle energy balance of stable and metastable lattice structures.

## I. INTRODUCTION

Metallic alloys play a crucial role in technology and are of continuing interest in basic research. The most simple alloys comprise two components; these so-called binary systems can usually be categorized according to whether the interaction between the two constituents is repulsive (positive mixing energy) or attractive (negative mixing energy). In the former case, examples for which include Cu-Ag<sup>1-3</sup> and Fe-Cu<sup>1,4-6</sup>, one commonly observes a wide two-phase region (often referred to as the miscibility gap). Attractive interactions, on the other hand, give rise to the formation of solid solutions, e.g., in Au-Ag<sup>1,7</sup> or W-V<sup>1,8</sup>, and the formation of intermetallic phases as in the case of Fe-Pt<sup>1,9-11</sup> or Ni-Al<sup>1,12,13</sup>.

The interaction between the constituents is usually symmetric, in the sense that if  $A$  dissolves in  $B$ , so does  $B$  in  $A$ . Exceptions from this behavior are rather uncommon; a prominent example is the Fe-Cr system<sup>14,15</sup>, for which the dissolution of Cr in Fe is energetically favorable whereas the opposite applies for Fe in Cr<sup>16,17</sup>. As a result of this inversion in the mixing energy, the phase diagram is very asymmetric with a large solubility on the Fe-rich and a very small solubility on the Cr-rich side. This behavior, which at first sight might be unexpected given a very small size mismatch and identical lattice structures, can be rationalized in terms of the magnetic structure<sup>17,18</sup> with Fe and Cr preferring ferro and antiferromagnetic ordering, respectively.

Here, we show that strongly asymmetric phase diagrams can also be obtained in non-magnetic systems as a result of an antisymmetry in lattice structures and their energetics. In doing so, we also demonstrate the usage of the variance constrained semi-grand canonical Monte Carlo technique<sup>19,20</sup> for extracting the complete free energy surfaces. Specifically, we consider the W-Ti system. Titanium exhibits a temperature driven transition from a low-temperature hexagonal closed packed (HCP,  $\alpha$ -Ti) phase to a high-temperature body-centered cubic (BCC) phase ( $\beta$ -Ti) that is stabilized by vibrations<sup>21</sup>. Tungsten is a refractory metal that maintains a body-centered cubic (BCC) structure up to the melting point. Close-packed structures including HCP are much higher in

energy and can only be stabilized at very high pressures<sup>22,23</sup>.

The W-Ti system is also of interest because its experimental assessment is aggravated by the high melting point of tungsten and the accompanying slow kinetics, which render the systematic exploration of the phase diagram, in particular the W-rich side, very cumbersome. Since experimental data points for tungsten concentrations  $\gtrsim 30\%$  are only available down to 1473 K<sup>24,25</sup>, the W-Ti system has been assessed using rather severe assumptions<sup>25-28</sup>. It must be emphasized, however, that in spite of slow kinetics the low-temperature phase diagram of refractory alloy systems have a bearing, e.g., for the behavior under intense irradiation conditions such as in fusion reactors in so far as they determine the thermodynamic driving forces. Tungsten alloys in particular are being considered for key components in fusion reactors that must sustain extreme mechanical and irradiation loads for prolonged periods of time<sup>29-31</sup>.

In the following, using a combination of density functional theory (DFT) calculations, alloy cluster expansions (CEs), Monte Carlo (MC) simulations in the variance constrained semi-grand canonical (VCSGC) ensemble, and thermodynamic data for the pure elements<sup>32</sup>, we provide a reassessment of the W-Ti phase diagram below the solidus line. In doing so, we demonstrate (*i*) that the solubility of Ti in W exceeds 20% down to zero temperature in stark contrast to previous thermodynamic assessments<sup>26-28</sup> while the inverse solubility is practically zero up to the HCP-BCC transition. Furthermore, it is shown (*ii*) that this asymmetry originates from a change of sign of the BCC-HCP free energy difference as a function of composition, which remains comparably small in magnitude. In addition to providing a new perspective on the W-Ti system, the present results illustrate how strongly asymmetric phase diagrams can originate in non-magnetic systems, and illustrate a methodology that can handle multiple miscibility gaps in systems with several different lattice types.

The remainder of this paper is organized as follows. The next section provides an overview of the computational techniques employed in this work. The thermodynamic framework used to analyze the free energy landscapes and construct the phase diagram is outlined in Sect. II D. The results of our computations are presented in Sect. III, after we discuss

the implications for the W–Ti system in particular and put the present results in context in Sect. IV.

## II. COMPUTATIONAL METHODOLOGY

### A. Alloy cluster expansions

In the present work, we employ lattice Hamiltonians to represent the energy of the system as a function of composition and distribution of the elements. These alloy cluster expansions (CE) can be written in the general form<sup>33</sup>

$$\Delta E = \Delta E_0 + \sum_{\alpha} m_{\alpha} J_{\alpha} \bar{\Pi}_{\alpha}(\boldsymbol{\sigma}), \quad (1)$$

where  $\Delta E$  denotes the mixing energy. The summation runs over all symmetry inequivalent clusters  $\alpha$  with multiplicity  $m_{\alpha}$  and effective cluster interaction (ECI)  $J_{\alpha}$ . The cluster correlations  $\bar{\Pi}_{\alpha}$  are computed as symmetrized averages of products over the pseudospin vector  $\boldsymbol{\sigma}$ . The latter represent the occupation of lattice sites by W ( $\sigma = -1$ ) and Ti ( $\sigma = +1$ ).

In the present work, we considered cluster vector spaces with up to 2,000 distinct clusters including clusters up to fifth order (quintuplets). Inclusion of clusters of high order was necessary due to the very asymmetric shape of the mixing energy as a function of composition (see below). In fact, it is probably possible to obtain more compact CEs by using concentration dependent ECIs<sup>34</sup>, yet for practical reasons in the present case we did not consider this option.

For training of CEs, we systematically enumerated all structures with up to 12 atoms in the unit cell<sup>35,36</sup>, which yields 10,846 and 5,777 structures for BCC and HCP lattices, respectively. Based on this pool of structures, we relaxed and evaluated the energy of more than 1,700 BCC and 900 HCP structures using density functional theory (DFT) as described in Sect. II C. Since both BCC-Ti<sup>21</sup> and HCP-W are structurally unstable, several configurations did not maintain their initial lattice structure.<sup>37</sup> To exclude these structures, each configuration was mapped back onto its respective ideal lattice structure. If the displacement of any atom exceeded 0.4 Å, the configuration was removed from the pool of structures.

The ECIs were obtained using the compressive sampling technique<sup>38</sup> adapted for CE construction<sup>39</sup> as implemented in our in-house integrated CE tool ICET. The split Bregman algorithm<sup>40,41</sup> was employed to solve the optimization problem using parameters of  $\mu = 0.1$  and  $\lambda = 35$  (see Refs. 39 and 41 for a discussion regarding the role of these parameters). These parameters were chosen based on a preliminary screening of CEs. We note that while their specific values have little effect on the final CE within reasonable bounds<sup>39</sup>, they impact the efficiency of the optimization procedure.

In order to construct CEs the sets of structures were separated into a training set (BCC: 1,350 structures; HCP: 500) and a validation set (BCC: 200; HCP: 50). Eighty different combinations of training and validation set were randomly drawn from the pool of available structures, and for each one a CE was generated. The final CEs were obtained by averaging over the CEs constructed for each lattice type. This

was followed by pruning step, during which clusters were removed, for which the absolute value of the ECI was less than half of the respective standard deviation. In our experience using statistical sampling over many training and validation sets provides a more conservative estimated for the predictive power of our CEs than the leave-one-out cross validation score. A similar approach was also adopted, e.g., in Ref. 42; here, however, we opted to use random structure selection for practical reasons.

### B. Monte Carlo simulations

The final CEs were sampled using Monte Carlo (MC) simulations. In order to be able to construct the full free energy landscape of the crystalline phases (see Sect. II D below), we require the free energy for BCC and HCP phases separately, as a *continuous* function of composition. This prevents us from using the semi-grand canonical (SGC) ensemble. While the latter does provide access to the first derivative of the free energy with respect to composition, it does not allow sampling multiphase regions, which as will be seen below are present for both BCC and HCP lattices. To overcome this limitation we employ the variance constrained semi-grand canonical (VCSGC) ensemble. It includes an additional term in the partition function that effectively imposes a constraint on the fluctuations of the concentration, which diverge in multiphase regions. The VCSGC-MC approach has been successfully employed previously to describe multiphase equilibria in, e.g., Fe–Cr<sup>19</sup> and Fe–Cu alloys<sup>43,44</sup>. The VCSGC ensemble is sampled by randomly selecting a site in the system, swapping its chemical identity, and accepting this trial move with probability<sup>19</sup>

$$\mathcal{P} = \min \left\{ 1, \exp \left[ -\beta \Delta E - \kappa \Delta N_B (\phi + \Delta N_B / N + 2N_B / N) \right] \right\}. \quad (2)$$

Here,  $\Delta E$  is the energy change associated with the move,  $\Delta N_B$  is the change in the number of particles of type  $B$ ,  $N$  is the total number of sites (atoms) in the simulation cell, and  $\phi$  and  $\kappa$  are the average and variance constraint parameters. We employed  $\kappa = 200$  throughout; this choice provides a contiguous sampling of the concentration axis while maintaining a high acceptance rate and, in our experience, works almost universally for the systems that we have considered so far. The average constraint parameter  $\phi$  was varied in steps of 0.02 from  $-2.2$  to  $0.2$ . In the VCSGC ensemble the first derivative of the free energy is related to the (ensemble) average of the concentration  $\langle c_B \rangle = \langle N_B \rangle / N$ ,

$$\beta \partial \Delta F / \partial c = \kappa (\phi + 2 \langle c_B \rangle), \quad (3)$$

which allows one to obtain the free energy of mixing.

MC simulations were carried out at temperatures between 400 and 1800 K in 100 K intervals using  $5 \times 5 \times 5$  and  $4 \times 4 \times 4$  supercells of the primitive unit cell for BCC and HCP structures, respectively. At each value of  $\phi$  the configuration was equilibrated for 50 MC cycles, followed by 150 MC cycles for gathering statistics.

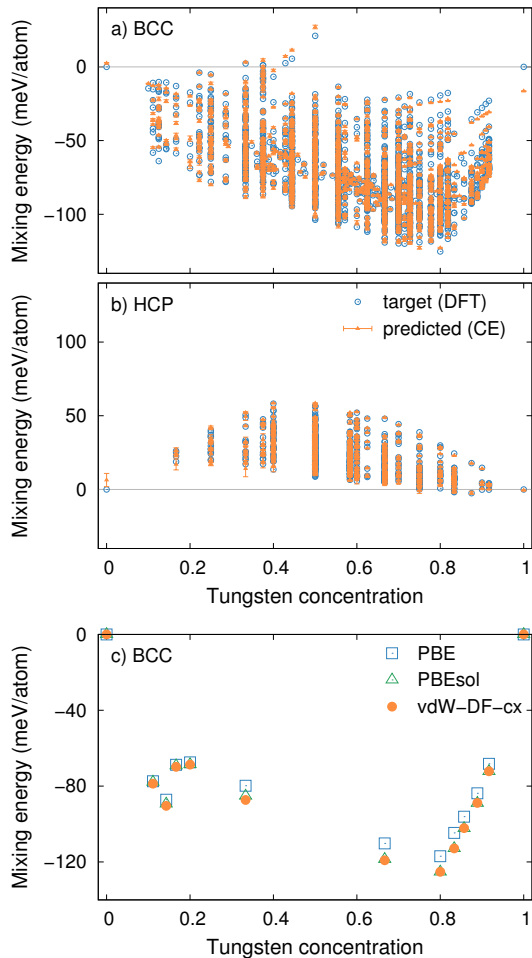


FIG. 1. Mixing energy for all (a) BCC and (b) HCP structures, for which DFT reference calculations were performed. The error bars represent the standard deviation that was computed by averaging over 80 different CEs that were constructed. Each CE corresponds to a different training and validation set. The final CE to be used in the MC simulations was obtained by averaging over these CEs as described in the text. (c) Comparison of the mixing energy computed using different exchange-correlation functionals for selected BCC structures.

### C. Density functional theory calculations

Density functional theory (DFT) calculations were carried out using the projector augmented wave method (PAW)<sup>45,46</sup> as implemented in the Vienna ab initio simulation package (VASP)<sup>47,48</sup>. Electronic semi-core states (W-5*p*, Ti-3*p*) were treated as part of the valence and calculations employed a plane wave energy cutoff of 450 eV. Brillouin zone integrations were carried out using  $\Gamma$ -centered *k*-point grids with an average spacing of 0.15/Å, corresponding to a 19 × 19 × 19 mesh relative to the primitive BCC cell and a 18 × 18 × 9 mesh relative to the primitive HCP cell. These computational settings are very tight and have been shown previously to yield well converged results<sup>49</sup>.

Using first-order Methfessel-Paxton smearing with a width

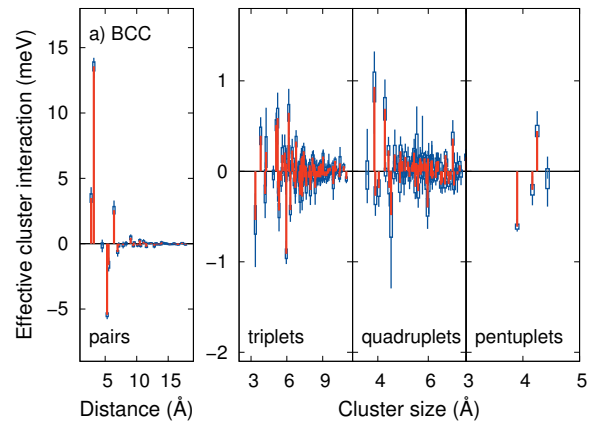


FIG. 2. Effective cluster interactions (ECIs) for the cluster expansion for the BCC lattice. The vertical bars and boxes indicate average and standard deviation of the respective ECI obtained from averaging over 80 CEs corresponding to different choices of training and validation set.

of 0.2 eV, both ionic positions and cell shapes were relaxed until residual forces were below 5 meV/Å and stresses below 0.5 kbar. The total energy of the final structures was subsequently computed without further relaxation using the tetrahedron method with Blöchl corrections.

Exchange and correlation effects were described using the van der Waals density functional (vdW-DF) method that captures nonlocal correlations<sup>50,51</sup> in combination with a consistent description of exchange (vdW-DF-cx)<sup>52</sup> as implemented in VASP<sup>53,54</sup>. We have recently established that this functional provides a description of the thermophysical properties of non-magnetic transition metals that is at least on par with but usually exceeds other constraint-based functionals<sup>55</sup>, notably PBE<sup>56</sup> and PBEsol<sup>57</sup>. To assess the effect of the exchange-correlation functional, we conducted supplementary calculations using the latter functionals for selected structures close to the BCC convex hull.

### D. Thermodynamic methodology

In order to construct the phase diagram, we consider the free energy landscape of the W-Ti system as a function of temperature *T*, W concentration *c*, and structure  $\alpha$ . From the MC simulations described above, we can extract the mixing free energy  $\Delta G_{\alpha}^{\text{mix}}(c, T)$  for  $\alpha = \text{BCC}$  or HCP, which includes the contributions due to mixing energy  $\Delta H_{\alpha}^{\text{mix}}(c, T)$  and configurational entropy  $\Delta S_{\alpha}^{\text{mix}}(c, T)$ . Here, since ionic and cell relaxations are implicitly included in the ECIs, we have  $\Delta G_{\alpha}^{\text{mix}} \approx \Delta F_{\alpha}^{\text{mix}}$  and from here on we will therefore refer only to  $\Delta G$  and  $\Delta H$ .

To obtain the full Gibbs free energy, we must also take into account the vibrational contributions, which are not accounted for in the CE. Since a full evaluation of the vibrational contribution as a function of composition is very demanding due to the importance of anharmonic contributions for Ti-rich BCC

and W-rich HCP structures, we here approximate the vibrational contribution by a linear interpolation of the elemental free energies plus a correction for the strong anharmonicity of the metastable BCC-Ti phase. We thus write the total Gibbs free energy for phase  $\alpha$  as

$$G_\alpha(c, T) = (1 - c) G_\alpha^W(T) + c G_\alpha^{\text{Ti}}(T) + \Delta G_{\text{mix}}(c, T) + \Delta H_\alpha^{\text{anh}}(c). \quad (4)$$

For both  $G_\alpha^W(T)$  and  $G_\alpha^{\text{Ti}}(T)$ , we resort to thermodynamic assessments available from the CALPHAD framework<sup>32</sup>. Equation 4 contains an anharmonic correction term  $\Delta H_\alpha^{\text{anh}}(c)$ , which is motivated by an analysis of the lattice energy of BCC and HCP-Ti that was carried out using molecular dynamics (MD) simulations. The latter were carried out using the LAMMPS code<sup>58</sup> and on a classical interatomic potential for Ti of the modified embedded atom method (MEAM) type<sup>59</sup>. Simulations were conducted for  $6 \times 6 \times 6$  and  $6 \times 6 \times 4$  supercells of BCC and HCP, respectively, using a Nosé-Hoover thermostat and barostat.

### III. RESULTS

#### A. Cluster expansions of mixing energies

The DFT calculations reveal a negative mixing energy for BCC structures [Fig. 1(a)], which is in contrast to previous thermodynamic assessments based on experimental data, which have assumed a positive mixing energy over the entire composition range<sup>26–28</sup>. The shape of the mixing energy is very asymmetric with several structures along the convex hull. The lowest mixing energy is obtained for a structure at 80% W. This structure has space group 166 ( $R\bar{3}m$ ) and contains 5 atoms in the primitive unit cell.<sup>60</sup> For selected structures along the convex hull, we recalculated the mixing energies using the PBE and PBEsol functionals [Fig. 1(c)]. In particular between the PBEsol and vdW-DF-cx functionals the deviations are below one percent.

In the CE formalism employed in the present work, reproducing the asymmetric shape of the mixing energy required including clusters up to fifth order and extending over rather long range [Fig. 2(a)]. The final CE to be used in the MC simulations was obtained by averaging over 80 different CEs each corresponding to a different choice of training and validation set (see Sect. II A for details). The average root mean square error over the validation sets is 4 meV/atom and the final CE generally achieves very good agreement with the DFT reference data [Fig. 1(a)]. The accuracy and predictiveness of the CE is also evident from the small variation of the mixing energy between different CEs [indicated by the error bars in Fig. 1].

In contrast to the BCC lattice, the mixing energy for the HCP lattice is positive yet also asymmetric [Fig. 1(b)]. Here, the average root mean square error over the validation sets is 5 meV/atom.

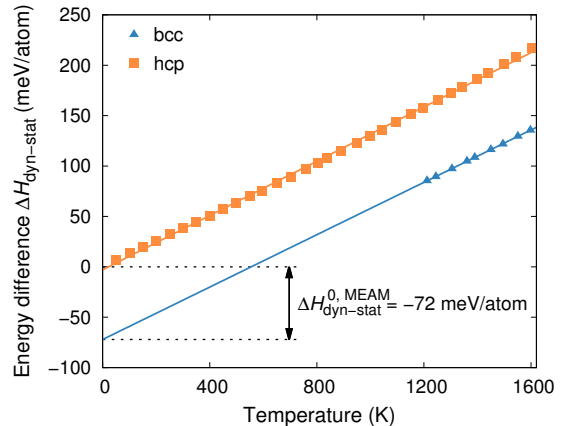


FIG. 3. Difference between the average potential energy at finite temperature and the static lattice energy for HCP and BCC-Ti as obtained from MD simulations using the Ti-MEAM potential from Ref. 59.

#### B. Anharmonicity

In classical simulations the average potential energy of a system approaches its static value as the temperature goes to zero (Fig. 3). This behavior is observed for example for HCP-Ti as described using the MEAM potential from Ref. 59. This potential was fitted to PBE-DFT data and provides a very accurate representation of not only the energetics of the HCP but also the BCC and  $\omega$  phases. The average potential energy of the BCC-Ti phase as described by this potential does not approach its static value but rather extrapolates to a value of  $\Delta H_{\text{dyn-stat}}^{0, \text{MEAM}} = -72$  meV/atom (Fig. 3).

This behavior originates from the metastable character of the BCC phase and its mechanical instability at zero K, which implies a strongly anharmonic potential well. By contrast, both BCC-W and HCP-Ti are stable at zero temperature and their dynamical behavior up to moderate temperatures can be comfortably described within the quasi-harmonic approximation<sup>55</sup>.

The  $\Delta H_{\text{dyn-stat}}^0$  term is effectively included in the difference of the Gibbs free energies for Ti  $G_{\text{BCC}}^{\text{Ti}}(T) - G_{\text{HCP}}^{\text{Ti}}(T)$  as described by the CALPHAD parametrization<sup>32</sup>. The mixing energy based on which the BCC-CE has been constructed, however, is computed relative to the static BCC-Ti energy. To achieve a consistent thermodynamic description we must thus account for the variation of  $\Delta H_{\text{dyn-stat}}^0$  with composition, i.e. we must express  $\Delta H_\alpha^{\text{anh}}(c)$  in Eq. (4). Unfortunately, a comprehensive analysis of anharmonic behavior is already computationally demanding for the elemental phases<sup>23,61,62</sup>. In the present case, we therefore make the basic assumption that  $\Delta H_\alpha^{\text{anh}}(c)$  smoothly approaches  $-\Delta H_{\text{dyn-stat}}^0$  with increasing W concentration, canceling out the implicit inclusion of this term in  $G_{\text{BCC}}^{\text{Ti}}(T) - G_{\text{HCP}}^{\text{Ti}}(T)$ . We chose a simple cubic functional form

$$\Delta H_{\text{BCC}}^{\text{anh}}(c) = -\Delta H_{\text{dyn-stat}}^0 \begin{cases} 1 - (1 - c/c_s)^3 & c < c_s \\ 1 & c \geq c_s \end{cases} \quad (5)$$

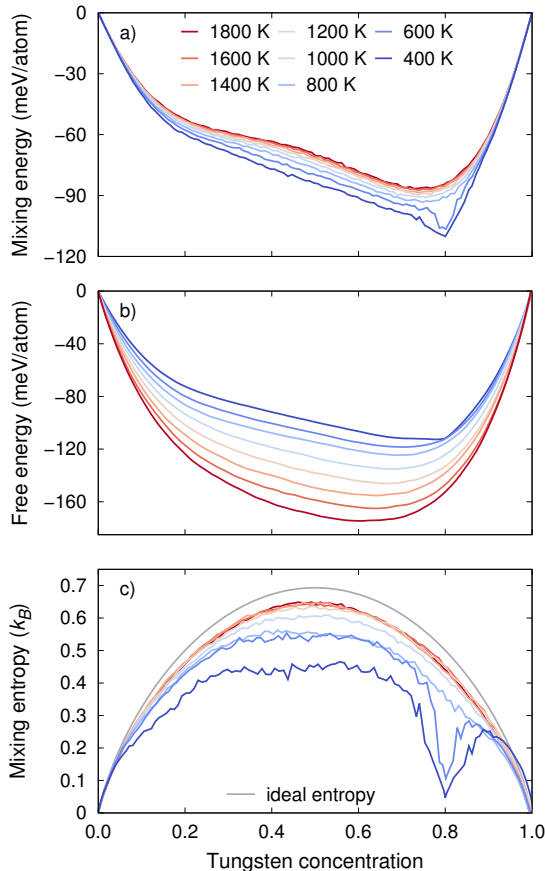


FIG. 4. (a) Mixing energy, (b) free energy of mixing, and (c) mixing entropy as a function of composition from VCSGC-MC simulations based on the CE constructed for BCC in this work.

where  $\Delta H_{\text{dyn-stat}}^0$  is given by the difference between the BCC-HCP free energy difference at the lowest temperature available from CALPHAD (298.15 K)<sup>32</sup> and the BCC-HCP energy difference from DFT  $\Delta H_{\text{dyn-stat}}^{0,\text{DFT}/\text{CALPHAD}} = -56$  meV/atom. Equation (5) then contains a single parameter  $c_s$  that determines the concentration at which the correction is fully applied. The thermodynamic analysis presented below was conducted using a value of  $c_s = 0.5$ , unless otherwise noted.

We note that a similar correction should in fact also be considered for HCP-W vs BCC-W. As a result of the much larger energy difference between these structures, this effect is, however, insignificant and has not been considered further (also see Sect. IV).

### C. Free energy landscape

The CEs for BCC and HCP lattices were sampled by MC simulations as detailed in Sect. II B. The (finite temperature) BCC mixing energy maintains the asymmetric shape of the zero-temperature data [Fig. 4(a)]. It also clearly reveals the emergence of a particularly stable configuration at 80% W, which corresponds to the ground state described above.

From the MC simulations, we furthermore obtained the first derivative of the free energy with respect to concentration via Eq. (3), which was integrated using the trapezoidal rule to yield the mixing free energy [Fig. 4(b)]. Below the free energy of mixing will be used to construct the convex hull and the phase diagram.

By combining mixing free energy and energy, one can extract the entropy of mixing according to

$$\Delta S_{\text{mix}} = (\Delta H_{\text{mix}} - \Delta G_{\text{mix}}) / T. \quad (6)$$

At low temperatures the actual mixing entropy deviates strongly from that of an ideal solution and the ordered structure at 80% W is clearly visible as a pronounced reduction in the mixing entropy [Fig. 4(c)]. At higher temperatures this feature is smoothed out and the mixing entropy becomes closer to that of an ideal solution. Nonetheless, the very pronounced features in the entropy clearly demonstrate the importance of an accurate treatment of alloy thermodynamics beyond simple approximations.

In the case of the HCP structures, mixing energies, free energies, and entropies were obtained in similar fashion as for the BCC lattice. Due to the positive mixing energy, these quantities are, however, much closer to those of an ideal solution and hence are not shown here explicitly. Their determination is nonetheless important in order to obtain a consistent and comprehensive description of the thermodynamics of the relevant crystalline phases.

### D. Phase diagram

After having determined the free energies of both BCC and HCP phases, one can construct the full temperature, composition, and structure dependent free energy landscape, from which the phase diagram can be extracted. To this end, the free energies for the different phases were combined as described in Sect. II D. In accordance with experimental reality, our analysis yields three distinct stable crystalline phases, namely a Ti-rich HCP phase (HCP-Ti), a Ti-rich BCC phase (BCC-Ti), and a W-rich BCC phase (BCC-W).

At a temperature of 600 K, the HCP-Ti phase is in equilibrium with BCC-W [Fig. 5(a)] with the latter phase exhibiting a wide stability range with a solubility limit of 64% W. This substantially differs from the values  $\gtrsim 80\%$  predicted by CALPHAD assessments based on partial experimental data supplemented by approximations for the mixing energy<sup>27,28,63</sup>. Similarly, at a temperature of 800 K we obtain all three phases [Fig. 5(b)].

In order to obtain a description of the phase diagram at all intermediate temperatures, we followed the common approach in alloy thermodynamics of representing the free energy of mixing in terms of a Redlich-Kister expansion

$$\Delta G(x, T) = x(1-x) \sum_{p=0}^n L_p(T)(1-2x)^p, \quad (7)$$

up to order  $n = 4$ . We then represented the temperature dependence of each of the ten (five per lattice) Redlich-Kister

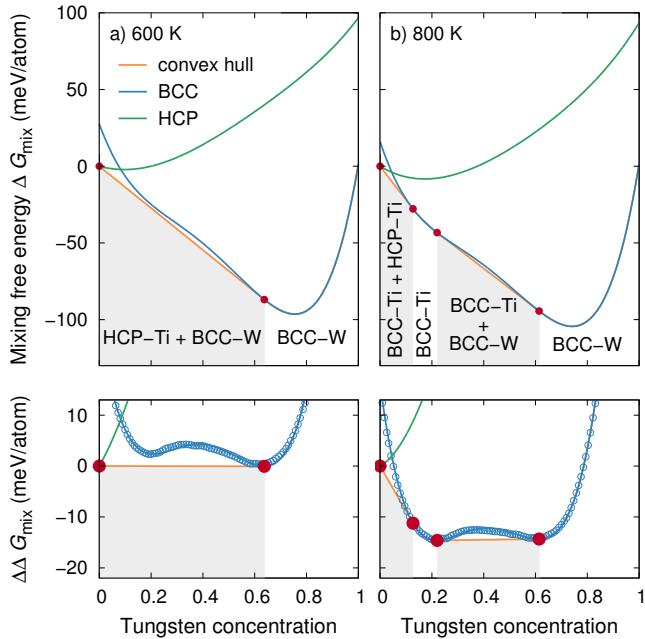


FIG. 5. Mixing free energy as a function of composition at (a) 600 K and (b) 800 K. The top row is based on the Redlich-Kister expansion of the free energy landscape obtained from VCSGC-MC simulations. The data obtained from the latter are shown by the open circles in the bottom row in comparison with the expansion (solid blue line). For clarity of the visualization, the bottom panel a linear term has been subtracted from the mixing energy,  $\Delta\Delta G_{\text{mix}}(c) = \Delta G_{\text{mix}}(c) - m \cdot c$ , where  $m$  has been chosen to yield zero slope for the convex hull in the central two-phase regions. The two-phase regions are highlighted in gray.

coefficients  $L_p$  by third-order polynomials. The interpolated mixing free energies are in very good agreement with our VCSGC-MC data [see points and blue lines in the bottom row of Fig. 5], which allows us to extract the phase boundaries as a continuous function of temperature.

The thus obtained phase diagram [Fig. 6] shows the same phases and phase equilibria as the experimental one. The calculated phase boundary between BCC-W and the BCC-Ti+BCC-W two-phase region intersects precisely the two experimental data points at 1400 K. Also the upper temperature of the BCC-Ti+BCC-W two-phase region of 1560 K is in good agreement with experiment, although the position of the maximum is predicted at a W concentration of 42% as opposed to approximately 30% in the experiments. The large high-temperature solubility thus results from a *negative* mixing energy on the BCC lattice, which also gives rise to *finite* solubility limit of  $> 20\%$  for Ti in BCC-Ti down to zero temperature.

The eutectoid on the Ti-rich side of the phase diagram is underestimated compared to experiment (646 K vs 1013 K), which comes with an overestimation of the eutectoid point (20% vs 9%). The larger errors on the Ti-rich side are unsurprising given the difficulties associated with the strong anharmonicity of BCC-Ti, which are only treated approximately in this work. We note that we tested different values for  $c_s$  pa-

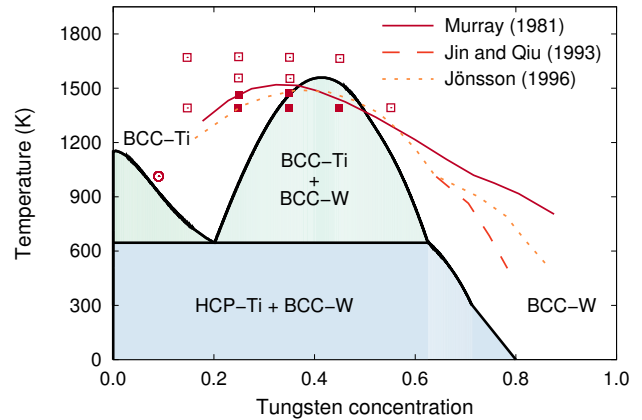


FIG. 6. Phase diagram predicted based on the simulations in the present work in comparison with experimental data (symbols) from Ref. 24 and thermodynamic assessments of the BCC-W phase boundary (lines) from Refs. 25, 28, and 63. Filled and empty squares indicate two-phase and single-phase regions, respectively.

rameter in Eq. (5) and found the general shape of the phase diagram to be unaffected. Larger (smaller) values of  $c_s$  shift the BCC-W solubility limit further to the W-rich side and tend to increase (decrease) the maximum of the BCC-Ti+BCC-W two phase region.

## IV. DISCUSSION AND CONCLUSIONS

### A. Relevance for the W-Ti system

Above we have demonstrated that the solubility of Ti in BCC-W at low temperatures is larger than previously predicted and remains finite as the temperature approaches zero. This conclusion was reached by combining DFT calculations with effective lattice Hamiltonians, Monte Carlo simulations, and thermodynamic modeling. By comparison, previous studies were based on experimental data, which is only available at temperatures above 1473 K. We note that while the low temperature region of the phase diagrams of refractory metals are exceedingly difficult to sample in equilibrium, they are nonetheless relevant as they determine the driving forces under extreme non-equilibrium situations such as encountered under ion irradiation.

### B. General implications

While the present finding pertains to our understanding of the W-Ti phase diagram, it has more general implications for alloy thermodynamics. As outlined in the introduction, binary phase diagrams of metals that exhibit strongly asymmetric solubility are relatively rare. While as demonstrated in the case of the Fe-Cr system, they can arise from competing forms of magnetic order, here we show that this effect can also

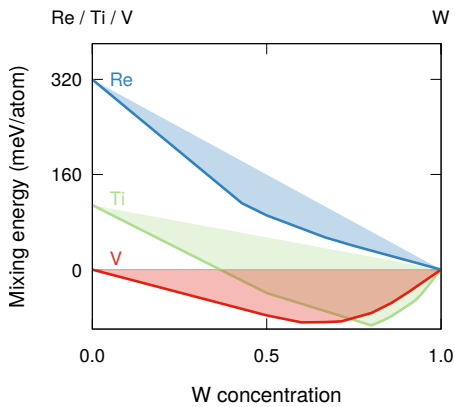


FIG. 7. Schematic illustration of mixing energies for BCC structures of W-V, W-Ti, and W-Re based on data from Ref. 64. In the case of the latter two alloys, the energy offset in the Ti/Re-rich limit represents the HCP-BCC energy difference. The figure illustrates that the occurrence of a finite solubility at zero temperature in the case of W-Ti is the result of a combination of a negative mixing energy on the BCC lattice and not-too-large HCP-BCC energy difference.

be observed in non-magnetic systems as a result of different lattice structures.

To illustrate this effect consider the mixing energies of W-V (BCC) and W-Re (BCC and HCP) in comparison with W-Ti (Fig. 7; data from Ref. 64). In the case of W-V both end members are BCC, the mixing energy is negative and the phase diagram shows an extended miscibility range (and is symmetric). In the case of W-Re, the calculations yield a negative mixing energy for BCC and an almost vanishing mixing energy for the HCP lattice, very similar to the case of W-Ti described above. The (free) energy difference between HCP-Re (the ground state) and BCC-Re is, however, much larger than in the case of Ti. As a result, the negative mixing energy of the BCC lattice is shifted upward such that the solubility of Re in BCC-W is rather small and approaches zero with vanishing temperature.

The comparison with W-V and W-Re demonstrates that the occurrence of an asymmetric phase diagram in W-Ti is the result of a negative mixing energy on the BCC lattice in combination with a HCP-BCC energy difference that is not too large. This reasoning implies that similar behavior can be expected

in other systems that combine different lattice structures with elements that have metastable structures. By extension, this should also apply to effective (“quasi”) phase diagrams between compounds.

### C. Computational modeling

Using conventional sampling techniques based on either the semi-grand canonical or canonical ensembles, one cannot simultaneously sample multi-phase regions and derivatives of the free energy.<sup>65</sup> In the present work, however, we have tackled a system that combines different lattice structures with miscibility gaps. This required the ability to obtain the free energy profile for the different phases as a continuous function of composition (and temperature). Here, we were able to achieve this by using the VCSGC-MC approach, and have thereby demonstrated the power of this methodology to extract free energies and phase diagram information. This suggests that in the future the VCSGC-MC method can be of great utility as the reach of *ab initio* alloy thermodynamics widens to address more complex and demanding challenges.

### D. Shortcomings and outlook

Arguably the biggest approximation adopted in the present work concerns the description of anharmonic contributions to the free energy. As alluded to above, a direct assessment of the vibrational contributions to the free energy as a function of composition is computationally very demanding<sup>23,61,62</sup>. While for vibrationally stable systems this can be achieved within the harmonic approximation<sup>66-68</sup>, a more comprehensive treatment of the anharmonicity in alloys will represent the next logical step in the development of computational alloy thermodynamics.

### ACKNOWLEDGMENTS

This work was supported by the Swedish Research Council and the Knut and Alice Wallenberg foundation. Computer time allocations by the Swedish National Infrastructure for Computing at NSC (Linköping) and PDC (Stockholm) are gratefully acknowledged.

\* erhart@chalmers.se

<sup>1</sup> T. Massalski, ed., *Binary Alloy Phase Diagram* (ASM International, Materials Park, Ohio, 1990).  
<sup>2</sup> R. Najafabadi, D. J. Srolovitz, E. Ma, and M. Atzmon, *Journal of Applied Physics* **74**, 3144 (1993).  
<sup>3</sup> P. L. Williams, Y. Mishin, and J. C. Hamilton, *Modelling and Simulation in Materials Science and Engineering* **14**, 817 (2006).  
<sup>4</sup> R. R. Hultgren and P. D. Desai, *Selected Thermodynamic Values and Phase Diagrams for Copper and Some of Its Binary Alloys* (International Copper Research Association, New York, 1971).

<sup>5</sup> J. Jiang, C. Gente, and R. Bormann, *Materials Science and Engineering: A* **242**, 268 (1998).  
<sup>6</sup> E. M. Lopasso, M. Caro, A. Caro, and P. E. A. Turchi, *Physical Review B* **68**, 214205 (2003).  
<sup>7</sup> V. Ozoliņš, C. Wolverton, and A. Zunger, *Phys. Rev. B* **57**, 6427 (1998).  
<sup>8</sup> M. Muzyk, D. Nguyen-Manh, K. J. Kurzydłowski, N. L. Baluc, and S. L. Dudarev, *Physical Review B* **84**, 104115 (2011).  
<sup>9</sup> O. Madelung, ed., *Landolt-Börnstein: Numerical Data and Functional Relationships in Science and Technology*, Vol. 5 (Springer

- Verlag, Heidelberg, 1996).
- <sup>10</sup> P. Fredriksson and B. Sundman, *Calphad* **25**, 535 (2001).
  - <sup>11</sup> J. Kim, Y. Koo, and B.-J. Lee, *Journal of Materials Research* **21**, 199208 (2006).
  - <sup>12</sup> I. Ansara, B. Sundman, and P. Willemin, *Acta Metallurgica* **36**, 977 (1988).
  - <sup>13</sup> G. P. Pun and Y. Mishin, *Philosophical Magazine* **89**, 3245 (2009).
  - <sup>14</sup> A. Caro, M. Caro, E. M. Lopasso, and D. A. Crowson, *Applied Physics Letters* **89**, 121902 (2006).
  - <sup>15</sup> G. Bonny, R. C. Pasianot, and L. Malerba, *Philosophical Magazine* **89**, 711 (2009).
  - <sup>16</sup> P. Olsson, I. A. Abrikosov, and J. Wallenius, *Physical Review B* **73**, 104416 (2006).
  - <sup>17</sup> T. P. C. Klaver, R. Drautz, and M. W. Finnis, *Physical Review B* **74**, 094435 (2006).
  - <sup>18</sup> G. J. Ackland, *Physical Review Letters* **97**, 015502 (2006).
  - <sup>19</sup> B. Sadigh and P. Erhart, *Physical Review B* **86**, 134204 (2012).
  - <sup>20</sup> B. Sadigh, P. Erhart, A. Stukowski, A. Caro, E. Martinez, and L. Zepeda-Ruiz, *Physical Review B* **85**, 184203 (2012).
  - <sup>21</sup> W. Petry, A. Heimig, J. Trampenau, M. Alba, C. Herzig, H. R. Schober, and G. Vogl, *Physical Review B* **43**, 10933 (1991).
  - <sup>22</sup> K. Einarsdotter, B. Sadigh, G. Grimvall, and V. Ozoliņš, *Physical Review Letters* **79**, 2073 (1997).
  - <sup>23</sup> V. Ozoliņš, *Physical Review Letters* **102**, 065702 (2009).
  - <sup>24</sup> E. Rudy and S. Windisch, *Transactions of the Metallurgical Society AIME* **242**, 953 (1968).
  - <sup>25</sup> J. L. Murray, *Bulletin of Alloy Phase Diagrams* **2**, 192 (1981).
  - <sup>26</sup> L. Kaufman and H. Nesor, *Metallurgical Transactions* **6A**, 2123 (1975).
  - <sup>27</sup> S. K. Lee and D. N. Lee, *CALPHAD* **10**, 61 (1986).
  - <sup>28</sup> S. Jönsson, *Zeitschrift für Metallkunde* **87**, 784 (1996).
  - <sup>29</sup> S. J. Zinkle and N. M. Ghoniem, *Fusion Engineering and Design* **51–52**, 55 (2000).
  - <sup>30</sup> M. Rieth, S. L. Dudarev, S. M. Gonzalez de Vicente, J. Aktaa, T. Ahlgren, S. Antusch, D. E. J. Armstrong, M. Balden, N. Baluc, M. F. Barthe, W. W. Basuki, M. Battabyal, C. S. Becquart, D. Blagoeva, H. Boldyryeva, J. Brinkmann, M. Celino, L. Ciupinski, J. B. Correia, A. De Backer, C. Domain, E. Gaganidze, C. García-Rosales, J. Gibson, M. R. Gilbert, S. Giusepponi, B. Gludovatz, H. Greuner, K. Heinola, T. Höschen, A. Hoffmann, N. Holstein, F. Koch, W. Krauss, H. Li, S. Lindig, J. Linke, C. Linsmeier, P. López-Ruiz, H. Maier, J. Matejcek, T. P. Mishra, M. Muhammed, A. Muñoz, M. Muzyk, K. Nordlund, D. Nguyen-Manh, J. Opschoor, N. Ordás, T. Palacios, G. Pintsuk, R. Pippan, J. Reiser, J. Riesch, S. G. Roberts, L. Romaner, M. Rosiński, M. Sanchez, W. Schulmeyer, H. Traxler, A. Ureña, J. G. van der Laan, L. Veleva, S. Wahlberg, M. Walter, T. Weber, T. Weitkamp, S. Wurster, M. A. Yar, J. H. You, and A. Zivelonghi, *J. Nucl. Mat.* **432**, 482 (2013).
  - <sup>31</sup> C. S. Becquart and C. Domain, *J. Nucl. Mat.* **385**, 223 (2009).
  - <sup>32</sup> A. T. Dinsdale, *CALPHAD* **15**, 317 (1991).
  - <sup>33</sup> J. M. Sanchez, F. Ducastelle, and D. Gratias, *Physica A* **128**, 334 (1984).
  - <sup>34</sup> J. M. Sanchez, *Physical Review B* **81**, 224202 (2010).
  - <sup>35</sup> G. L. Hart and R. W. Forcade, *Physical Review B* **77**, 224115 (2008).
  - <sup>36</sup> G. L. Hart and R. W. Forcade, *Physical Review B* **80**, 014120 (2009).
  - <sup>37</sup> We note that in the case of the related W–Re system it has been shown that the BCC lattice remains dynamically stable up to approximately 70% Re<sup>69</sup>.
  - <sup>38</sup> E. J. Candès and M. B. Wakin, *IEEE Signal Processing Magazine* **25**, 21 (2008).
  - <sup>39</sup> L. J. Nelson, G. L. W. Hart, F. Zhou, and V. Ozoliņš, *Physical Review B* **87**, 035125 (2013).
  - <sup>40</sup> W. Yin, S. Osher, D. Goldfarb, and J. Darbon, *SIAM Journal on Imaging sciences* **1**, 143 (2008).
  - <sup>41</sup> T. Goldstein and S. Osher, *SIAM Journal on Imaging sciences* **2**, 323 (2009).
  - <sup>42</sup> L. J. Nelson, V. Ozoliņš, C. S. Reese, F. Zhou, and G. L. W. Hart, *Physical Review B* **88**, 155105 (2013).
  - <sup>43</sup> P. Erhart and B. Sadigh, *Physical Review Letters* **111**, 025701 (2013).
  - <sup>44</sup> P. Erhart, J. Marian, and B. Sadigh, *Physical Review B* **88**, 024116 (2013).
  - <sup>45</sup> P. E. Blöchl, *Physical Review B* **50**, 17953 (1994).
  - <sup>46</sup> G. Kresse and D. Joubert, *Physical Review B* **59**, 1758 (1999).
  - <sup>47</sup> G. Kresse and J. Hafner, *Physical Review B* **47**, 558 (1993).
  - <sup>48</sup> G. Kresse and J. Furthmüller, *Computational Materials Science* **6**, 15 (1996).
  - <sup>49</sup> L. Gharaee and P. Erhart, *Journal of Nuclear Materials* **467**, 448 (2015).
  - <sup>50</sup> H. Rydberg, M. Dion, N. Jacobson, E. Schröder, P. Hyldgaard, S. Simak, D. C. Langreth, and B. I. Lundqvist, *Physical Review Letters* **91**, 126402 (2003).
  - <sup>51</sup> M. Dion, H. Rydberg, E. Schröder, D. C. Langreth, and B. I. Lundqvist, *Physical Review Letters* **92**, 246401 (2004).
  - <sup>52</sup> K. Berland and P. Hyldgaard, *Physical Review B* **89**, 035412 (2014).
  - <sup>53</sup> J. Klimeš, D. R. Bowler, and A. Michaelides, *Physical Review B* **83**, 195131 (2011).
  - <sup>54</sup> T. Björkman, *The Journal of Chemical Physics* **141**, 074708 (2014).
  - <sup>55</sup> L. Gharaee, P. Erhart, and P. Hyldgaard, *Physical Review B* **95**, 085147 (2017).
  - <sup>56</sup> J. P. Perdew, K. Burke, and M. Ernzerhof, *Physical Review Letters* **77**, 3865 (1996), erratum, *ibid.* **78**, 1396(E) (1997).
  - <sup>57</sup> J. P. Perdew, A. Ruzsinszky, G. I. Csonka, O. A. Vydrov, G. E. Scuseria, L. A. Constantin, X. Zhou, and K. Burke, *Physical Review Letters* **100**, 136406 (2008).
  - <sup>58</sup> S. Plimpton, *Journal of Computational Physics* **117**, 1 (1995).
  - <sup>59</sup> R. G. Hennig, T. J. Lenosky, D. R. Trinkle, S. P. Rudin, and J. W. Wilkins, *Physical Review B* **78**, 054121 (2008).
  - <sup>60</sup> The lattice parameters of the ground state structure at 80% W are  $a = 4.447 \text{ \AA}$ ,  $c = 13.708 \text{ \AA}$ , when referred to the conventional (15-atom) unit cell. The sole Ti atom is located at Wyckoff site  $1a$  ( $x, y, z = 0, 0, 0$ ), while two tungsten atoms occupy two Wyckoff sites of type  $2c$  ( $x = y = z$ ) each with  $x = 0.20323$  and  $x = 0.40105$ , respectively. All parameters quoted here are from calculations using the vdW-DF-cx method and do not include zero-point motion.
  - <sup>61</sup> O. Hellman, P. Steneteg, I. A. Abrikosov, and S. I. Simak, *Physical Review B* **87**, 104111 (2013).
  - <sup>62</sup> S. Kadkhodaei, Q.-J. Hong, and A. van de Walle, *Physical Review B* **95**, 064101 (2017).
  - <sup>63</sup> Z.-P. Jin and C. Qiu, *Materials Science and Technology* **9**, 378 (1993).
  - <sup>64</sup> L. Gharaee, J. Marian, and P. Erhart, *Journal of Applied Physics* **120**, 025901 (2016).
  - <sup>65</sup> We note that the semi-grand canonical and canonical ensemble could be combined to carry out sampling and evolution of the system, respectively. By alternating these techniques it would then in principle be possible to recover information about the first derivative of the free energy. The resulting scheme is, however, costly as it would commonly require many more MC cycles than the VCSGC-MC approach.

- <sup>66</sup> A. van de Walle and G. Ceder, *Review of Modern Physics* **74**, 11 (2002).
- <sup>67</sup> L.-F. Huang, B. Grabowski, J. Zhang, M.-J. Lai, C. C. Tasan, S. Sandlbes, D. Raabe, and J. Neugebauer, *Acta Materialia* **113**, 311 (2016).
- <sup>68</sup> R. Chinnappan, B. Panigrahi, and A. van de Walle, *Calphad* **54**, 125 (2016).
- <sup>69</sup> M. Ekman, K. Persson, and G. Grimvall, *Journal of Nuclear Materials* **278**, 273 (2000).